Centre Eau Terre Environnement

ÉVALUATION DE LA CONTRIBUTION DES EAUX SOUTERRAINES À LA TEMPÉRATURE DES EAUX DE SURFACE DANS DES RIVIÈRES DU QUÉBEC NORDIQUE

Par

Milad Fakhari

Thèse présenté pour l'obtention du grade

de Philosophiae Doctor (Ph.D.)

en sciences de la Terre

Jury d'évaluation

Président du jury et examinateur interne	Claudio Paniconi INRS-ETE
Examinateur externe	Michel Baraer Département de génie de la construction École de technologie supérieure Université du Québec
Examinateur externe	Grant Ferguson Department of Civil, Geological and Environmental Engineering, University of Saskatchewan
Directeur de recherche	Jasmin Raymond INRS-ETE
Codirecteur de recherche	Richard Martel INRS-ETE

REMERCIEMENTS

Tout d'abord, je tiens à remercier mon directeur, Jasmin Raymond, et mon codirecteur, Richard Martel, de m'avoir donné l'opportunité de travailler avec eux et apprendre d'eux au cours de ce projet de doctorat. Je les remercie tous les deux pour leur soutien et leurs conseils durant mes études.

Je remercier les membres de mon comité de thèse, Claudio Paniconi, Michel Baraer et Grant Ferguson d'avoir accepté d'évaluer mon travail.

Je tiens à remercier Normand Bergeron, Stephen Dugdale, Jean-Philippe Drolet, Olivier Bour et Maria Klepikova pour leurs contributions à mes articles et leur aide lors des campagnes de terrain ou de l'analyse des données.

Je remercie également Émilie Reny-Nolin, André St-Hilaire, Nicolò Giordano, Erwan Gloaguen, Maxime Claprood, Bernard Giroux, Félix-Antoine Comeau, Richard Levesque, Thomas Robert et Michel Parent pour leurs conseils et leur aide dans l'organisation du travail sur le terrain ou des analyses de laboratoire pendant mes études.

Je tiens à remercier le projet MiraNor et le programme Foncer-Tedgieer, en particulier leurs directeurs respectifs, Patrice Couture et Patrick Drogui, pour le soutien financier apporté à ce projet.

Remerciement spécial à mes parents qui m'ont toujours soutenu dans mes études. Sans vous, je ne serais pas arrivé là où je suis aujourd'hui.

Et merci à mon ami Ramin, dont l'amitié a rendu ces années plus agréables.

En terminant, je voudrais exprimer ma plus profonde gratitude à ma copine, Elahe, pour son soutien indéfectible tout au long de ce parcours difficile qui a consisté à réaliser mon doctorat.

Elahe, tes encouragements, ta compréhension, et ton amour ont été comme des piliers qui ont rendu le tout ça possible. Ta patience, tes paroles motivantes quand j'avais des doutes, et ta façon de célébrer chaque petite avancée, signifie tellement pour moi.

RÉSUMÉ

L'interaction entre les eaux souterraines (GW) et les eaux de surface (SW) des rivières peut affecter la quantité d'eau (disponibilité) et sa température, ce qui a un impact sur la vie aquatique. L'objectif de cette étude est de mieux comprendre et de quantifier l'interaction GW-SW à l'endroit de rivières nordiques affectées par les changements climatiques. Les travaux réalisés se sont attardés à identifier les zones d'écoulement de GW dans les rivières, analyser leurs caractéristiques hydrogéomorphologiques, quantifier le rôle de GW dans le bilan thermique des rivières et anticiper les changements dans l'interaction entre le GW et le SW en considérant les scénarios de changement climatique prévus. Deux rivières ont été sélectionnées pour l'étude afin d'évaluer les mécanismes physiques qui gouvernent l'interaction GW-SW selon deux climats différents et dans des conditions avec et sans pergélisol, soit pour la rivière Sainte-Marguerite localisée au sud de la province de Québec et sans pergélisol ainsi que la rivière Bérard au nord et avec un pergélisol discontinu. La méthodologie a consisté en une combinaison de techniques pour la collecte des données sur le terrain et des travaux de modélisation numérique pour simuler l'écoulement de l'eau et son comportement thermique. Les mesures sur le terrain ont consisté en l'imagerie thermique aérienne (TAI) des rivières, des mesures de radon dans l'eau pour l'identification des refuges thermiques et des zones de refroidissement, l'installation de piézomètres en berge et dans le lit des rivières ainsi que le suivi du niveau d'eau et la température avec des capteurs submersibles. De plus, des essais à l'infiltromètre et de traçage passif et actif de la chaleur dans le lit des cours d'eau ont permis de quantifier le taux d'infiltration de GW dans les rivières. Les données récoltées ont ensuite été utilisées pour le développement et l'étalonnage de modèles numériques couplés d'écoulement d'eau et de transfert de chaleur qui a permis la simulation de scénarios de changements climatiques. Selon l'analyse de TAI des rivières étudiées, 89 % des refuges thermiques identifiés et environ 60 % des zones de refroidissement étaient contrôlés par le GW. Les concentrations en radon mesurées dans les zones de refroidissement ont montré une contribution évidente de GW à la température de SW et ainsi, GW a été considérée comme le principal contributeur d'eau froide dans les rivières. La continuité du pergélisol et la forme de la vallée fluviale se sont avérées être les principaux paramètres contrôlant la distribution des refuges thermiques et des zones de refroidissement. Les simulations numériques ont démontré que le GW peut affecter le bilan thermique des rivières selon plus de 30 % pendant les vagues de chaleur au cours des saisons chaudes et à faible débit. Pour la section de la rivière Bérard modélisée en coupe, les simulations ont démontré que selon les

scénarios de changement climatique prévus, le dégel du pergélisol dans les régions septentrionales du Québec est inévitable d'ici 2100. Le dégel du pergélisol fera augmenter brusquement l'infiltration de GW dans le lit de la rivière par plus de trois ordres de grandeur. Pour la section modélisée de la rivière Sainte-Marguerite dans la zone sans pergélisol, l'augmentation d'infiltration de GW est progressive et considérable, mais inférieure à 50 %. La modification du taux d'infiltration de GW peut entrainer à l'avenir un changement de l'emplacement des zones de refroidissement des rivières et des refuges thermiques, et donc des différences dans la répartition des poissons dans les rivières.

Mots-clés : Modélisation hydrothermale, transfert de chaleur, température des cours d'eau, interaction entre les eaux de surface et les eaux souterraines, imagerie thermique aérienne, radon, traçage thermique, infiltromètre, refuge thermique, zones de refroidissement, pergélisol.

ABSTRACT

The interaction between groundwater (GW) and surface water (SW) in rivers can affect the quantity of water (availability) and its temperature, which has an impact on aquatic life. The objective of this study is to better understand and quantify the GW-SW interaction in northern rivers affected by climate change. The work conducted focused on identifying GW flow zones in rivers, analyzing their hydrogeomorphological characteristics, quantifying the role of GW in the thermal balance of rivers, and anticipating changes in the interaction between GW and SW considering projected climate change scenarios. Two rivers were selected for the study to evaluate the physical mechanisms governing GW-SW interaction under two different climates and conditions with and without permafrost, namely the Sainte-Marguerite River located in the southern part of Quebec without permafrost and the Berard River in the northern part with discontinuous permafrost. The methodology involved a combination of field data collection techniques and numerical modeling to simulate water flow and its thermal behavior. Field measurements included thermal aerial imagery (TAI) of rivers, radon measurements in the water to identify thermal refuges and cooling zones, installation of shoreline and riverbed piezometers, as well as monitoring of water level and temperature using submersible sensors. Additionally, infiltration tests and passive and active heat tracing in riverbeds were conducted to quantify the rate of GW infiltration into the rivers. The collected data were then used for the development and calibration of coupled numerical models of water flow and heat transfer, enabling the simulation of climate change scenarios. According to the analysis of TAI for the studied rivers, approximately 89% of identified thermal refuges and around 60% of cooling zones were influenced by GW. Radon concentrations measured in cooling zones showed a clear contribution of GW to the SW temperature, establishing GW as the primary contributor of cold water to the rivers. Permafrost continuity and valley shape were found to be the main parameters controlling the distribution of thermal refuges and cooling zones. Numerical simulations demonstrated that GW could affect the thermal balance of rivers by over 30% during heat waves in warm and low-flow seasons. For the modeled section of the Berard River, simulations showed that, based on projected climate change scenarios, permafrost thaw in northern Quebec regions is inevitable by 2100. The permafrost thaw will abruptly increase GW infiltration into the riverbed by more than three orders of magnitude. In the studied segment of the Sainte-Marguerite River located in the region without permafrost, the rise in GW infiltration was gradual and considerable, but below 50%. Changes in

GW infiltration rates may lead to future shifts in the location of river cooling zones and thermal refuges, thereby influencing the distribution of fish in the rivers.

Keywords: Hydrothermal modeling, heat transfer, river water temperature, interaction between SW and GW; thermal aerial imaging, radon, thermal tracing, infiltrometer, thermal refuge, cooling zones, permafrost.

TABLE DES MATIÈRES

REMERCIEMENTS ..... **III**
RÉSUMÉ ..... **V**
ABSTRACT ..... **VII**
TABLE DES MATIÈRES ..... **IX**
LISTE DES FIGURES ..... **XIII**
LISTE DES TABLEAUX ..... **XVII**
LISTE DES ÉQUATIONS ..... **XIX**
LISTE DES ABRÉVIATIONS ..... **XX**
NOMENCLATURE ..... **XXI**
1 INTRODUCTION **1**
1.1 CONTEXTE GÉNÉRAL 1
1.2 OBJECTIF DE L'ÉTUDE 3
1.3 QUESTIONS DE RECHERCHE 3
1.4 SÉLECTION DU SITE D'ÉTUDE 4
1.5 MÉTHODOLOGIE 6
1.5.1 Mesures sur le terrain *6*
1.5.2 Modélisation numérique *10*
1.6 STRUCTURE DE LA THÈSE ET RÉSULTATS ATTENDUS 12
1.7 CONTRIBUTIONS 13
1.8 RÉFÉRENCES 17
2 IDENTIFICATION OF THERMAL REFUGES AND WATER TEMPERATURE PATTERNS IN SALMONID-BEARING SUBARCTIC RIVERS OF NORTHERN QUEBEC **25**
2.1 INTRODUCTION 28
2.2 STUDY AREA 29
2.3 MATERIALS AND METHODS 34
2.3.1 Airborne imagery *34*
2.3.2 Links to landscape metrics *36*
2.4 RESULTS 37
2.4.1 Inventory of thermal heterogeneity *37*
2.4.2 Links to landscape metrics *42*
2.5 DISCUSSION 50
2.6 CONCLUSIONS 52
2.7 REFERENCES 55

3 ANALYSIS OF LARGE-SCALE GROUNDWATER-DRIVEN COOLING ZONES IN RIVERS USING THERMAL INFRARED IMAGERY AND RADON MEASUREMENTS 61

3.1 INTRODUCTION 64

3.2 STUDY AREA 65

3.3 MATERIALS AND METHODS 67

3.3.1 Aerial TIR imagery 67

3.3.2 Radon measurements 69

3.4 RESULTS 72

3.4.1 River temperature profile 72

3.4.2 Radon measurements 73

3.5 DISCUSSION 80

3.5.1 TIR imaging method 80

3.5.2 Radon measurements 81

3.6 CONCLUSIONS 85

3.7 REFERENCES 87

4 ON THE COMPLEMENTARINESS OF MULTIPLE IN-SITU TECHNIQUES FOR SPATIOTEMPORAL ASSESSMENT OF GROUNDWATER-SURFACE WATER EXCHANGES 93

4.1 INTRODUCTION 96

4.2 STUDY AREA 97

4.3 METHODOLOGY 98

4.3.1 Seepage meters 98

4.3.2 Piezometers and water level loggers 99

4.3.3 Active heat tracing 101

4.3.4 Passive heat tracing 103

4.3.5 Statistical T-test analysis 105

4.4 RESULTS 106

4.4.1 Seepage meters 106

4.4.1 Piezometers and water-level loggers 107

4.4.2 Active heat tracing 110

4.4.3 Underground temperature sensors 112

4.5 DISCUSSION 112

4.5.1 Seepage meters 113

4.5.2 Piezometer and water-level loggers 114

4.5.3 Active heat tracing 115

4.5.4 Passive heat tracing 116

4.5.5 Method comparison 116

4.6 CONCLUSIONS 118

4.7 REFERENCES 121

5 HYDROTHERMAL MODELING OF GROUNDWATER AND RIVER INTERACTIONS UNDER SHORT-TERM EXTREME ATMOSPHERIC EVENTS AND LONG-TERM CLIMATE CHANGE SCENARIOS 127

5.1 INTRODUCTION 130

5.2 STUDY SITE 132

5.3 METHODOLOGY 133

5.3.1 3D heat wave simulations 134

5.3.2 2D climate change simulations 143

5.4 RESULTS 149

5.4.1 Sensitivity analysis and calibration 149

5.4.2 Short-term heat wave of 2020 151

5.4.3 Long-term climate change scenarios 151

5.5 DISCUSSION 153

5.5.1 Assumptions and limitations 153

5.5.2 Impacts of heat waves and climate change 154

5.6 CONCLUSIONS 156

5.7 REFERENCES 159

6 DISCUSSION GÉNÉRALE 165

6.1 LIMITATIONS 165

6.2 RECOMMANDATIONS 167

6.3 CONCLUSIONS 168

6.4 RÉFÉRENCES 171

7 ANNEXE I : DONNÉES GÉOCHIMIQUES 173

8 ANNEXE II : PROPRIETES THERMIQUES 176

9 ANNEXE III : PROPRIETES HYDRAULIQUES 178

10 ANNEXE IV : DÉBIT DE LA RIVIÈRE 180

11 ANNEXE V : DONNÉES GÉOPHYSIQUE 181

12 RÉFÉRENCES EN ANNEXES 183

13 DISPONIBILITÉ DES DONNÉES 184

LISTE DES FIGURES

FIGURE 1.1 EMPLACEMENT DES RIVIÈRES ÉTUDIÉES AU QUÉBEC, MONTRANT LA DISTRIBUTION DU PERGÉLISOL (A, ADAPTÉ DE LEMIEUX ET AL., 2016) ET LA CLASSIFICATION CLIMATIQUE DE KÖPPEN (B, BASÉ SUR GOUVERNEMENT DU QUÉBEC, 2021). 5

FIGURE 1.2 ORGANIGRAMME MONTRANT LA MÉTHODOLOGIE SIMPLIFIÉE DU PROJET. 6

FIGURE 1.3 EXEMPLES DE REFUGES THERMIQUES DUS À L'INFILTRATION DE GW (A) ET À L'APPORT D'UN AFFLUENT À TEMPÉRATURE PLUS FROIDE (B). 8

FIGURE 2.1 LOCATION OF THE NORTHERN VILLAGES IN NUNAVIK REGION OF QUEBEC PROVINCE (A), AND SURVEYED SECTION OF THE BERARD RIVER (B) AND KOROC RIVER (C). 31

FIGURE 2.2 PERMAFROST MAP OF UNGAVA BAY REGION (ADAPTED FROM L'HÉRAULT ET AL., 2018). 32

FIGURE 2.3 SURFACE DEPOSITS MAP OF BERARD (A) AND KOROC (B) RIVERS (BASED ON SIGÉOM, 2022). 33

FIGURE 2.4 EXAMPLE OF A TIR IMAGE SHOWING LOCATION OF MANUALLY SELECTED THREE POINTS FOR MAKING RIVER WATER TEMPERATURE AVERAGE AND ZONES OF TEMPERATURE ANOMALIES CAUSED BY CAMERA VIBRATION. 36

FIGURE 2.5 SCHEMATIC OF RIVER GEOMORPHOLOGY PARAMETERS USED FOR CHARACTERIZATION OF THE COOLING ZONES. 37

FIGURE 2.6 LOCATION OF IDENTIFIED THERMAL REFUGES (THEIR TYPE HAS BEEN EXPLAINED IN TABLE 2.1) ON STUDIED SECTION OF BERARD (A) AND KOROC (B) RIVERS. 38

FIGURE 2.7 RIVER WATER TEMPERATURE PROFILE OF THE BERARD RIVER (A) AND KOROC RIVER (B) WITH LOCATION OF TRIBUTARIES ENTERING THE RIVER AND SURFACE DEPOSIT TYPE ON EACH SIDE OF THE RIVER (COLOR CODE FOR SOIL TYPE IS THE SAME AS IN FIGURE 2.3). 40

FIGURE 2.8 CORRELATION BETWEEN COOLING ZONE LENGTH AND NUMBER OF THERMAL REFUGES IN THE KOROC RIVER. (B) CORRELATION BETWEEN WATER TEMPERATURE DECREASE AND COOLING ZONE LENGTH IN THE BERARD RIVER. (C) CORRELATION BETWEEN COOLING ZONE LENGTH AND NUMBER OF CHANNELS ENTERING THE KOROC RIVER. 42

FIGURE 2.9 SCHEMATIC VIEW OF THE RIVER VALLEY SHOWING WALL-BASE CHANNELS TYPE A AND B AND SPRING BROOKS. 43

FIGURE 2.10 ENTRENCHMENT RATIO RANGE FOR EACH THERMAL REFUGE CLASS (ABBREVIATION OF REFUGE CLASSES IN TABLE 2.1), SHOWING MAXIMUM AND MINIMUM BY WHISKERS, FIRST AND THIRD QUARTILE BY BOX, MEDIAN BY HORIZONTAL LINE AND MEAN BY CROSS. 44

FIGURE 2.11 LAND COVER (A, BASED ON FORETOUVERTE, 2018) AND SURFACE DEPOSITS (B, BASED ON SIGÉOM, 2022) OF THE KOROC RIVER STUDY AREA. 46

FIGURE 2.12 LAND COVER (A, BASED ON FORETOUVERTE, 2018) AND SURFACE DEPOSITS (B, BASED ON SIGÉOM, 2022) OF THE BERARD RIVER STUDY AREA. 47

FIGURE 2.13 LOCATION OF KOROC RIVER THERMAL REFUGES AND COOLING ZONES ON PERMAFROST CONTINUITY MAP (ADAPTED FROM LEMIEUX ET AL., 2016). 48

FIGURE 2.14 SATELLITE IMAGERY (JUNE 2013 GOOGLE EARTH LANDSAT IMAGES) OF BERARD (A) AND KOROC (B) RIVERS SHOWING PRESENCE OF THERMOKARST LAKES AND BEADED STREAMS (EXAMPLES INSIDE YELLOW CIRCLES). 49

FIGURE 2.15 SCHEMATIC CROSS-SECTION SHOWING THE DIFFERENT TYPES OF AQUIFERS AND GW FLOW PATHS IN PRESENCE OF PERMAFROST (ADAPTED FROM LEMIEUX ET AL., 2016). 52

FIGURE 3.1 LOCATION OF THE TWO STUDIED RIVERS ON PERMAFROST DISTRIBUTION MAP (A, ADAPTED FROM LEMIEUX ET AL., 2016) AND KÖPPEN CLIMATE CLASSIFICATION MAP (B, FROM GOUVERNEMENT DU QUÉBEC, 2021) OF THE QUEBEC PROVINCE. 66
FIGURE 3.2 BEDROCK GEOLOGY ACROSS THE SAINTE-MARGUERITE RIVER (BASED ON SIGÉOM, 2022). . 67
FIGURE 3.3 BEDROCK GEOLOGY ACROSS THE BERARD RIVER (BASED ON SIGÉOM, 2022). 68
FIGURE 3.4 SCHEMATIC OF THE SEEPAGE METER DEVICE. 71
FIGURE 3.5 SCATTER PLOT SHOWING TEMPERATURE PROFILE OF SAINTE-MARGUERITE RIVER AND COLUMNS SHOWING LOCATION OF RADON SAMPLING AND MEASURED CONCENTRATION. 72
FIGURE 3.6 SCATTER PLOT SHOWING TEMPERATURE PROFILE OF BERARD RIVER AND COLUMNS SHOWING LOCATION OF RADON SAMPLING AND MEASURED CONCENTRATION (LABELS SAME AS FIGURE 3.5). 73
FIGURE 3.7 COOLING ZONES AND RADON SAMPLING POINTS OF SAINT-MARGUERITE RIVER. 74
FIGURE 3.8 BOX AND WHISKER PLOT OF RADON CONCENTRATION FOR COOLING AND WARMING ZONES OF SAINTE-MARGUERITE RIVER SHOWING SIGNIFICANT DIFFERENCE AT 95% CONFIDENCE LEVEL T-TEST. 74
FIGURE 3.9 COOLING ZONES AND RADON SAMPLING POINTS OF BERARD RIVER. 75
FIGURE 3.10 BOX AND WHISKER PLOT OF RADON CONCENTRATION FOR COOLING AND WARMING ZONES OF BERARD RIVER SHOWING SIGNIFICANT DIFFERENCE AT 95% CONFIDENCE LEVEL T-TEST. 76
FIGURE 3.11 CROSS SECTION OF SAINTE-MARGUERITE RIVER AT LOCATION OF PIEZOMETERS. 77
FIGURE 3.12 RADON CONCENTRATION OF SAINTE-MARGUERITE RIVER PIEZOMETERS AND SW. 77
FIGURE 3.13 CROSS SECTION OF BERARD RIVER AT LOCATION OF PIEZOMETERS. 78
FIGURE 3.14 WATER TEMPERATURE OF THE SIDE CHANNEL AND MAIN STEM FROM TIR IMAGING (A) AND RADON CONCENTRATION IN BERARD RIVER PIEZOMETERS AND SW (B). 78
FIGURE 4.1 LOCATION OF THE RIVER REACH OF SAINTE-MARGUERITE RIVER ON A TOPOGRAPHIC MAP OF THE RIVER CATCHMENT (RED DOT IN A) AND PLAN VIEW OF THE SELECTED RIVER REACH SHOWING LOCATION OF THE SANDBAR AND TOPOGRAPHIC CONTOUR LINES IN MASL (B). 100
FIGURE 4.2 EXAMPLE OF THERMAL RESPONSE CURVE (A) AND GRAPHICAL INTERPRETATION WITH THE MILS MODEL (B). 103
FIGURE 4.3 SCHEMATIC SECTION (A) AND PLAN (B) VIEW OF ALL METHODS USED IN THE STUDY SECTION. 105
FIGURE 4.4 BOX PLOT OF T-TEST SHOWING SIGNIFICANT DIFFERENCE OF AVERAGE MEASURED SEEPAGE RATE IN TWO RIVERBED MATERIALS USING SEEPAGE METERS. 107
FIGURE 4.5 MEASURED GW FLUX BY SEEPAGE METERS BASED ON CONDUCTED TESTS DURING MORNING AND NIGHT (A), RIVER WATER DEPTH FROM THE BOTTOM OF THE RIVER AT THE SAME TIME OF SEEPAGE METER MEASUREMENTS (B) AND BOX PLOT OF T-TEST SHOWING SIGNIFICANT DIFFERENCE OF MEASURED SEEPAGE DURING MORNING AND NIGHT USING SEEPAGE METERS (C). 108
FIGURE 4.6 PIEZOMETERS' LOCATION, CALCULATED HYDRAULIC CONDUCTIVITY FROM SLUG TESTS, MEASURED HYDRAULIC HEAD AT THE DAY OF INSTALLATIONS AND HYDRAULIC HEAD CONTOUR LINES (A) AND CALCULATED HORIZONTAL DARCY FLOW VELOCITY VECTORS BETWEEN NEIGHBORING PIEZOMETERS (B) 108
FIGURE 4.7 TEMPORAL VARIABILITY OF HORIZONTAL DARCY FLOW FROM PIEZOMETERS P1 TO P4. 109
FIGURE 4.8 TEMPORAL VARIABILITY OF VERTICAL DARCY FLOW FROM THE RIVERBED TO THE RIVER ACCORDING TO PIEZOMETERS P4 AND R2. 110

FIGURE 4.9 TEMPERATURE INCREASE OF SELECTED TEMPERATURE SENSORS DURING THE HEAT INJECTION TEST. 111
FIGURE 4.10 BOX PLOT OF T-TEST ON CALCULATED FLOW RATE (A), THERMAL CONDUCTIVITY (B) AND HEAT CAPACITY (C) IN FINE AND COARSE SAND MATERIALS AT THE STUDY SITE USING THE MILS METHOD AND ACTIVE HEAT TRACING. 111
FIGURE 4.11 RECORDED TEMPERATURE OF THE RIVERBED AT TWO DEPTHS (A) AND DAILY GW-SW INTERACTION FLUX FROM VFLUX (BLUE DOTS) AND AVERAGE YEARLY VALUE (RED LINE) (B) ACCORDING TO UNDERGROUND TEMPERATURE SENSORS. 113
FIGURE 5.1 SIMPLIFIED CROSS-SECTION OF STUDY SITES SHOWING GEOLOGICAL UNITS OF SAINTE-MARGUERITE RIVER (A) AND BERARD RIVER (B). 133
FIGURE 5.2 SCHEMATIC CROSS-SECTION VIEW OF THE RIVER SHOWING LOCATION OF INSTALLED INSTRUMENTS. 134
FIGURE 5.3 SCHEMATIZATION OF FLOW AND HEAT TRANSFER SYSTEM FOR SHORT-TERM SIMULATIONS OF 3D MODELS. 136
FIGURE 5.4 EXPECTED GROUND TEMPERATURE PROFILE OF BERARD RIVER (BASED ON SMITH ET AL., 2002; LÉVESQUE ET AL., 1990; ALLARD ET AL., 2020; GRAY ET AL., 1979). 137
FIGURE 5.5 3D MODEL GEOMETRY OF SAINTE-MARGUERITE RIVER (A) AND BERARD RIVER (B) STUDY SITE. 137
FIGURE 5.6 BOUNDARY CONDITIONS OF THE FLOW (LEFT) AND HEAT TRANSFER (RIGHT) MODELS. 140
FIGURE 5.7 INITIAL CONDITION FOR HEAT TRANSFER SIMULATION. 140
FIGURE 5.8 MESH OF 3D MODELS. 141
FIGURE 5.9 DAILY MAXIMUM TEMPERATURE RECORDED DURING THE SELECTED EXTREME ATMOSPHERIC EVENT IN SAINTE-MARGUERITE RIVER. 142
FIGURE 5.10 DAILY MAXIMUM TEMPERATURE RECORDED DURING THE SELECTED EXTREME ATMOSPHERIC EVENT IN BERARD RIVER. 143
FIGURE 5.11 SCHEMATIZATION OF FLOW AND HEAT TRANSFER SYSTEM FOR LONG-TERM SIMULATIONS WITH 2D MODELS. 144
FIGURE 5.12 INTRODUCED Ω FACTOR DESCRIBING PHASE CHANGE. 145
FIGURE 5.13 BOUNDARY CONDITIONS OF THE FLOW (LEFT) AND HEAT TRANSFER (RIGHT) MODELS. 146
FIGURE 5.14 MESH OF 2D MODELS. 147
FIGURE 5.15 PREDICTED SAINTE-MARGUERITE RIVER (SACRE-COEUR) MEAN ANNUAL TEMPERATURE (LEFT) AND TOTAL PRECIPITATION (RIGHT) BASED ON LOW, MEDIUM, AND HIGH CARBON EMISSION SCENARIOS (FROM CLIMATEDATA.CA, 2021). 148
FIGURE 5.16 PREDICTED BERARD RIVER (TASIUJAQ) MEAN ANNUAL TEMPERATURE (LEFT) AND TOTAL PRECIPITATION (RIGHT) BASED ON LOW, MEDIUM, AND HIGH CARBON EMISSION SCENARIOS (FROM CLIMATEDATA.CA, 2021). 149
FIGURE 5.17 EXAMPLE OF SENSITIVITY ANALYSIS RESULTS SHOWING EFFECT OF PARAMETERS ON SIMULATED RIVERBED TEMPERATURE OF BERARD RIVER 2D MODEL. 150
FIGURE 5.18 OBSERVED AIR (GREEN) AND RIVER WATER (BLUE) TEMPERATURE COMPARED WITH SIMULATED RIVER WATER TEMPERATURE WITH THE M:R (BLACK DASHED LINE) AND M:R+GW (SOLID BLACK LINE) MODELING APPROACHES FOR SAINTE-MARGUERITE RIVER (LEFT) AND BERARD RIVER (RIGHT). 151
FIGURE 5.19 SIMULATED GW FLOW SYSTEM OF SAINTE-MARGUERITE STUDY SITE. 152

FIGURE 5.20 RIVERBED TEMPERATURE AND GW SEEPAGE RATE OF SAINTE-MARGUERITE RIVER STUDY SITE BASED ON RCP2.6 AND RCP8.5 CLIMATE SCENARIOS. 152
FIGURE 5.21 CROSS-SECTION VIEW OF BERARD RIVER STUDY SITE SHOWING GW FLOW LINES (BLACK LINES) AND GROUND CALCULATED TEMPERATURE. 153
FIGURE 5.22 RIVERBED TEMPERATURE AND GW SEEPAGE RATE OF BERARD RIVER STUDY SITE BASED ON RCP2.6 AND RCP8.5 CLIMATE SCENARIOS. 153
FIGURE 8.1 CONDUCTIVITÉ THERMIQUE (À GAUCHE) ET CAPACITÉ THERMIQUE (À DROITE) DES ÉCHANTILLONS DE SOL DE LA RIVIÈRE SAINTE-MARGUERITE EN CONDITION IN SITU TEL QUE RÉCOLTÉS SUR LE TERRAIN. 176
FIGURE 8.2 CONDUCTIVITÉ THERMIQUE (À GAUCHE) ET CAPACITÉ THERMIQUE (À DROITE) DES ÉCHANTILLONS DE SOL DE LA RIVIÈRE BÉRARD EN CONDITIONS IN SITU TEL QUE RÉCOLTÉS SUR LE TERRAIN. 176
FIGURE 8.3 CONDUCTIVITÉ THERMIQUE (À GAUCHE) ET CAPACITÉ THERMIQUE (À DROITE) D'ÉCHANTILLONS DE SOL DES RIVIÈRES SAINTE-MARGUERITE (SM-SS#) ET BÉRARD (B-SS#) EN CONDITION COMPLÈTEMENT SATURÉE. 177
FIGURE 8.4 CONDUCTIVITÉ THERMIQUE (À GAUCHE) ET CAPACITÉ THERMIQUE (À DROITE) D'ÉCHANTILLONS DE SOL DES RIVIÈRES SAINTE-MARGUERITE (SM-SS#) ET BÉRARD (B-SS#) EN CONDITION COMPLÈTEMENT SÈCHE. 177
FIGURE 9.1 CONDUCTIVITÉ HYDRAULIQUE DES ÉCHANTILLONS DE DÉVERSEMENTS COLLECTÉS DANS LA RIVIÈRE SAINTE-MARGUERITE (À GAUCHE) ET DE LA RIVIÈRE BÉRARD (À DROITE) BASÉE SUR DES ESSAIS DE PERMÉABILITÉ. 178
FIGURE 9.2 CONFIGURATION POUR LES ESSAIS DE PERMÉABILITÉ À CHARGE CONSTANTE ET DESCENDANTE. 178
FIGURE 9.3 CONDUCTIVITÉ HYDRAULIQUE CALCULÉE AVEC LES ESSAIS LUGEONS DANS LES PIÉZOMÈTRES DE LA RIVIÈRE SAINTE-MARGUERITE (À GAUCHE) ET DE LA RIVIÈRE BÉRARD (À DROITE). 179
FIGURE 10.1 EXEMPLE DE DÉBIT DE LA RIVIÈRE SAINTE-MARGUERITE DE 6,5 M^3/S MESURÉ AVEC APPAREIL ADCP. 180
FIGURE 10.2 EXEMPLE DE DÉBIT DE LA RIVIÈRE BERARD DE 18,5 M^3/S MESURÉ AVEC APPAREIL ADCP. 180
FIGURE 11.1 EXEMPLE D'ANALYSE ERT LE LONG DE LA RIVIÈRE SAINTE-MARGUERITE. 181
FIGURE 11.2 EXEMPLE D'ANALYSE GPR PRÈS DE LA RIVIÈRE BERARD. 182

LISTE DES TABLEAUX

TABLE 2.1 THERMAL REFUGE CLASSIFICATION, SHOWING THERMAL REFUGE TYPES AND THE ABBREVIATIONS USED IN MAPS (MODIFIED FROM DUGDALE ET AL., 2015). 35

TABLE 2.2 IDENTIFIED THERMAL REFUGES 38

TABLE 2.3 IDENTIFIED COOLING ZONES' CHARACTERISTICS. 41

TABLE 3.1 CALCULATED FRACTION OF GW IN THE IDENTIFIED COOLING SECTIONS OF THE RIVERS. 79

TABLE 4.1 MEASURED GW FLOW THROUGH RIVERBED IN M/S FROM THREE CONSECUTIVE 12-HOUR SEEPAGE METER TESTS (2019). 106

TABLE 4.2 CALCULATED FLOW RATE AND MAPE OF SELECTED TEMPERATURE SENSORS. 112

TABLE 4.3 SUMMARY OF MEASURED GW SEEPAGE WITH DIFFERENT METHODS. 118

TABLE 5.1 HYDRAULIC PROPERTIES OF GEOLOGICAL UNITS. 138

TABLE 5.2 THERMAL PROPERTIES OF GEOLOGICAL UNITS' SOLIDS. 138

TABLE 5.3 ANNUAL AIR TEMPERATURE AND TOTAL PRECIPITATION INCREASE RATE BASED ON LOW AND HIGH CARBON EMISSION CLIMATE SCENARIOS FOR THE SELECTED RIVERS. 149

TABLEAU 7.1 CONCENTRATION D'ANIONS, L'ALCALINITÉ, LE PH, LA CONDUCTIVITÉ ÉLECTRIQUE, LE CARBONE ORGANIQUE ET INORGANIQUE DÉTECTÉS DANS LES ÉCHANTILLONS D'EAU DE LA RIVIÈRE SAINTE-MARGUERITE. 174

TABLEAU 7.2 CONCENTRATION D'ANIONS, L'ALCALINITÉ, LE PH, LA CONDUCTIVITÉ ÉLECTRIQUE, LE CARBONE ORGANIQUE ET INORGANIQUE DÉTECTÉS DANS LES ÉCHANTILLONS D'EAU DE LA RIVIÈRE BÉRARD. 174

TABLEAU 7.4 CONCENTRATION DES MÉTAUX DÉTECTÉS DANS LES ÉCHANTILLONS D'EAU DE LA RIVIÈRE BÉRARD. 175

TABLEAU 7.3 CONCENTRATION DES MÉTAUX DÉTECTÉS DANS LES ÉCHANTILLONS D'EAU DE LA RIVIÈRE SAINTE-MARGUERITE. 175

LISTE DES ÉQUATIONS

ÉQUATION 3.1 ……70
ÉQUATION 3.2 ……70
ÉQUATION 3.3 ……72
ÉQUATION 3.4 ……72
ÉQUATION 4.1 ……101
ÉQUATION 4.2 ……101
ÉQUATION 4.3 ……101
ÉQUATION 4.4 ……102
ÉQUATION 4.5 ……102
ÉQUATION 4.6 ……103
ÉQUATION 4.7 ……103
ÉQUATION 4.8 ……104
ÉQUATION 4.9 ……104
ÉQUATION 4.10 ……104
ÉQUATION 4.11 ……104
ÉQUATION 5.1 ……139
ÉQUATION 5.2 ……139
ÉQUATION 5.3 ……139
ÉQUATION 5.4 ……139
ÉQUATION 5.5 ……144
ÉQUATION 5.6 ……145
ÉQUATION 5.7 ……145
ÉQUATION 5.8 ……145

LISTE DES ABRÉVIATIONS

Abréviation	Terme anglais	Terme français
ADCP	Acoustic doppler current profiler	Profileur de courant acoustique à effet Doppler
A.T.	Air temperature	Température de l'air
CMIP6	Coupled model intercomparison project phase 6	Phase 6 du projet de comparaison de modèles couplés
DTS	Distributed temperature sensing	Détection de température distribuée
ERT	Electrical resistivity tomography	Tomographie de résistivité électrique
FO	Fiber-optic	Fibre optique
GPR	Ground-penetrating radar	Radar à pénétration de sol
GW	Groundwater	Eau(x) souterraine(s)
GW.S.R.	Groundwater seepage rate of the riverbed	Taux d'infiltration des eaux souterraines du lit de la rivière
MAPE	Mean absolute percentage error	Erreur moyenne en pourcentage absolu
MILS	Moving infinite line source	Source linéique infinie et mobile
R.B.T.	Riverbed temperature	Température du lit de la rivière
RCP	Representative concentration pathway	Voie de concentration représentative
SW	Surface water	Eau(x) de surface
TAI	Thermal aerial imagery	Imagerie thermique aérienne
TIR	Thermal infrared	Infrarouge thermique
T.P.	Total precipitation	Précipitations totales

NOMENCLATURE

Symbole	Définition	Unités
A	Amplitude	(-)
c	Capacité thermique spécifique	(J/kg K)
C	Concentration de radon	(Bq/L)
D	Diffusivité thermique	(m^2/s)
E	Puissance de chauffage linéaire constant	(W/m)
f	Rapport entre les infiltrations de l'eau souterraine et le débit de la rivière	(-)
i	Gradient hydraulique	(m/m)
k	Conductivité hydraulique	(m/s)
L	Période du signal de température	(s)
P	Probabilité calculée du test *T*	(-)
q	Débit spécifique	(m/s)
Q	Débit	(m^3/s)
r	Distance entre l'emplacement de la sonde de température à (x,y) et la source de chaleur située à (0,0)	(m)
S	Surface	(m^2)
t	Temps	(s)
T	Température	(°C)
v	Vitesse	(m/s)

V	Volume d'eau collectée	(m^3)
z	Profondeur	(m)
α	Niveau de signification	(-)
β	Intervalle de confiance	(-)
Δt	Décalage temporel	(s)
ΔT	Différence de température	(°C)
Δz	Différence de profondeur	(m)
ε	Porosité	(-)
λ	Conductivité thermique	(W/m K)
ρ	Densité	(kg/m^3)
ω	Facteur décrivant le changement de phase de l'eau entre -4 °C et 0 °C	(-)

Indice	Définition
bg	background
eq	equilibrium
f	frozen
gw	groundwater
h	horizontal
i	ice
ob	observed
r	ratio
s	Soil particles
si	simulated
sw	surface water
t	At time=t
uf	Unfrozen
v	vertical
w	water
z	At depth=z

1 INTRODUCTION

1.1 Contexte général

Les eaux souterraines (GW) et les eaux de surface (SW) sont connectées et leur niveau d'interconnexion dépend du climat et du contexte géologique (Brunke et al., 1997; Hayashi et al., 2002; Spanoudaki et al., 2009). La recharge de GW par les précipitations ou par l'infiltration de SW dans l'aquifère sous-jacent (downwelling) ainsi que la décharge de GW vers le SW (upwelling) sont deux processus importants du cycle hydrologique dans les bassins versants. GW se mélange aux cours d'eau par le biais d'écoulements verticaux et latéraux dans la zone souterraine située en dessous et à proximité d'un cours d'eau. Cette zone est appelée la zone hyporhéique, qui connecte le cours d'eau à d'autres environnements terrestres (Merill et al., 2014; Brunke et al, 1997). Les liens GW et SW à travers la zone hyporhéique transitoire sont contrôlés par plusieurs processus complexes d'interactions (Sterte et al., 2018). Les changements dans la quantité ou la qualité de GW dus aux changements climatiques (réduction ou augmentation des précipitations et de la recharge) ou à l'activité humaine (extraction ou contamination de l'eau) peuvent avoir une influence directe sur la quantité, la qualité et la température de SW des lacs ou des rivières (Havril et al., 2018; Saha et al., 2017; Hancock, 2002).

Dans les régions arides ou semi-arides, l'importance de la contribution de GW aux rivières (débit de base) est plus évidente. Les précipitations et le ruissèlement sont limités dans les régions arides et semi-arides et le débit de base provenant de GW est la principale composante (source d'eau) dans les rivières permanentes de ces régions (McDonough et al., 2011). Dans les régions arides ou semi-arides, les échanges entre GW et SW sont plus importants en termes de quantité d'eau et de débits des rivières, en particulier pendant les saisons d'étiage (Lamontagne et al., 2005; Hassan et al., 2014; Tian et al., 2015).

Dans d'autres conditions climatiques où les précipitations sont plus abondantes, l'effet de l'interaction GW-SW est plus visible sur la qualité et la température de SW. GW peut jouer un rôle de moyen de transport pour la contamination ou la chaleur vers SW. La vitesse d'écoulement de GW est lente (selon Harter (2003), entre 0,15 et 15 mètres par jour dans un aquifère sablonneux ou graveleux), comparativement à celle de SW. Ainsi, la contamination telle que les métaux lourds, les engrais ou les pesticides provenant de zones avec des activités minières ou agricoles peuvent apparaitre dans les rivières après plusieurs années, par le biais de l'écoulement de GW, même si la source de contamination a été précédemment éliminée (Goel, 2006).

Le régime thermique des rivières joue également un rôle important dans la santé des écosystèmes aquatiques. L'interaction GW-SW est l'un des éléments qui contrôlent le bilan thermique des rivières. GW a moins de variations quotidiennes et saisonnières que SW, donc GW peut être considéré comme une source d'eau froide ou chaude respectivement en été et en hiver (Caissie, 2006).

La présence de pergélisol peut rendre le processus d'interaction GW-SW plus complexe (Walvoord et al., 2012). En outre, le pergélisol est une source importante de carbone organique, qui peut être rejeté dans les rivières et l'atmosphère et affecter la qualité de l'eau et de l'air en raison de sa fonte. De plus, avec le dégel du pergélisol, GW peut-être mieux connecté aux plans d'eau et le débit du GW peut-être considérablement augmenté en raison de la perméabilité plus élevée du sol non gelé par rapport à son état gelé. L'effet du dégel du pergélisol sur la qualité et de la quantité de l'eau des rivières est donc important (Neilson et al., 2018).

Les variations spatiotemporelles de l'interaction entre le GW et le SW peuvent avoir un impact significatif sur les écosystèmes fluviaux (Tang et al., 2015; Zhang et al., 2004; Hynes, 1983). Par exemple, la population et la répartition des habitats de poissons dans les rivières et les lacs peuvent être affectées par l'écoulement de GW vers les rivières. GW peut influencer la répartition des poissons, le succès de la reproduction, la biomasse et la productivité, le comportement des poissons ainsi que leurs déplacements dans les rivières pendant les températures extrêmes en saison chaude, ou lorsque les rivières sont affectées par la glace, ainsi que dans les rivières à faible débit (Power et al., 1999; Saltveit et, al., 2013; Willms et al., 2016).

L'interaction GW-SW est un processus complexe qui dépend de plusieurs paramètres de contrôle et joue un rôle important dans l'hydrologie des bassins versants (Brunke et al., 1997; Spanoudaki et al., 2009; Evans et al., 2017). Disposer d'un modèle hydrothermique multidimensionnel entièrement couplé considérant GW et SW est utile pour une meilleure compréhension des écoulements d'eau, des transferts de chaleur et du transport des contaminants dans le bassin versant (McKenzie et al., 2007; Cho et al., 2010; Gualtieri, 2010; Tian et al., 2012; Grenier et al., 2018). De meilleures perspectives peuvent être évaluées pour les écosystèmes aquatiques à l'aide de tels modèles en considérant différents scénarios résultant des changements climatiques, de l'urbanisation et des impacts humains (Hancock, 2002; Walvoord et al., 2007; Hunt et al., 2016; Dugdale et al., 2017; Havril et al., 2018).

1.2 Objectif de l'étude

Cette recherche se concentre sur les rivières situées dans la province de Québec, au Canada. Les rivières du Québec sont connues pour l'abondance de salmonidés (truites de rivière, truites de lac et truites de mer, ombles chevaliers et saumons de l'Atlantique). La pêche est importante pour les communautés locales et génère des revenus issus de la pêche sportive (Poesch et al., 2016). La plage de température optimale pour la croissance des salmonidés varie selon les espèces, mais se situe généralement entre 7 °C et 17 °C, tandis que la plage de température létale est de 25 à 27 °C (Jensen et al., 1989; Finstad et al., 2012; Nyanti et al., 2018). En été, les salmonidés font face à un stress thermique dans les rivières en raison de températures d'eau plus élevées en moyenne. Cela affecte leur croissance et menace même leur survie. Certaines zones spécifiques dans les rivières constituent des refuges thermiques qui permettent aux poissons de se sentir plus à l'aise pour grandir et survivre dans certains cas extrêmes (Lorenz et al., 1989; Geist et al., 1998). L'une des principales sources de refuges thermiques est la contribution de GW aux rivières par résurgence dans le lit de la rivière ou infiltration latérale. (Power et al., 1999; Saltveit et al., 2013). Les conditions extrêmes sont susceptibles de se produire plus fréquemment dans les rivières du Québec en raison des changements climatiques (Power, 1999; Palko et al., 2017). Par conséquent, l'objectif de cette étude est de comprendre et quantifier le processus affectant les refuges thermiques contrôlés par GW dans les rivières, ainsi que l'échange de chaleur de GW vers SW, et d'anticiper l'interaction future entre le GW et le SW en raison du changement climatique, ce qui revêt d'un intérêt fondamental.

1.3 Questions de recherche

En lien avec l'objectif de l'étude, les questions de recherche fondamentale sont les suivantes :

1. À quels endroits l'interaction entre le GW et le SW est-elle plus susceptible de se produire dans une rivière ?
2. Quels paramètres géomorphologiques ont un impact sur l'interaction GW-SW ?
3. Comment peut-on mesurer l'étendue spatiotemporelle de l'interaction GW-SW ?
4. Dans quelle mesure GW peut-elle influencer le bilan thermique des rivières ?
5. À quel point un scénario de changement climatique peut-il modifier le flux de GW vers une rivière ?

1.4 Sélection du site d'étude

Le pergélisol est présent dans de vastes zones du Québec (Figure 1.1), avec différentes classes de continuité et d'épaisseur (Hachem et al., 2009; O'Neill et al., 2019). Pour étudier l'effet de la couche de pergélisol sur l'écoulement de GW et son impact sur SW, deux sites ont été sélectionnés : l'un dans une zone sans pergélisol et l'autre dans une zone de pergélisol discontinu.

Le climat peut également affecter l'interaction GW-SW (Sophocleous, 2002). Le Québec couvre une vaste superficie et les températures et les précipitations varient en fonction de la latitude. Il existe trois principaux types des climats au Québec selon la classification de Köppen (Figure 1.1). Le sud du Québec (en dessous de 51° de latitude) présente un climat continental froid et humide. Le nord du Québec, entre 51° et 58° de latitude, a un climat continental subpolaire, tandis qu'au-dessus de 58° de latitude, on retrouve un climat de toundra polaire.

Selon les données météorologiques disponibles entre 1960 et 2010, on observe une tendance à la hausse de la température moyenne annuelle, ce qui montre l'effet du réchauffement climatique au Québec (Yagouti et al., 2003). La température annuelle moyenne a augmenté de 1,3 °C au cours de cette période dans la province de Québec. Les parties sud-ouest et ouest de la province sont les zones présentant les plus grandes variations, avec une augmentation légèrement supérieure à 1,5 °C. Dans le reste de la province, l'augmentation a été plus faible, variant de 0,9 °C à 1,5 °C (Yagouti et al., 2006). L'augmentation de la température concerne principalement la température minimale moyenne (entre 1,5 °C et 2,1 °C), tandis que la température maximale moyenne n'a pas changé autant (de 0,9 °C à 1,5 °C). Les tendances à partir de 1960 ne sont cependant pas claires dans le nord du Québec. À partir de 1992, on a observé une augmentation significative de la température minimale moyenne au Nunavik (par exemple, une augmentation d'environ 3 °C à Kuujjuaq et à Salluit, basé sur Bégin, 2006). Les indices de changements ont été principalement observés en hiver et se traduisent par des cycles de gel-dégel et de fonte de neige plus précoces.

Comme le nord et le sud du Québec ont des climats différents, l'augmentation de la température moyenne annuelle résultant du changement climatique a des effets différents sur ces deux régions (Lepage et al., 2012). Dans le sud, la température maximale moyenne de l'air et de l'eau des rivières est plus élevée que dans le nord. Par conséquent, dans les rivières du sud du Québec, la plage de température létale de 25 °C à 27 °C pour les poissons peut être atteinte plus tôt et plus fréquemment pendant l'été. Cependant, le changement climatique dans le nord influence directement et indirectement les cycles de vie des poissons arctiques et les schémas

de migration (Reist et al., 2006). Bien que la température létale puisse ne pas être atteinte, la température maximale plus élevée ainsi qu'une période chaude plus longue ont un impact sur la croissance et la productivité des poissons atlantiques (Poesch et al., 2016).

Les deux rivières sélectionnées pour les études principales sont la rivière Sainte-Marguerite, située à environ 200 km au nord-est de Québec, et la rivière Bérard qui se jette dans la baie d'Ungava près de Tasiujaq. La rivière Sainte-Marguerite se trouve dans le sud du Québec, dans une zone sans pergélisol et dans un climat continental froid et humide. La rivière Bérard se situe dans le nord de la province, dans une zone avec un pergélisol discontinu et dans un climat continental subpolaire. Ces deux rivières ont été choisies pour représenter deux conditions différentes. De plus, ce ne sont pas des rivières de grande taille et elles sont accessibles par la route, ce qui les rend appropriées pour les travaux sur le terrain et la collecte de données.

Par ailleurs, la rivière Koroc, située à la limite du pergélisol continu et discontinu près de Kangiqsualujjuaq, a été partiellement étudiée car l'accès à cette rivière était difficile et, en raison de sa taille, elle ne se prêtait pas à l'instrumentation.

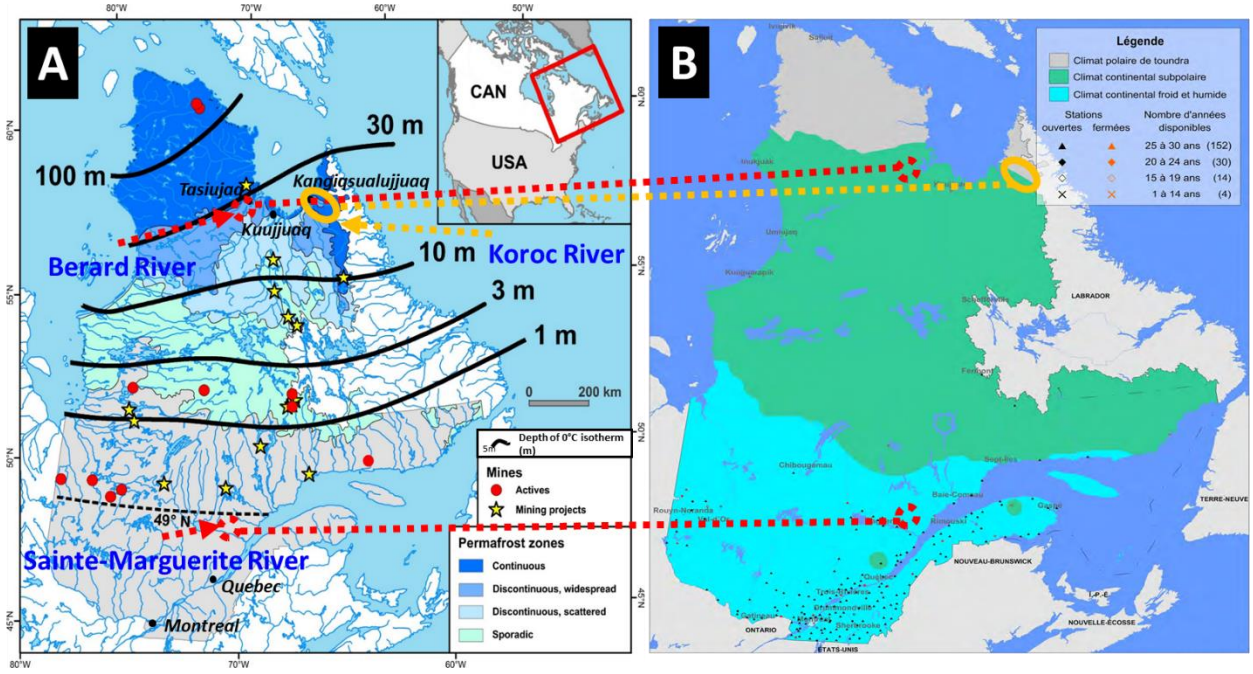

Figure 1.1 **Emplacement des rivières étudiées au Québec, montrant la distribution du pergélisol (A, adapté de Lemieux et al., 2016) et la classification climatique de Köppen (B, basé sur Gouvernement du Québec, 2021).**

1.5 Méthodologie

La méthodologie mise de l'avant est une combinaison de collecte de données sur le terrain et de modélisation numérique prédictive. La méthodologie générale de la recherche est résumée dans l'organigramme de la Figure 1.2.

Étant donné qu'il existe peu de données disponibles pour les rivières sélectionnées dans la littérature, une collecte de données a été nécessaire. Des analyses ont été effectuées sur les données collectées puis utilisées pour l'étalonnage et la construction de modèles numériques pour mieux comprendre les processus d'écoulement et de transfert de chaleur. Ils ont permis de simuler le mouvement de l'eau et de la chaleur dans les milieux poreux aux abords et dans les rivières selon différentes conditions, et ainsi de prédire le comportement futur de la ressource en eau.

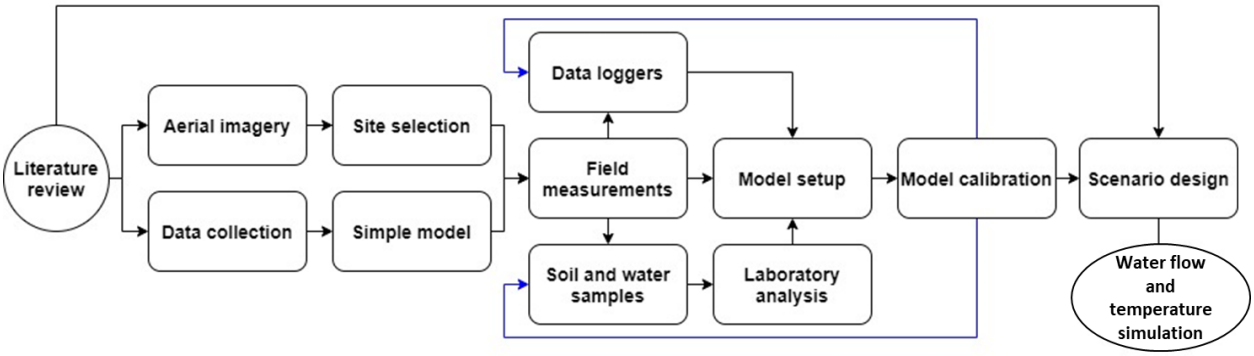

Figure 1.2 Organigramme montrant la méthodologie simplifiée du projet.

1.5.1 Mesures sur le terrain

Les mesures de terrain effectuées peuvent être regroupées en deux catégories principales : les mesures à grande échelle et celles à petite échelle. Les mesures à grande échelle sont celles qui couvrent des zones plus vastes, de quelques kilomètres le long du parcours d'une rivière à une rivière entière, comme l'imagerie aérienne. Les mesures à petite échelle sont des mesures ponctuelles sur un site sélectionné avec une couverture de moins d'un kilomètre carré, par exemple la collecte de données de température à différents endroits et à différentes profondeurs. Le travail a commencé par des mesures à grande échelle afin de mieux définir les zones présentant le plus grand potentiel d'interaction GW-SW et d'identifier les sites appropriés pour les mesures à petite échelle. Une approche multitechnique a été utilisée dans cette thèse afin d'éviter les limites potentielles des méthodes et de suggérer des méthodes fiables pour les travaux futurs. La méthode et les équipements utilisés sont résumés dans les sections suivantes.

1.5.1.1 Analyse de l'imagerie thermique aérienne

Les images thermiques des rivières ont été obtenues à l'aide d'une caméra FLIR SC660 montée sur un hélicoptère. Les l'imagerie thermique aérienne (TAI) des rivières, avec une empreinte pixel de 0,5×0,5 m au sol, permettent de détecter les zones d'eau froide dans les rivières, appelées refuges thermiques, et d'évaluer la distribution spatiale de température de la rivière.

Les refuges thermiques dans les rivières peuvent avoir différentes sources, comme l'eau plus froide des petits affluents ou les infiltrations de GW dans les rivières (Dugdale et al., 2013). L'analyse des images thermiques (infrarouges) et optiques (visuelles normales) de la rivière permet de détecter la localisation et le type de refuges thermiques. Par exemple, dans la Figure 1.3-A, l'eau froide provenait des infiltrations de GW, alors que dans la Figure 1.3-B, l'eau froide provient d'un affluent de rivière plus petit. Les TAI doivent être pris dans des conditions de faible débit dans les rivières et au cours d'une journée chaude afin que la différence entre les zones froides des refuges thermiques et la température de l'eau de la rivière soit plus prononcée.

En outre, les TAI ont été utilisés pour tracer le profil de température latérale de la rivière en attribuant une température moyenne de l'eau à chaque photo et en définissant la température en fonction de la distance par rapport à l'aval. Le paradigme du réchauffement asymptotique (Fullerton et al., 2015) suppose que la température de l'eau de la rivière devrait augmenter progressivement à mesure que l'on descend en aval de la rivière en raison des échanges d'énergie à l'interface air-eau. Cependant, dans des conditions naturelles, les profils de température le long de la rivière s'écartent fréquemment de cette tendance, principalement en raison de l'advection provenant des interactions GW-SW. En conséquence, des zones de refroidissement importantes, s'étendant de 100 à 1000 mètres, sont souvent observées dans le profil de température d'une rivière. Ainsi, les régions du profil de température de la rivière présentant une diminution de température ont été utilisées pour identifier la présence et l'étendue d'une zone de refroidissement. Tout comme les refuges thermiques qui sont considérés comme des zones avec un potentiel plus élevé d'infiltration de GW, les zones de refroidissement peuvent être considérées comme des zones avec une infiltration de GW, ce qui les rend plus adaptées à une analyse approfondie et à la mise en place d'instruments sur le terrain.

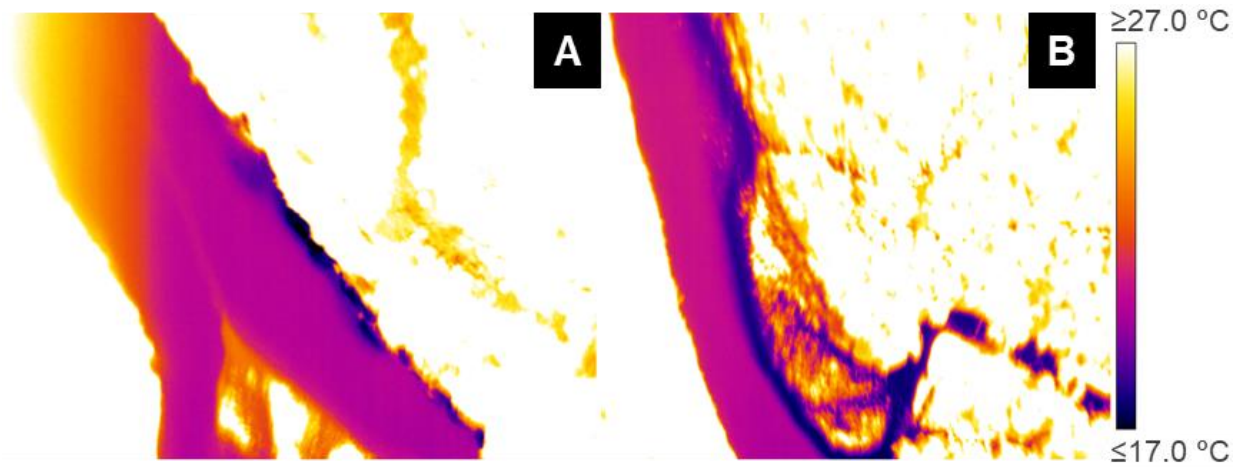

Figure 1.3 **Exemples de refuges thermiques dus à l'infiltration de GW (A) et à l'apport d'un affluent à température plus froide (B).**

1.5.1.1 Mesures du radon

Au cours des deux ou trois dernières décennies, le radon naturellement dissous dans l'eau a été identifié comme étant un traceur fiable pour l'étude des interactions GW-SW (Wu et al., 2004; Ortega et al., 2015; Bertln et al., 1994). L'échantillonnage de l'eau et l'analyse de sa concentration en radon ont été utilisés pour vérifier si GW est la source des zones de refroidissement des rivières identifiées par TAI. Plusieurs points d'échantillonnage ont été sélectionnés dans les zones de refroidissement de chaque rivière afin de confirmer la présence d'infiltrations de GW dans ces zones. De plus, des échantillons de GW prélevés à partir de piézomètres installés en berge ont été utilisés pour calculer la concentration en radon dans GW. En ayant la concentration de radon dans GW ainsi que les concentrations en amont et en aval d'une portion de rivière, la fraction de GW dans la rivière a été quantifiée en calculant le bilan de masse du radon. Cette fraction peut donner une estimation approximative du taux d'infiltration de GW dans un tronçon de rivière lorsque le débit de la rivière est connu.

1.5.1.2 Piézomètres et enregistreurs de niveau d'eau

Des piézomètres ont été mis en place pour mesurer les niveaux et la température de GW en continu via des enregistreurs de données, ainsi que pour échantillonner GW pour en vérifier la qualité si nécessaire. De plus, des essais à choc hydraulique ont été effectués dans chaque puits pour évaluer la conductivité hydraulique des sédiments. Les piézomètres ont été installés à différentes profondeurs et emplacements afin de pouvoir évaluer la direction d'écoulement de GW et mesurer l'interaction GW-SW. Les gradients hydrauliques et les directions d'écoulement

de GW peuvent varier continuellement en fonction des régimes d'écoulement des rivières à fort et faible débit (haut et bas niveau). Pour surveiller ces changements, des enregistreurs de niveau d'eau ont été installés à l'intérieur des piézomètres et dans la rivière. Le capteur de pression mesure la hauteur d'eau par rapport à un point de référence. La pression hydraulique et la température jouent un rôle important dans la quantification des interactions GW-SW (Rosenberry et al., 2008; Lee et al., 2013). Les enregistreurs de données ont été programmés pour obtenir une mesure toutes les 15 minutes sur une période d'un an (de l'été 2019 à l'été 2020) afin de comparer l'interaction GW-SW pendant les saisons chaude et froide.

1.5.1.3 Traçage thermique passif

Les enregistreurs de température fournissent des données continues de température de l'eau, de l'air et du sol. Ils ont été enfouis dans le sol (dans le lit et les berges des rivières) à différentes profondeurs. L'analyse des séries chronologiques de températures enregistrées à deux profondeurs différentes et la résolution d'équations de transfert de chaleur 1D ont permis d'évaluer un taux d'infiltration d'eau entre les deux capteurs (Gordon et al., 2012).

1.5.1.4 Traçage thermique actif

Dans des études précédentes, des câbles en fibre optique (FO) chauffés activement ont été utilisés pour cartographier les variations spatiales des interactions GW-SW (Read et al., 2014; Gao et al., 2017; Simon et al., 2021a). Cependant, pour la thèse, nous avons conçu et utilisé une solution alternative aux câbles FO normalement couteux. La solution proposée consistait à fixer des capteurs de température à un câble chauffant et à enterrer le câble dans le lit de la rivière. La courbe de réponse de température enregistrée à chaque capteur a été analysée avec l'équation de la source linéique infinie et mobile (MILS), précédemment employée avec les mesures pour les câbles FO (Simon et al., 2021b). L'utilisation de la méthode MILS permet de quantifier les propriétés thermiques des sédiments et du flux de GW à l'emplacement de chaque capteur de température.

1.5.1.5 Infiltromètre (Seepage meter)

L'infiltromètre (*Seepage meter*), utilisé depuis les années 1940, est un dispositif simple conçu pour mesurer directement le flux de GW à travers les sédiments du lit d'un cours d'eau en isolant une zone spécifique du lit de la rivière (Rosenberry, 2008; Rosenberry et al., 2008). Des essais

d'infiltration ont été effectués pour quantifier l'eau que la rivière perd ou gagne à travers son lit. Les infiltromètres installés à différents endroits dans le lit de la rivière permettent d'observer la variabilité du flux d'eau (échange) entre la rivière et l'aquifère situé sous-jacent. En raison de leur simplicité et de leur facilité d'utilisation dans les rivières peu profondes et non turbulentes, l'utilisation d'infiltromètres demeure une méthode largement répandue pour mesurer le flux de GW dans les petits cours d'eau. En outre, la simplicité de l'analyse des données a contribué à leur popularité (USGS, 2014).

1.5.1.6 Échantillonnage du sol et mesures en laboratoire

Des forages peu profonds, d'une profondeur maximale d'environ 3 m, ont été réalisés pour prélever des échantillons de différentes couches de sédiments. Les échantillons ont été prélevés par enfoncement d'une cuillère fendue comportant un cylindre métallique de 7 cm de diamètre et 15 cm de hauteur. Les échantillons de sédiments ont été analysés pour déterminer leurs caractéristiques hydrauliques et thermiques, telles que la conductivité hydraulique et thermique, la porosité et la capacité thermique. En mesurant le poids sec et le poids saturé des échantillons ainsi que leur volume, les propriétés physiques des sédiments tels que la densité apparente, la porosité et la saturation en eau ont être déterminées. La courbe de distribution des grains et le pourcentage de matière organique ont également été évalués. La conductivité hydraulique des échantillons de sédiment a été quantifiée par des essais à charge constante sur les cylindres de sol prélevés (Larrabee, 2010). La capacité et la conductivité thermique des échantillons de sol ont été mesurées à l'aide de la sonde à aiguille KD2 pro (Decagon Devices, 2016). Toutes ces données ont servi à définir la gamme de propriétés physiques des unités géologiques peu profonde du lit de la rivière et des rives considérées comme intrants des modèles numériques développés pour la simulation des processus physiques aux sites à l'étude.

1.5.2 Modélisation numérique

GW et SW sont considérés comme une seule source (Winter et al., 1999; Sophocleous, 2002) et l'interconnexion hydrogéologique et thermique entre eux est un critère important pour la santé de l'écosystème aquatique (Brookfield et al., 2009). Bien que les autorités responsables de l'eau essaient de gérer GW et SW comme une source unique, la modélisation des flux est souvent effectuée séparément par simplicité et pour gagner du temps et limiter les efforts (Hunt et al., 2016). Une méthode courante pour relier les modèles de GW et de SW consiste à utiliser les résultats d'un modèle comme entrée pour l'autre. De cette manière, seules les simulations

moyennes dans le temps ou à long terme (c'est-à-dire en régime permanent) sont significatives (Hunt et al., 2016). Au Québec, de grandes variations saisonnières de la température de l'air (selon le Gouvernement du Québec (2021), de -20 °C à 20 °C) et les changements dans le sol gelé dus aux cycles de gel-dégel peuvent affecter le bilan thermique de GW et de SW. Par conséquent, les modèles en régime permanent ne peuvent pas simuler le système de façon adéquate. Montrer les changements à court terme, tels que les variations quotidiennes et saisonnières de la température de l'eau dans les rivières affectées par les infiltrations de GW, nécessite des simulations GW-SW couplées de l'écoulement et du transfert de chaleur. Plusieurs études combinant l'écoulement et le transfert de chaleur dans un modèle hydrothermique, où la combinaison de l'écoulement en nappe libre et en milieu poreux ont vu le jour ces dernières années. Les modèles couplés d'écoulement de GW et de transfert de chaleur sont bien établis et ont été largement utilisés dans des études hydrogéologiques (Ingebritsen et al., 2006) et géothermiques (Raymond et al., 2014), ainsi que récemment pour la simulation de l'évolution du pergélisol (Kurylyk et al., 2016). Des modèles combinés GW-SW ont été utilisés pour évaluer la quantité de ressources en eau disponibles (Rathfelder, 2016), la qualité de l'eau (Wayland et al., 2002), et les effets du changement climatique sur l'avenir des ressources en eau (Havril et al., 2018). Cependant, l'étude du transfert de chaleur dans un système d'écoulement couplé GW-SW demeure limitée. Un modèle hydrothermal transitoire d'écoulement couplé à surface libre en milieu poreux qui prend en compte différents types d'écoulement, comporte un grand nombre de variables est complexe. Un modèle entièrement dépendant du temps (en régime transitoire) de l'écoulement à surface libre (ou SW) et en milieu poreux (ou GW), intégrant les transferts thermiques, a été développé pour la simulation d'évènements atmosphériques à court terme (vagues de chaleur) enregistrés sur les sites d'étude sélectionnés. De plus, des modèles couplés d'écoulement et de transfert de chaleur qui considèrent l'effet du changement de phase dû aux cycles de gel-dégel ont été utilisés pour simuler des scénarios de changement climatique à long terme. Les résultats de simulations ont démontré l'effet du GW sur l'atténuation de la température de l'eau des rivières pendant les vagues de chaleur et les changements dans le système d'écoulement de GW ainsi que son interaction avec les rivières en raison du changement climatique.

Le modèle couplé d'écoulement et de transfert de chaleur a impliqué la résolution des équations de bilan d'eau et d'énergie pour le système. Pour gérer le couplage complexe de toutes les équations, le logiciel COMSOL Multiphysics a été utilisé. Ce logiciel utilise un modèle numérique en éléments finis, bien adapté à diverses applications d'ingénierie (COMSOL, 2023). Des modèles hydrothermaux en 2D du milieu poreux considérant le changement de phase ainsi que

des modèles hydrothermaux en 3D de surfaces libres et en milieu poreux ont été utilisés pour simuler respectivement des scénarios de changement climatique à long terme et des simulations à court terme de vagues de chaleur. Les modèles ont été calibrés sur la base de mesures de terrain telles que la température de l'eau et du sol et le taux d'infiltration d'eau à travers le lit de la rivière. Les différents scénarios ont été conçus sur la base des modèles climatiques disponibles et des vagues de chaleur enregistrées.

1.6 Structure de la thèse et résultats attendus

Le but de cette recherche doctorale était de mieux comprendre l'influence de GW sur l'apparition de refuges thermiques dans les rivières, dans un contexte de contraste climatique allant des conditions continentales humides aux conditions subarctiques où le pergélisol peut affecter les mécanismes d'écoulement et de transfert de chaleur. Les résultats de la thèse qui répondent aux questions de recherche sont présentés dans quatre articles scientifiques. Les trois premiers répondent aux trois premières questions de recherche, et le quatrième article répond aux deux dernières questions.

Dans **le premier article (chapitre 2)**, l'objectif était d'évaluer l'effet de l'interaction GW-SW, ainsi que des refuges thermiques contrôlés par GW, sur l'atténuation de la température de l'eau dans les rivières du nord avec la présence de pergélisol discontinu. Cela a été réalisé en cartographiant la distribution des refuges thermiques et des zones de refroidissement dans SW à l'aide de TAI et en examinant le contexte hydromorphologique du paysage riverain de chaque refuge et de chaque zone de refroidissement pour identifier les paramètres critiques affectant la température de l'eau. L'article met en évidence le rôle de GW dans la variabilité de la température des rivières dans une région sujette au pergélisol.

Dans **le deuxième article (chapitre 3)**, l'objectif était de vérifier la présence de GW dans les zones de refroidissement identifiées à l'aide de TAI et d'estimer le taux d'infiltration de GW dans la rivière au sein de ces zones en mesurant la concentration en radon dans GW et SW. Le deuxième article suit la même méthode d'analyse de TAI que le premier article et présente une étude de cas commune avec le premier article (la rivière Bérard).

Dans **le troisième article (chapitre 4)**, deux objectifs ont été définis. Le premier objectif était d'utiliser une combinaison de méthodes simples, courantes et populaires pour démontrer la variation spatiale et temporelle de l'interaction GW-SW à l'échelle d'une petite portion de rivière et d'évaluer l'importance de ces variations mineures dans le taux d'interaction entre GW et SW. Le deuxième objectif était de comparer les méthodes et d'évaluer leurs avantages et leurs

limitations pour définir la variation spatiale et temporelle de l'interaction GW-SW à l'échelle d'une petite portion de rivière. Cela a également inclus l'évaluation du potentiel de notre nouvelle approche, qui utilise une combinaison de capteurs de température et d'un câble chauffant, comme outil de traçage thermique actif dans les lits de rivière pour quantifier le taux d'interaction GW-SW ainsi que les propriétés thermiques des matériaux du lit de la rivière. Le site d'étude dans cet article était une petite portion de la rivière Sainte-Marguerite, sélectionnée en fonction des résultats du deuxième article, qui comprenait une étude à grande échelle de la même rivière.

Dans **le quatrième article (chapitre 5)**, nous avons utilisé un modèle entièrement couplé d'écoulement et de transfert de chaleur entre GW et SW pour quantifier le rôle de GW dans la neutralisation de l'augmentation de la température de l'eau des rivières causée par des phénomènes atmosphériques (vagues de chaleur). De plus, nous avons évalué les changements dans le système de GW anticipés en considérant des scénarios de changement climatique et de leurs effets sur la température de l'eau des rivières. Les sites d'étude sélectionnés sur les rivières Bérard et Sainte-Marguerite ont été choisis en fonction des résultats du deuxième article. Les modèles ont été calibrés sur la base d'études sur le terrain menées en utilisant les méthodes décrites dans le troisième article.

1.7 Contributions

Les résultats de cette étude ont été publiés dans des revues et présentés lors de différentes conférences et ateliers.

Articles de revues scientifiques :

Fakhari, M.; Raymond, J.; Martel, R.; Dugdale, S.J.; Bergeron, N. (2022) Identification of Thermal Refuges and Water Temperature Patterns in Salmonid-Bearing Subarctic Rivers of Northern Quebec. Geographies, 2, 528-548. https://doi.org/10.3390/geographies2030032. **Publié.**

Fakhari, M.; Raymond, J.; Martel, R.; Drolet, J.-P.; Dugdale, S.J.; Bergeron, N. (2023) Analysis of Large-Scale Groundwater-Driven Cooling Zones in Rivers Using Thermal Infrared Imagery and Radon Measurements. Water, 15, 873. https://doi.org/10.3390/w15050873. **Publié.**

Fakhari, M.; Raymond, J.; Martel, R., Klepikova, M. Bour, O. (2023) On the Complementariness of Multiple In-Situ Techniques for Spatiotemporal Assessment of Groundwater-Surface Water Exchanges. **Soumis au *Hydrogeology Journal***.

Fakhari, M.; Raymond, J.; Martel, R. (2023) Hydrothermal Modeling of Ground and River Interactions Under Short-Term Extreme Atmospheric events and Long-Term Climate Change Scenarios. **Soumis au *Journal of Hydrology***.

Autres publications :

Fakhari M., Raymond J. and Martel, R. (2019) Assessment of groundwater contribution to surface water quantity, quality and temperature in rivers of northen Quebec (part 1). Rapport des travaux de terrain de l'été 2019, soumis au conseil d'administration de Tasiujaq, le 15 novembre, Tasiujaq, Québec, Canada, 10 p.

Fakhari M., Raymond J. and Martel, R. (2021) Assessment of groundwater contribution to river water temperature. Article de conférence, Geoniagara 2021, 26-29 septembre, Niagara Falls, Ontario, Canada.

Fakhari M., Raymond J. and Martel, R. (2021) Assessment of groundwater contribution to surface water quantity, quality and temperature in rivers of northen Quebec (part 2). Rapport des travaux de terrain de l'été 2021, soumis au conseil d'administration de Tasiujaq, le 9 novembre, Tasiujaq, Québec, Canada, 12 p.

Reny-Nolin E., Fakhari M., Raymond J. and Martel, R. (2022) Identifying groundwater discharge in the Berard River, Tasiujaq. Article pour le magazine Taqralik publié par la Société Makivik, Kuujjuaq, Québec, Canada. Available online at: https://www.makivvik.ca/article/identifying-groundwater-discharge-in-tasiujaqs-berard-river/

Présentation orale :

Fakhari M., Raymond J. and Martel, R. (2019) Assessment of groundwater contribution to rivers in terms of water quantity, quality and temperature. 20th Journée des Sciences de la Terre et de l'Environnement (JSTE), 14 mars, Université Laval, Québec, Québec, Canada.

Fakhari M., Raymond J. and Martel, R. (2019) Assessment of groundwater contribution to surface water quantity, quality and temperature in rivers of northern Quebec. 22nd edition of the annual conference of Centre Interuniversitaire de Recherche sur le Saumon Atlantique (CIRSA), 8 et 9 mai, Laval University, Quebec, Quebec, Canada.

Fakhari M., Raymond J. and Martel, R. (2019) Évaluation de la contribution des eaux souterraines face à la quantité, la qualité, et la température de l’eau des rivières du nord du Québec. 2019 édition de Mon projet nordique, 23 mai, Musée de la Civilisation, Québec, Québec, Canada.

Fakhari M., Raymond J. and Martel, R. (2020) Assessment of groundwater contribution to rivers in terms of water quantity, quality and temperature. 1st Virtual Eastern Canadian Symposium on Water Quality, 6 novembre, 2020, en ligne.

Fakhari M., Raymond J. and Martel, R. (2021) Assessment of groundwater contribution to rivers in terms of water quantity, quality and temperature. Réunion Comité de suivi MiraNor, 25 octobre, en ligne.

Fakhari M., Raymond J. and Martel, R. (2021) Assessment of groundwater contribution to river water temperature. 2021 Virtual Atlantic and Eastern Canadian Symposium on Water Quality Research, 2&3 novembre, en ligne.

Fakhari M., Raymond J. and Martel, R. (2022) Assessment of groundwater contribution to rivers in terms of water quantity, quality and temperature. Réunion Comité de suivi MiraNor, 7 avril , en ligne.

Fakhari M., Raymond J. and Martel, R. (2022) Identification of thermal refuges in the rivers by use of thermal aerial imagery. GAC-MAC-IAH-CNC-CSPG joint meeting, 15-18 mai, Halifax, Nova Scotia, Canada.

Présentations par affiche :

Fakhari M., Raymond J. and Martel, R. (2019) Assessment of groundwater contribution to surface water quantity, quality and temperature in rivers of northen Quebec. 33rd Eastern Canadian Symposium on Water Quality, 25&26 octobre, Concordia University, Quebec, Quebec, Canada.

Fakhari M., Raymond J. and Martel, R. (2019) Assessment of groundwater contribution to rivers in terms of water quantity, quality and temperature. 1st Congres Eau Terre Environnement, 7&8 novembre, Institut national de la recherche scientifique (INRS), Québec, Québec, Canada.

Fakhari M., Raymond J. and Martel, R. (2019) Assessment of groundwater contribution to surface water quantity, quality and temperature in rivers of northen Quebec. 1st Canadian Geothermal Students' Day, 21&22 novembre, Institut national de la recherche scientifique (INRS), Québec, Québec, Canada.

Fakhari M., Raymond J. and Martel, R. (2020) Assessment of groundwater contribution to rivers in terms of water quantity, quality and temperature. 21st Journée des Sciences de la Terre et de l'Environnement (JSTE), 12 mars, Institut national de la recherche scientifique (INRS), Québec, Québec, Canada.

Fakhari M., Raymond J. and Martel, R. (2021) Assessment of groundwater contribution to river water temperature. Geoniagara Conference, 26-29 septembre, Scotiabank Convention Centre, Niagara Falls, Ontario, Canada.

Fakhari M., Raymond J. and Martel, R. (2023) Assessment of groundwater contribution to rivers in terms of water quantity, quality and temperature. Journée Scientifique de l'INRS, 10 mars, Institut national de la recherche scientifique (INRS), Québec, Québec, Canada.

Fakhari M., Raymond J. and Martel, R. (2023) Assessment of groundwater contribution to rivers in terms of water quantity, quality and temperature. Le Grand rendez-vous INRS, 22&23 mars, Hôtel Le Germain Charlevoix, Baie-Saint-Paul, Québec, Canada.

1.8 Références

Bégin Y. (2006) « Le changement climatique en cours dans le Nord du Québec. » Centre d'études nordiques, Rapport présenté à Parliamentary Commission on Transport and the Environment, under the theme of the impact of global warming in Northern Quebec, Assemblée nationale du Québec, September 18 Quebec, Quebec, Canada. http://www.uqac.ca/vision2025/forumnordique/ccnq.pdf.

Bertln C. et Bourg A.C.M. (1994) « Radon-222 and Chloride as Natural Tracers of the Infiltration of River Water into an Alluvial Aquifer in Which There Is Significant River/Groundwater Mixing. » Environmental Science and Technology 28 (5): 794-798. doi:10.1021/es00054a008.

Breton M.-P., Cloutier G. et Waygood E.O.D. (2017) « QUEBEC. » Chapitre de livre Dans Climate risks and adaptation practices for the Canadian transportation sector, K. Palko and D.S. Lemmen (Eds.), 181-216. Government of Canada. Ottawa, ON, Canada.

Brookfield A.E., Sudicky E.A., Park Y.J. et Conant B. (2009) « Thermal transport modelling in a fully integrated surface/subsurface framework. » Hydrological Processes 23 (15): 2150-2164. doi:10.1002/hyp.7282.

Brunke M. et Gonser T. (1997) « The ecological significance of exchange processes between rivers and groundwater. » Freshwater Biology 37 (1): 1-33. doi:10.1046/j.1365-2427.1997.00143.x.

Caissie D. (2006) « The thermal regime of rivers: A review. » Freshwater Biology 51 (8): 1389-1406. doi:10.1111/j.1365-2427.2006.01597.x.

Cho J., Mostaghimi S. et Kang M.S. (2010) « Development and application of a modeling approach for surface water and groundwater interaction. » Agricultural Water Management 97 (1): 123-130. doi:10.1016/j.agwat.2009.08.018.

COMSOL (2023) « COMSOL Multiphysics® Simulation Software. » Manuel du logiciel, COMSOL, Inc., MA, USA. https://www.comsol.com/comsol-multiphysics.

Decagon Devices Inc. (2016) « KD2 Pro Thermal Properties Analyzer. » Manuel de l'appareil. Decagon Devices, Inc WA, United States https://library.metergroup.com/Manuals/13351_KD2%20Pro_Web.pdf.

Dugdale S.J., Bergeron N.E. et St-Hilaire A. (2013) « Temporal variability of thermal refuges and water temperature patterns in an Atlantic salmon river. » Remote Sensing of Environment 136. Elsevier Inc.: 358-373. doi:10.1016/j.rse.2013.05.018. http://dx.doi.org/10.1016/j.rse.2013.05.018.

Dugdale S.J., Hannah D.M. et Malcolm I.A. (2017) « River temperature modelling: A review of process-based approaches and future directions. » Earth-Science Reviews 175 (January). Elsevier: 97-113. doi:10.1016/j.earscirev.2017.10.009. https://doi.org/10.1016/j.earscirev.2017.10.009.

Evans S.G. et Ge S. (2017) « Contrasting hydrogeologic responses to warming in permafrost and seasonally frozen ground hillslopes. » Geophysical Research Letters 44 (4): 1803-1813. doi:10.1002/2016GL072009.

Finstad A.G. et Jonsson B. (2012) « Effect of incubation temperature on growth performance in Atlantic salmon. » Marine Ecology Progress Series 454 (1): 75-82. doi:10.3354/meps09643.

Fullerton A.H., Torgersen C.E., Lawler J.J., Faux R.N., Steel E.A., Beechie T.J., Ebersole J.L. & Leibowitz S.G. (2015) « Rethinking the longitudinal stream temperature paradigm region-wide comparison of thermal infrared imagery reveals unexpected complexity of river temperatures. » Hydrological Processes 29 (22): 4719–4737. doi:10.1002/hyp.10506.

Gao T., Liu J., Zhang T., Hu Y., Shang J., Wang S., Xiao X., Liu C., Kang S., Sillanpaa M. et Zhang Y. (2017) « Estimating interaction between surface water and groundwater in a permafrost region using heat tracing methods. » The Cryosphere (September): 1-24. doi:10.5194/tc-2017-176.

Geist D.R. et Dauble D.D. (1998) « Redd site selection and spawning habitat use by fall chinook salmon: The importance of geomorphic features in large rivers. » Environmental Management 22 (5): 655-669. doi:10.1007/s002679900137.

Goel P. K. (2006) « Water Pollution: Causes, Effects and Control. » New Age International, second. New Delhi, Delhi: New Age International. https://books.google.ca/books?id=4R9CYYoiFCcC&dq=groundwater+and+river+polutipon+caused+by+agricultural+activities&lr=&source=gbs_navlinks_s.

Gordon R.P., Lautz L.K., Briggs M.A. et McKenzie J.M. (2012) « Automated calculation of vertical pore-water flux from field temperature time series using the VFLUX method and computer program. » Journal of Hydrology 420-421. Elsevier B.V.: 142-158. doi:10.1016/j.jhydrol.2011.11.053. http://dx.doi.org/10.1016/j.jhydrol.2011.11.053.

Gouvernement du Québec (2021) « Normales climatiques 1981-2010. » Ministère de l'Environnement et de la Lutte contre les changements climatiques. Page Web, consulté le 1er septembre 2021 à l'adresse https://www.environnement.gouv.qc.ca/climat/normales/climat-qc.htm.

Grenier C., Anbergen H., Bense V., Chanzy Q., Coon E., Collier N., Costard F., Ferry M., Frampton A., Frederick J., Gonçalvès J., Holmén J., Jost A., Kokh S., Kurylyk B., McKenzie, John Molson J., Mouche E., Orgogozo L., Pannetier R., Rivière A., Roux N., Rühaak W., Scheidegger J., Selroos J.O., Therrien R., Vidstrand P. et Voss C. (2018) « Groundwater flow and heat transport for systems undergoing freeze-thaw: Intercomparison of numerical simulators for 2D test cases. » Advances in Water Resources 114. Elsevier Ltd: 196-218. doi:10.1016/j.advwatres.2018.02.001. https://doi.org/10.1016/j.advwatres.2018.02.001.

Gualtieri C. (2010) « Numerical simulation of transition layer at a fluid-porous interface. » Article de conférence dans Modelling for Environment's Sake: Proceedings of the 5th Biennial Conference of the International Environmental Modelling and Software Society, iEMSs 2010, 1:399-409. Ottawa, Canada.

Hachem S., Allard M. et Duguay C. (2009) « Using the modis land surface temperature product for mapping permafrost: An application to northern Québec and Labrador, Canada. » Permafrost and Periglacial Processes 20 (4): 407-416. doi:10.1002/ppp.672.

Hancock P.J. (2002) « Human impacts on the stream-groundwater exchange zone. » Environmental Management 29 (6): 763-781. doi:10.1007/s00267-001-0064-5.

Harter T. (2003) « Basic Concepts of Groundwater Hydrology. » Reference Sheet 8083. Oakland, California, U.S: UNIVERSITY OF CALIFORNIA Division of Agriculture and Natural Resources. doi:10.3733/ucanr.8083. http://groundwater.ucdavis.edu/files/156562.pdf.

Hassan, S.M.T., Lubczynski M.W, Niswonger R.G. et Su Z. (2014) « Surface-groundwater interactions in hard rocks in Sardon Catchment of western Spain: An integrated modeling approach. » Journal of Hydrology 517. Elsevier B.V.: 390-410. doi:10.1016/j.jhydrol.2014.05.026. http://dx.doi.org/10.1016/j.jhydrol.2014.05.026.

Havril T., Tóth A., Molson J.W., Galsa A. et Mádl-Szőnyi J. (2018) « Impacts of predicted climate change on groundwater flow systems: Can wetlands disappear due to recharge reduction? » Journal of Hydrology 563: 1169-1180. doi:10.1016/j.jhydrol.2017.09.020.

Hayashi M. et Rosenberry D.O. (2002) « Effects of ground water exchange on the hydrology and ecology of surface water. » Ground Water 40 (3): 309-316. doi:10.1111/j.1745-6584.2002.tb02659.x.

Hunt R.J., Westenbroek S.M., Walker J.F., Selbig W.R., Regan R.S, Leaf A.T. et Saad D.A. (2016) « Simulation of climate change effects on streamflow, groundwater, and stream temperature using GSFLOW and SNTEMP in the Black Earth Creek Watershed, Wisconsin. » Scientific Investigations Report 2016–5091. USGS, Reston, Virginia. doi:10.3133/sir20165091. http://pubs.er.usgs.gov/publication/sir20165091.

Hynes H.B.N. (1983) « Groundwater and stream ecology. » Hydrobiologia 100 (1): 93-99. doi:10.1007/BF00027424.

Ingebritsen S.E., Sanford W.E. et Neuzil C.E. (1998) « Groundwater in Geologic Processes. » Second Edition. Cambridge University Press, Cambridge, U. K. doi:10.1111/j.1468-8123.2009.00253.x.

Jensen A.J., Johnsen B.O. et Saksgard L. (1989) « Temperature requirements in Atlantic salmon (Salmo salar), brown trout (Salmon trutta), and Arctic char (Salvelinus alpinus) from hatching to initial feeding compared with geographic distribution. » Canadian Journal of Fisheries and Aquatic Sciences 46 (5): 786-789. doi:10.1139/f89-097.

Kurylyk B.L., Hayashi M., Quinton W.L., McKenzie J.M. et Voss C.I. (2016) « Influence of vertical and lateral heat transfer on permafrost thaw, peatland landscape transition, and groundwater flow. » Water Resources Research 52: 1-20. doi:10.1002/2015WR018057.

Lamontagne S., Leaney F.W. et Herczeg A.L. (2005) « Groundwater-surface water interactions in a large semi-arid floodplain: Implications for salinity management. » Hydrological Processes 19 (16): 3063-3080. doi:10.1002/hyp.5832.

Larrabee A.C. (2010) « Determination of hydraulic conductivity using the Permeafor. » Thèses de maîtrise. 598, University of New Hampshire, Durham. https://scholars.unh.edu/thesis/598

Lee J.Y., Lim H.S., Yoon H.L. et Park Y. (2013) « Stream water and groundwater interaction revealed by temperature monitoring in agricultural areas. » Water (Switzerland) 5 (4): 1677-1698. doi:10.3390/w5041677.

Lemieux J.-M., Fortier R, Talbot-Poulin M.-C., Molson J.W., Therrien R, Ouellet M, Banville D, Cochand M et Murray R. (2016) « Groundwater occurrence in cold environments: examples from Nunavik, Canada. » Hydrogeology Journal 24 (6): 1497-1513. doi:10.1007/s10040-016-1411-1.

Lepage M.-P. et Bourdages L. (2011) « Interpretation of Climate Change Scenarios in order to Improve Agricultural Risk Management. » Rapport préparé pour Centre de référence en agriculture et agroalimentaire du Québec (CRAAQ) Québec, Canada..

Lorenz J.M. et Filer J.H. (1989) « Spawning Habitat and Redd Characteristics of Sockeye Salmon in the Glacial Taku River, British Columbia and Alaska. » Transactions of the American Fisheries Society 118 (5): 495-502. doi:10.1577/1548-8659(1989)118<0495:sharco>2.3.co;2. http://citeseerx.ist.psu.edu/viewdoc/download?doi=10.1.1.586.132&rep=rep1&type=pdf.

McDonough O.T., Hosen J.D. et Palmer M.A. (2011) « Temporary streams: The hydrology, geography, and ecology of non-perennially flowing waters. » Chapitre de livre dans River Ecosystems: Dynamics, Management and Conservation. Hannah S. Elliot et Lucas E. Martin. 259-290. Hauppauge, New York, United States: Nova Science Publishers, Incorporated.

McKenzie J.M., Voss C.I. et Siegel D.I. (2007) « Groundwater flow with energy transport and water-ice phase change: Numerical simulations, benchmarks, and application to freezing in peat bogs. » Advances in Water Resources 30 (4): 966-983. doi:10.1016/j.advwatres.2006.08.008.

Merill L. et Tonjes D.J. (2014) « A review of the hyporheic zone, stream restoration, and means to enhance denitrification. » Revues critiques dans Environmental Science and Technology 44 (21). Stony Brook: 2337-2379. doi:10.1080/10643389.2013.829769. https://commons.library.stonybrook.edu/techsoc-articles.

Neilson B.T., Cardenas B.M., O'Connor M.T., Rasmussen M.T., King T.V. et Kling G.W. (2018) « Groundwater Flow and Exchange Across the Land Surface Explain Carbon Export Patterns in Continuous Permafrost Watersheds. » Geophysical Research Letters 45 (15): 7596-7605. doi:10.1029/2018GL078140.

Nyanti L., Soo C.L., Ahmad-Tarmizi N.N., Abu-Rashid N.N.K., Ling T.Y., Sim S.F., Grinang J., Ganyai T. et Lee K.S.P. (2018) « Effects of water temperature, dissolved oxygen and total suspended solids on juvenile barbonymus schwanenfeldii (Bleeker, 1854) and Oreochromis Niloticus (Linnaeus, 1758). » AACL Bioflux 11 (2): 394-406.

O'Neill H.B., Wolfe S.A. et Duchesne C. (2019) « New ground ice maps for Canada using a paleogeographic modelling approach. » Cryosphere 13 (3): 753-773. doi:10.5194/tc-13-753-2019.

Ortega L., Manzano M., Custodio E., Hornero J. et Rodríguez-Arévalo J. (2015) « Using 222Rn to identify and quantify groundwater inflows to the Mundo River (SE Spain). » Chemical Geology

395. Elsevier B.V.: 67-79. doi:10.1016/j.chemgeo.2014.12.002. http://dx.doi.org/10.1016/j.chemgeo.2014.12.002.

Poesch M.S., Chavarie L., Chu C., Pandit S.N. et Tonn W. (2016) « Climate Change Impacts on Freshwater Fishes: A Canadian Perspective. » Fisheries 41 (7): 385-391. doi:10.1080/03632415.2016.1180285. http://dx.doi.org/10.1080/03632415.2016.1180285.

Power G., Brown R.S. et Imhof J. G. (1999) « Groundwater and fish - Insights from northern North America. » Hydrological Processes 13 (3): 401-422. doi:10.1002/(SICI)1099-1085(19990228)13:3<401::AID-HYP746>3.0.CO;2-A.

Rathfelder K. (2016) « Modelling Tools for Estimating Effects of Groundwater Pumping on Surface Waters. » Publication technique Rapport parMinistry of Environment, Water Science Series WSS2016-09, Province of British Columbia.

Raymond J. et Therrien R. (2014) « Optimizing the design of a geothermal district heating and cooling system located at a flooded mine in Canada. » Hydrogeology Journal 22 (1): 217-231. doi:10.1007/s10040-013-1063-3.

Read T., Bour O., Selker J.S., Bense V.F., Le Borgne T., Hochreutener R. et Lavenant N. (2014) « Active-distributed temperature sensing to continuously quantify vertical flow in boreholes. » Water Resources Research 50: 3706-3713. doi:10.1002/2014WR015273.

Reist J.D., Wrona F.J., Prowse T.D., Power M., Dempson J.B., Beamish R.J., King J.R., Carmichael T.J. et Sawatzky C.D. (2006) « General effects of climate change on arctic fishes and fish populations. » Ambio 35 (7): 370-380. doi:10.1579/0044-7447(2006)35[370:GEOCCO]2.0.CO;2.

Rosenberry D.O. (2008) « A seepage meter designed for use in flowing water. » Journal of Hydrology 359 (1-2): 118-130. doi:10.1016/j.jhydrol.2008.06.029.

Rosenberry D.O. et LaBaugh J.W. (2008) « Field Techniques for Estimating Water Fluxes Between Surface Water and Ground Water Techniques and Methods 4 – D2. » Publication technique Rapport par U.S. Geological Survey, Reston, Virginia..

Saha G.C., Li J., Thring R.W., Hirshfield F. et Paul S.S. (2017) « Temporal dynamics of groundwater-surface water interaction under the effects of climate change: A case study in the Kiskatinaw River Watershed, Canada. » Journal of Hydrology 551. Elsevier B.V.: 440-452. doi:10.1016/j.jhydrol.2017.06.008. http://dx.doi.org/10.1016/j.jhydrol.2017.06.008.

Saltveit S.J. et Brabrand A. (2013) « Incubation, hatching and survival of eggs of Atlantic salmon (Salmo salar) in spawning redds influenced by groundwater. » Limnologica 43 (5). Elsevier GmbH.: 325-331. doi:10.1016/j.limno.2013.05.009. http://dx.doi.org/10.1016/j.limno.2013.05.009.

Schnoor J.L. (1996) Environmental Modeling: Fate and Transport of Pollutants in Water, Air, and Soil. Journal of Environment Quality. Vol. 26. New York: John Wiley and Sons. doi:10.2134/jeq1997.00472425002600040037x.
https://www.cabdirect.org/cabdirect/abstract/19971902407.

Simon N., Bour O., Lavenant N., Porel G., Nauleau B., Pouladi B., Longuevergne L. et Crave A. (2021a) « Numerical and Experimental Validation of the Applicability of Active-DTS Experiments to Estimate Thermal Conductivity and Groundwater Flux in Porous Media. » Water Resources Research 57 (1): 1-27. doi:10.1029/2020WR028078.

Simon N., Bour O., Faucheux M., Lavenant N., Lay H.L., Fovet O, Thomas Z. et Longuevergne L. (2021b) « Combining passive- and active-DTS measurements to locate and quantify groundwater discharge into streams. » Hydrology and Earth System Sciences Discussions (June): 1-36. doi:10.5194/hess-2021-293.

Sophocleous M. (2002) « Interactions between groundwater and surface water: The state of the science. » Hydrogeology Journal 10 (1): 52-67. doi:10.1007/s10040-001-0170-8.

Spanoudaki K., Stamou A.I. et Nanou-Giannarou A. (2009) « Development and verification of a 3-D integrated surface water-groundwater model. » Journal of Hydrology 375 (3-4). Elsevier B.V.: 410-427. doi:10.1016/j.jhydrol.2009.06.041. http://dx.doi.org/10.1016/j.jhydrol.2009.06.041.

Sterte E.J., Johansson E., Sjöberg Y., Karlsen R.H. et Laudon H. (2018) « Groundwater-surface water interactions across scales in a boreal landscape investigated using a numerical modelling approach. » Journal of Hydrology 560. The Authors: 184-201. doi:10.1016/j.jhydrol.2018.03.011. https://doi.org/10.1016/j.jhydrol.2018.03.011.

Tang Q., Kurtz W., Brunner P., Vereecken H. et Hendricks Franssen H.J. (2015) « Characterisation of river-aquifer exchange fluxes: The role of spatial patterns of riverbed hydraulic conductivities. » Journal of Hydrology 531. Elsevier B.V.: 111-123. doi:10.1016/j.jhydrol.2015.08.019. http://dx.doi.org/10.1016/j.jhydrol.2015.08.019.

Tian W., Li X., Cheng G.D., Wang X.S. et Hu B. X. (2012) « Coupling a groundwater model with a land surface model to improve water and energy cycle simulation. » Hydrology and Earth System Sciences 16 (12): 4707-4723. doi:10.5194/hess-16-4707-2012.

Tian Y., Zheng Y., Wu B., Wu X., Liu J. et Zheng C. (2015) « Modeling surface water-groundwater interaction in arid and semi-arid regions with intensive agriculture. » Environmental Modelling and Software 63. Elsevier Ltd: 170-184. doi:10.1016/j.envsoft.2014.10.011. http://dx.doi.org/10.1016/j.envsoft.2014.10.011.

USGS. 2014. « Field Techniques and Measurments. » http://pubs.usgs.gov/tm/04d02/.

Walvoord M.A. et Striegl R.G. (2007) « Increased groundwater to stream discharge from permafrost thawing in the Yukon River basin: Potential impacts on lateral export of carbon and nitrogen. » Geophysical Research Letters 34 (12). doi:10.1029/2007GL030216.

Walvoord M.A., Voss C.I. et Wellman T.P. (2012) « Influence of permafrost distribution on groundwater flow in the context of climate-driven permafrost thaw: Example from Yukon Flats Basin, Alaska, United States. » Water Resources Research 48 (7): 1-17. doi:10.1029/2011WR011595.

Wayland K.G., Hyndman D.W., Boutt D., Pijanowski B.C. et Long D.T. (2002) « Modelling the impact of historical land uses on surface-water quality using groundwater flow and solute-

transport models. » Lakes and Reservoirs: Research and Management 7 (3): 189-199. doi:10.1046/j.1440-1770.2002.00187.x.

Willms T. et Whitworth G. (2016) « Mapping of critical summer thermal refuge habitats for Chinook salmon, Coho salmon, steelhead and bull trout in the Nicola River Watershed - 2016. » Rapport du Habitat Stewardship Program for Species at Risk. Vol. 3. Fraser Basin Council: Kamloops, BC, Canada.

Winter T.C., Harvey J.W., Franke O.L. et Alley W.M. (1999) « Ground Water and Surface Water A Single Resource. » Publication technique Rapport par U.S. Geological Survey, circular : 1139. Denver, Colorado. doi:10.1088/1751-8113/44/8/085201. https://pubs.er.usgs.gov/publication/cir1139.

Wu Y., Wen X. et Zhang Y. (2004) « Analysis of the exchange of groundwater and river water by using Radon-222 in the middle Heihe Basin of northwestern China. » Environmental Geology 45 (5): 647-653. doi:10.1007/s00254-003-0914-y.

Yagouti, A., Boulet O.G. & Vescovi L., (2006) « Homogénéisation des séries de températures et analyse de la variabilité spatiotemporelle de ces séries au Québec méridional. » Rapport No. 4 CONSORTIUM OURANOS, Ministère du Développement durable, de l'Environnement et des Parcs du Québec. Québec, Québec, Canada.

Zhang Y.K. et Schilling K. (2004) « Temporal scaling of hydraulic head and river base flow and its implication for groundwater recharge. » Water Resources Research 40 (3): 1-9. doi:10.1029/2003WR002094.

2 IDENTIFICATION OF THERMAL REFUGES AND WATER TEMPERATURE PATTERNS IN SALMONID-BEARING SUBARCTIC RIVERS OF NORTHERN QUEBEC

Identification des refuges thermiques et des profils de température de l'eau dans les rivières subarctiques à salmonidés du nord du Québec

Milad Fakhari [1,*], Jasmin Raymond [1], Richard Martel [1], Stephen J. Dugdale [2], Normand Bergeron [1]

1 Institute national de la recherche scientifique, Centre Eau Terre Environnement, Quebec City, QC G1K 9A9, Canada

2 School of Geography, University of Nottingham, Nottingham NG7 2RD, UK

* Correspondance: milad.fakhari@inrs.ca

Publié dans ***geographies*** 2022, 2, 528–548

Publié le 2 septembre 2022

doi.org/10.3390/ geogra-phies2030032

Contribution des auteurs :

Conceptualisation, Milad Fakhari, Jasmin Raymond et Richard Martel; méthodologie, Stephen J. Dugdale et Normand Bergeron; analyse formelle, Milad Fakhari; conservation des données, Milad Fakhari; rédaction - préparation de la version originale, Milad Fakhari; rédaction - révision et édition, Milad Fakhari, Jasmin Raymond, Richard Martel, Stephen J. Dugdale et Normand Bergeron; visualisation, Milad Fakhari. Tous les auteurs ont lu et approuvé la version publiée du manuscrit.

Lien entre l'article ou les articles précédents et le suivant :

Dans cet article, nous avons identifié les refuges thermiques et les zones de refroidissement à l'aide de TAI. Dans le prochain article, les zones de refroidissement identifiées sur l'une des rivières étudiées dans cet article (la rivière Bérard) ont été analysées à l'aide d'une autre méthode (mesures de radon) en guise de comparaison et d'alternative au TAI et à sa vérification.

Abstract: Salmonids can experience thermal stress during extreme weather conditions in summer. This may affect their growth and even threaten their survival. Cool water zones in rivers constitute thermal refuges, allowing fish to be more comfortable to grow and survive in extreme events. Therefore, identifying and understanding the spatiotemporal variability of discrete thermal refuges and larger scale cooling zones in rivers is of fundamental interest. This study allowed to analyze thermal refuges as well as cooling zones in two salmonid rivers in a subarctic climate by use of thermal infrared (TIR) imagery. The two studied rivers are the Koroc and Berard Rivers, in Nunavik, Quebec, Canada. On the 17 km studied section of the Berard River, four thermal refuges and five cooling zones were detected, covering 46% of the surveyed section of the river. On the 41 km section studied for the Koroc River, 67 thermal refuges and five cooling zones were identified which represent 32% of the studied section of the river. 89% of identified thermal refuges and about 60% of cooling zones are groundwater-controlled. Continuity of permafrost and shape of the river valley were found to be the main parameters controlling the distribution of refuges and cooling zones. These data provide important insights into planning and conservation measures for the salmonid population of subarctic Nunavik rivers.

Résumé : Les salmonidés peuvent subir un stress thermique lors de conditions météorologiques extrêmes en été. Cela peut affecter leur croissance et même menacer leur survie. Les zones d'eau fraiche dans les rivières constituent des refuges thermiques, permettant aux poissons d'être plus à l'aise pour grandir et survivre lors d'évènements extrêmes. L'identification et la compréhension de la variabilité spatiotemporelle des refuges thermiques discrets et des zones de refroidissement à plus grande échelle dans les rivières sont donc d'un intérêt fondamental. Cette étude a permis l'analyse les refuges thermiques ainsi que les zones de refroidissement dans deux rivières à salmonidés dans un climat subarctique en utilisant l'imagerie infrarouge thermique (TIR). Les deux rivières étudiées sont les rivières Koroc et Bérard, au Nunavik, Québec, Canada. Sur la section étudiée de 17 km de la rivière Bérard, quatre refuges thermiques

et cinq zones de refroidissement ont été détectés, couvrant 46 % de la section étudiée de la rivière. Sur la section de 41 km étudiée pour la rivière Koroc, 67 refuges thermiques et cinq zones de refroidissement ont été identifiés, ce qui représente 32% de la section étudiée de la rivière. 89% des refuges thermiques identifiés et environ 60% des zones de refroidissement sont contrôlés par les eaux souterraines. La continuité du pergélisol et la forme de la vallée fluviale se sont avérées être les principaux paramètres contrôlant la distribution des refuges et des zones de refroidissement. Ces données fournissent des informations importantes pour la planification et les mesures de conservation de la population de salmonidés des rivières subarctiques du Nunavik.

2.1 Introduction

Rivers in northern Quebec are known for their abundance of salmonids (brook trout, Arctic char, and Atlantic salmon). Fish were an important food source for Indigenous peoples, then for the first settlers (MINISTÈRE DES FORÊTS, 2016). Today, fishing is still important for local communities and for revenues from sport fishing (Poesch et al., 2016). The optimal temperature range for salmonid growth varies according to species, but is generally between 7 °C and 17 °C while the lethal temperature range is 25–27 °C (Finstad et al., 2012; Nyanti et al., 2018; Jensen et al., 1989). In summer, salmonids experience thermal stress in rivers as a result of higher average water temperature usually occurring on warm days with air temperature above 30 °C (Gunn et al., 2010). This affects their growth and even threatens survival. Similarly, during winter, water temperature plays an important role on spawning time and survival of buried eggs into the gravel substratum (Jonsson et al., 2009). Extreme conditions in Quebec rivers are likely to occur more frequently due to climate change (Breton et al., 2017; Power et al., 1999). This will have a negative impact on the population of salmonids in the future, especially as certain northern species (e.g., Arctic char) are the most vulnerable with regard to thermal stress (Jonsson et al., 2009; Baroudy et al., 1994). However, cool water zones in rivers constitute thermal refuges allowing fish to grow and to survive, even under climate extremes (Lorenz et al., 1989; Geist et al., 1998). The use of thermal refuges by fish during heatwaves has been well documented (Breau et al. 2007; Berman et al., 1991). Therefore, identifying and understanding the spatiotemporal variability of discrete thermal refuges and larger scale cooling zones in rivers is of fundamental interest to understanding fish habitat vulnerability, but still remains difficult to address at large scales.

Thermal infrared (TIR) imagery is one of the relatively low-cost solutions to evaluate large-scale surface water (SW) temperature (Dugdale et al., 2013). TIR images have been used to map river water temperature (Torgersen et al., 2001), thermal refuges (Dugdale et al., 2013; Dugdale et al., 2015), surface water-groundwater exchange (Casas-Mulet et al., 2020; Dole-Olivier et al., 2019) and more specifically to monitor the thermal refuge of fish habitats (Bergeron et al., 2012; Dugdale et al., 2016; Willms et al., 2016). TIR images have been used for identifying types of thermal refuges in addition to important parameters affecting them with regard to landscape variables in different rivers and watersheds (Dugdale et al., 2015; Casas-Mulet et al., 2020; Monk et al., 2013). However, previous studies have not examined rivers in Arctic and subarctic regions where permafrost is present. In the presence of permafrost, groundwater (GW) flow is limited (Liao et al., 2017). Furthermore, its interaction with rivers has more complex processes that are prone to evolve due to climate change (Lamontagne-Hallé et al., 2020). Moreover, GW-dependent refuges

are most abundant and less temporally variable in rivers (Dugdale et al., 2013; Dugdale et al., 2015). Therefore, studying processes and parameters controlling thermal refuges in rivers of high-latitude river environments is important to better anticipate their variability under climate change and thawing of permafrost.

During warm days (as targeted for this study), in a river where there is no GW seepage or if the GW seepage is constant along the river, the 'asymptotic warming paradigm' (Fullerton et al., 2015) indicates that river water temperature will increase from upstream to downstream since it is in contact with solar radiation for a longer period. However, in reality, a river's longitudinal temperature profile is considerably more complex, often due to the presence of cooling zones where high GW seepage occurs into the active channel. We therefore also examine these larger, diffuse GW-driven cooling zones with a view to shedding light on their controlling processes in permafrost-prone regions (as opposed to more southerly rivers, e.g., Dugdale et al., 2015; Fullerton et al., 2015).

The main objective of this paper is to evaluate the effect of GW-SW interaction and GW-controlled thermal refuges on river water temperature mitigation in northern rivers with the presence of permafrost. This paper therefore analyzes thermal refuges as well as cooling zones in two rivers in Nunavik, a subarctic region of Quebec, Canada (between 58° N and 59° N latitude). First, we map the distribution of thermal refuges and cooling zones using TIR imagery. We then investigate the riverscape hydromorphologic context of each refuge and cooling zone to identify critical parameters affecting water temperature, highlighting the role of GW in driving river temperature heterogeneity in a permafrost-prone region.

2.2 Study area

The two studied rivers are the Koroc River and the Berard River. Both rivers are located in a subarctic climate of Nunavik, northern Quebec, Canada, and drain into Ungava Bay (Figure 2.1-A). In previous studies, Arctic char, salmon and trout have been identified in these rivers and fishing is important for local communities (Mainguy et al., 2019; Kativik Regional Government, 2005).

The Berard River's source is in highlands close to the limit of the watershed of Melezes River. The river flows northwards, crosses several water bodies and lakes along its path, and ends in Ungava Bay in the northern village of Tasiujaq. The imagery of this river is for a length of 17 km downstream of Berard Lake (Figure 2.1-B).

The Koroc River's source is located in the heights of the Torngat Mountains at the border of Labrador and Quebec, in eastern Canada. The Koroc River is located in a valley shaped by glaciers. The river runs westward and drains into the eastern shore of Ungava Bay, 18 km north of the northern village of Kangiqsualujjuaq. Thermal imagery of the Koroc River is focused on a 41 km stretch between upstream of the river delta, where the river is braided and wide, and downstream of waterfalls in the uplands, where the river flows over bedrock (Figure 2.1-C).

The Berard and Koroc Rivers are located in a continental subpolar climate based on 2001 to 2010 weather data and Köppen–Geiger climate classification method (Gouvernement du Québec, 2021). The annual average temperatures in Tasiujaq and Kangiqsualujjuaq for the 1951–1980 period were −5.7 °C and −5.4 °C, respectively. For the 1981–2010 period, however, the values were −5.2 °C and −4.9 °C. Based on high emission climate scenarios, the annual average temperature is expected to become −0.3 °C and −0.2 °C for Tasiujaq and Kangiqsualujjuaq for the 2021–2050 period (ClimateData.ca, 2021).

Average annual precipitation for the 1951–1980 period were 447 mm and 478 mm for Tasiujaq and Kangiqsualujjuaq, respectively. Based on high emission climate scenarios for the 2021–2050 period, an increase of 11% and 12% is predicted for Tasiujaq and Kangiqsualujjuaq (ClimateData.ca, 2021). This indicates severe trends of climate change in the Nunavik region.

The Berard River is located in the zone of discontinuous and widespread permafrost, while the Koroc River and its floodplain are in a zone of discontinuous and dispersed permafrost. However, further from the flood plain of the Koroc River, permafrost is discontinuous and widespread (Figure 2.2). Considering climate change trends in the region, the permafrost condition is prone to evolve (L'Hérault et al., 2018). The permafrost map shown in Figure 2.2 is based on surface temperature modeling, snow cover and other surface land metrics. This map has cells with a size of 250 m^2 (L'Hérault et al., 2018).

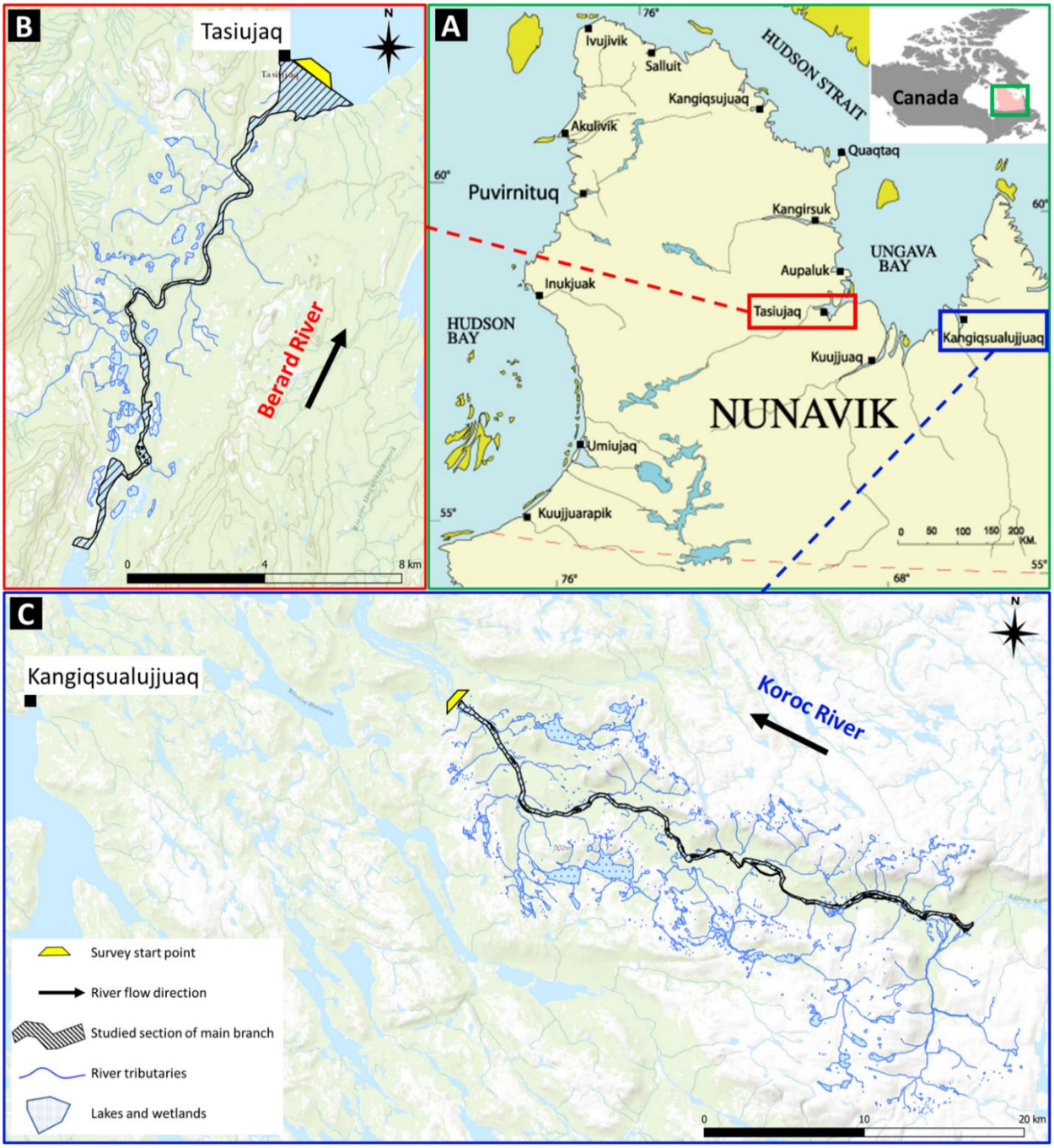

Figure 2.1 **Location of the northern villages in Nunavik region of Quebec Province (A), and surveyed section of the Berard River (B) and Koroc River (C).**

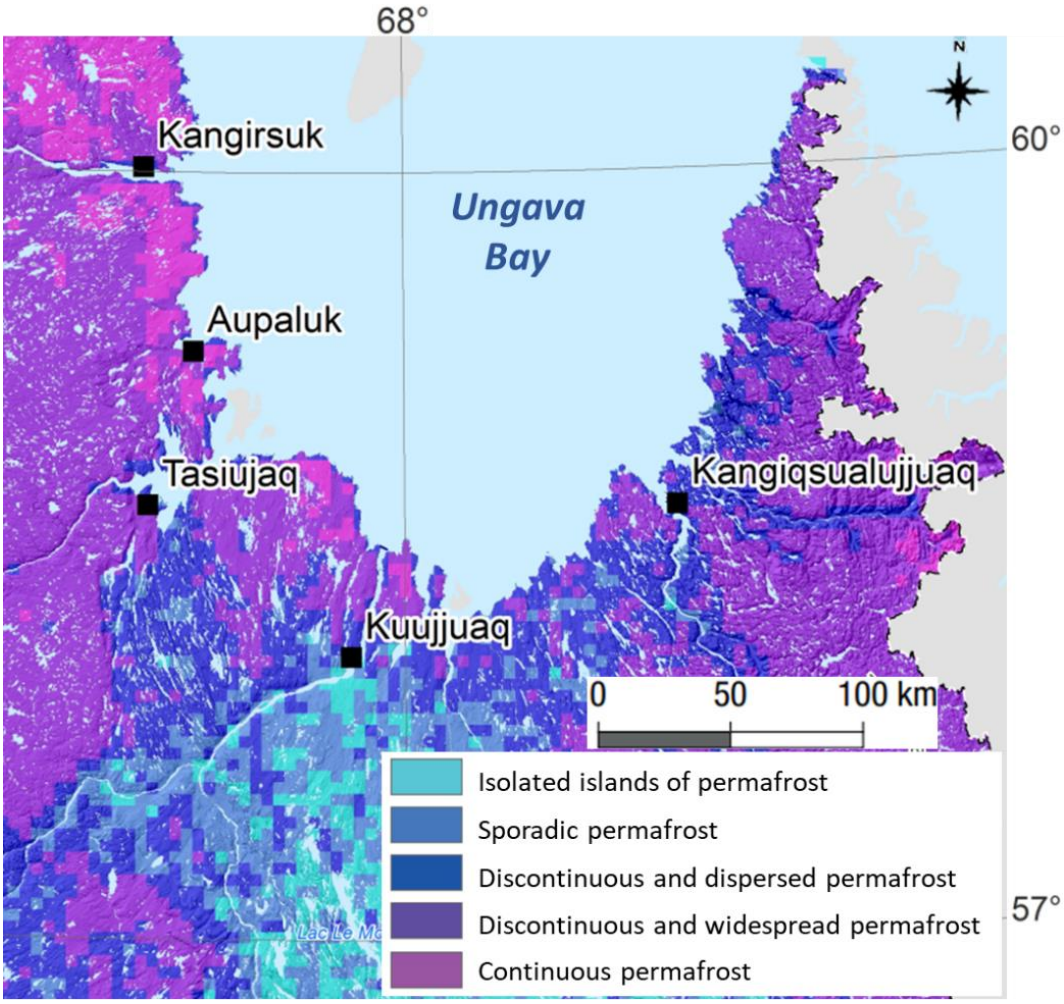

Figure 2.2 Permafrost map of Ungava Bay region (adapted from L'Hérault et al., 2018).

The quaternary geology of both studied rivers consists of shallow sediments with a minimum thickness of 1 m. Berard River is located on glaciomarine sediments and partly on recent alluvial deposits (Figure 2.3-A). Koroc River is located completely on alluvial deposits in the river valley and above the river valley the geology is mainly made of unconfined till and exposed bedrock (Figure 2.3-B). The bedrock under both rivers is a mix of different types of volcanic, intrusive igneous and metamorphic rocks such as basalt, granite, marble, quartzite and gneiss belonging to Churchill Province (SIGÉOM, 2022).

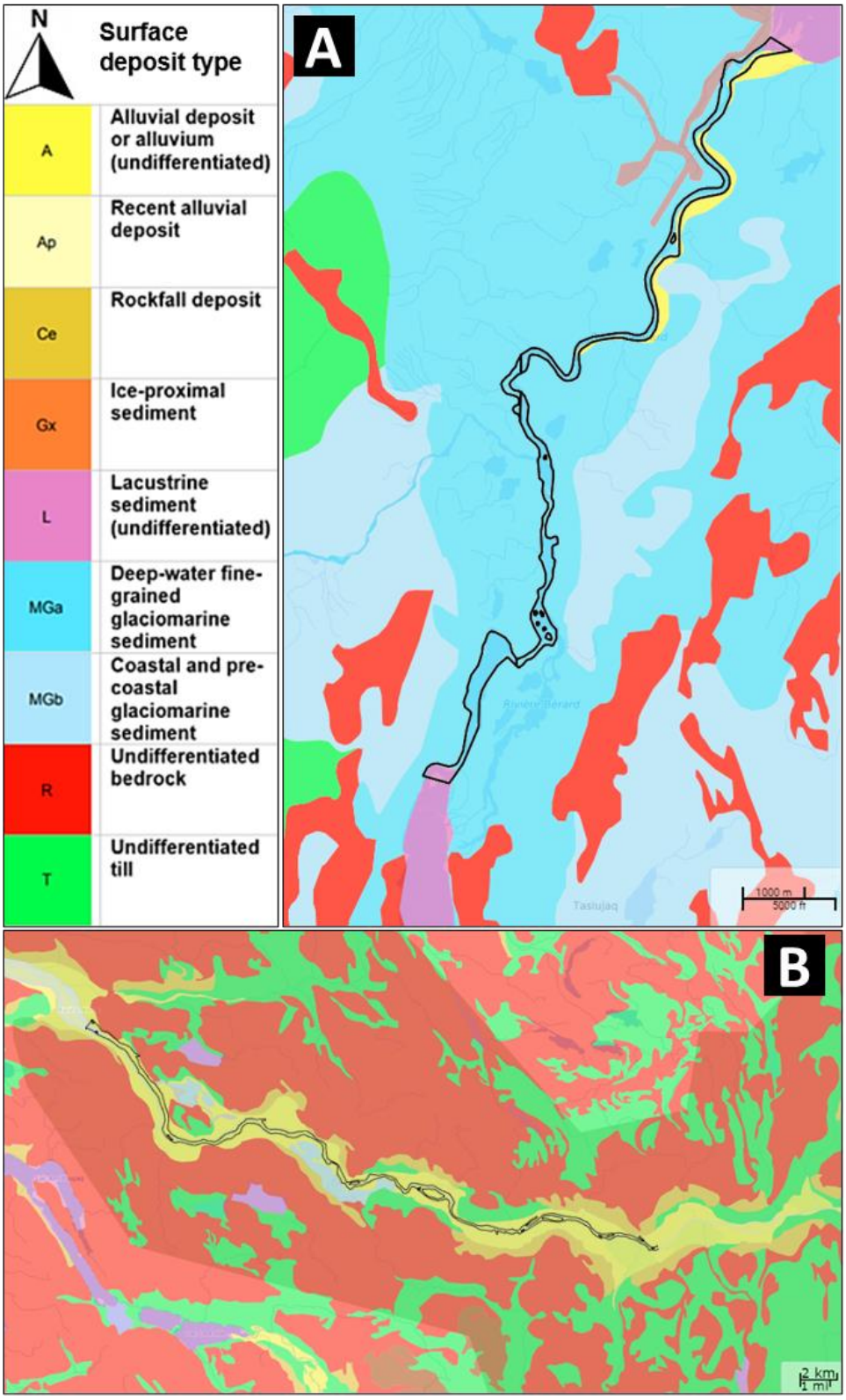

Figure 2.3 **Surface deposits map of Berard (A) and Koroc (B) rivers (based on SIGÉOM, 2022).**

2.3 Materials and methods

2.3.1 Airborne imagery

Airborne optical and TIR imagery of the two rivers were acquired in early August of 2019, using methods and equipment described by Dugdale et al. (Dugdale et al., 2013; Dugdale et al., 2015). For optimal identification of cold water patches, the flights were conducted between 12:00 and 16:00 on a sunny day to target maximum sunlight (for optical imagery) and high river temperature (for thermal imagery), as well as low flow (based on local forecasts). Each thermal image has a 620 by 480 pixel resolution. Mean flight altitude was ~750 m above ground level. Therefore, in each TIR image every pixel has a footprint of less than 0.5 × 0.5 m^2 on the ground. An image and GPS point were acquired every two seconds. Given the low groundspeed of the helicopter during survey flights, imagery has >75% overlap.

Thermal refuges were defined as a zone at least 0.5 °C cooler than the main river water temperature and an area larger than 1 m^2 (Dugdale et al., 2015). Using the classification scheme in Dugdale et al. (2013), the thermal refuges were divided into seven types (eight considering subgroup for wall-base channels, Table 2.1). Using the GPS point of each imagery and comparing the TIR and optical image pairs, we mapped the location and type of each thermal refuge. We also inspected aerial photos to confirm that thermal refuges were not false positives (e.g., shadow).

In addition to the identification of cold water zones in the river (thermal refuges), the aerial images were used to extract the temperature profile for each study river. The average river water temperature in each TIR image was calculated by averaging the temperature of three pixels in each thermal image, which were selected manually on the river central line (Figure 2.4, inside green). The relatively low (three) number of temperature sampling points in each image is due to: 1) anomalies at the edges of each thermal image due to vibration of the camera during flights (Figure 2.4, inside pink), meaning that averaging the value of the entire wetted area might introduce temperature error; 2) the high degree of overlap and position of the river channel in the center of each image meant that the inclusion of a larger number of sampling points did not change mean temperature (see the very similar temperature of all SP points in Figure 2.4 analysis result table).

Table 2.1 Thermal refuge classification, showing thermal refuge types and the abbreviations used in maps (modified from Dugdale et al., 2015).

Refuge Type	Abbreviation	Description
Tributary confluence plume	T.C.P.	Cold water plume created by discharge of tributary
Lateral seep	L.S.	Bank-side cold water patch created through direct intersection of water table by river channel
Spring brook	S.B.	Cold channel emerging from floodplain depressions, springs or wetlands
Cold side channel	C.S.C.	Secondary cold channel alongside main river stem; may be ephemeral
Cold alcove	C.A.	Cold water patch at downstream end of bar; often coincides with emergence of abandoned/relict channel
Hyporheic upwelling	H.U.	Hyporheic resurgence found downstream of bars, riffles and meanders
Wall-base channel A	W.C. (A)	Cold channels formed by runoff at base of terrace (A)
Wall-base channel B	W.C. (B)	Cold channels formed by runoff on valley wall (B)

In the next step, the mean temperature for each image was assigned with its distance from downstream, the distance of the center of each TIR image from the survey start point (yellow trapezoid shown in Figure 2.1). Plotting the mean water temperature of each image against its distance from downstream thus gives the temperature profile of the river.

Cooling zones were then identified using the river temperature profile. By moving downstream (value of 0 on the horizontal axis of the graph), zones that exhibited a temperature decrease >0.25 °C were identified as cooling zones. The 0.25 °C has been selected as the threshold to avoid random variation of water temperature on the graph which can be due to errors in recorded temperature by a camera in motion during the flight or the possible presence of small patches of clouds.

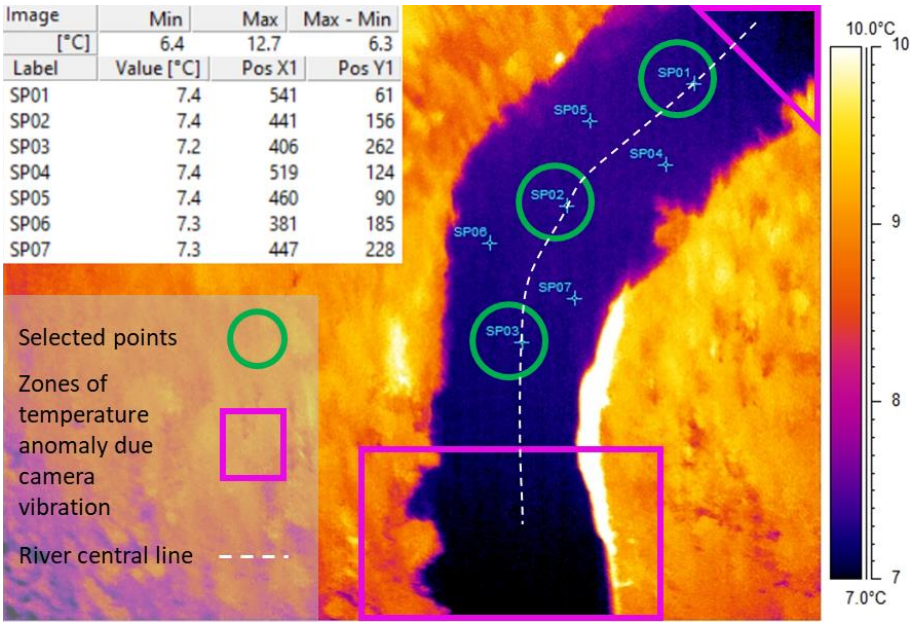

Figure 2.4 **Example of a TIR image showing location of manually selected three points for making river water temperature average and zones of temperature anomalies caused by camera vibration.**

2.3.2 Links to landscape metrics

Different landscape metrics in three major groups mentioned below were considered for the description of the thermal refuges and cooling zones in the rivers. The landscape metrics used are those previously demonstrated to correspond to the occurrence or distribution of thermal refuges based on the work of Dugdale et al. (Dugdale et al., 2015). Parameters that show a good correlation with the occurrence of thermal refuges and cooling zones can be analyzed for the identification of potential cool water, in the absence of thermal imaging.

2.3.2.1 Drainage network

This group focuses on the channels and tributaries entering the main stem and their density. In the case of cooling zones, we quantified the number of tributaries in each zone. Aerial imagery and freely available water feature maps (Natural Resources Canada, 2019) were used for the identification of tributaries.

2.3.2.2 River geomorphology

In this category, parameters such as river and valley width were studied. For the thermal refuge parameters at the site and for the cooling zones average of these values within the zone has been

considered. In addition, river sinuosity in the cooling zone reach has been addressed (Figure 2.5). Measurements of width and length are based on Open TopoMap, freely available in QGIS, with a resolution of about 30 m (1 arcsecond).

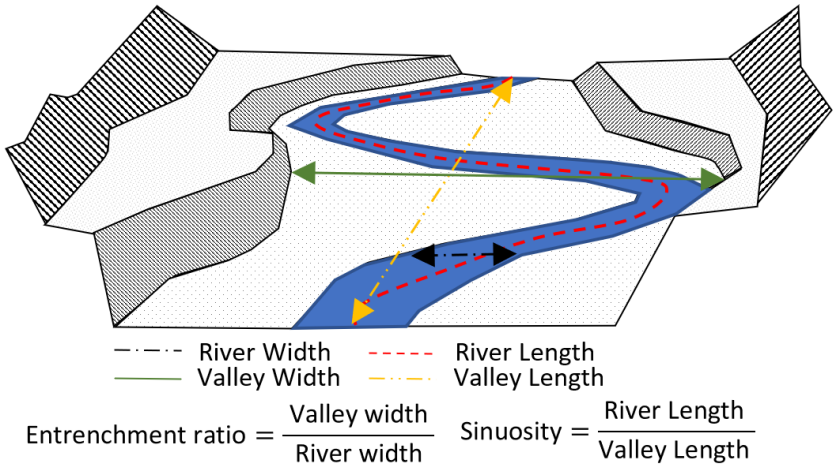

Figure 2.5 **Schematic of river geomorphology parameters used for characterization of the cooling zones.**

2.3.2.3 Geology and land cover

Vegetation and sediment type are the main factors studied in this category. Moreover, potential links to permafrost are inspected by use of available open-source maps and satellite imagery (e.g., Landsat imagery, from Google Earth imagery).

2.4 Results

2.4.1 Inventory of thermal heterogeneity

2.4.1.1 Thermal refuges

In the studied section of the Berard River, four thermal refuges were detected: two cold side channels and two lateral seeps (Figure 2.6-A). Considerably more thermal refuges (67) were identified in the studied section of Koroc River (Figure 2.6-B). Considering the studied length of rivers, thermal refuge densities are 0.23 and 1.63 per kilometer for Berard and Koroc Rivers, respectively.

Sixty percent of identified thermal refuges were GW-controlled. The other 40% were tributary confluence plumes and wall-base channels, which were all detected on the Koroc River. Although GW can affect water temperature in the tributaries entering the river, tributary confluence plume

and wall-base channels are not considered as GW–controlled thermal refuges. In terms of GW-controlled refuges, 49% were spring brooks, 32% lateral seeps, 11% cold alcoves, 6% cold side channels, and 2% hyporheic upwelling (Table 2.2).

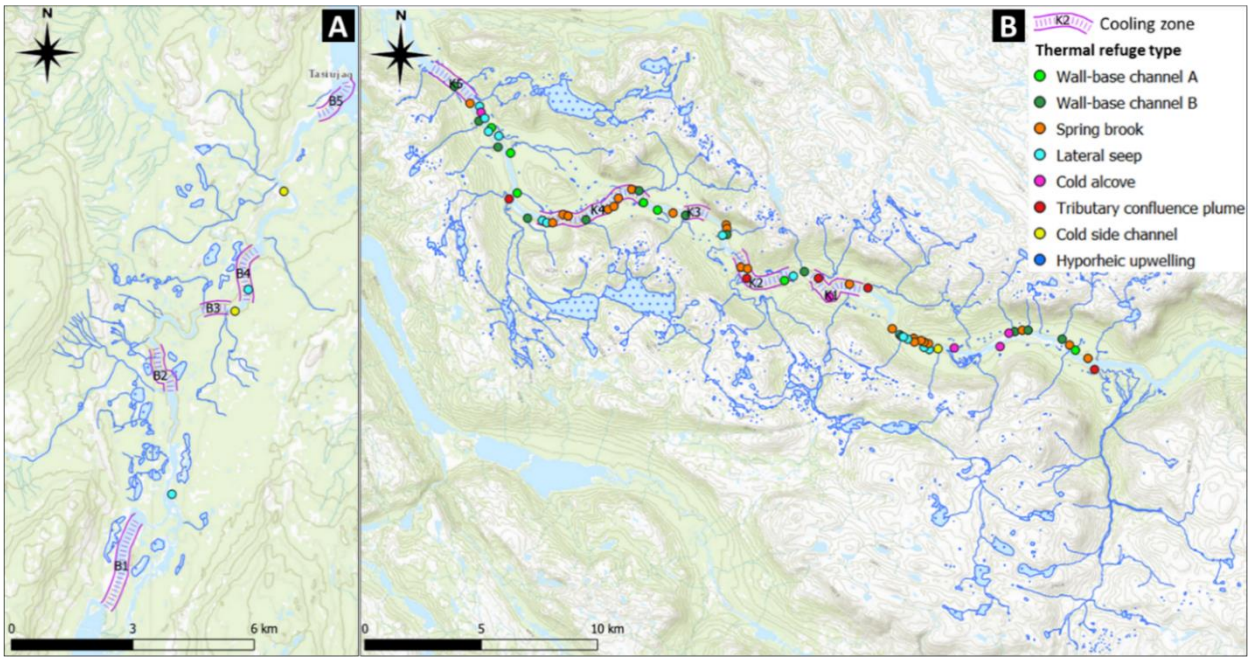

Figure 2.6 **Location of identified thermal refuges (their type has been explained in Table 2.1) on studied section of Berard (A) and Koroc (B) rivers.**

Table 2.2 **Identified thermal refuges.**

Thermal Refuge Type	Koroc River	Berard River
Spring brook	23	
Wall-base channel	20	
Lateral seep	13	2
Cold alcove	5	
Tributary confluence plume	4	
Cold side channel	1	2
Hyporheic upwelling	1	

2.4.1.2 Cooling zones

On the 17 km studied section of Berard River, five cooling zones (B1 to B5) were detected (Figure 2.7-A), with a total length of 7.8 km, representing 46% of the surveyed section of the river. On the 41 km studied section of Koroc River, also five cooling zones (K1 to K5) were identified (Figure 2.7-B), with a total length of 12.5 km, which is 32% of the studied section of the river. Since the width of rivers is wide relative to the height/shading of trees, the impact of shade on river temperature is negligible. The dominant cold water source (GW-SW interaction or tributaries) for each cooling zone will be investigated in the coming sections.

2.4.1.3 Correlation between thermal refuges and cooling zones

When comparing the location of thermal refuges and cooling zones, occurrence of thermal refuges does not guarantee the existence of cooling zones in the river, and these two phenomena might be a response to different factors. For instance, the highest temperature decrease rate for both rivers does not correspond to the highest number of thermal refuges present within a cooling zone (Table 2.3). However, a relationship between cooling zone length and the number of thermal refuges in the same section can be seen for the Koroc River (Figure 2.8-A). This is not the case for Berard River. Due to the low number of identified thermal refuges on this river, only one or no thermal refuge is present in each cooling zone. Nonetheless, there is a significant correlation between the rate of water temperature decrease and the length of the cooling zone on the Berard River (Figure 2.8-B). Moreover, since a large number of thermal refuges are wall-base channels and spring brooks in the Koroc, there is a good correlation between cooling zone length and the number of channels entering the river (Figure 2.8-C). Different types of trendlines have been tested as correlation equation and the second degree exponential had the highest R^2 and best fit similar to a previous similar study (Dugdale et al., 2015). Additionally, the calculated p-values based on Pearson type goodness of fit tests showed that the chosen second degree exponential equation has a good fit to the data. Pearson type goodness of fit tests showed a p-value of 0.002 for first and second graphs (Figure 2.8-A&B) and a p-value of 0.043 for the third graph (Figure 2.8-C).

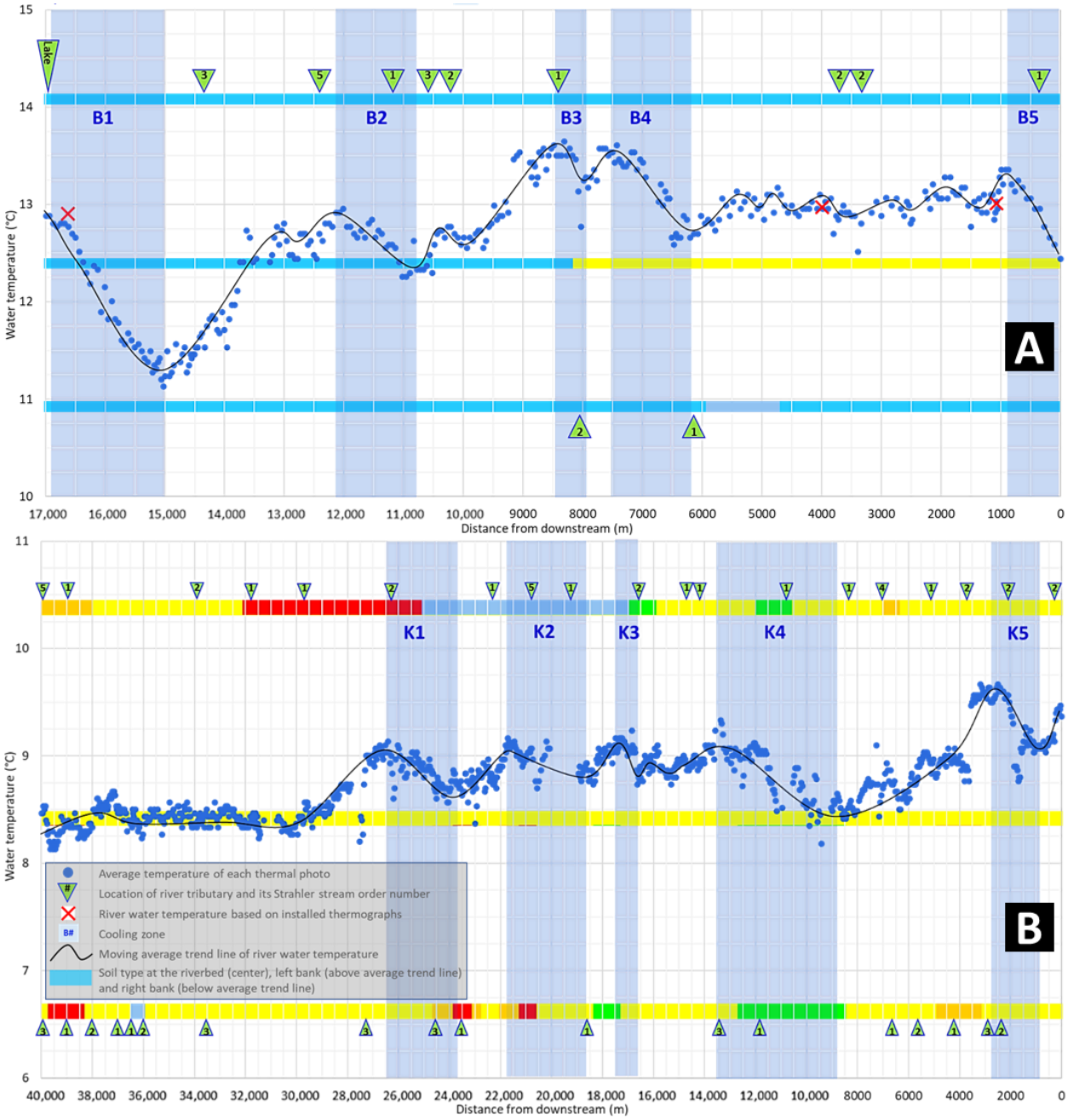

Figure 2.7 **River water temperature profile of the Berard River (A) and Koroc River (B) with location of tributaries entering the river and surface deposit type on each side of the river (color code for soil type is the same as in Figure 2.3).**

Table 2.3 Identified cooling zones' characteristics.

River	Zone	Water Temperature Decrease (°C)	Cooling Zone Length (m)	Temperature Decrease Rate (°C/km)	Valley Length (m)	Sinuosity	Average Channel Width (m)	Average Valley Width (m)	Entrenchment Ratio	Number of Thermal Refuges
Berard	**B1**	1.6	2363	0.68	2335	1.01	159	2154	13.57	0
	B2	0.6	1251	0.48	1100	1.14	61	1965	32.36	0
	B3	0.4	668	0.60	634	1.05	54	1526	28.26	1
	B4	0.9	1620	0.56	1433	1.13	55	2332	42.10	1
	B5	0.9	1885	0.48	1034	1.82	62	1982	32.09	0
	mean	0.9	1557.4	0.56	1307.2	1.2	78.1	1991.7	29.7	0.4
	SD	0.4	573.6	0.08	573.2	0.3	40.4	268.3	9.3	0.5
Koroc	**K1**	0.5	2753	0.18	2103	1.31	148	1397	9.45	3
	K2	0.3	3085	0.10	2462	1.25	236	1119	4.73	4
	K3	0.3	976	0.31	906	1.08	202	1521	7.52	1
	K4	0.7	5175	0.14	4576	1.13	201	1522	7.59	12
	K5	0.6	2253	0.27	2181	1.03	279	850	3.05	2
	mean	0.5	2512.4	0.25	2445.6	1.0	213.2	1281.9	6.5	4.4
	SD	0.2	1543.8	0.13	1191.4	0.3	43.2	261.2	2.3	3.9

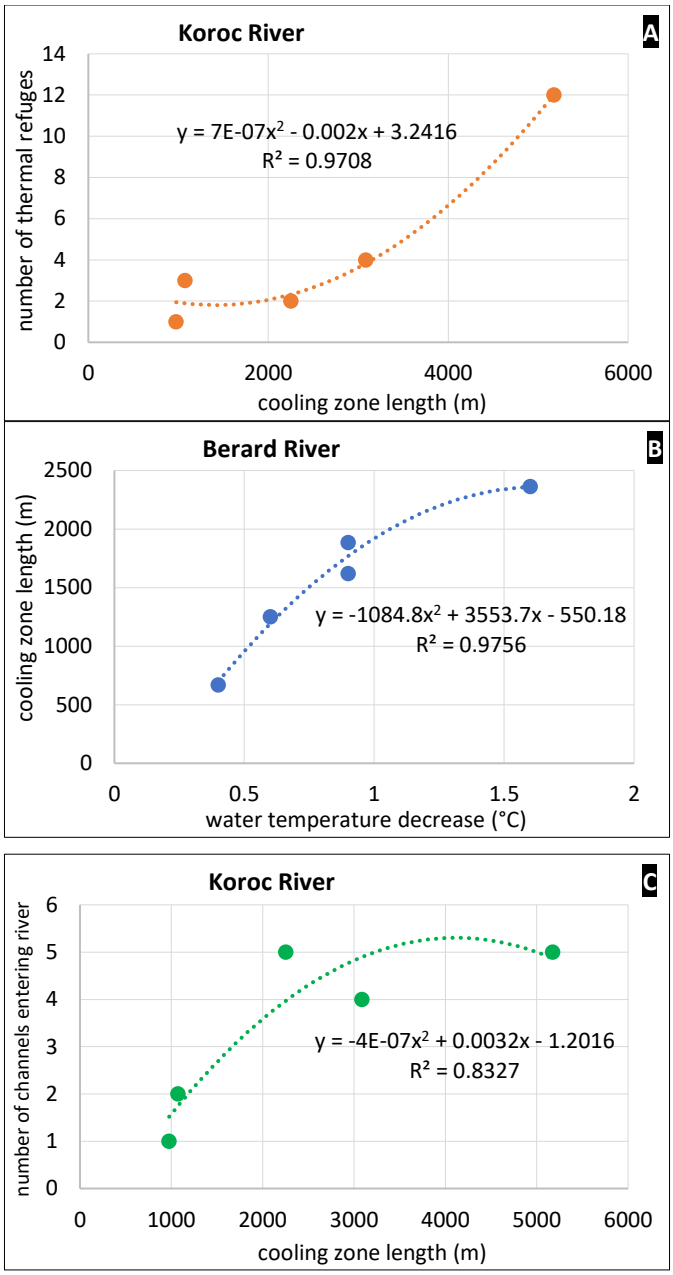

Figure 2.8 **Correlation between cooling zone length and number of thermal refuges in the Koroc River. (B) Correlation between water temperature decrease and cooling zone length in the Berard River. (C) Correlation between cooling zone length and number of channels entering the Koroc River.**

2.4.2 Links to landscape metrics

2.4.2.1 Drainage network

Tributary confluence plumes were only located on the Koroc River. The Berard River has only one significant tributary (5th order) in the studied section. Although this tributary is approximately

1 °C colder than the average main stem water temperature, it did not generate a confluence plume. This may be due to a fast mixing of cold water with the main stem river or the limited tributary discharge. Similar phenomena also occur in the Koroc River at the first cooling zone (K1), where a cold tributary enters the river without a cold water plume observed. This suggests that for better detection of potential cold tributary confluence plume, hydraulic parameters such as the discharge and velocity of the main stem versus the tributary should be considered.

The drainage network in addition to large tributaries includes smaller channels. Smaller cold channels entering the river can form wall-base channels and spring brooks. However, differentiating between spring brooks and wall-base channels was not easy due to their morphological (but not process-based) similarity. We used drainage network analysis to aid our classification; spring brooks were considered streams formed in floodplain depressions that are only visible in the thermal or visible images but not present in the drainage network maps, whereas wall-base channels were those formed by runoff and therefore visible in the drainage network based on topographical maps. Wall-base channels are in general wider and closer to the valley walls, compared to spring brooks, which can sometimes be very narrow and only visible in thermal photos and flowing close to the river channel (Figure 2.9). Moreover, wall-based channels which are numerous in the studied section of the Koroc River can be classified into two types (Figure 2.9). The first type of channel is located within the river valley, and brings collected runoff to the river (Type A). The second type is sourced from the top of the river valley and usually connected to lakes, bringing lake outflow to the river after periods of rainfall (Type B).

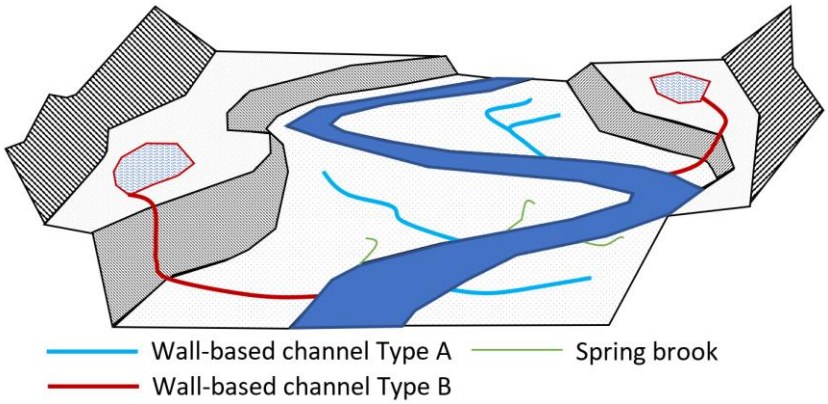

Figure 2.9 **Schematic view of the river valley showing wall-base channels Type A and B and spring brooks.**

As seen, there is a good relationship between the number of channels entering the river and the length of a cooling zone. This suggests the cooling zones are not only the result of GW influence but also SW drainage network. Looking at the maps of cooling zones and thermal refuges (Figure

2.6), the first two cooling zones of Koroc and Berard rivers seem to be mainly controlled by SW rather than GW. The first cooling zone in the Berard River (B1) receives cold water from an upstream lake. The second cooling zone (B2) is located after the main tributary of the Berard River having already cold water. For the Koroc River tributary confluence plumes are present within the first two cooling zones (K1 and K2). Tributary confluence plumes often have a larger effect in cooling the river compared to other (smaller) types of thermal refuges, highlighting the importance of the drainage network on the river temperature profile.

2.4.2.2 River morphology

The occurrence of spring brooks and wall-base channels are related to valley shape and width. In the studied section of the Koroc River, the valley is more than 1000 m in width except for a few sections. This gives sufficient space for the development of numerous wall-base channels and spring brooks. To show the relationship of these thermal refuge types to the valley form, we calculated the entrenchment ratio by dividing valley width by river width (Figure 2.5). Figure 2.10 shows the narrowest range of entrenchment ratios for spring brooks compared to other types followed by wall-base channel Type A. This indicates that spring brooks and wall-base channels exist in a relatively narrow range of moderate entrenchment values and are more likely to occur where valley width is on average about eight times bigger than channel width. This is different for river tributaries existing in wider valley reaches with an average entrenchment ratio of about 11 (Figure 2.10).

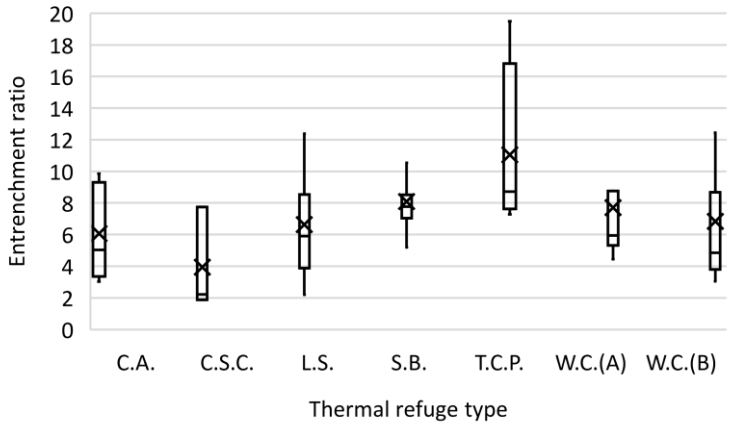

Figure 2.10 **Entrenchment ratio range for each thermal refuge class (abbreviation of refuge classes in Table 2.1), showing maximum and minimum by whiskers, first and third quartile by box, median by horizontal line and mean by cross.**

In the case of the cooling zones, the entrenchment ratio and sinuosity values for the Berard and Koroc Rivers vary considerably (Table 2.3) and moreover, are averaged over the entire zones. Therefore, a correlation cannot readily be achieved for the identification of potential cooling zones based on sinuosity or entrenchment ratio of the river.

The rate of temperature decrease for cooling zones on the Berard River is generally higher than those of the Koroc River (mean thermal gradient of −0.56 °C/km and −0.25 °C/km for Berard and Koroc Rivers, respectively). The lower average temperature decrease rate in Koroc River may be linked to its larger average width, meaning a larger effective surface area for energy exchanges (i.e., radiative/turbulent heating).

The shape of river valleys plays an important role in controlling GW-SW interaction, and can be classified as confined, semi-confined and unconfined (Figure 8 in Dugdale et al. (2015)). While the Koroc River's rugged, steep valley is readily apparent from topographic maps (Figure 2.6, background map), the Berard River's corridor is predominantly flat. Based on the entrenchment ratio, the Koroc River is semi-confined. The upstream parts of the Berard River (upstream of B2 cooling zone and near the lake) are semi-confined, the downstream section is principally unconfined.

This difference in entrenchment ratio also explains the high number of thermal refuges in the Koroc River in comparison to the Berard. In the Koroc, local GW flow has an influential role in driving refuge distribution, whereas in the Berard River, the river valley is flatter, therefore, thermal refuges which are derived by local GW flow are limited.

2.4.2.3 Geology and land cover

The main vegetation cover of the Koroc River valley is a coniferous forest in four subgroups of tree cover. However, on top of the river valley, the vegetation cover has lower density and more exposed bedrock (Figure 2.11-A). Surface deposits under the Koroc River and within the river valley consist mainly of alluvium (A), although in some zones of the river valley, costal and pre-costal glaciomarine sediments (MGa) as well as rockfall deposits (Ce) are also present. The sediments in the river valley are more permeable than other surface deposits such as till (T) and bedrock (R) present on top of the river valley (Figure 2.11-B).

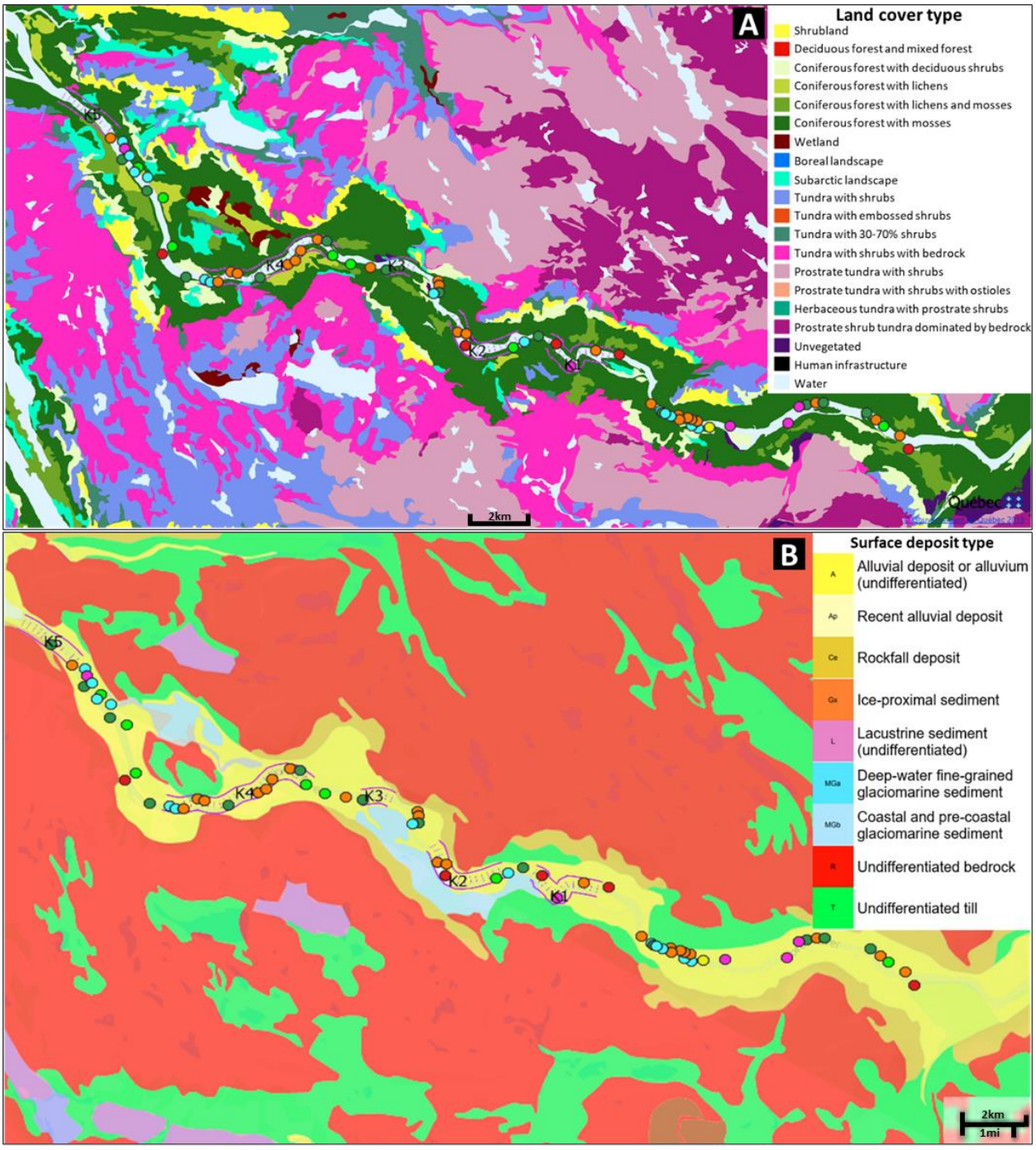

Figure 2.11 **Land cover (A, based on Foretouverte, 2018) and surface deposits (B, based on SIGÉOM, 2022) of the Koroc River study area.**

Note. Legend for thermal refuges and cooling zones same as in Figure 2.6.

At the studied section of the Berard River, the land cover is predominantly composed of shrublands with a mix of wetlands and tundra with shrubs (Figure 2.12-A). Surface deposits below

and next to the Berard River are mainly deep-water fine-grained glaciomarine sediments. Based on available morpho-sedimentological maps, alluvium is only present in the downstream section of the Berard River (Figure 2.12-B). The difference in scale of the Berard River compared to the Koroc River can suggest a lower potential for sedimentation and shallower alluvium for the Berard River.

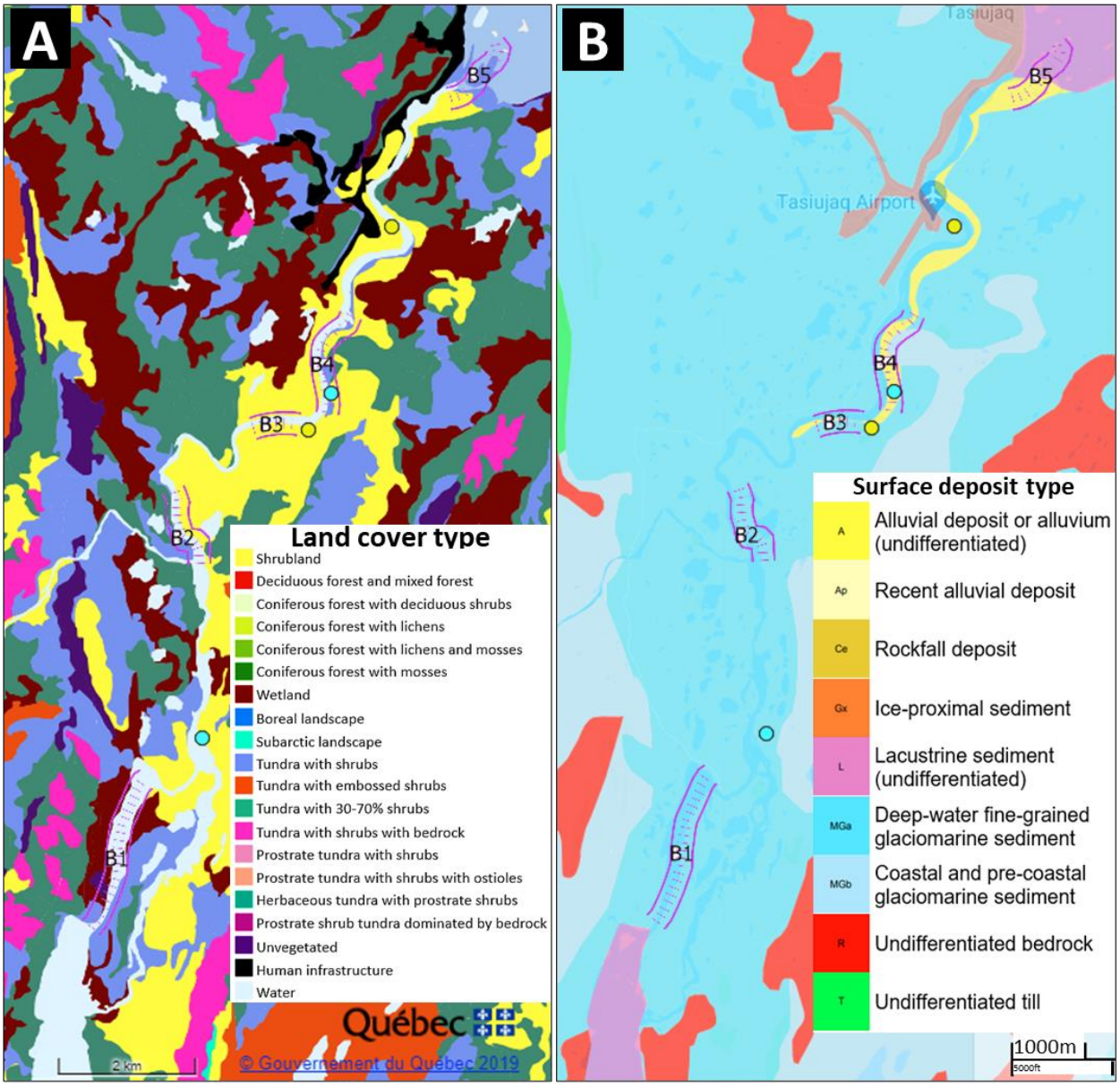

Figure 2.12 **Land cover (A, based on Foretouverte, 2018) and surface deposits (B, based on SIGÉOM, 2022) of the Berard River study area.**

Note. Legend for thermal refuges and cooling zones same as in Figure 2.6.

The presence of a specific soil or vegetation type cannot be used to pinpoint the existence of thermal refuge. In the case of the Koroc River, the entire studied section of the river is on alluvium and surrounded by coniferous forest. For the Berard River case, all thermal refuges are located in land cover comprising shrubland vegetation; three of them are on alluvium and one on glaciomarine deposits. The difference in the number of thermal refuges between the two studied rivers indicates that a higher density of vegetation and the presence of thicker permeable materials may be linked to higher thermal refuge density.

While we hoped to assess linkages between permafrost coverage and the location of thermal refuges, the resolution of permafrost maps (Figure 2.2) for the region is insufficient for establishing any such relationships. Based on Figure 2.2, both studied rivers are located entirely on one type of permafrost, potentially limiting further analysis. However, other available permafrost maps suggest discontinuous permafrost closer to Ungava Bay for the Koroc River (Figure 2.13). This dataset indicates that all cooling zones and more than 60% of thermal refuges on the Koroc River are located on downstream sections where discontinuous permafrost is present. This suggests discontinuity of permafrost may favor higher GW-SW interaction and the existence of abundant thermal refuges.

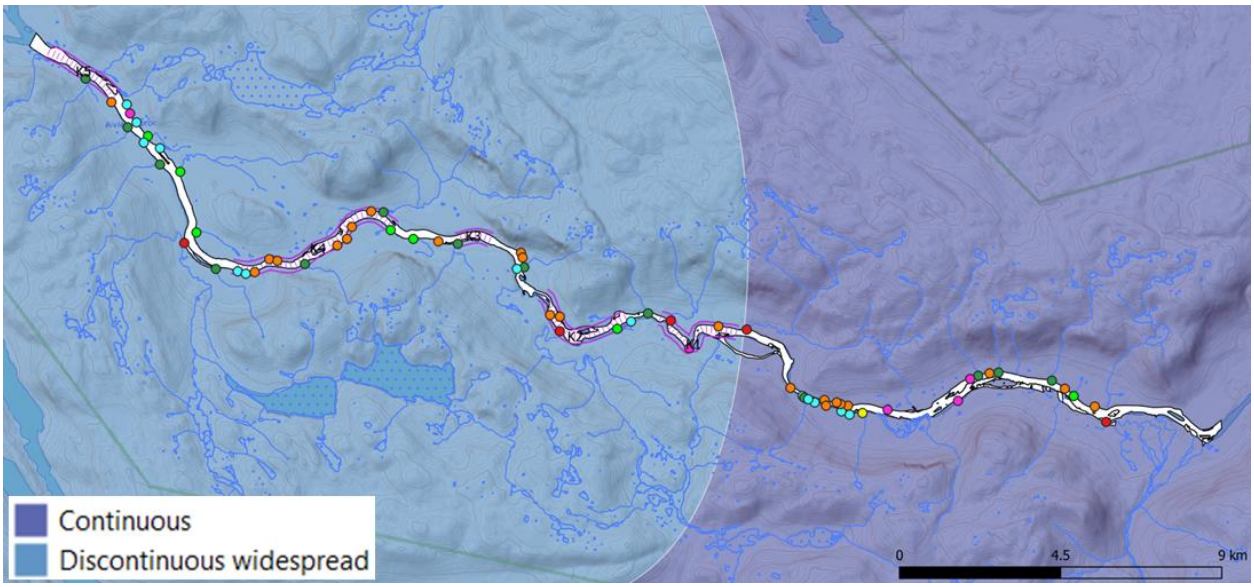

Figure 2.13 **Location of Koroc River thermal refuges and cooling zones on permafrost continuity map (adapted from Lemieux et al., 2016).**

Aerial and satellite imagery can further be used for permafrost mapping and monitoring (Philipp et al., 2021), with a view to examining links to the distribution of thermal refuges or riverine cooling zones. The presence of thermokarst lakes around the Berard and Koroc Rivers suggests the existence of permafrost near these two rivers (Figure 2.14). A thermokarst lake forms when land

subsidence caused by a thaw of permafrost is filled by water (Allard et al., 2012). The absence of such lakes inside the Koroc River valley is also an indicator of the absence of continuous permafrost. Both increase (Ulrich et al., 2017) or decrease (Duguay et al., 2005) in the size of thermokarst lakes show degradation of permafrost. The decrease or increase in size depends on different factors and thawing stage of permafrost, and have been used in remote sensing studies to monitor permafrost condition in arctic regions. Comparing Figure 2.14, a decrease in the size of the lake south of the Tasiujaq airport can be observed suggesting internal drainage of the lake to the Berard River, through degradation of shallow permafrost. Regarding Koroc River obvious changes in the size of lakes are not observed in available satellite images, which can suggest a more stable condition for permafrost. The stability of permafrost near Koroc River can be due to the absence of significant sedimentary deposits at the top of the river valley which sits on the bedrock. Another thermokarst landform, beaded streams, forms when thermokarst lakes connect and form a river with pools and riffles (Arp et al., 2015) (Figure 2.14). These types of streams are regularly found on the plateau outside of the Koroc River's valley. The Berard River itself can be considered as a beaded stream. Especially upstream of its main tributary, there are parts of the river that are wider and deeper and form pools. Since a pool section of a river is deeper, it is more probable that permafrost is degraded and the river connects to the aquifer. However, under shallow riffle sections of river permafrost can be present. These observations (based on satellite imagery) again suggest better continuity of permafrost nearer the Berard River and less potential for GW-SW interaction compared to Koroc River.

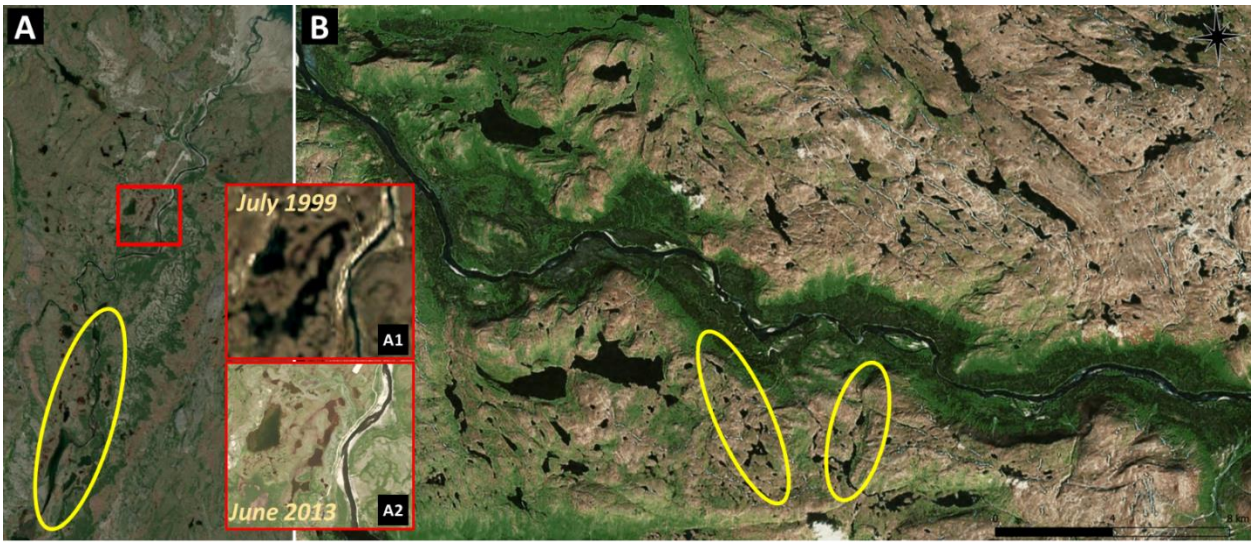

Figure 2.14 **Satellite imagery (June 2013 Google earth Landsat images) of Berard (A) and Koroc (B) Rivers showing presence of thermokarst lakes and beaded streams (examples inside yellow circles).**

2.5 Discussion

The difference in the number of identified thermal refuges between Koroc and Berard rivers can be related to a range of hydromorphic, environmental and geologic characteristics, such as valley confinement, geology, vegetation cover and permafrost condition. The semi-confined shape of Koroc River valley explains both the abundance of wall-base channels relating to runoff processes within/on the valley, and also spring brook refuges where contact between valley wall and floor can drive GW seepage (e.g., Dugdale et al., 2015). Due to less permeable surface deposits and less vegetated land cover, the valley tops are prone to runoff. On the other hand, in the river valley the presence of more permeable materials and higher vegetation cover favor GW infiltration/seepage and GW-SW interconnection (e.g., Owuor et al., 2016). This, in combination with less continuous permafrost around the Koroc River compared to the Berard River, can explain the large difference in the number and density of thermal refuges between the two rivers (i.e., higher density in the Koroc River).

Machine learning and remote sensing combinations have been used to identify the location of thermal refuges and GW-SW interaction zones in numerous rivers (e.g., Dugdale et al., 2015; Gerlach et al., 2022; Belknap et al., 1998; Ebersole et al., 2015). In these studies, key landscape parameters (e.g., channel confinement, location of dry valleys) have been noted as potential predictors for the location of thermal refuges. In our paper, such relationships have not been achieved for either the Koroc and Berard Rivers because: (1) the two rivers have different characteristics (valley shape, size, etc.), (2) a reliable dataset to build and train such models (length of studied river sections and the number of identified thermal refuges and cooling zones) has not yet been achieved, and (3) detailed data such as LiDAR topographic maps or permafrost map from geophysical field measurements are not available. Therefore, the results of river morphology and geology subsections under links to landscape metrics sections is not as clear or in detail as intended. Nevertheless, the effect of the number of channels (i.e., tributary valley distance) and entrenchment ratio on river water temperature is apparent for both rivers (similar to findings by Dugdale et al., 2015). Our study also shows that the use of TIR aerial images is a reliable way to detect cool zones in subarctic rivers. TIR images show good results for the identification of spring brook and low-order wall-base channels that cannot be identified from lower resolution DEMs that are typical in such data-sparse regions. The large number of spring brooks and wall-base channels suggested that studying the temperature of channels entering the river and identifying possible locations where GW-fed channels can appear is important when it

comes to the identification of potential spawning and juvenile salmonid habitats (e.g., Belknap et al., 1998; Peterson et al., 1984) in subarctic rivers.

The available permafrost maps were developed at a regional scale using a model and are thus unsuited to analyze linkages to individual thermal refuges or cooling zones in the studied rivers. The use of airborne GPR (ground-penetrating radar) alongside with TIR imagery could be a possible solution to establish such a correlation between thermal refuges and the existence of permafrost or depth of active layer where discontinuous permafrost exists (e.g., Liu et al., 2011; Campbell et al., 2018)). Nevertheless, the results from satellite imagery and results from the permafrost map for the Koroc River study site (Figure 2.13) suggest a possible linkage to the continuity of permafrost.

The results of this study were more qualitative than quantitative since the focus was on remote sensing (aerial imaging) and not field measurements. However, based on these results some explanations regarding the possible mechanism of GW and river interaction can be given mostly with regard to permafrost continuity. The role of permafrost in GW-SW interaction for northern rivers is well known (Liao et al., 2017; Lamontagne-Hallé et al., 2020; Lemieux et al., 2016). Open taliks can be formed under SW bodies where lakes or rivers are larger and deeper, such as the Koroc River. A talik refers to soil that is unfrozen throughout the year and normally present under thermokarst lakes and rivers. Open taliks connect the subpermafrost aquifer and the river (Figure 2.15); therefore, the presence of GW-based cooling zones is probable in these areas. In the case of smaller rivers like the Berard River, only closed taliks are formed; therefore, river can only interact with suprapermafrost aquifer (Figure 2.15). The suprapermafrost is less thick, meaning that the GW flow is limited, but since it flows over permafrost, water temperature is generally colder. GW flow over permafrost can therefore explain existence of cold thermal refuges within cooling zones or in general in arctic rivers of this study that have generally cooler water temperature compared to rivers in the south.

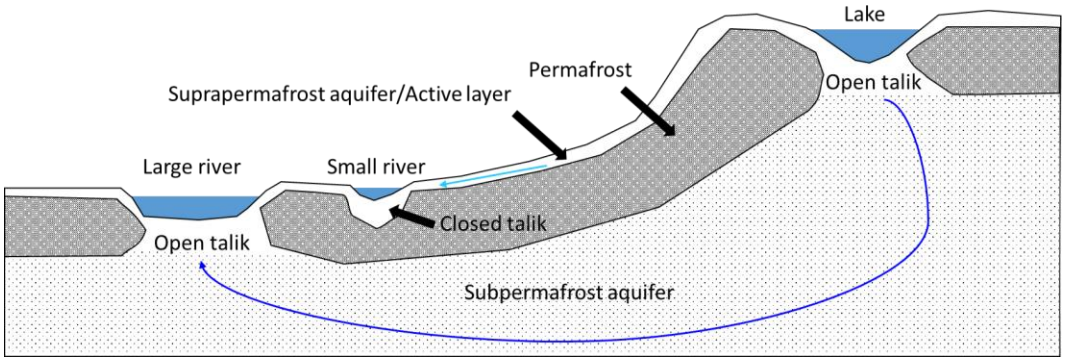

Figure 2.15 **Schematic cross-section showing the different types of aquifers and GW flow paths in presence of permafrost (adapted from Lemieux et al., 2016).**

Changes in the size of thermokarst lakes near the Berard River can be an indication of evolving GW-SW interaction caused by the thaw of permafrost. Considering the changing climate of northern Quebec and the predicted thaw of the permafrost (L'Hérault et al., 2018), the GW influence on the thermal budget of rivers in arctic and subarctic regions may become more important in the future. It is possible that more GW thermal refuges will appear in the future, potentially offsetting the climatic warming of SW because the thaw of permafrost changes GW flow patterns. However, this is far from certain, and the future evolution of river temperature patterns in the region is currently unknown. Nevertheless, even if increased GW contributions may offset other climate-forced river temperature warming (and thus in-stream heat-stress events), any river temperature change will likely change fish migration patterns (since the spawning and upstream migration cues are dependent on water temperature (Jonsson et al., 2009), with potential other serious consequences for northern salmonid populations.

2.6 Conclusions

In total, 71 thermal refuges over 58 km studied reaches of the Koroc and Berard Rivers, Nunavik, Quebec, were identified. The majority of identified thermal refuges are GW-controlled, but non-GW-controlled thermal refuges were present in substantial numbers (i.e., wall-base channels and tributary confluence plumes). Five cooling zones on each river were also observed. 40% of observed cooling zones are under influence of SW inlets either from upstream lakes or tributaries. For the other 60%, the absence of such SW intakes suggests that the cooling zone is the effect of GW-SW interaction. Therefore, it can be confirmed that GW plays an important role in river temperature mitigation.

Due to the small case study size and differences between the two studied rivers, no parameter within the three groups of landscape metrics showed a direct connection to the existence of

thermal refuges or cooling zones. However, similar to previous studies, river entrenchment ratio and shape of the river valley were nonetheless linked to the occurrence of thermal refuges. Further investigation specific to northern latitude rivers is therefore needed to better identify important parameters in driving the occurrence of thermal refuges.

Permafrost continuity plays an important role in the degree of GW-SW interaction for northern rivers. The permafrost for the Berard River is more continuous than the Koroc River and as a result, fewer thermal refuges are present. Based on previous studies, GW-controlled thermal refuges were shown to be less temporally variable (Dugdale et al., 2013). However, the same cannot be confirmed for northern rivers. Permafrost can partly or completely freeze and restrict GW flow. Therefore, thermal refuges driven from suprapermafrost aquifer can vary seasonally. Moreover, regarding a longer time scale, satellite imagery analysis near Berard River suggests that changes in the permafrost condition for the region have started. Thaw of permafrost will lead to higher GW recharge, thus potentially to higher GW flow. Here, the increased outflow of these lakes to the nearby river is expected. Therefore, GW flow will have more influence on river water temperature, and the number of GW-controlled thermal refuges may increase in the future. The speed of changes depends on other features such as the sediment and bedrock types. Zones with potentially continuous permafrost for the Koroc River are on bedrock and, thus, changes in the GW flow system are less visible and may appear later. Future implementation of such studies will better show temporal variation of thermal refuges and GW influence on river thermal budget. This study has helped to better understand GW-SW interaction on river water temperature for future application in fish habitat monitoring and river management of northern Quebec.

2.7 References

Allard M., Lemay M., Barrette C., L'Hérault E. & Sarrazin D. (2012) « Permafrost and climate change in Nunavik and Nunatsiavut : Importance for municipal and transportation » book chapter In Nunavik and Nunatsiavut: From science to policy. An Integrated Regional Impact Study (IRIS) of climate change and modernization, Mickaël Lemay Michel Allard, 171-197.: ArcticNet Inc. Quebec, Quebec, Canada. https://www.mun.ca/geog/people/faculty/Chapter_6.pdf.

Arp C.D., Whitman M.S., Jones B.M., Grosse G., Gaglioti B.V. & Heim K.C. (2015) « Distribution and biophysical processes of beaded streams in Arctic permafrost landscapes. » Biogeosciences 12 (1): 29-47. doi:10.5194/bg-12-29-2015.

Baroudy E. & Elliott J.M. (1994) « The critical thermal limits for juvenile Arctic charr Salvelinus alpinus. » Journal of Fish Biology. doi:10.1111/j.1095-8649.1994.tb01071.x.

Belknap W. & Naiman R. J. (1998) « A GIS and TIR procedure to detect and map wall-base channels in Western Washington. » Journal of Environmental Management 52 (2): 147-160. doi:10.1006/jema.1997.0169.

Bergeron N.E. & Carbonneau P.E. (2012) « Geosalar: Innovative Remote Sensing Methods for Spatially Continuous Mapping of Fluvial Habitat at Riverscape Scale. » book chapter In Fluvial Remote Sensing for Science and Management, P. E. Carbonneau & H. Piegay, First, 193-213. Chichester, UK: John Wiley and Sons. doi:10.1002/9781119940791.ch9.

Berman C.H. & Quinn T.P. (1991) « Behavioural thermoregulation and homing by spring chinook salmon, Oncorhynchus tshawytscha (Walbaum), in the Yakima River. » Journal of Fish Biology 39 (3): 301-312. doi:10.1111/j.1095-8649.1991.tb04364.x.

Breau C., Cunjak R.A. & Bremset G. (2007) « Age-specific aggregation of wild juvenile Atlantic salmon Salmo salar at cool water sources during high temperature events. » Journal of Fish Biology 71 (4): 1179-1191. doi:10.1111/j.1095-8649.2007.01591.x.

Breton M.-P., Cloutier G. et. Waygood E.O.D. (2017) « QUEBEC. » book chapter In Climate risks and adaptation practices for the Canadian transportation sector, K. Palko and D.S. Lemmen (Eds.), 181-216. Government of Canada. Ottawa, ON, Canada..

Campbell S., Affleck R.T. & Sinclair S. (2018) « Ground-penetrating radar studies of permafrost, periglacial, and near-surface geology at McMurdo Station, Antarctica. » Cold Regions Science and Technology 148 (November 2016): 38-49. doi:10.1016/j.coldregions.2017.12.008.

Casas-Mulet R., Pander J., Ryu D., Stewardson M.J. & Geist J. (2020) « Unmanned Aerial Vehicle (UAV)-Based Thermal Infra-Red (TIR) and Optical Imagery Reveals Multi-Spatial Scale Controls of Cold-Water Areas Over a Groundwater-Dominated Riverscape. » Frontiers in Environmental Science 8 (May): 1-16. doi:10.3389/fenvs.2020.00064.

ClimateData.ca (2021) « Data Source: Environment and Climate Change Canada and (ClimateData.ca) See: https://eccc-msc.github.io/open-data/licence/readme_en/. » Page Web, consulté le 1er septembre 2021 à l'adresse

https://climatedata.ca/explore/location/?loc=EJLMJ&location-select-temperature=tx_mean&location-select-precipitation=rx1day&location-select-other=frost_days.

Dole-Olivier M.J., Wawzyniak V., des Châtelliers C. & Marmonier P. (2019) « Do thermal infrared (TIR) remote sensing and direct hyporheic measurements (DHM) similarly detect river-groundwater exchanges? Study along a 40 km-section of the Ain River (France). » Science of the Total Environment 646. Elsevier B.V.: 1097-1110. doi:10.1016/j.scitotenv.2018.07.294. https://doi.org/10.1016/j.scitotenv.2018.07.294.

Dugdale S.J., Bergeron N.E. & St-Hilaire A. (2013) « Temporal variability of thermal refuges and water temperature patterns in an Atlantic salmon river. » Remote Sensing of Environment 136. Elsevier Inc.: 358-373. doi:10.1016/j.rse.2013.05.018. http://dx.doi.org/10.1016/j.rse.2013.05.018.

Dugdale S.J., Bergeron N.E. & St-Hilaire A. (2015) « Spatial distribution of thermal refuges analysed in relation to riverscape hydromorphology using airborne thermal infrared imagery. » Remote Sensing of Environment 160. Elsevier Inc.: 43-55. doi:10.1016/j.rse.2014.12.021. http://dx.doi.org/10.1016/j.rse.2014.12.021.

Dugdale S.J., Franssen J., Corey E., Bergeron N.E., Lapointe M. & Cunjak R.A. (2016) « Main stem movement of Atlantic salmon parr in response to high river temperature. » Ecology of Freshwater Fish 25 (3): 429-445. doi:10.1111/eff.12224.

Duguay C.R., Zhang T., Leverington D.W. & Romanovsky V.E. (2005) « Satellite remote sensing of permafrost and seasonally frozen ground. » Geophysical Monograph Series 163 (January): 91-118. doi:10.1029/163GM06.

Ebersole J.L., Wigington P.J., Leibowitz S.G., Comeleo R.L. & Van Sickle J. (2015) « Predicting the occurrence of cold-water patches at intermittent and ephemeral tributary confluences with warm rivers. » Freshwater Science 34 (1): 111-124. doi:10.1086/678127.

Finstad A.G. & Jonsson B. (2012) « Effect of incubation temperature on growth performance in Atlantic salmon. » Marine Ecology Progress Series 454 (1): 75-82. doi:10.3354/meps09643.

Foretouverte (2018) « Cartographie écologique de la VÉGÉTATION du NORD QUÉBÉCOIS. » Ministère des Forêts, de la Faune et des Parcs Direction des inventaires forestiers. Page Web, consulté le 10 juin 2021 à l'adresse https://www.foretouverte.gouv.qc.ca/

Fullerton A.H., Torgersen C.E., Lawler J.J., Faux R.N., Steel E.A., Beechie T.J. & Ebersole J.L., Leibowitz S.G (2015) « Rethinking the longitudinal stream temperature paradigm region-wide comparison of thermal infrared imagery reveals unexpected complexity of river temperatures. » Hydrological Processes 29 (22): 4719–4737. doi:10.1002/hyp.10506.

Geist D.R. & Dauble D.D. (1998) « Redd site selection and spawning habitat use by fall chinook salmon: The importance of geomorphic features in large rivers. » Environmental Management 22 (5): 655-669. doi:10.1007/s002679900137.

Gerlach M.E., Rains K.C., Guerrón-Orejuela E.J., Kleindl W.J., Downs J., Landry S.M. & Rains M.C. (2022) « Using remote sensing and machine learning to locate groundwater discharge to salmon-bearing streams. » Remote Sensing 14 (1). doi:10.3390/rs14010063.

Gouvernement du Québec (2021) « Normales climatiques 1981-2010. » Ministère de l'Environnement et de la Lutte contre les changements climatiques. Page Web, consulté le 1er septembre 2021 à l'adresse https://www.environnement.gouv.qc.ca/climat/normales/climat-qc.htm.

Gunn J. & Snucins E. (2010) « Brook charr mortalities during extreme temperature events in Sutton River, Hudson Bay Lowlands, Canada. » Hydrobiologia 650 (1): 79-84. doi:10.1007/s10750-010-0201-3.

Jensen A.J., Johnsen B.O. & Saksgard L. (1989) « Temperature requirements in Atlantic salmon (Salmo salar), brown trout (Salmon trutta), and Arctic char (Salvelinus alpinus) from hatching to initial feeding compared with geographic distribution. » Canadian Journal of Fisheries and Aquatic Sciences 46 (5): 786-789. doi:10.1139/f89-097.

Jonsson B. & Jonsson N. (2009) « A review of the likely effects of climate change on anadromous Atlantic salmon Salmo salar and brown trout Salmo trutta, with particular reference to water temperature and flow. » Journal of Fish Biology 75 (10): 2381-2447. doi:10.1111/j.1095-8649.2009.02380.x.

Kativik Regional Government (2005) « Kuururjuaq Park Project (Monts-Torngat-et-Rivière Koroc). » Status Report, Kativik Regional Government, Kuujjuaq, Québec.

L'Hérault E. & Allard M. (2018) « Production de la 2ième approximation de la carte de pergélisol du Québec en fonction des paramètres géomorphologiques, écologiques, et des processus physiques liés au climat. » Rapport produit pour le compte du Ministère des Forêts, de la Faune et des Parcs, Centre d'études nordiques, Université Laval, Québec, Québec, Canada.

Lamontagne-Hallé P., McKenzie J.M., Kurylyk B.L., Molson J.W. & Lyon L.N. (2020) « Guidelines for cold-regions groundwater numerical modeling. » Wiley Interdisciplinary Reviews: Water 7 (6): 1-26. doi:10.1002/wat2.1467.

Lemieux J.-M., Fortier R., Talbot-Poulin M.-C., Molson J.W., Therrien R., Ouellet M., Banville D., Cochand M. & Murray R. (2016) « Groundwater occurrence in cold environments: examples from Nunavik, Canada. » Hydrogeology Journal 24 (6): 1497-1513. doi:10.1007/s10040-016-1411-1.

Liao C. & Zhuang Q. (2017) « Quantifying the Role of Permafrost Distribution in Groundwater and Surface Water Interactions Using a Three-Dimensional Hydrological Model. » Arctic, Antarctic, and Alpine Research 49 (1): 81-100. doi:10.1657/AAAR0016-022.

Liu S. & Feng Y. (2011) « AIRBORNE GPR : ADVANCES AND NUMERICAL SIMULATION College of Geo-exploration Sci & Tech , Jilin University , Changchun , China 130026 The third Railway Survey and Design Institute Group Corporation , Tianjin , China 300142. » IEEE: 3397-3400.

Lorenz J.M. & Filer J.H. (1989). « Spawning Habitat and Redd Characteristics of Sockeye Salmon in the Glacial Taku River, British Columbia and Alaska. » Transactions of the American Fisheries Society 118 (5): 495-502. doi:10.1577/1548-8659(1989)118<0495:sharco>2.3.co;2. http://citeseerx.ist.psu.edu/viewdoc/download?doi=10.1.1.586.132&rep=rep1&type=pdf.

Mainguy J. & Beaupré L. (2019) « Établissement d'un état de référence pour la population d'omble chevalier de la rivière Bérard à Tasiujaq. » Report by ministère des Forêts, de la Faune et des Parcs, Direction de l'expertise sur la faune aquatique et Direction de la gestion de la faune du Nord-du-Québec, 29 p.

MINISTÈRE DES FORÊTS, DE LA FAUNE ET DES PARCS (2016) « Atlantic salmon management plan 2016-2026. » Report by ministère des Forêts, de la Faune et des Parcs, Direction générale de l'expertise sur la faune et ses habitats, Direction de la faune aquatique, Québec, 40 p.

Monk W.A., Wilbur N.M., Curry R.A., Gagnon R. & Faux R.N. (2013) « Linking landscape variables to cold water refugia in rivers. » Journal of Environmental Management 118. Elsevier Ltd: 170-176. doi:10.1016/j.jenvman.2012.12.024. http://dx.doi.org/10.1016/j.jenvman.2012.12.024.

Natural Resources Canada (2019) « Lakes, Rivers and Glaciers in Canada - CanVec Series - Hydrographic Features. » Government of Canada; Natural Resources Canada;Strategic Policy and Innovation Sector. https://open.canada.ca/data/en/dataset/9d96e8c9-22fe-4ad2-b5e8-94a6991b744b .

Nyanti L., Soo C.L., Ahmad-Tarmizi N.N., Abu-Rashid N.N.K., Ling T.Y., Sim S.F., Grinang J., Ganyai T. & Ping Lee K.S. (2018) « Effects of water temperature, dissolved oxygen and total suspended solids on juvenile barbonymus schwanenfeldii (Bleeker, 1854) and Oreochromis Niloticus (Linnaeus, 1758). » AACL Bioflux 11 (2): 394-406.

Owuor S.O., Butterbach-Bahl K., Guzha A.C., Rufino M.C., Pelster D.E., Díaz-Pinés E. & Breuer L. (2016) « Groundwater recharge rates and surface runoff response to land use and land cover changes in semi-arid environments. » Ecological Processes 5 (1). Ecological Processes. doi:10.1186/s13717-016-0060-6. http://dx.doi.org/10.1186/s13717-016-0060-6.

Peterson N.P. & Reid L.M. (1984) « Wall-base channels: their evolution, distribution, and use by juvenile coho salmon in the Clearwater River, Washington. » In Olympic wild fish conference, (J.M.Walton, Peninsula College, Port Angeles, WA), 215-225. Port Angeles, WA: J.M.Walton, Peninsula College.

Philipp M., Dietz A., Buchelt S. & Kuenzer C. (2021) « Trends in satellite earth observation for permafrost related analyses-a review. » Remote Sensing 13 (6): 1-57. doi:10.3390/rs13061217.

Poesch M.S., Chavarie L., Chu C., Pandit S.N. & Tonn W. (2016) « Climate Change Impacts on Freshwater Fishes: A Canadian Perspective. » Fisheries 41 (7): 385-391. doi:10.1080/03632415.2016.1180285. http://dx.doi.org/10.1080/03632415.2016.1180285.

Power G., Brown R.S. & Imhof J.G. (1999) « Groundwater and fish - Insights from northern North America. » Hydrological Processes 13 (3): 401-422. doi:10.1002/(SICI)1099-1085(19990228)13:3<401::AID-HYP746>3.0.CO;2-A.

SIGÉOM (2022) « Surface deposits map. » système d'information géominière du Québec. Page Web, consulté le 1er juin 2020 à l'adresse https://sigeom.mines.gouv.qc.ca/signet/classes/I1108_afchCarteIntr.

Torgersen C.E., Faux R.N., McIntosh B.A., Poage N.J. & Norton D.J. (2001) « Airborne thermal remote sensing for water temperature assessment in rivers and streams. » Remote Sensing of Environment 76 (3): 386-398. doi:10.1016/S0034-4257(01)00186-9.

Ulrich M., Matthes H., Schirrmeister L., Schütze J., Park H., Iijima Y. & Fedorov A.N. (2017) « Differences in behavior and distribution of permafrost-related lakes in Central Yakutia and their response to climatic drivers. » Water Resources Research RESEARCH 53 (2): 1167-1188. doi:doi:10.1002/2016WR019267.

Willms T. & Whitworth G. (2016) « Mapping of critical summer thermal refuge habitats for Chinook salmon, Coho salmon, steelhead and bull trout in the Nicola River Watershed - 2016. » Report of Habitat Stewardship Program for Species at Risk. Vol. 3. Fraser Basin Council: Kamloops, BC, Canada.

3 ANALYSIS OF LARGE-SCALE GROUNDWATER-DRIVEN COOLING ZONES IN RIVERS USING THERMAL INFRARED IMAGERY AND RADON MEASUREMENTS

Analyse des zones de refroidissement à grande échelle alimentées par les eaux souterraines dans les rivières à l'aide de l'imagerie infrarouge thermique et des mesures de radon

Milad Fakhari [1,*], Jasmin Raymond [1], Richard Martel [1], Jean-Philippe Drolet [1], Stephen J. Dugdale [2], Normand Bergeron [1]

1 Institut national de la recherche scientifique, Centre Eau Terre Environnement, Québec, QC G1K 9A9, Canada

2 School of Geography, University of Nottingham, Nottingham NG7 2RD, UK

* Correspondance: milad.fakhari@inrs.ca

Publié dans ***Water*** 2023, 15, 873

Publié le 24 février 2023

doi.org/ 10.3390/w15050873

Contribution des auteurs :

Conceptualisation, Milad Fakhari, Jasmin Raymond et Richard Martel; méthodologie, Milad Fakhari; analyse formelle, Milad Fakhari; conservation des données, Milad Fakhari; rédaction - préparation de la version originale, Milad Fakhari; rédaction - révision et édition, Milad Fakhari, Jasmin Raymond, Richard Martel, Jean-Philippe Drolet, Stephen J. Dugdale et Normand Bergeron; visualisation, Milad Fakhari. Tous les auteurs ont lu et approuvé la version publiée du manuscrit.

Lien entre l'article ou les articles précédents et le suivant :

Les résultats de l'article précédent concernant les zones de refroidissement identifiées dans la rivière Bérard ont été sélectionnés pour une analyse plus approfondie dans cet article. Sur la base des résultats de cet article, un site a été sélectionné pour une analyse plus approfondie de la rivière Sainte-Marguerite dans le prochain article avec différentes méthodes de terrain implémentées à petite échelle.

Abstract: The role of groundwater (GW) discharge on surface water (SW) quantity, quality and temperature is known to be important. Moreover, the effect of GW contributions to the river thermal budget is critical in natural rivers considering that water temperature plays a vital role in fish survival during extreme heat events. The identification of zones with GW input in rivers can, thus, help river management plans. However, detecting these zones at the watershed scale can be a challenge. This work combines thermal infrared (TIR) imagery of rivers and water sampling for radon measurements for better documentation of GW in rivers. The Sainte-Marguerite and Berard Rivers, both located in Quebec, Canada, are known for their abundance of salmonids. Their water temperature profiles were plotted using TIR imagery, and five cooling zones in the Berard River and two for the Sainte-Marguerite River were identified in which notable GW–SW exchange was the suspected cause. Radon concentrations measured within the cooling zones showed clear GW contribution to SW. TIR imagery is an effective and fast way to identify GW seepage at the watershed scale. Radon can be used as a complementary natural tracer of GW in rivers at finer scales. The combination of both methods was shown to be reliable for the identification of GW in rivers. This can help for a better anticipation of GW effects in management plans to deal with extreme heat waves that are predicted to occur more frequently under future climate change scenarios.

Résumé : Le rôle de l'écoulement des eaux souterraines sur la quantité, la qualité et la température des eaux de surface est connu pour être important. En outre, l'effet des contributions des eaux souterraines sur le bilan thermique des rivières est crucial dans les rivières naturelles, étant donné que la température de l'eau joue un rôle vital dans la survie des poissons pendant les épisodes de chaleur extrême. L'identification des zones d'apport d'eau souterraine dans les cours d'eau peut donc aider les plans de gestion des cours d'eau. Cependant, la détection de ces zones à l'échelle du bassin versant peut s'avérer difficile. Ce travail combine l'imagerie infrarouge

thermique (TIR) des rivières et l'échantillonnage de l'eau pour les mesures de radon afin de mieux documenter l'apport d'eau souterraine dans les rivières. Les rivières Sainte-Marguerite et Bérard, toutes deux situées au Québec, Canada, sont connues pour leur abondance de salmonidés. Leurs profils de température de l'eau ont été tracés à l'aide de l'imagerie TIR, et cinq zones de refroidissement dans la rivière Bérard et deux dans la rivière Sainte-Marguerite ont été identifiées, dans lesquelles un échange GW-SW notable était la cause présumée. Les concentrations de radon mesurées dans les zones de refroidissement ont montré une contribution évidente du GW au SW. L'imagerie TIR est un moyen efficace et rapide d'identifier les infiltrations d'eau souterraine à l'échelle du bassin versant. Le radon peut être utilisé comme traceur naturel complémentaire des eaux souterraines dans les rivières à des échelles plus fines. La combinaison des deux méthodes s'est avérée fiable pour l'identification des eaux souterraines dans les rivières. Cela peut aider à mieux anticiper les effets de l'eau souterraine dans les plans de gestion des vagues de chaleur extrême qui devraient se produire plus fréquemment dans les futurs scénarios de changement climatique.

3.1 Introduction

Groundwater (GW) exchanges in rivers deliver base flow, affect water quality, mitigate water temperature, and provide thermal refuge for fish (Power et al., 1999). Heat has been used as a tracer for the identification of groundwater–surface water (GW–SW) exchange (Anderson, 2005). GW temperature varies less throughout the year compared to surface water (SW), such that it can influence a river's temperature profile, providing cool water to rivers during summer and warm water during winter. Over the winter, warm water is important for survival of fish from eggs to alevin (Geist et al., 1998; Baxter et al., 2000). During summer when river water temperature goes above thermal optimal for fish and other ectotherms, they seek shelter in zones of GW seepage known as thermal refuges (Dugdale et al., 2016; Frechette et al., 2018; Ebersole et al., 2003). In the context of climate change, extreme temperature events are expected to occur more frequently in the future (Colombo et al., 1999; Fortin et al., 2017; Breton et al., 2017). Therefore, it is important to study the effects of GW in rivers to better understand temperature regimes and evaluate the impact on fish habitats (Gunn et al., 2010; Poesch et al., 2016). This calls for GW-related studies to be considered for a better freshwater fishery management plan.

Thermal infrared (TIR) imagery is an effective monitoring tool for the identification of spatiotemporal variability of discrete thermal refuges and larger scale cooling zones in rivers (Willms et al., 2016; Torgersen et al., 2012; Mejia et al., 2020). In addition to the identification of thermal refuges and cooling zones, understanding the sources of these cool water patches is important to better understand their potential response to climate change. Thermal refuges can be classified based on their location and shape in the river and, accordingly, their source (either SW or GW) can be identified (Dugdale et al., 2015; Dugdale et al., 2013). In addition to these discrete thermal refuges, rivers can often exhibit larger-scale 'diffuse' cooling zones (Dugdale et al. 2016). The source of cold water for these larger-scale river cooling zones can be from small or large tributaries that enter the main stem or from GW seepage.

Identifying the exact source of cold water for these larger cooling zones by relying on TIR imagery alone can be difficult (Fakhari et al., 2022), and the exact sources of cooling water inputs have rarely been the subject of previous TIR-based studies (e.g., Mejia et al., 2020; Wawrzyniak et al., 2012). Thus, the hypothesis of consistently higher GW seepage in large cooling zones remains unverified. The present study combines the use of 222Rn (henceforward referred as radon) as a natural tracer for the detection of GW in the river cooling zones to overcome the limits of the TIR imagery method in validating this hypothesis.

Naturally dissolved radon in water was proven to be a reliable tracer for GW–SW interaction investigation during the last two to three decades (Wu et al., 2004; Ortega et al., 2015; Berth et al., 1994). Radon has a short half-life of 3.8 days, and when in water, it tends to attach to air bubbles that can escape to the atmosphere via gas exchange. Consequently, its concentration in GW is one or more orders of magnitude higher than SW (Wu et al., 2004; Ortega et al., 2015). Therefore, where radon concentration in the river is high, an active exfiltration of radon-bearing GW is present (Hoehn et al., 1989; Rogers, 1958). Radon measurement in SW and GW can be used for the identification of GW flow paths near SW bodies, its recharge or discharge (Hoehn et al., 1989; Schubert et al., 2006) and quantification of this infiltration or exfiltration rate (Wu et al., 2004; Ortega et al., 2015; Berth et al., 1994; Yi et al., 2018; Cook et al., 2006; Corbett et al., 1997; Burnett et al., 2010). The objective of this study was, therefore, to verify the presence of GW in the identified cooling zones with TIR imagery and estimate the GW seepage rate into the river within these zones by measuring the radon concentration in SW and GW. Similar studies have been carried out for marine environments (e.g., Kelly et al., 2019) and lakes (e.g., Wilson et al., 2016), but are limited for rivers (e.g., Malard et al., 1999).

3.2 Study area

The two rivers selected for this study are the Sainte-Marguerite River, which drains into the Saguenay River about 12 km from the Sacre-Coeur municipality in the Côte-Nord region of the Quebec Province, and the Berard River, which discharges into Ungava Bay in the northern village of Tasiujaq in Nunavik, northern Quebec (Figure 3.1).

The Sainte-Marguerite River is in the south of the province, without permafrost (Figure 3.1-A) and in a continental cold and humid climate (Figure 3.1-B) with an annual average temperature of 3 °C and an average annual precipitation of 980 mm. The Berard River is in the northern part of the province, in a discontinuous permafrost zone (Figure 3.1-A) and in a continental subpolar climate (Figure 3.1-B) with an annual average temperature of −5.2 °C and an average annual precipitation of 447 mm (ClimateData.ca, 2021).

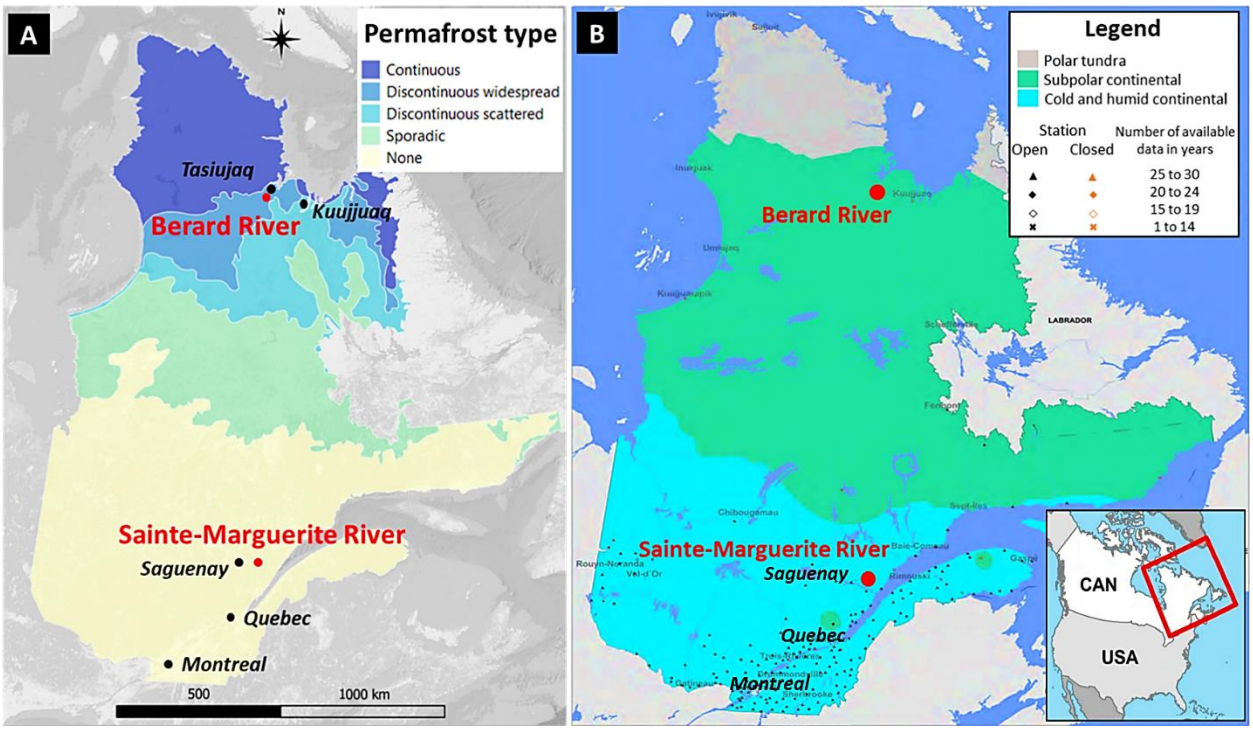

Figure 3.1 **Location of the two studied rivers on permafrost distribution map (A, adapted from Lemieux et al., 2016) and Köppen climate classification map (B, from Gouvernement du Québec, 2021) of the Quebec Province.**

The studied section of the Sainte-Marguerite River is from the junction of the main branch with the north-east branch for a length of ~40 km (Figure 3.2). At the Sainte-Marguerite River study site, the bedrock geology consists of metamorphic rocks, mostly gneiss, migmatite, and orthopyroxene granitoids such as charnockite, mangerite, jotunite and hypersthene syenite (Figure 3.2). The shallow aquifer under and adjacent to the Sainte-Marguerite River is made of fine sand and sandy silt material, which is recent and ancient river terrace alluvial deposit with a variable thickness of 1–30 m, underlaid with less permeable deltaic and prodeltaic glaciomarine sediment (SIGÉOM, 2022). However, based on field observations, the near-surface riverbed material of the Sainte-Marguerite River is highly permeable recent river deposits made of coarse sand, gravel and boulders with a thickness of <5 m.

The Berard River study site covers 17.5 km downstream of Berard Lake to the river's mouth in Ungava Bay (Figure 3.3). The bedrock geology across the Berard River is a mix of sedimentary rocks dominantly made of conglomerate, sandstone, siltstone, mudrock, wacke and quartz arenite. Near the bay and further from the river valley, igneous rocks dominantly made of gabbro, diorite, quartz diorite, gabbronorite, anorthosite, granite and granodiorite are also present (Figure 3.3). Some bedrock formations contain a considerable amount of iron (orange in Figure 3.3). Based on field observation, the shallow aquifer below the Berard River is made of recent alluvium.

From 0 to about 0.75 m depth, a hardpan with boulders and rocks with a diameter of 1 cm to > 50 cm is present. Low-permeability deep-water fine-grained glaciomarine sediment is present underneath the shallow alluvial aquifer (SIGÉOM, 2022).

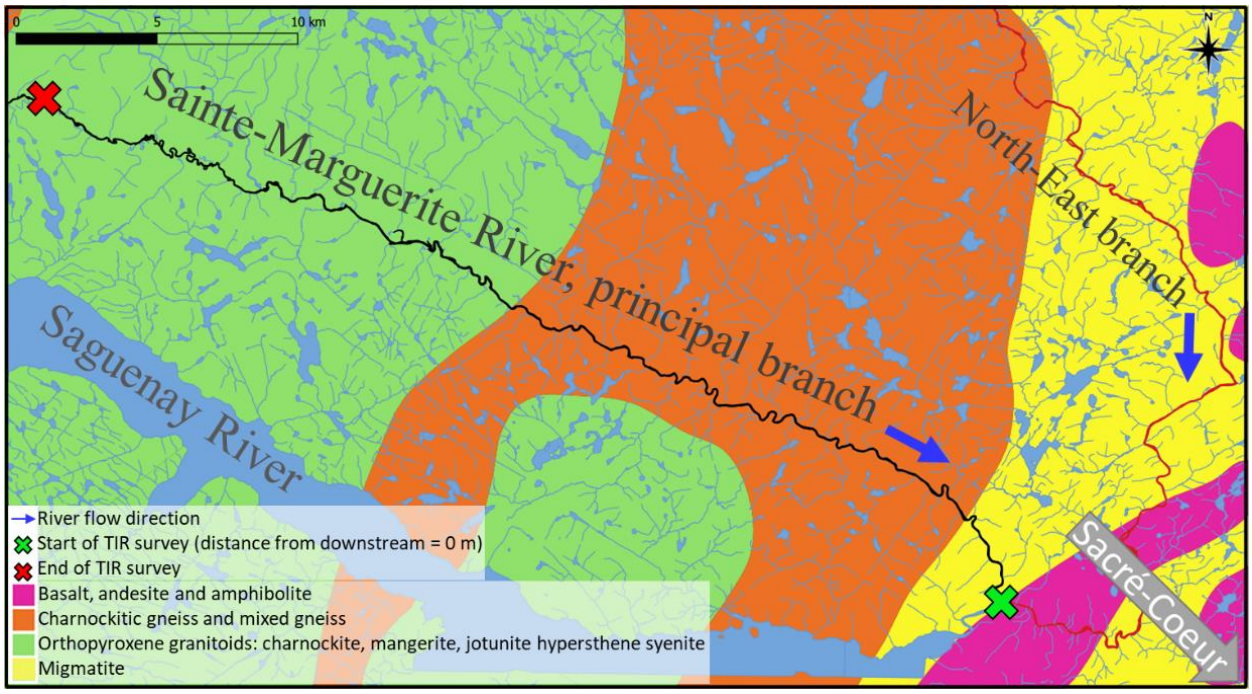

Figure 3.2 Bedrock geology across the Sainte-Marguerite River (based on SIGÉOM, 2022).

3.3 Materials and methods

3.3.1 Aerial TIR imagery

The details about the acquisition method and equipment regarding TIR image acquisition can be found in (Dugdale et al., 2015; Dugdale et al., 2013), but information specific to this study is presented here. The thermal imagery of the rivers was acquired with an FLIR SC660 camera attached to a helicopter. Imagery was acquired in mid-September 2019 (the low flow season of the studied rivers), during a warm sunny day near midday with air temperature around 20 °C. This ensures maximum contrast between river water temperature and GW-fed cooling zones, for ease of their identification. Flights were conducted at an altitude of approximately 400 m above ground, which resulted in a thermal image resolution of ~25 cm. Additionally, the low ground speed of the helicopter lead to a good image overlap (more than 75%). RGB images (3 cm resolution) were collected at the same time to provide visual context for the thermal images.

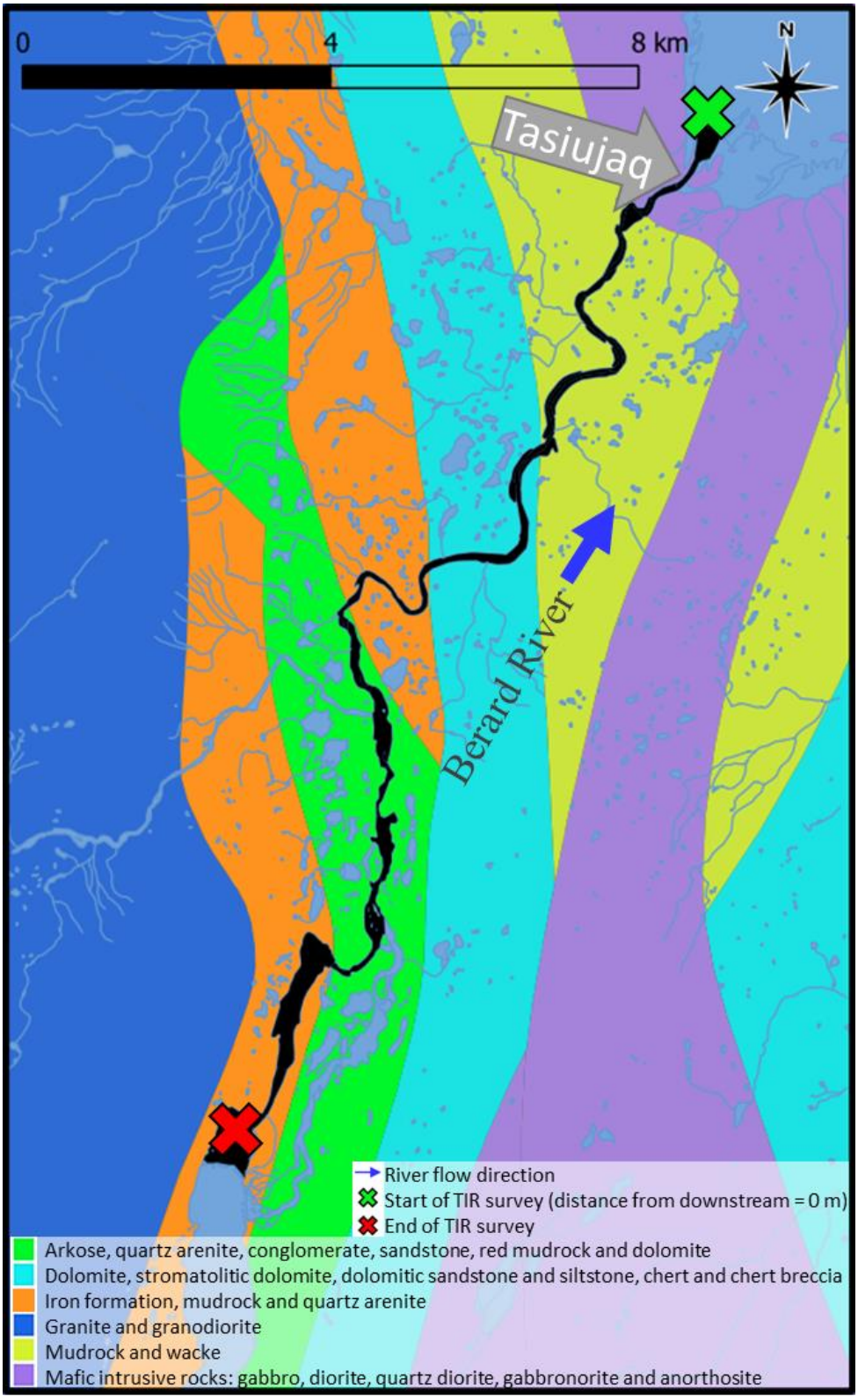

Figure 3.3 Bedrock geology across the Berard River (based on SIGÉOM, 2022).

River temperature profiles were generated by plotting mean river water temperature against distance downstream. The mean river temperature of each thermal image was calculated by averaging the temperature of three points in the river central line (details in Fakhari et al., 2022). TIR-derived temperatures were validated using Onset HOBO MX2201 Pendant temperature loggers installed in the river, following the approaches detailed in (Dugdale et al., 2015; Dugdale et al., 2013).

The asymptotic warming paradigm (Fullerton et al., 2015) states that river water temperature should increase when moving from upstream to downstream as a function of energy exchanges at the air–water interface. However, temperature long profiles rarely follow this trend in nature, due partially to advection from either SW or GW exchanges. As such, large-scale cooling zones in the order of 100–1000 m are often present in a river's temperature profile. For the purposes of this study, we defined a cooling zone as a section of profile with a sustained temperature decrease of 0.25 °C or greater. Areas of the river temperature profile that exhibited a temperature decrease greater than this magnitude were, thus, used to identify the presence and length of a cooling zone. Since GW seepage can be the source of cold water, the cooling zone's existence is expected to be temporally persistent. Therefore, these cooling zones were selected for further investigation regarding the presence of GW in the rivers.

3.3.2 Radon measurements

Radon is naturally produced from the decay of background uranium in soil, rock and water. Therefore, its presence in GW depends on the lithology and aquifer geochemistry (Ortega et al., 2015; Elzain, 2014). Thus, bedrock type has been considered for the interpretation of radon sampling results. Additionally, water sampling was avoided during or after rainy days when the water level was high, since radon concentration in rain is very low and dilutes the radon level in SW and GW.

Nine sampling points on each river were considered. Selected sampling points for radon measurement correspond to the identified cooling zones from TIR imagery analysis. One or more sampling points inside the cooling zone were selected and one point before or after cooling zones. The radon sampling points were selected at the center of the river, since river temperature profile is based on three measurements points on the river center line. In addition, as the aim was to verify the presence of GW seepage, sampling points were located as close as possible to the bottom of the river. Radon can escape from the water samples via gas exchange, so the samples were taken by submerging the bottles and closing the cap under water. Moreover, samples from

two shallow piezometers (depth of about 2 m from the ground surface), installed close to the river, were also collected to verify the difference in radon concentration in GW and SW. GW samples were collected by the use of a peristaltic pump set to a low flow to avoid air bubbles entering the samples. One duplicate (representing 10% of samples collected) from GW samples and one for SW samples at each studied river were analyzed to validate the accuracy of the sampling and measurements.

Water samples were analyzed within 24 h of the sampling period to avoid radon complete decay before its analysis. Radon concentration was measured by the use of an AB-5R portable radiation monitor device (Pylon, 2022). Radon was first extracted into cells designed for AB-5R by the use of a WG-1001 device (Pylon, 2022). The AB-5R device then counted the emitted alpha particles from radon decay inside the cell. For each sample, five 5 min counting cycles were considered. The counts were later translated to radon concentration in Bq/L by applying a correction factor considering the time between the sampling event and the analysis.

The GW flow pattern can be verified by having radon concentration in the installed piezometers at different locations in the studied section of the river. Few SW samples were collected near the piezometers to estimate the GW flow path (Schubert et al., 2006).

Moreover, by using the mass conservation theory (Equation (3.1)), the fraction of GW in the river (*f*), which is the ratio of GW seepage flow rate (Q_{gw}) (m^3/s) to river discharge (Q_{sw}) (m^3/s), can be approximated by Equation (3.2), where radon concentration in GW and in SW at the study site are C_{gw} (Bq/L) and C_{sw} (Bq/L), respectively, and C_{bg} (Bq/L) is background concentration, which is the concentration in SW upstream of the study area (Wu et al., 2004).

$$C_{sw}Q_{sw} = C_{gw}Q_{gw} + C_{bg}(Q_{sw} - Q_{gw}) \tag{3.1}$$

$$f = \frac{Q_{gw}}{Q_{sw}} \times 100\% = \frac{C_{sw} - C_{bg}}{C_{gw} - C_{bg}} \times 100\% \tag{3.2}$$

The mass balance theory is solved for a selected area of the river by selecting an upstream and a downstream section. The radon concentrations used in Equation (3.2) should be calibrated considering the loss of radon by gas exchange and radioactive decay (Wu et al., 2004). The gas exchange correction factor is applied to take into account the loss of radon via gas exchange between the upstream and downstream section. If the flow in between the upstream and downstream section is not turbulent, the gas exchange within the zone is negligible. The radioactive decay correction factor is to adjust the radon concentration loss for the sampling time

difference between upstream and downstream sections. If the sampling of these two sections is carried out relatively simultaneously, the correction factor is very small, and the results are not different from the case if the two samples are taken at the same time at the upstream and downstream sections. Therefore, calibration factors were not applied in this study as a simplification. Instead, we considered C_{bg} as the radon concentration in the upstream warming zone, C_{sw} as the radon concentration in the cooling zone (average if multiple sampling within the zone is present) and C_{gw} as the average radon concentration in the shallow piezometers on shore.

The results of GW seepage flow rates from radon mass balance methods were then compared to GW seepage measured by seepage meters in the Sainte-Marguerite River (Figure 3.4). Seepage meters measure the amount of GW gained or lost from the isolated section of the riverbed by the barrel. Several seepage meters were installed on the riverbed close to the location of piezometers for a duration of 6 to 24 h. By knowing the amount of water in the plastic bags (*V*) (m^3), the duration of the measurement (*t*) (s) and area of the barrel (*S*) (m^2), the vertical GW flow rate (*q*) (m/s) into the river can be calculated from Equation (3.3) (Rosenberry et al., 2008).

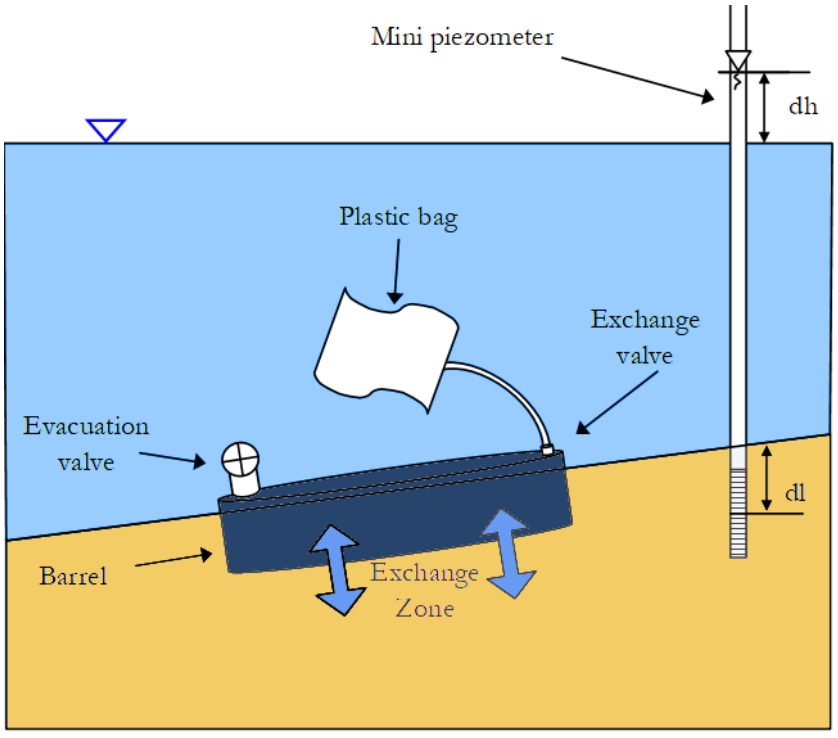

Figure 3.4 Schematic of the seepage meter device.

Moreover, the horizontal GW flow rate can be calculated by using the mean hydraulic conductivity (*k*) (m/s) of the riverbank material from slug tests in the piezometers close to the river shore and

the hydraulic gradient (*i*) (m/m) between the piezometer and river water levels with the Darcy equation (Equation (3.4)).

$$q = \frac{V}{St} \tag{3.3}$$

$$q = ki \tag{3.4}$$

3.4 Results

3.4.1 River temperature profile

The river temperature profile from TIR imagery of the Sainte-Marguerite River shows two cooling zones, named S1 and S2, which have a length of two and seven kilometers, respectively. These cooling zones cover approximately 22.5% of the studied river length (Figure 3.5).

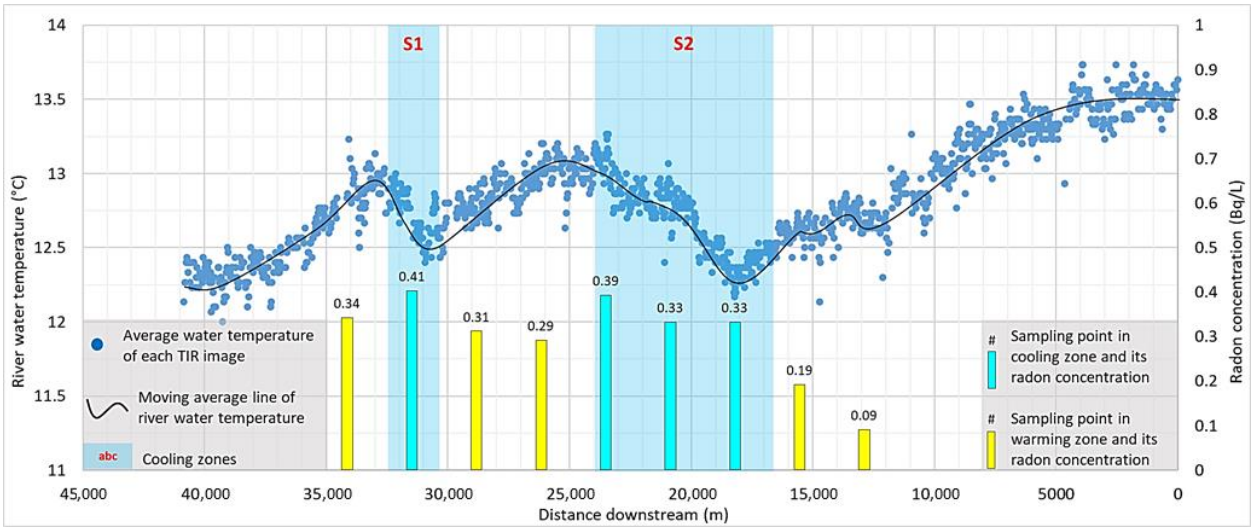

Figure 3.5 **Scatter plot showing temperature profile of Sainte-Marguerite River and columns showing location of radon sampling and measured concentration.**

The Berard River temperature profile shows five cooling zones with a length varying between 665 m and 2365 m and a total length of 7.8 km, which is 46% of the total studied length of the river (Figure 3.6).

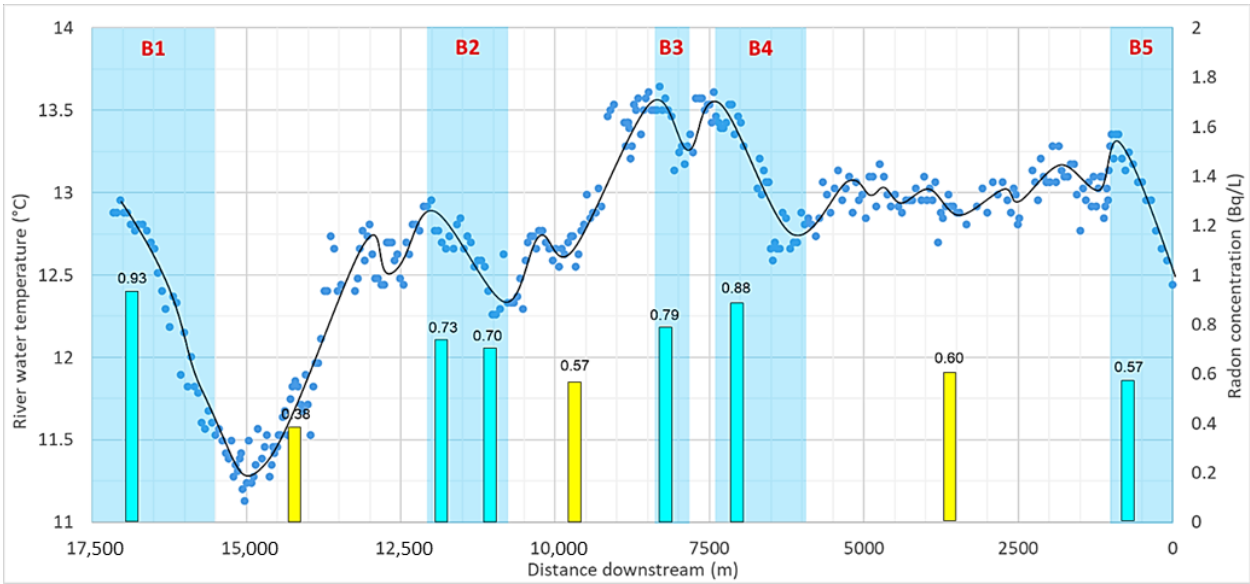

Figure 3.6 **Scatter plot showing temperature profile of Berard River and columns showing location of radon sampling and measured concentration (labels same as Figure 3.5).**

3.4.2 Radon measurements

Four of the nine sampling points on the Sainte-Marguerite River were in cooling zones and five in warming (or temperature stable) zones. The identified cooling zones in this river are lengthy, thus, multiple sampling points in them were selected to have at least one point for every two kilometers. The measured radon concentration in the cooling zones varies between 0.33 Bq/L and 0.41 Bq/L, with an average of 0.35 Bq/L, while for the warming zones, the concentration range was 0.09 Bq/L to 0.34 Bq/L with an average of 0.25 Bq/L (Figure 3.7). This difference in average values was meaningful based on t-tests (Figure 3.8). The average radon concentration for GW samples of the Sainte-Marguerite River was 6.23 Bq/L.

Six sampling points are located in the cooling zones of the Berard River and three in warming or stable zones. One sampling point in each cooling zone and one in each warming zone in between the cooling zones were selected. However, in B2 (second most downstream zone), two sampling points were selected, one before and one after the entrance of the large tributary to the main stem. This aids in the assessment of the effect of mixing of the tributary and the main stem water on the measured radon concentration. The radon concentration for points in cooling zones ranges between 0.57 Bq/L and 0.93 Bq/L, and the average was 0.76 Bq/L, while the concentration of points in warming zones has a range between 0.38 Bq/L and 0.60 Bq/L, with an average of 0.51 Bq/L (Figure 3.9). This difference in average values was significant based on t-tests (Figure 3.10). The GW samples had an average radon concentration of 10.85 Bq/L.

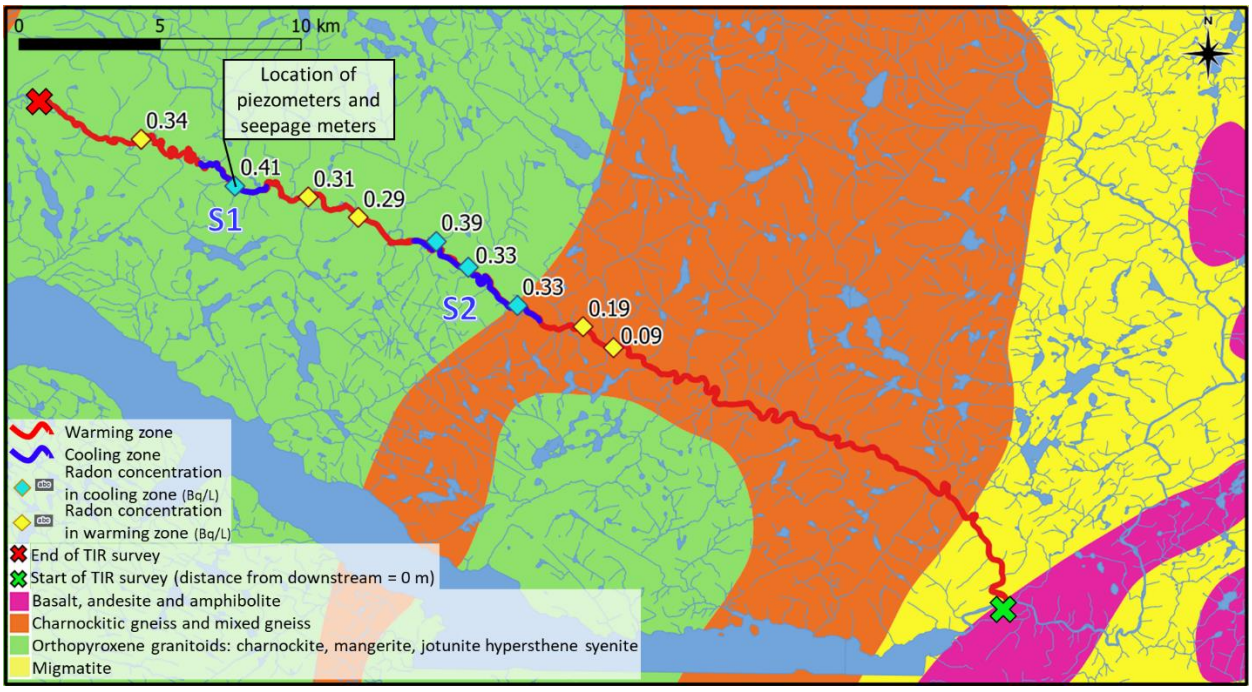

Figure 3.7 **Cooling zones and radon sampling points of Saint-Marguerite River.**

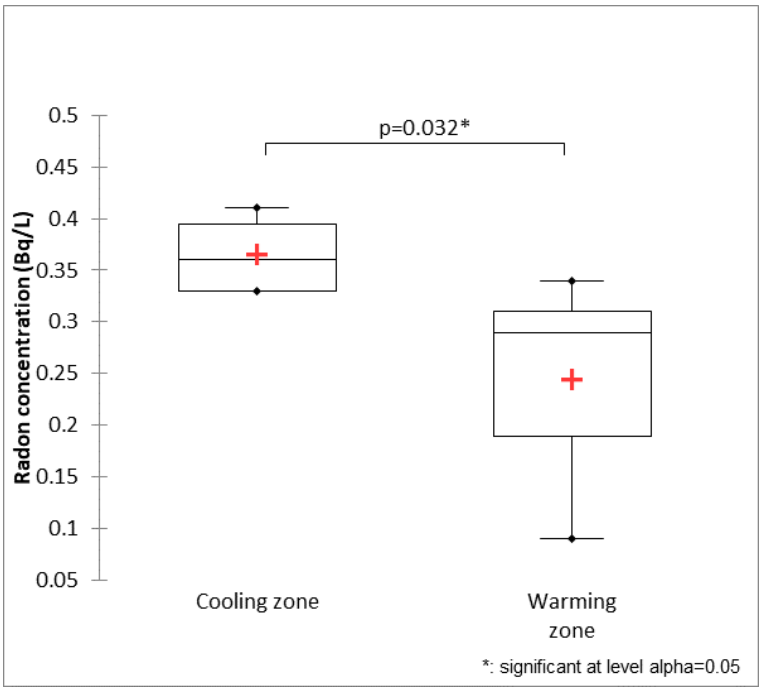

Figure 3.8 **Box and whisker plot of radon concentration for cooling and warming zones of Sainte-Marguerite River showing significant difference at 95% confidence level t-test.**

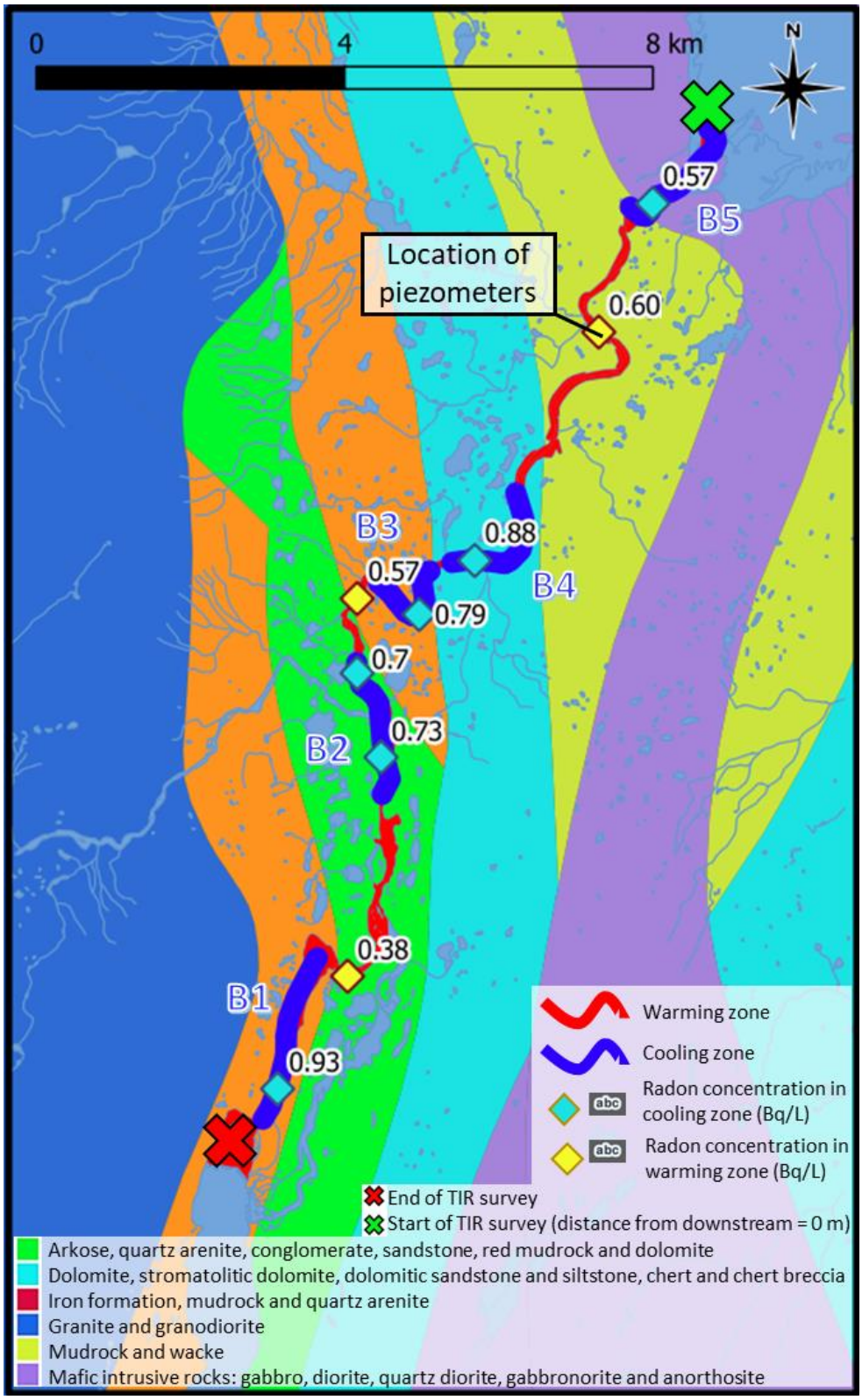

Figure 3.9 **Cooling zones and radon sampling points of Berard River.**

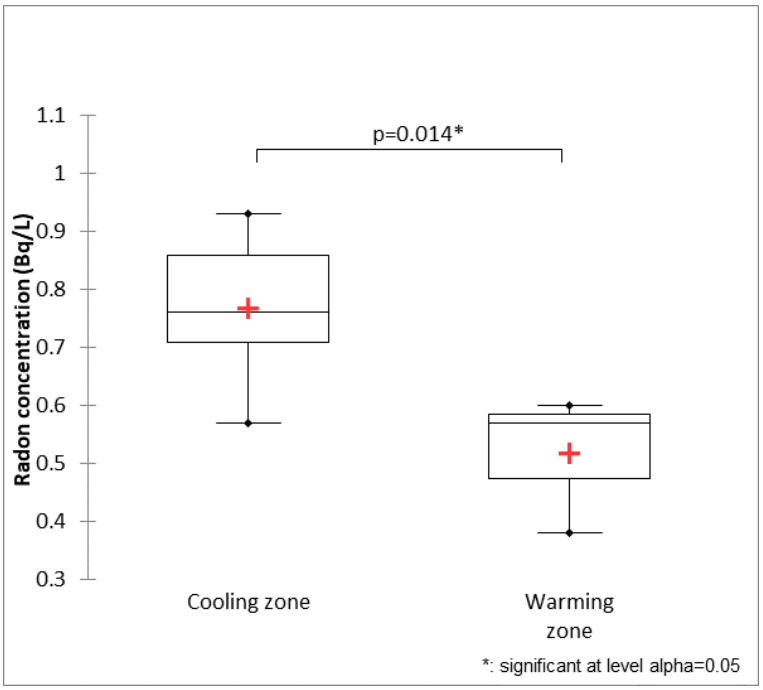

Figure 3.10 **Box and whisker plot of radon concentration for cooling and warming zones of Berard River showing significant difference at 95% confidence level t-test.**

The radon concentration in the piezometers and river were compared to identify GW seepage into the rivers. For the Sainte-Marguerite River, the piezometers are located in a large-scale cooling zone of the river (S1) on the north-east (left) bank of the river, where GW seepage to the river was expected due to the slope of the riverbank (Figure 3.11). The geometric average hydraulic conductivity (*k*) of riverbank materials based on slug tests in the two piezometers is about 0.0011 m/s (0.002 m/s for PS1 and 0.0006 m/s for PS2). The pressure head difference between these two piezometers was about 7 cm at the time of measurements, considering the distance between two piezometers of 13 m the horizontal hydraulic gradient (i) was 0.0054 m/m. The GW temperature was about 5 °C, while the river water temperature was about 12 °C.

The radon concentration in the piezometer further from the river (PS2 in Figure 3.12) was higher than the one close to the river (PS1 in Figure 3.12), which is prone to dilution and mixing with SW. Moreover, the radon concentration in the river from SS1 to SS3 decreases. This shows that GW seepage reduces by moving from the left riverbank to the right riverbank.

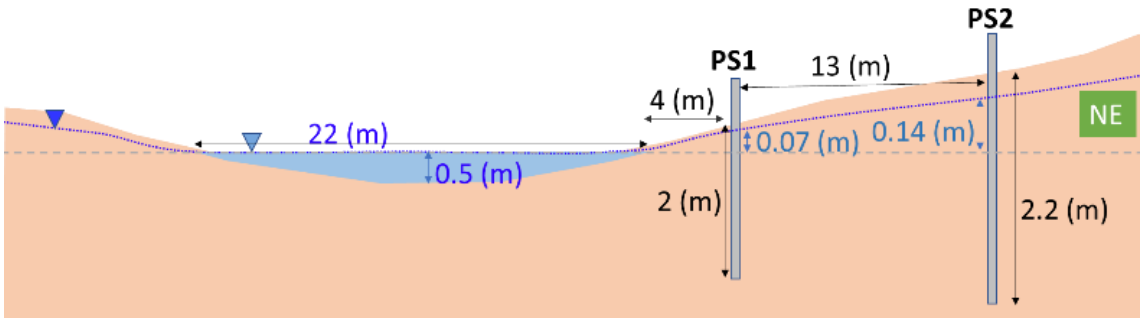

Figure 3.11 **Cross section of Sainte-Marguerite River at location of piezometers.**

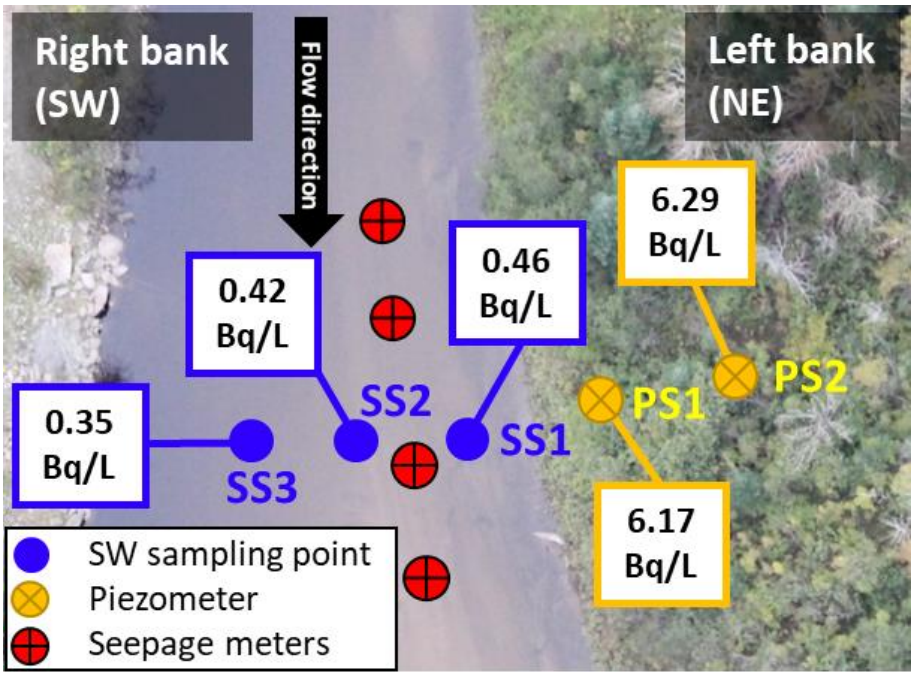

Figure 3.12 **Radon concentration of Sainte-Marguerite River piezometers and SW.**

Piezometers on the Berard River were installed in a warming zone on the left (south-west) bank of the river (Figure 3.13). However, this location was a cold GW-fed side channel, which was identified through TIR imaging (Figure 3.14-A). The hydraulic conductivity of riverbank material is about 0.003 m/s based on slug tests in piezometer PB1. PB2 was not used for hydraulic conductivity measurements since it is located on a sand and gravel bar in between the main stem and side channel and is not representative of riverbank material. The GW level in PB1 was 1 cm higher than the SW level at the time of measurements. Considering the distance between PB1 and side channel shoreline, 5 m, the horizontal hydraulic gradient was 0.002 m/m. The GW temperature was about 1 °C, while the river water temperature was about 11 °C in the main branch and 7 °C in the side channel. GW seepage is more noticeable in the upstream section, and the temperature difference with the main stem is about 5 °C, while the difference is lower and

near 3.5 °C further downstream (Figure 3.14-A). To confirm the effect of radon on sampling location, several SW and GW samples were collected from piezometers at this site (Figure 3.14-B). Radon concentration in the main stem was 0.60 Bq/L and within the range of other SW measurements of the river. However, the concentration in GW of the piezometers and side channel was more than ten times higher. The concentration upstream of the side channel, where GW discharges, was 19.33 Bq/L, which is close to the measured value of 21.27 Bq/L in piezometers at the shore of the river at a depth of about 1.8 m below ground level. This confirms that the source of cold water in this channel is GW. The radon concentration at the downstream section of the side channel was 8.30 Bq/L. The measured radon concentration in the piezometer located between the side channel and the main stem (PB2 in Figure 3.14-B) was 15.44 Bq/L.

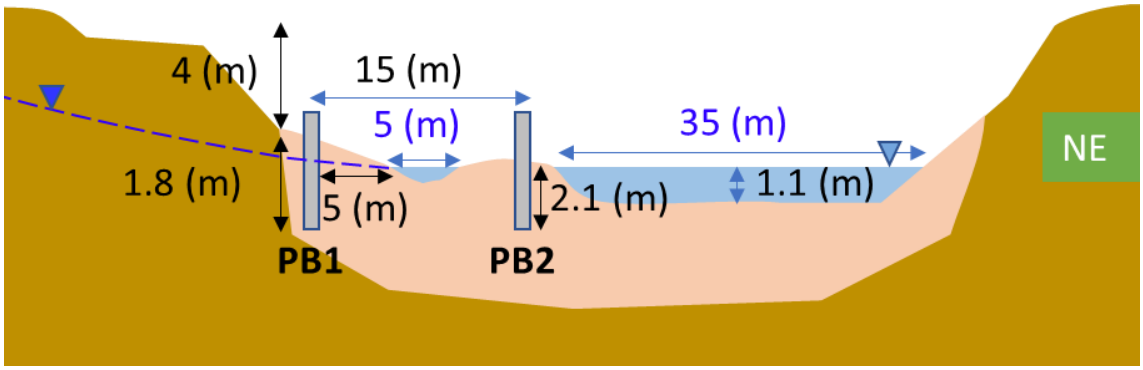

Figure 3.13 **Cross section of Berard River at location of piezometers.**

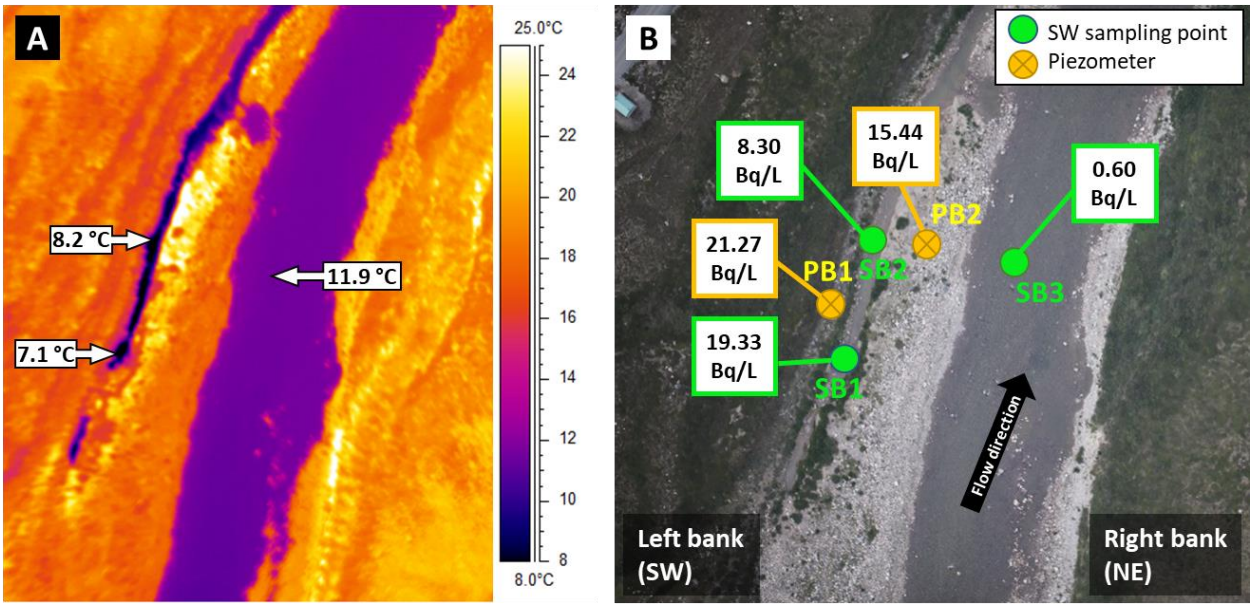

Figure 3.14 **Water temperature of the side channel and main stem from TIR imaging (A) and radon concentration in Berard River piezometers and SW (B).**

Based on Equation (3.2) and simplifications mentioned in the methodology section, the fraction of GW in the river was calculated for the identified cooling zones (Table 3.1), except for the first and last cooling zones of the Berard River (B1 and B5). The upstream (background) concentration for B1 was not measured due to difficulty of sampling in the deep lake. The radon concentration in the B5 cooling zone is lower than the upstream hotter section, and Equation (3.2) considers this section a GW-losing section.

The average GW seepage compared to river discharge is about 1% and 2.75% for the studied section of the Sainte-Marguerite River and Berard River, respectively.

Table 3.1 Calculated fraction of GW in the identified cooling sections of the rivers.

River	Cooling Zone	C_{gw} (Bq/L)	C_{bg} (Bq/L)	C_{sw} (Bq/L)	f (%)
St-Marguerite	**S1**	6.23	0.34	0.41	1.1
	S2		0.29	0.34	0.9
Berard	**B1**	10.85	-	0.93	-
	B2		0.38	0.72	3.2
	B3		0.57	0.79	2.1
	B4		0.57	0.88	3.0
	B5		0.60	0.57	-

The river flow rate was 6.5 m^3/s in the first cooling zone of the Saint-Marguerite River. Thus, a 1.1% GW fraction translates into a 0.07 m^3/s GW flow through the riverbed between the two most upstream sampling sites in this river (values of 0.34 Bq/L and 0.41 Bq/L in Figure 3.7). The length of the river between these two sampling points is about 5.75 km, and the average width of the river is 18 m, which gives a GW seepage velocity of 6.9×10^{-7} m/s through the riverbed sediments in this section. This GW seepage velocity is very close to the measured GW seepage with seepage meters of 6.45×10^{-7} m/s. This value is an extrapolation of the measured GW discharge by seepage meters to the same river reach.

The river flow rate of the Berard River a bit downstream of piezometer installation site was about 18.5 m^3/s. Considering the same flow rate for the B4 cooling zone, the 3% GW fraction results in a GW seepage rate of 6.2×10^{-6} m/s, which is a rough estimation due to the simplifications.

Verification of the GW seepage fraction with seepage meters was only carried out for the first cooling zone of the Sainte-Marguerite River. Installation of seepage meters for other cooling zones of the Berard and Sainte-Marguerite Rivers was not possible due to accessibility issues, high water depth and the riverbed being covered with pebbles and boulders. However, the horizontal GW flow toward the river was calculated with the Darcy equation (Equation (3.4)). The calculated Darcy flow (q) was 5.9×10^{-6} m/s and 6×10^{-6} m/s for the Sainte-Marguerite and Berard River, respectively.

3.5 Discussion

3.5.1 TIR imaging method

TIR imaging analysis is a fast and reliable method for evaluating river temperature profiles (e.g., Faux et al., 2001) over large spatial scales, compared to in-river techniques such as fiber-optic distributed temperature sensing (e.g., Kaandorp et al., 2019). River temperature profiles clearly showed large-scale cooling zones in rivers. However, the exact source of cool water (GW or SW) cannot be detected in some cases. For example, the first cooling zone of the Berard River is located after a lake, and so its presence could ostensibly have been attributed to this; similarly, a large tributary (1 °C colder) enters the main stem in the middle of second cooling zone, potentially obfuscating the source of this cooling zone. Conversely, other small tributaries in the Berard River were clearly not the source of cooling zones as the lack of riparian vegetation meant that these tributaries, clearly visible in TIR images at a temperature similar to the main stem, were not responsible for cooling of the observed magnitude. On the other hand, the same observation could not be made for the Sainte-Marguerite River, since the riparian canopy renders small tributaries almost invisible in TIR images. While measuring the temperature of each individual tributary entering the main stem is a possible solution to verify if they provide cool water to the main stem, as is the installation of piezometers along the river to measure GW temperature, these options are time consuming, difficult to achieve depending on accessibility and partially negate the benefits of using TIR. Therefore, while TIR (and, more broadly, temperature) can be useful as a tracer for identifying the source of cool zones in rivers (e.g., Fakhari et al., 2022; Mejia et al., 2020; Wawrzyniak et al., 2012; Dugdale et al., 2019), it cannot conclusively highlight GW–SW

exchanges. Therefore, comparison and combination with another method such as radon measurement is advantageous.

3.5.2 Radon measurements

The average radon concentration of cooling zones was higher than the average radon concentration in warming zones for both the Sainte-Marguerite and Berard Rivers. The difference was significant based on 0.05 significance level t-tests, and the calculated *p* values were 0.032 and 0.014 for the Sainte-Marguerite and Berard Rivers, respectively. Additionally, radon concentration was generally higher in cooling zones compared to neighboring warming zones. The only exception is the concentration in the last cooling zones of the Berard River near the bay (B5 in Figure 3.6), which could be due to different reasons such as the influence of sea water that can lower radon concentration or the influence of igneous rock underlying this section with lower radon potential. Moreover, by looking at Figure 3.6, it can be seen that the measured 0.60 Bq/L radon concentration is not actually in a warming zone and rather in a zone with constant temperature (zone between B4 and B5), which can be a sign of GW seepage in this section that offsets the atmospheric warming of the river channel. Higher radon concentration can be a proof that the assumption of higher GW seepage in cooling zones was correct and the identified cooling zones were GW-fed.

The timing of sampling was shown to be very important, as it was observed in previous studies that radon concentration can change depending on the season and river water level (e.g., Schubert et al., 2006; Yi et al., 2018). In this study, two sets of samples were collected for both the Sainte-Marguerite and Berard Rivers. The first set was collected in a relatively high flow rate after rainy days. The radon concentrations in these samples were very low and almost not detected since radon concentration in rain water is almost zero. The results from these samples were not used for further analysis and are not presented in this article. Sampling after rainy days should be avoided since the water in the river will be mainly runoff and the GW effect in the river cannot be detected with radon concentration. This is also true for TIR surveying, which should not be carried out after rainy days.

The assumption was that a higher measured radon concentration is present in the cooling zone since there is a discharge of radon/uranium-rich GW with a lower temperature. However, the higher measured radon concentration could be due to a higher radon content in the bedrock (Hahn et al., 2015; Ershaidat et al., 2008). To verify if this was not the case, the type of bedrock at each sampling point in the river was evaluated.

Water samples from the Sainte-Marguerite River were collected in a metamorphic bedrock setting with six samples on orthopyroxene granitoids (light green in Figure 3.7) and three downstream on gneiss (orange in Figure 3.7). These bedrock units are a mix of several rock types. Orthopyroxene granitoids contain mangerite and monzonite, which are igneous intrusive rocks with a moderate silica content. The higher the silica content in bedrock, the higher the potential for this type of rock to be a radon source (Drolet et al., 2013). High silica content tends to precipitate uranium in the bedrock, and the uranium will emit radon during its decay. In the Canadian Shield, 69 dwellings that were built over monzonite were sampled for radon concentration in air of their basement. The average radon concentration of these indoor radon measurements was 0.28 Bq/L, which highlighted monzonite as a major radon source in Quebec (Drolet et al., 2013). Gneiss is acidic-granitic bedrock and might be associated with a high level of radon. Based on this information, it is possible to have more radon in a gneiss unit than in monzonite. However, this effect was not clear in the Sainte-Marguerite River case. The two sampling locations downstream have very low radon concentrations. The effect of bedrock is limited since the water level was very low and concentration loss can occur by gas exchange.

It was complicated to estimate if a bedrock unit is prone to radon emission for the Berard River, since multiple rock types are merged together into larger bedrock units in the available geological maps (Figure 3.9). However, the results of radon measurements at the selected study site on the Berard River showed that the depth and location of piezometers can reveal interesting results about GW seepage and mixing with SW. The measured radon concentration in the piezometer located between the side channel and the main stem (PB2 in Figure 3.14-B) was lower than the one measured in the piezometer on the riverbank (PB1 in Figure 3.14-B) and upstream of the side channel (SB1 in Figure 3.14-B). This could be the result of GW mixing with SW of the main stem in the hyporheic zone below the ground surface.

The inferred fraction of GW in the rivers of this study using the radon concentration method seems low (<3%). However, it did not seem out of range and close to the lower calculated value in similar studies (Wu et al., 2004; Ortega et al., 2015; Yi et al., 2018; Cook et al., 2006; Corbett et al., 1997; Burnett et al., 2010). Methods with natural tracers such as radon for the quantification of GW–SW exchange can have large uncertainties (Xie et al., 2016). In this study, the shallow depth of sampling for both GW and SW, human error, the presence of air bubbles in samples and lack of correction factors can be reasons for the low measured values. The shallow depth of piezometers means water at this depth is in contact with the unsaturated zone (i.e., air) and can lose radon through gas exchange. At the river sampling locations, the rivers were shallow, although the

samples were taken close to the riverbed. As a consequence, it is possible for radon to escape due to gas exchange. Samples were taken by submerging the bottles in water and closing the cap, which can introduce errors if samples were not airtight or air bubbles were present. Therefore, to minimize the impact of such potential errors, we focused on the identification of GW in rivers by comparing radon concentration at different locations instead of quantifying the exchange rate with a radon mass balance calculation. The quantification of the fraction of GW in the river is accurate when all required measurements needed for the calculation of correction factors are feasible (i.e., when it is possible to have a reliable evaluation of the thickness of the stagnant film, the average depth of the stream and the velocity of the stream water at location of each SW sampling point for radon (Wu et al., 2004)). Nonetheless, the calculated GW seepage rate with radon mass balance was not far from the seepage meter measurements extrapolated to the same river reach for the cooling zone in the Sainte-Marguerite River where the seepage meters were installed. However, the calculated GW discharge rate with radon mass balance and seepage meters was lower than the calculated flow with the Darcy equation at the river cross section of both rivers where piezometers were located. The calculated GW flow for the Berard River from the radon mass balance (6.2×10^{-6} m/s) and Darcy equation (6×10^{-6} m/s) are relatively close and in the same order of magnitude. The GW flow for the Sainte-Marguerite River from radon mass balance (6.9×10^{-7} m/s) and seepage meters (6.45×10^{-7} m/s) were close, but they were one order of magnitude lower than the GW flow calculated with the Darcy equation (5.9×10^{-6} m/s). The riverbed material at the Sainte-Marguerite River study site was shown to be anisotropic, with ten times higher horizontal hydraulic conductivity compared to vertical hydraulic conductivity. A higher GW flow of one order of magnitude when calculated with the Darcy equation and piezometric data characteristics of horizontal flow compared to seepage meters providing vertical flux measurements is not unrealistic. Moreover, the location of the piezometers was known to be an optimal GW discharge zone, either based on TIR imagery or hydrodynamics of the river cross section (sloped riverbank and presence of permeable material). Additionally, the piezometers were placed in a location with loose material to facilitate the manual installation. As a result, the measured hydraulic conductivity with slug tests was relatively high for the material intercepted by the piezometers. Thus, the calculated Darcy flow with this method is likely overestimated since maximum parameters are considered for a section in which there can be important subsurface heterogeneities. Radon measurements can quantify the GW seepage of a section of the riverbed (here a cooling zone). Installing seepage meters in different locations within the same section of the river (or the same cooling zone) can also give us an estimate of riverbed seepage rate. On the other had, the use of Darcy equation and piezometers gives average GW

flow toward the river between two points (i.e., two piezometers), one inside and one next to the river. Therefore, we suggest the use of seepage meters, for validation of the flow rate from radon mass balance. Moreover, the installation of seepage meters can be easier than piezometers. This appears to be a better alternative than calculating the Darcy flow from limited piezometer data, which may have overestimated the GW flow in our study cases.

This study was focused on the shallow GW system close to the river since sampling points for GW were in piezometers at about 2 m depth. Shallow piezometers next to rivers have been used in previous similar studies to show the GW–SW exchange (e.g., Hoehn et al., 1989; Schubert et al., 2006). Choosing this depth of investigation for GW was appropriate because the recorded water level with pressure loggers inside piezometers was above the river water level and the screens of piezometers were in the saturated zone. Therefore, the samples collected from piezometers were representative of GW. Moreover, since the alluvial aquifer below these rivers is not deep and is underlaid by a low permeable layer, there is limited connection of the river to the deep GW system. However, deep observation wells would be required for better characterization of the GW to the river and the consideration of the deep GW system expected to supply radon.

The AB-5R radon measurement device is portable and allowed us to analyze the samples in the field without the need for fast shipment of samples for laboratory analysis, which is required to avoid radon decay in collected samples before analysis. However, the number of required cells for the AB-5R device was limited (three). Each cell should be cleaned by air and rest for 24 h before the next use. The resulting analysis time for water samples was about 3 days. A larger number of samples would imply a longer period between the first and last sample measurements, which could result in different weather and river flow conditions. The weather and river flow conditions were almost the same by limiting the sampling of the river to three consecutive days, which allowed us to better compare radon concentration along the river. In any cases, having more GW and SW samples can improve our interpretation of GW–SW exchange with a better spatial resolution. This would require either more AB-5R cells or sending samples to an external lab for analysis. Furthermore, repeating radon measurement at the same locations can provide better reliability and may reveal a temporal variability of GW seepage into the river (Schubert et al., 2006).

3.6 Conclusions

TIR imaging is effective and fast in identifying river temperature anomalies and a useful tool for generating river temperature profiles. Simple sampling requirements and fast analysis (with proper equipment) associated with radon measurements make it an efficient method for application to large-scale studies. Radon measurements can, therefore, constitute a useful complementary technique for TIR to verify if GW is the source of cool water in a river. Based on results of radon measurements, it was verified that all cooling zones were the result of GW seepage. Combining the TIR and radon measurements for pinpointing the sampling locations that show more interest regarding GW influence can be effective since SW sampling at various points of rivers can be difficult due to limited accessibility and difficulty of analysis of a high number of samples. Unlike TIR imagery, which gives indicative results, radon measurements can provide quantitative measures of GW–SW exchange. In this study, the river discharge was not measured at different sampling sites and the exact GW seepage flow cannot be calculated. Nevertheless, calculated values give an approximation of GW flow to the river compared to river discharge or hyporheic exchange. The combination of TIR imagery and radon measurements can give reliable results for the identification of zones with high potential of GW–SW interaction. To obtain better results from radon mass balance calculation and improve the future implementation of this method, it would be ideal to have measurement of river flow at different cross sections of a cooling zone (at least two at the start and the end), installation of several seepage meters within the cooling zone and installation of piezometers next to the river at different locations of the studied river reach. In this way, the correction factors that were not used in this study could also be taken into account. Moreover, the GW–SW exchange rate could be calculated with a thermal budget analysis by installation of piezometers with temperature data loggers next to the river at different locations for different sections of rivers, providing another comparative method. These steps were not applicable in this study due to the nature of the selected rivers. Deep water and high flows made a wide-scale installation of seepage meters impossible. The presence of hardpan with boulder and rocks in the top soil prevented the manual installation of piezometers. The remoteness of the rivers and lack of drilling equipment did not allow deep observation wells. In such difficult environments for field instrumentation, modeling can be a solution for better understanding of GW–SW interaction. Models can be built based on available data and can then be calibrated based on field measurements. In future works, a coupled GW–SW model of flow and heat transfer for the studied rivers will be built to quantify the GW–SW exchange rate and its spatiotemporal variation to anticipate the changes in river water temperature and the effects on fish species, which are important for local communities.

3.7 References

Anderson M.P. (2005) « Heat as a ground water tracer. » Ground Water 43 (6): 951-968. Doi:10.1111/j.1745-6584.2005.00052.x.

Baxter C.V. & Hauer F.R. (2000) « Geomorphology, hyporheic exchange, and selection of spawning habitat by bull trout (Salvelinus confluentus). » Canadian Journal of Fisheries and Aquatic Sciences 57 (7): 1470-1481. Doi:10.1139/cjfas-57-7-1470.

Berth C. & Bourg A.C.M. (1994) « Radon-222 and Chloride as Natural Tracers of the Infiltration of River Water into an Alluvial Aquifer in Which There. » Environmental Science & Technology 1994 (5): 794-798.

Breton M.-P., Cloutier G. & Waygood E.O.D. (2017) « QUEBEC. » book chapter In Climate risks and adaptation practices for the Canadian transportation sector, K. Palko and D.S. Lemmen (Eds.), 181-216. Government of Canada. Ottawa, ON, Canada.

Burnett W.C., Peterson R.N., Santos I.R. & Hicks R.W. (2010) « Use of automated radon measurements for rapid assessment of groundwater flow into Florida streams. » Journal of Hydrology 380 (3-4). Elsevier B.V.: 298-304. Doi:10.1016/j.jhydrol.2009.11.005. http://dx.doi.org/10.1016/j.jhydrol.2009.11.005.

ClimateData.ca (2021) « Data Source: Environment and Climate Change Canada and (ClimateData.ca) See: https://eccc-msc.github.io/open-data/licence/readme_en/. » Page Web, consulté le 1er septembre 2021 à l'adresse : https://climatedata.ca/explore/location/?loc=EJLMJ&location-select-temperature=tx_mean&location-select-precipitation=rx1day&location-select-other=frost_days.

Colombo A.F., Etkin D. & Karney B.W. (1999) « Climate variability and the frequency of extreme temperature events for nine sites across Canada: Implications for power usage. » Journal of Climate 12 (8 PART 2): 2490-2502. Doi:10.1175/1520-0442(1999)012<2490:cvatfo>2.0.co;2.

Cook P.G., Lamontagne S., Berhane D. & Clark J.F. (2006) « Quantifying groundwater discharge to Cockburn River, southeastern Australia, using dissolved gas tracers 222Rn and SF6. » Water Resources Research 42 (10): 1-12. Doi:10.1029/2006WR004921.

Corbett D.R, Burnett W.C., Cable P.H. & Clark S.B. (1997) « Radon tracing of groundwater input into Par Pond, Savannah River Site. » Journal of Hydrology 203 (1-4): 209-227. Doi:10.1016/S0022-1694(97)00103-0.

Drolet J.-P., Martel R., Poulin P., Dessau J.-C., Lavoie D, Parent M & Lévesque B. (2013) « An approach to define potential radon emission level maps using indoor radon concentration measurements and radiogeochemical data positive proportion relationships. » Journal of Environmental Radioactivity 124. Elsevier Ltd: 57-67. Doi:10.1016/j.jenvrad.2013.04.006. http://dx.doi.org/10.1016/j.jenvrad.2013.04.006.

Dugdale S.J., Bergeron N.E. & St-Hilaire A. (2013) « Temporal variability of thermal refuges and water temperature patterns in an Atlantic salmon river. » Remote Sensing of Environment 136.

Elsevier Inc.: 358-373. Doi:10.1016/j.rse.2013.05.018. http://dx.doi.org/10.1016/j.rse.2013.05.018.

Dugdale S.J., Bergeron N.E. & St-Hilaire A. (2015) « Spatial distribution of thermal refuges analysed in relation to riverscape hydromorphology using airborne thermal infrared imagery. » Remote Sensing of Environment 160. Elsevier Inc.: 43-55. Doi:10.1016/j.rse.2014.12.021. http://dx.doi.org/10.1016/j.rse.2014.12.021.

Dugdale S.J., Franssen J., Corey E., Bergeron N.E., Lapointe M. & Cunjak R.A. (2016) « Main stem movement of Atlantic salmon parr in response to high river temperature. » Ecology of Freshwater Fish 25 (3): 429-445. Doi:10.1111/eff.12224.

Dugdale S.J., Kelleher C.A., Malcolm I.A., Caldwell S. & Hannah D.M. (2019) « Assessing the potential of drone-based thermal infrared imagery for quantifying river temperature heterogeneity. » Hydrological Processes 33 (7): 1152-1163. Doi:10.1002/hyp.13395.

Ebersole J.L., Liss W.J. & Frissell C.A. (2003) « Cold water patches in warm streams: Physicochemical characteristics and the influence of shading. » Journal of the American Water Resources Association 39 (2): 355-368. Doi:10.1111/j.1752-1688.2003.tb04390.x.

Elzain A.-E.A. (2014) « Measurement of Radon-222 concentration levels in water samples in Sudan. » Advances in Applied Science Research 5 (2): 229-234.

Ershaidat N.M., Al-Bataina B.A. & Al-Shereideh S.A. (2008) « Characteristics of soil radon transport in different geological formations. » Environmental Geology 55 (1): 29-35. Doi:10.1007/s00254-007-0961-x.

Fakhari M., Raymond J, Martel R., Dugdale S.J. & Bergeron N.E. (2022) « Identification of Thermal Refuges and Water Temperature Patterns in Salmonid-Bearing Subarctic Rivers of Northern Quebec. » Geographies 2 (3) : 528-548. Doi :10.3390/geographies2030032.

Faux R.N., Maus P, Lachowski H., Torgersen C.E. & Boyd M.S. (2001) « New approaches for monitoring stream temperature: Airborne thermal infrared remote sensing. » Report Prepared for: Inventory & Monitoring Steering Committee San Dimas Technology & Development Center, CA, USA.

Fortin G., Acquaotta F. & Fratianni S. (2017) « The evolution of temperature extremes in the Gaspé Peninsula, Quebec, Canada (1974–2013). » Theoretical and Applied Climatology 130 (1-2). Theoretical and Applied Climatology: 163-172. Doi:10.1007/s00704-016-1859-x.

Frechette D.M., Dugdale S.J., Dodson J.J. & Bergeron N.E. (2018) « Understanding summertime thermal refuge use by adult Atlantic salmon using remote sensing, river temperature monitoring, and acoustic telemetry1. » Canadian Journal of Fisheries and Aquatic Sciences 75 (11): 1999-2010. Doi:10.1139/cjfas-2017-0422.

Fullerton A.H., Torgersen C.E, Lawler J.J, Faux R.N., Steel E.A., Beechie T.J., Ebersole J.L. & Leibowitz S.G. (2015) « Rethinking the longitudinal stream temperature paradigm region-wide comparison of thermal infrared imagery reveals unexpected complexity of river temperatures. » Hydrological Processes 29 (22): 4719–4737. Doi:10.1002/hyp.10506.

Geist D.R. & Dauble D.D. (1998) « Redd site selection and spawning habitat use by fall chinook salmon: The importance of geomorphic features in large rivers. » Environmental Management 22 (5): 655-669. Doi:10.1007/s002679900137.

Gouvernement du Québec (2021) « Normales climatiques 1981-2010. » Ministère de l'Environnement & de la Lutte contre les changements climatiques. Page Web, consulté le 1er septembre 2021 à l'adresse https://www.environnement.gouv.qc.ca/climat/normales/climat-qc.htm.

Gunn J. & Snucins E. (2010) « Brook charr mortalities during extreme temperature events in Sutton River, Hudson Bay Lowlands, Canada. » Hydrobiologia 650 (1): 79-84. Doi:10.1007/s10750-010-0201-3.

Hahn E.J., Gokun Y., Andrews W.M., Overfield B.L., Robertson H., Wiggins A. & Rayens M.K. (2015) « Radon potential, geologic formations, and lung cancer risk. » Preventive Medicine Reports 2: 342-346. Doi:10.1016/j.pmedr.2015.04.009.

Hoehn E. & Von Gunten H.R. (1989) « Radon in groundwater: A tool to assess infiltration from surface waters to aquifers. » Water Resources Research 25 (8): 1795-1803. Doi:10.1029/WR025i008p01795.

Kaandorp V.P., Doornenbal P.J., Kooi H., Broers H.P. & de Louw P.G.B. (2019) « Temperature buffering by groundwater in ecologically valuable lowland streams under current and future climate conditions. » Journal of Hydrology X 3. The Authors: 100031. Doi:10.1016/j.hydroa.2019.100031. https://doi.org/10.1016/j.hydroa.2019.100031.

Kelly J.L., Dulai H., Glenn C.R. & Lucey P.G. (2019) « Integration of aerial infrared thermography and in situ radon-222 to investigate submarine groundwater discharge to Pearl Harbor, Hawaii, USA. » Limnology and Oceanography. Doi:10.1002/lno.11033.

Lemieux J.M., Fortier R., Talbot-Poulin M.C., Molson J.W., Therrien R., Ouellet M., Banville D., Cochand M. & Murray R. (2016) « Groundwater occurrence in cold environments: examples from Nunavik, Canada. » Hydrogeology Journal 24 (6): 1497-1513. Doi:10.1007/s10040-016-1411-1.

Malard F., Tockner K. & Ward J.V. (1999) « Shifting dominance of subcatchment water sources and flow paths in a glacial floodplain, Val Roseg, Switzerland. » Arctic, Antarctic, and Alpine Research 31 (2): 135-150. Doi:10.2307/1552602.

Mejia F.H., Torgersen C.E., Berntsen E.K., Maroney J.R., Connor J.M., Fullerton A.H., Ebersole J.L. & Lorang M.S. (2020) « Longitudinal, lateral, vertical, and temporal thermal heterogeneity in a large impounded river: Implications for cold-water refuges. » Remote Sensing 12 (9): 29p. doi:10.3390/RS12091386.

Ortega L., Manzano M., Custodio E., Hornero J. & Rodríguez-Arévalo J. (2015) « Using 222Rn to identify and quantify groundwater inflows to the Mundo River (SE Spain). » Chemical Geology 395. Elsevier B.V.: 67-79. Doi:10.1016/j.chemgeo.2014.12.002. http://dx.doi.org/10.1016/j.chemgeo.2014.12.002.

Poesch, M.S., Chavarie L., Chu C., Pandit S.N. & Tonn W. (2016) « Climate Change Impacts on Freshwater Fishes: A Canadian Perspective. » Fisheries 41 (7): 385-391. Doi:10.1080/03632415.2016.1180285. http://dx.doi.org/10.1080/03632415.2016.1180285.

Power G., Brown R.S. & Imhof J.G. (1999) « Groundwater and fish – Insights from northern North America. » Hydrological Processes 13 (3): 401-422. Doi:10.1002/(SICI)1099-1085(19990228)13:3<401::AID-HYP746>3.0.CO;2-A.

Pylon (2022) « Pylon AB5 portable Radiation Monitor. » Device Manual, Pylon Electronic Inc, ON, Canada. https://pylonelectronics-radon.com/wp-content/uploads/2019/08/DS138R2-AB7.pdf.

Rogers A.S. (1958) « Physical behavior and geologic control of radon in mountain streams. » Trace Elements Investigations Report 619, USGS, UNITED STATES GOVERNMENT PRINTING OFFICE, WASHINGTON, United States.

Rosenberry D.O. & LaBaugh J.W. (2008) « Field Techniques for Estimating Water Fluxes Between Surface Water and Ground Water Techniques and Methods 4 – D2. » Technical Publication Report by U.S. Geological Survey, Reston, Virginia.

Schubert M., Knoeller K., Treutler H.C., Weiss H. & Dehnert J. (2006) « 222Rn as a tracer for the estimation of infiltration of surface waters into aquifers. » Radioactivity in the Environment 8 Fra nce: 326-334. doi:10.1016/S1569-4860(05)08026-5.

SIGÉOM (2022) « Surface deposits map. » système d'information géominière du Québec. Page Web, consulté le 1er juin 2020 ' l'adresse https://sigeom.mines.gouv.qc.ca/signet/classes/I1108_afchCarteIntr.

Torgersen C. & Ebersole J. (2012) « Primer for identifying cold-water refuges to protect and restore thermal diversity in riverine landscapes. » Report prepared for Region 10, U.S. Environmental Protection Agency, Seattle, Washington under EPA Interagency Agreement No. DW-14-95755001-0. doi:EPA 910-c-12-001. http://scholar.google.com/scholar?hl=en&btnG=Search&q=intitle:Primer+for+Identifying+Cold-Water+Refuges+to+Protect+and+Restore+Thermal+Diversity+in+Riverine+Landscapes#0.

Wawrzyniak V., Piégay H. & Poirel A. (2012) « Longitudinal and temporal thermal patterns of the French Rhône River using Landsat ETM+ thermal infrared images. » Aquatic Sciences 74 (3): 405-414. doi:10.1007/s00027-011-0235-2.

Willms T. & Whitworth G. (2016) « Mapping of critical summer thermal refuge habitats for Chinook salmon, Coho salmon, steelhead and bull trout in the Nicola River Watersh–d - 2016. » Report of Habitat Stewardship Program for Species at Risk. Vol. 3. Fraser Basin Council: Kamloops, BC, Canada.

Wilson J. & Rocha C. (2016) « A combined remote sensing and multi-tracer approach for localising and assessing groundwater-lake interactions. » International Journal of Applied Earth Observation and Geoinformation 44. Elsevier B.V.: 195-204. doi:10.1016/j.jag.2015.09.006. http://dx.doi.org/10.1016/j.jag.2015.09.006.

Wu Y., Wen X. & Zhang Y. (2004) « Analysis of the exchange of groundwater and river water by using Radon-222 in the middle Heihe Basin of northwestern China. » Environmental Geology 45 (5): 647-653. doi:10.1007/s00254-003-0914-y.

Xie Y., Cook P.G., Shanafield M., Simmons C.T. & Zheng C. (2016) « Uncertainty of natural tracer methods for quantifying river-aquifer interaction in a large river. » Journal of Hydrology 535. Elsevier B.V.: 135-147. doi:10.1016/j.jhydrol.2016.01.071. http://dx.doi.org/10.1016/j.jhydrol.2016.01.071.

Yi P., Luo H., Chen L., Yu z., Jin H., Chen X., Wan C., Aldahan A., Zheng M. & Hu Q. (2018) « Evaluation of groundwater discharge into surface water by using Radon-222 in the Source Area of the Yellow River, Qinghai-Tibet Plateau. » Journal of Environmental Radioactivity 192 (November 2017). Elsevier: 257-266. doi:10.1016/j.jenvrad.2018.07.003. https://doi.org/10.1016/j.jenvrad.2018.07.003.

4 ON THE COMPLEMENTARINESS OF MULTIPLE IN-SITU TECHNIQUES FOR SPATIOTEMPORAL ASSESSMENT OF GROUNDWATER-SURFACE WATER EXCHANGES

Sur la complémentarité de plusieurs techniques in situ pour l'évaluation spatiotemporelle des échanges entre les eaux souterraines et les eaux de surface

Milad Fakhari[1*], Jasmin Raymond[1], Richard Martel[1], Maria Klepikova[2], Olivier Bour[2]

1 Institut national de la recherche scientifique, Centre Eau Terre Environnement, Québec, QC G1K 9A9, Canada

2 Univ Rennes, CNRS, Géosciences Rennes, UMR 6118, 35000 Rennes, France

* Correspondance: milad.fakhari@inrs.ca

Soumis au ***Hydrogeology Journal***

Soumis le 29 novembre 2023

Numéro du manuscrit : HYJO-D-23-00415

Contribution des auteurs :

Conceptualisation, Milad Fakhari, Jasmin Raymond et Richard Martel; méthodologie, Milad Fakhari, Jasmin Raymond, Richard Martel, Maria Klepikova, Olivier Bour; analyse formelle, Milad Fakhari; conservation des données, Milad Fakhari; rédaction - préparation de la version originale, Milad Fakhari; rédaction - révision et édition, Milad Fakhari, Jasmin Raymond, Richard Martel, Maria Klepikova, Olivier Bour; visualisation, Milad Fakhari.

Lien entre l'article ou les articles précédents et le suivant :

Un site d'étude sur la rivière Sainte-Marguerite, qui a été analysé dans l'article précédent avec des mesures du TAI et du radon, a été sélectionné pour une analyse plus approfondie avec l'utilisation de plusieurs méthodes pour la quantification de l'interaction GW-SW et l'identification des variabilités spatiotemporelles. Les résultats de cet article sont utilisés dans le prochain article pour la construction et l'étalonnage des modèles.

Abstract: Groundwater-surface water interaction was proven to be important for aquatic life in rivers and streams. This interaction rate can be both spatially and temporally variable, especially at a small scale such as in river reach with length of tens of meters or less. The objective of this study is to compare a set of simple to complex methods to estimate the groundwater-surface water exchange rate and its spatiotemporal variability with regard to different riverbed materials and temporal variation of seepage rate from seasonal to sub-daily time scale, while showing methods strengths and drawbacks. A 40 m reach of the Sainte-Marguerite River in the Quebec Province, Canada, was selected for field instrumentation, where the average river width is about 20 m, and the river was easily accessible. Seepage meters, piezometers and water-level loggers, in addition to active and passive heat tracing have been used in this study to quantify groundwater discharge to the river. The measured spatial variation of the exchange rate at the selected study site due to the presence of a sandbar with coarse material showed to be meaningful based on statistical tests. Additionally, temporal analysis helped identify variations of groundwater flux even during the cold season when GW flow seems limited due to frozen ground and low infiltration from the snow-covered ground surface. A combination of in-situ field measurements was advantageous to avoid the limits of each method when used alone. Seepage meters and active heat tracing allowed for a spatial analysis of groundwater-surface water interaction, while piezometers and water-level loggers and passive heat tracing with installed temperature sensors in the riverbed were convenient to identify temporal variation of groundwater-river exchange rate. Combination of temperature sensors and a heating cable was used for the first time as a tool for active heat tracing to evaluate riverbed thermal properties and riverbed seepage rate. The moving infinite line source method for interpretation of the temperature response curves, which was used for active temperature sensing with fiber-optic cables before, was applied to data from this new method and showed valuable results. This indicates a high potential of this method as a simple alternative to expensive fiber-optic cables.

Résumé : L'interaction entre les eaux souterraines et les eaux de surface s'est avérée importante pour la vie aquatique dans les rivières et les cours d'eau. Ce taux d'interaction peut varier à la fois dans l'espace et dans le temps, surtout à une petite échelle, comme dans un tronçon de rivière d'une longueur de quelques dizaines de mètres ou moins. L'objectif de cette étude est de comparer un ensemble de méthodes simples à complexes pour estimer le taux d'échange entre les eaux souterraines et les eaux de surface, ainsi que sa variabilité spatiotemporelle, en tenant compte des différents matériaux du lit de la rivière et des variations temporelles du débit de suintement, allant de l'échelle saisonnière à l'échelle sous-journalière, tout en mettant en évidence les forces et les faiblesses des méthodes. Un tronçon de 40 mètres de la rivière Sainte-Marguerite dans la province de Québec, au Canada, a été sélectionné pour l'instrumentation sur le terrain, où la largeur moyenne de la rivière est d'environ 20 mètres et la rivière est facilement accessible. Des piézomètres, des enregistreurs de niveau d'eau, ainsi que du traçage thermique actif et passif a été utilisé dans cette étude pour quantifier le débit de la nappe vers la rivière. La variation spatiale mesurée du taux d'échange sur le site d'étude sélectionné en raison de la présence d'un banc de sable avec des matériaux grossiers s'est avérée significative sur la base de tests statistiques. De plus, l'analyse temporelle a permis d'identifier des variations du flux d'eaux souterraines même pendant la saison froide, lorsque le débit des eaux souterraines semble limité en raison du sol gelé et de la faible infiltration à partir de la surface enneigée. Une combinaison de mesures sur le terrain in situ s'est avérée avantageuse pour éviter les limites de chaque méthode utilisée individuellement. Les piézomètres, les enregistreurs de niveau d'eau et le traçage thermique passif avec des capteurs de température installés dans le lit de la rivière ont été pratiques pour identifier la variation temporelle du taux d'échange entre les eaux souterraines et la rivière, tandis que les inflitromètres et le traçage thermique actif ont permis une analyse spatiale de l'interaction entre les eaux souterraines et les eaux de surface. La combinaison de capteurs de température et d'un câble chauffant a été utilisée pour la première fois comme outil de traçage thermique actif pour évaluer les propriétés thermiques du lit de la rivière et le taux de suintement du lit de la rivière. La méthode de la source infinie en mouvement pour l'interprétation des courbes de réponse de température, qui avait déjà été utilisée pour la détection de température active avec des câbles à fibre optique, a été appliquée aux données de cette nouvelle méthode et a montré des résultats précieux. Cela indique un fort potentiel pour cette méthode en tant qu'alternative simple aux câbles à fibre optique couteux.

4.1 Introduction

The importance of groundwater (GW) and surface water (SW) interactions is well known and lead to the concept of considering GW and SW as a single source through water management studies (Winter et al., 1999). This interaction can affect aquatic life by influencing SW ecology and hydrology (Hayashi et al., 2002). Additionally, GW-SW interaction can affect the distribution of river water temperature (Surfleet et al., 2018). Water temperature plays an important role for aquatic life such as fish. For instance, salmonid spawning, feeding, growth and survivability were shown to be affected by river temperature variation (Fraser et al., 1993; Jensen et al., 1989) and more specifically localized GW input to stream (Power et al., 1999; Saltveit et al., 2013; Baxter et al., 2000; Zimmermann et al., 2005). Therefore, spatiotemporal assessment of GW-SW exchanges is of fundamental interest.

In the past decades, many methods have been developed for better understanding and quantification of the complex processes governing GW-SW interaction and hyporheic exchange (Winter, 1995; Sophocleous, 2002; Rosenberry et al., 2008), which is commonly affected by small-scale heterogeneities in riverbed materials and morphology (Rosenberry et al., 2012; Tonina et al., 2016; Cardenas, 2008). The small-scale heterogeneities are commonly disregarded and simplified in large- or regional-scale studies (Magliozzi et al., 2017; Banks et al., 2011; Gleeson et al., 2014). However, small-scale studies of GW-SW interaction variations due to site-specific spatial heterogeneity factors of hydrological processes are important in GW-sensitive ecosystems, where informed decision-making and management of water resources are required (Malcolm et al., 2003; Miller et al., 2016). Therefore, the main objective of this study was to compare common, and popular methods to demonstrate the spatial and temporal variation of GW-SW interaction at a small river reach scale and evaluate the significance of local variations in GW-SW interaction rate.

Selected field measurements were made in shallow aquifer and sediments under or adjacent to a river reach. One such method is the use of seepage meters installed in the riverbed. Seepage meters are simple devices that have been used since the 1940s and can measure the GW flux through the riverbed sediments directly by isolating an area of the riverbed (Rosenberry, 2008; Rosenberry et al., 2008). Additionally, mini-piezometers alongside with seepage meters allow to calculate the hydraulic conductivity of riverbed sediments. Ease of use in shallow non-turbulent rivers and simple data analysis makes seepage meters a commonly used method for small streams. Another widely used field measurement approach is water level monitoring and flow-net analysis, often called as Darcy approach. The resulting Darcy flow calculation allows to evaluate

flow rate and its direction with continuously measured water level with water-level loggers (Rosenberry et al., 2008) in a network of piezometers (or observation wells in deep GW studies). Moreover, slug tests can be made in piezometers to determine the aquifer hydraulic conductivity (Fritz et al., 2016). Other commonly used methods for quantifying GW flow and heterogeneity of porous medium is the use of heat as a tracer (Stonestrom et al., 2003; Anderson, 2005; Ren et al., 2018). Heat tracing can be done with active or passive approaches. Active measurements involve the analysis of heat diffusion from an external source and quantifying the GW flow and thermal properties of materials (Simon et al., 2021a; Briggs et al., 2016; Angermann et al., 2012; Pouladi et al., 2021). Alternatively, the ground natural temperature variations are analyzed for calculation of GW flow and its spatiotemporal variations with passive temperature monitoring (Lay et al., 2019; Munz et al., 2016; Briggs et al., 2012). In many of the recent heat tracing studies mentioned above, fiber-optic (FO) cables have been used for active or passive distributed temperature sensing (DTS) (e.g., Simon et al., 2021b). High resolution of the FO-DTS measurements enables evaluation of the spatial variation of GW-SW exchange with details, which is a strong advantage of FO-DTS. However, FO-DTS sensing requires expensive instruments. Monitoring and analyzing recorded temperature of the porous media at different locations and depths can be a cheaper alternative to FO-DTS (e.g., Giordano et al., 2021). A combination of a heating cables and attached temperature sensors can be used as an active heat tracing method. To the authors' knowledge, the use of this combination as a cheaper alternative of active FO-DTS is new and has not been previously used in riverbeds to analyze the GW-SW interaction rate. Time series analysis of installed temperature sensors in the riverbed can be used as a passive temperature sensing method to show the temporal changes in GW-SW interaction rate. The second objective of this study was therefore comparing the four above-mentioned methods (seepage meters, piezometer installation and water level monitoring, active heat tracing with combination of heating cable and attached temperature sensors and passive heat tracing with installed temperature sensors in the riverbed) and evaluating their merits and shortcomings when characterizing the spatial and temporal variation of GW-SW interaction of a river reach. This additionally allowed to investigate the potential of our new active heat tracing approach in riverbeds to quantify GW-SW interaction rate and characterize riverbed materials thermal properties.

4.2 Study area

The selected study site is located on Sainte-Marguerite River main branch 36 km upstream from the river’s mouth in Saguenay River (Figure 4.1-A) near Sacre-Coeur municipality in the Cote-

Nord (North-Shore) region of Quebec Province, Canada. The presence of *salmo salar* (Atlantic salmon) and other fish species that can be dependent to GW input as a source of cool or warm water during extreme heat/cold events, the importance of sport fishing in this river and its accessibility made it a good candidate for our study. The Sainte-Marguerite River is in the south of the province in a continental cold and humid climate with an annual average temperature of 3 °C and an average annual precipitation of 980 mm based on 1970-2010 data (ClimateData.ca, 2021).

The selected river reach is within a cooling zone of the river where higher GW seepage was expected (Fakhari et al., 2023). River instrumentation was focused on the left half of the river and the left (north-east) bank of the river, due to presence of a steeper slope with higher potential of GW flow. The north-east bank is free of human influence and a larger amount of alluvial material is present, which made equipment installation in the ground easier. The river has an average width of 21 m at the selected reach. Based on geomorphological studies and available cross sections downstream near the mouth of the river, Quaternary sediments consist of glacial till with a maximum thickness of 30 m and alluvial sand, sandy silt and gravel with 1-30 m thickness while at upstream sections the river is embedded in the rocky embankment of the Laurentian (Canadian) Shield (SIGÉOM, 2022; CERM, 2015; BAPE, 1993). The riverbed is made of two main materials, coarse sand and gravel and fine sand and silty sand close to riverbanks (Figure 4.1-B). In the middle of the river, within the coarse sand and gravel part, a sandbar is present. Its location can be roughly seen in the riverbed by following the 0.5 m topography (Figure 4.1-B) lines mapped with more than 100 point measurements using a GPS survey station with accuracy of ± 1 cm (Trimble, 2009). This sandbar can be out of water during low flow periods, especially at downstream of the reach, where its elevation is higher.

4.3 Methodology

4.3.1 Seepage meters

Seepage meters used are metal barrels open at one end with inner diameter of 0.5 m and height of 0.2 m (Figure 4.3-A). Measuring the difference in the amount of water in the connected plastic bag at the beginning and end of the test (m^3) for the duration of the test (s) allow to calculate the GW-SW exchange rate (m^3/s). Knowing the surface area of the exchange zone (i.e., surface area inside the barrel in m^2), the exchange rate can be translated to flux rate in m/s.

In July 2019, three 12 hours tests with eight seepage meters were conducted. The positions of the seepage meters were set to have a better spatialization of GW-SW exchange considering riverbed material and topography of the riverbed (Figure 4.3-B). Additionally, in July 2020, two additional tests with six seepage meters were completed to see the effect of the river water level on measured seepage rate by simultaneously monitoring river water level with a logger (Figure 4.3-B).

4.3.2 Piezometers and water level loggers

Shallow piezometers and water-level loggers were used to analyze flow network near the river and GW flow to the river. Stainless steel piezometers with a drive point at the end were hammered into the ground to the deepest level possible and in a way that the top of the screen was at least 0.5 m below the water table to make sure that the piezometer won't be dry throughout the year. The screen length was 0.08 m and the depth of penetration from the ground surface was between 0.85 m and 3 m. Three piezometers in the riverbank were installed in a triangle shape to identify the GW flow direction in the 2D horizontal field. Additionally, one piezometer was installed in the riverbed for quantification of GW seepage/infiltration in the river (Figure 4.3) by considering both the 2D horizontal and 2D vertical fields.

Inside the piezometers, level loggers were installed to record the pressure and temperature with 15-minute intervals and 0.005 mH_2O and 0.05 °C accuracy, respectively. In addition, one level logger was attached to the casing of the piezometer below the water level in the river to record the river water level and temperature.

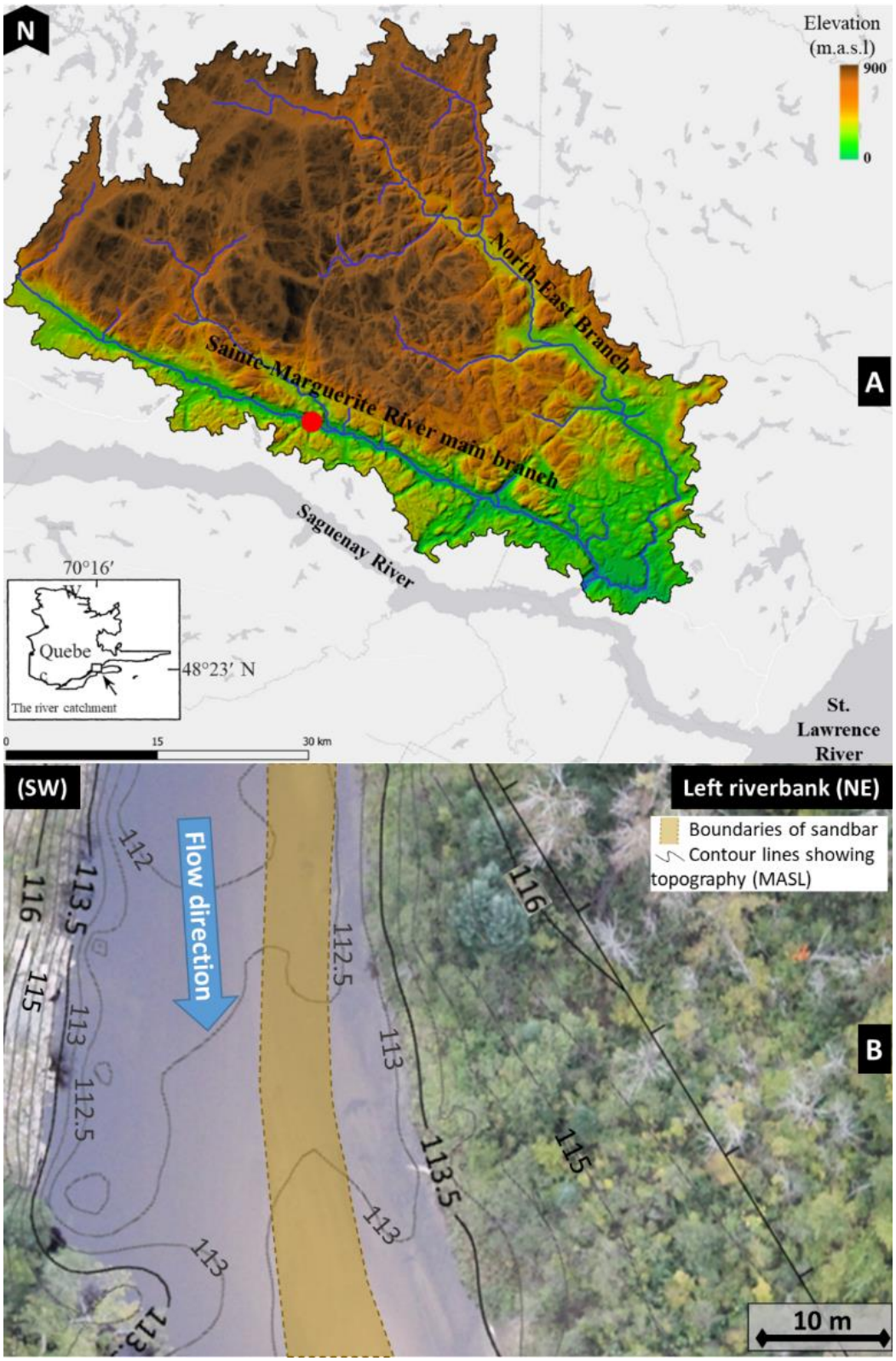

Figure 4.1 **Location of the river reach of Sainte-Marguerite River on a topographic map of the river catchment (red dot in A) and plan view of the selected river reach showing location of the sandbar and topographic contour lines in MASL (B).**

4.3.3 Active heat tracing

As the active heat tracing method, heat injection tests with a constant injection rate were performed with a doubled 150 m long heating cable (70 m effective coverage of riverbed) and a heating unit connected to a generator. The power output during the tests was 22.5 W/m. Thirty-five temperature sensors with an accuracy of ± 0.2 °C and a resolution of 0.032 °C were used to monitor temperature during the tests. All temperature sensors were attached to the heating cable at every 2 m using electrical tape. The heating cable was then buried into the riverbed sediments at a depth of < 5 cm. A zigzag pattern was chosen to have the most coverage of the riverbed material types and topography of the sandbar at the selected site (Figure 4.3). The temperature was recorded every 5 minutes. Two long tests with a duration of about 9 hours were carried out.

The study site is a natural river and the expected riverbed temperature changes can be due to both natural river water temperature fluctuations during the day/night and heat injection from cable. Based on the recorded riverbed temperature with a temperature sensor installed at a depth of < 5 cm and 40 cm (independent from heat injection tests), the riverbed temperature at shallow depth was not constant and closely followed daily river temperature fluctuation pattern, while the temperature of deeper sensor had almost no daily fluctuations. Although the temperature variations attenuate with depth, the daily temperature fluctuations were present at this depth since the heating cable was very shallow (< 5 cm depth). Thus, the natural temperature fluctuations extracted from installed independent temperature sensor at depth of 5 cm were subtracted from total temperature increase measured by temperature sensors installed on the heating cable.

The thermal properties of porous medium and the GW flux can be estimated by using the moving infinite line source (MILS) equation (Eq. 4.1) and reproducing the measured temperature increase caused by heat injection (Simon et al., 2021a). The MILS method has been used in this study since it was previously shown to be a valid approach for analysis of recorded temperature with a certain distance from heating source (des Tombe et al., 2019). Based on Simon et al. (2021a), the governing equations are as follows:

$$\Delta T_{MILS}(x,y,t) = \frac{E}{4\pi\lambda} exp\left[\frac{qx}{2D}\tau\right] \int_{\psi}^{\infty} \frac{1}{\psi} exp\left[-\psi - \frac{r^2 q^2}{16 D^2 \psi}\tau^2\right] d\psi \quad (4.1)$$

$$D = \frac{\lambda}{\rho c} \quad (4.2)$$

$$r^2 = x^2 + y^2 \quad (4.3)$$

$$\tau = \frac{\rho_w c_w}{\rho c} \tag{4.4}$$

$$\psi = \frac{r^2}{4Dt} \tag{4.5}$$

ΔT is the temperature increase (°K or °C), E is the constant linear heating power (W/m), q is the GW flux or specific discharge (m/s), ρ is density (kg/m^3) and c is specific heat capacity (J/kg K); therefore, ρc is the volumetric heat capacity of the matrix (J/m^3 K), and $\rho_w c_w$ is the volumetric heat capacity of water (J/m^3 K), D (Eq. 4.2) is the bulk thermal diffusivity (m^2/s) and depends on λ, the bulk thermal conductivity (W/m K), r (Eq. 4.3) is the distance (m) between location of temperature sensing at (x,y) and the heat source located at (0,0); 1 cm was set as r which was the distance between the center of heating cable and the center of pill-shaped temperature sensor, both having a 1 cm diameter. τ (Eq. 4.4) and ψ (Eq. 4.5) are integration parameters.

The graphical interpretation of thermal response curve with MILS model is described in detail in Simon et al. (2021a). This graphical interpretation can be simplified by dividing the thermal response curve into two zones of conduction-dominant and advection-dominant (Figure 4.2-A). Before the conduction-dominant zone, a conduction-affected zone that is affected by heat storage and conduction in the heating cable and temperature sensors is also visible, which is explained in detail by Simon et al. (2021a). The thermal properties of the porous media can be estimated by fitting the MILS model to conduction-dominant section of the curve while considering no flow conditions (q=0 in Eq. 4.1) in the MILS Model (solid blue line in Figure 4.2-B) (Simon et al., 2021a). Thermal conductivity and heat capacity of materials from this method were compared to values from lab analysis with KD2 pro device (Decagon Devices Inc., 2016) on several soil samples within each zone. The GW flow at location of each temperature sensor was then estimated by fitting the MILS analytical solution graph to the advection-dominant section of the observation data (solid black line in Figure 4.2-B). To calculate GW flux, a steady state (constant temperature) at the end of observation data graph facilitates the estimation and reduces the uncertainty (Simon et al., 2021a) (stabilization zone in Figure 4.2-A).

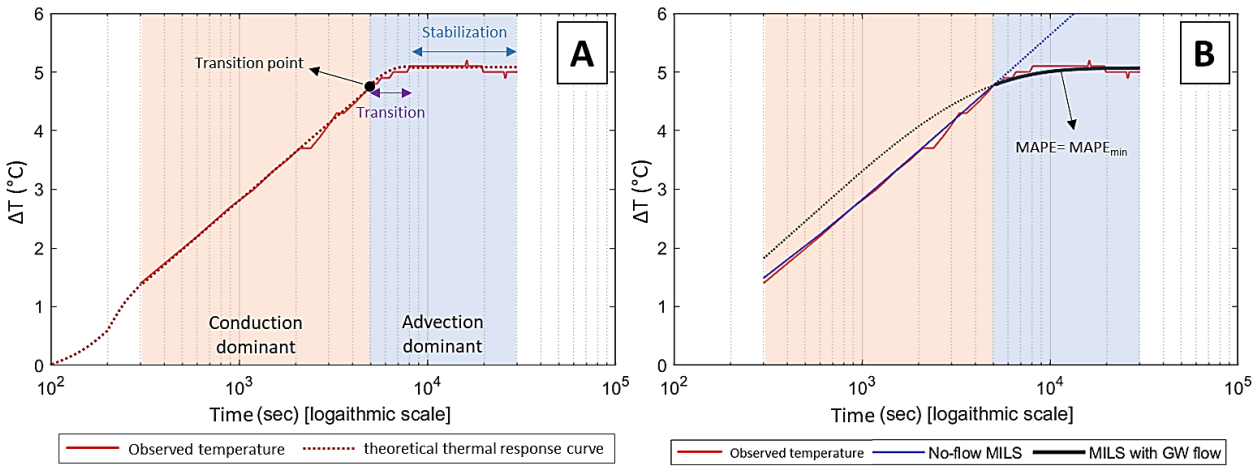

Figure 4.2 Example of thermal response curve (A) and graphical interpretation with the MILS model (B).

Mean absolute percentage error (MAPE) was used as a controlling parameter for evaluating the quality of the fit. MAPE was calculated as follows (Eq. 4.6):

$$MAPE = \frac{1}{n}\sum_{t=1}^{n}\left|\frac{T_{ob,t} - T_{si,t}}{T_{ob,t}}\right| \times 100 \quad (4.6)$$

where $T_{ob,t}$ is the observed/recorded temperature with temperature sensors and $T_{si,t}$ is the simulated temperature with MILS model both at time=t.

4.3.4 Passive heat tracing

A common passive heat tracing method consists of analyzing recorded temperature at different depths and calculating the upward GW flux to the stream or downward GW recharge from the one-dimensional heat transport equation (Eq. 4.7) (Gordon et al., 2012):

$$\frac{\delta T}{\delta t} = D\frac{\delta^2 T}{\delta z^2} - q\frac{\rho_w c_w}{\rho c}\frac{\delta T}{\delta z} \quad (4.7)$$

where *T* is temperature (°C), *t* is time (s), and *z* is depth (m).

VFlux is a *Matlab* code developed by Gordon et. al. (2012) (Gordon et al., 2012) for processing raw temperature time series and calculating vertical water flux in shallow subsurface systems by solving the above one-dimensional heat transport equation (Eq. 4.7). Similar codes such as *Ex-Stream* (Swanson et al., 2011) and *Flux-Bot* (Munz et al., 2017) can be used for calculation of flux by having temperature time series at different depths. However, ease of use and comprehensive equations were the main reasons for selecting *Vflux* in this study. *VFlux* uses the

analytical solution provided by Hatch et al. (2006). Hatch et al. (2006) equations for solving the one-dimensional heat transport is as follows (Gordon et al., 2012):

$$q = \frac{\rho c}{\rho_w c_w}\left(\frac{2D}{\Delta z}\ln A_r + \sqrt{\frac{a+v^2}{2}}\right) \tag{4.8}$$

$$|q| = \frac{\rho c}{\rho_w c_w}\sqrt{a - 2\left(\frac{4\pi\Delta t D}{L\Delta z}\right)} \tag{4.9}$$

where A_r is the ratio of amplitudes (a measure of amplitude attenuation) between the lower sensor and the upper sensor (dimensionless), Δz is the distance between the two sensors in the streambed (m), v is the velocity of the thermal front (m/s), Δt is the time lag (a measure of the speed of signal propagation) between the two temperature signals (s), L is the period of the temperature signal (s), and a is defined by Eq. 4.10:

$$a = \sqrt{v^4 + \left(\frac{8\pi D}{L}\right)^2} \tag{4.10}$$

The amplitude ratio, A_r, is calculated by Eq. 4.11:

$$A_r = \frac{A_{z+\Delta z,t+\Delta t}}{A_{z,t}} \tag{4.11}$$

where $A_{z,t}$ is the amplitude of the sensor at depth z and at time t, and $A_{z+\Delta z,t+\Delta t}$ is the amplitude of the sensor deeper by Δz at time $t+\Delta t$.

In this study, two temperature loggers with accuracy of ± 0.5 °C were installed in the riverbed material, one just below the riverbed at a depth of < 5 cm and the second at 40 cm depth below riverbed (Figure 4.3). The loggers were set to record the temperature every 15 minutes. The time series of the flux between these two temperature sensors was calculated considering fixed properties of the riverbed sediments based on lab measurements on collected soil samples in the *VFlux* code. The material between the sensors is considered uniform with porosity of 0.4 (-), thermal conductivity of 1.7 W/m K and volumetric heat capacity of 3 M J/m^3 K were used in the *VFlux* analysis of this study.

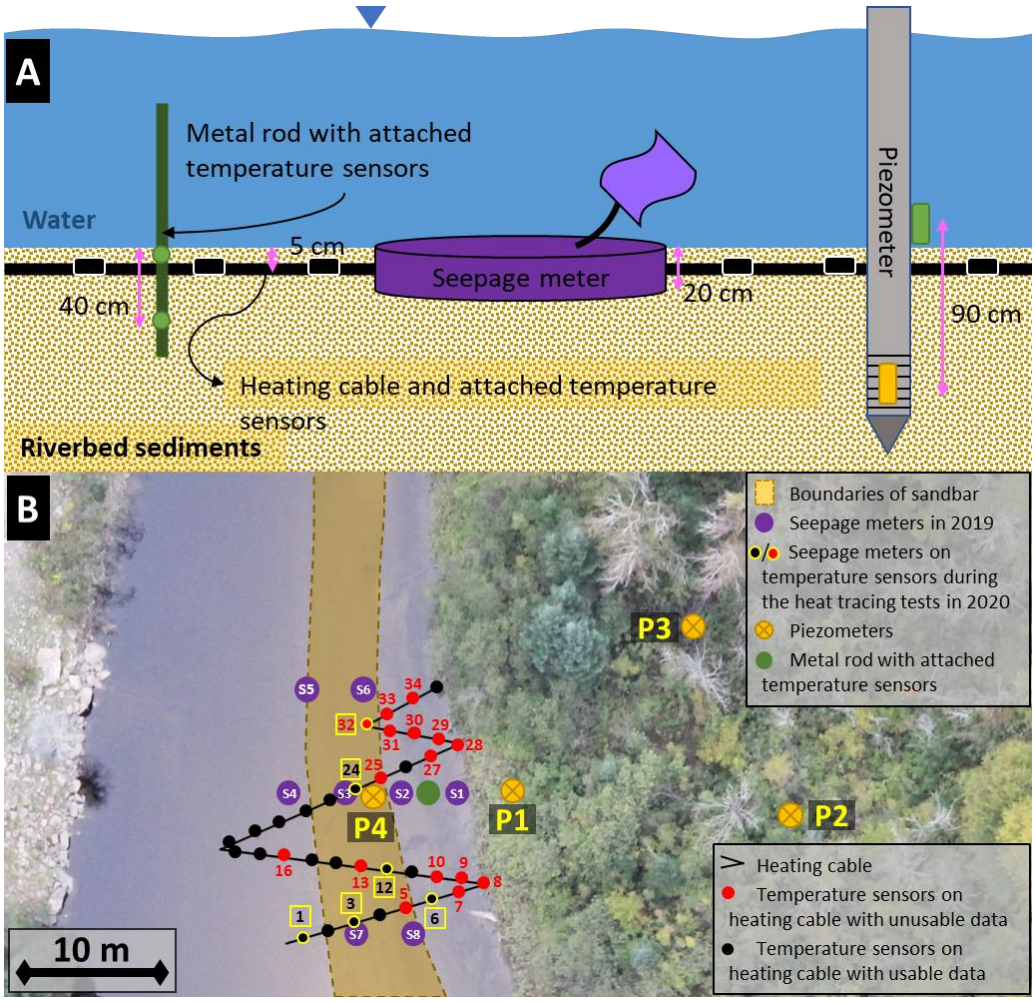

Figure 4.3 **Schematic section (A) and plan (B) view of all methods used in the study section.**

4.3.5 Statistical T-test analysis

Different methods were used to show the spatial and temporal variation of GW-SW interaction rate. To see if the measured differences are meaningful or not, an independent two-sample t-test with 95 % confidence interval (β=0.95) was applied to two data sets. The level of significance (α) is 5 % with β=95 % confidence interval (α=1-β → α=1-0.95=0.05). A 5 % significance level is most common in scientific studies (Helsel et al., 2020). T-test can be performed in two different ways. A two-tailed test is used to show if there is a difference between two data sets. On the other hand, one-tailed test should be performed when the hypothesis is that one set is higher or lower than the other. However, we were interested to evaluate whether the mean value of one data set is higher or lower than the other (e.g., GW seepage is higher in coarse sand compared to fine sand riverbed materials). Thus, one-tailed t-tests were used. A null hypothesis was assumed, which implies that there is no difference between two data means. Our assumption of significant

difference between two data sets is correct when the null hypothesis is rejected, and it could be confirmed that there is a statistically significant difference between two data sets and the difference is not due to random sampling error. The data analysis toolbox in Excel was used to calculate the *p* (probability) value. The null hypothesis was rejected when the calculated *p* value was less than the selected significance level (α=0.05).

4.4 Results

4.4.1 Seepage meters

Results from three consecutive 12-hour seepage meter tests conducted in 2019 are shown in Table 4.1. Based on average values, the seepage measured in the coarse material of the sandbar was about 50 % higher than those measured in fine materials and this difference was statistically significant considering 5 % significance level (α) since the calculated probability was 0.002 (p=0.002 < α=0.05; Figure 4.4). The tests in which the seepage meters bags were either empty or competently full at the end were marked as inconclusive. After each inconclusive result, the tubing and bag of respective seepage meter were changed to resolve the few problems encountered and the seepage meter was placed at its original location to improve measurements.

Table 4.1 Measured GW flow through riverbed in m/s from three consecutive 12-hour seepage meter tests (2019).

Seepage meter	Test1	Test2	Test3	Average
S1	1.3×10^{-7}	1.1×10^{-7}	1.5×10^{-7}	1.3×10^{-7}
S2	1.1×10^{-7}	1.5×10^{-7}	1.2×10^{-7}	1.3×10^{-7}
S3*	2.1×10^{-7}	4.8×10^{-8}	3.4×10^{-7}	2.0×10^{-7}
S4	inconclusive	5.6×10^{-8}	2.2×10^{-7}	1.4×10^{-7}
S5	6.2×10^{-8}	9.3×10^{-8}	2.3×10^{-7}	1.3×10^{-7}
S6*	4.6×10^{-7}	1.0×10^{-7}	3.4×10^{-7}	3.0×10^{-7}
S7*	inconclusive	3.2×10^{-7}	2.2×10^{-7}	2.7×10^{-7}
S8*	inconclusive	inconclusive	2.0×10^{-7}	2.0×10^{-7}

*Seepage meters located on the sandbar (coarse sand material).

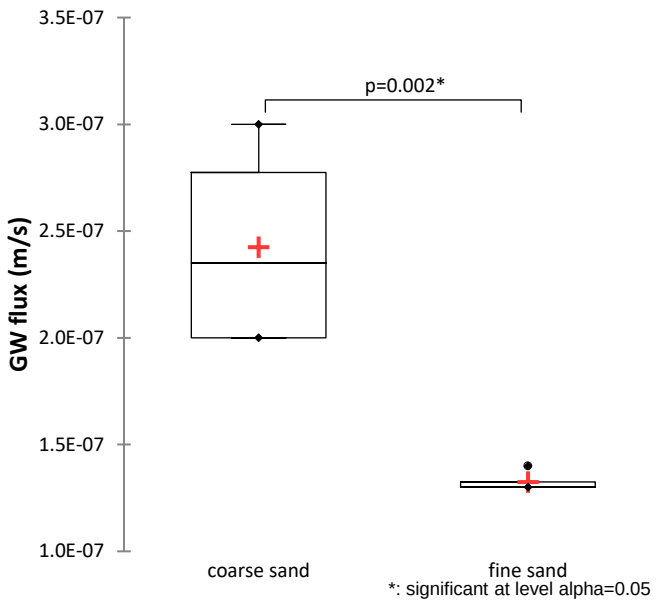

Figure 4.4 **Box plot of T-test showing significant difference of average measured seepage rate in two riverbed materials using seepage meters.**

Based on measurements conducted in 2020, the calculated GW-SW interaction flux during the day (from 9 AM to 3 PM) were generally higher compared to the measurements during the night (from 6 PM to 9 AM; Figure 4.5-A). Higher flux during the day coincides with lower river water level (orange line of graph in Figure 4.5-B) compared to the night-time (blue line of graph in Figure 4.5-B). This difference was statistically significant at 5 % significance level since p=0.004 < α=0.05 (Figure 4.5-C).

4.4.1 Piezometers and water-level loggers

4.4.1.1 Horizontal flow

Figure 4.6 shows the location of piezometers, the water level from sea level at the day of installation, and the calculated mean horizontal hydraulic conductivity based on three slug tests in each piezometer. The geometric average hydraulic conductivity of two neighboring piezometers and the head difference between them from measurements at the day of installation was considered to calculate Darcy flow velocity and its 2D horizontal direction (Figure 4.6-B). The approximated GW flow direction in Figure 4.6-A is drawn perpendicular to hydraulic head contour lines and its direction is the same as the sum of all vectors shown in Figure 4.6-B.

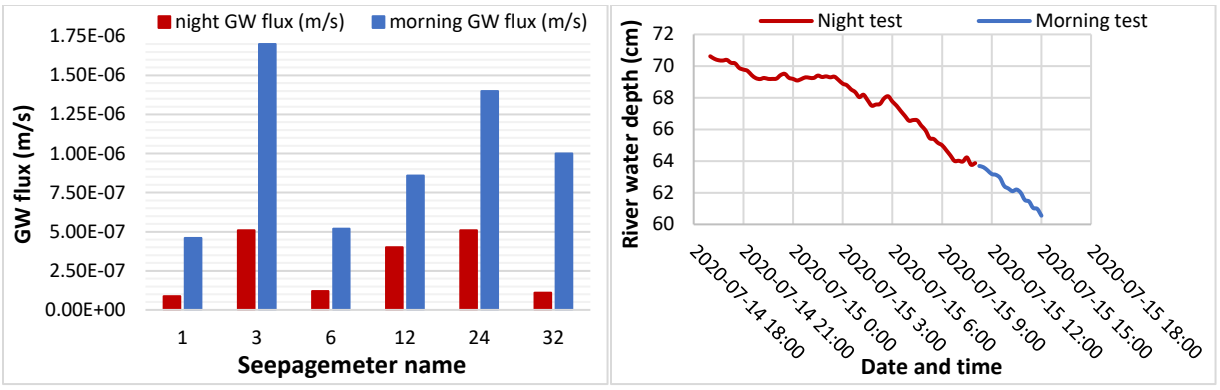

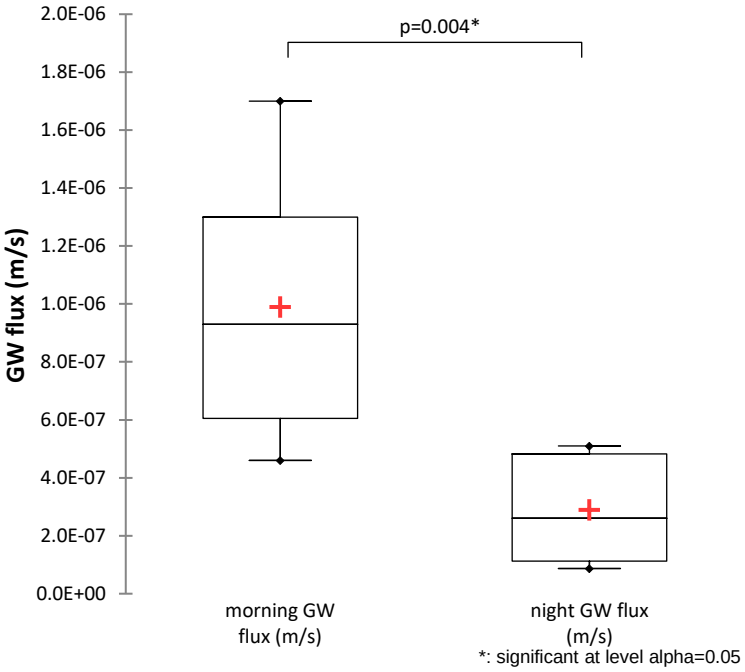

Figure 4.5 **Measured GW flux by seepage meters based on conducted tests during morning and night (A), river water depth from the bottom of the river at the same time of seepage meter measurements (B) and box plot of T-test showing significant difference of measured seepage during morning and night using seepage meters (C).**

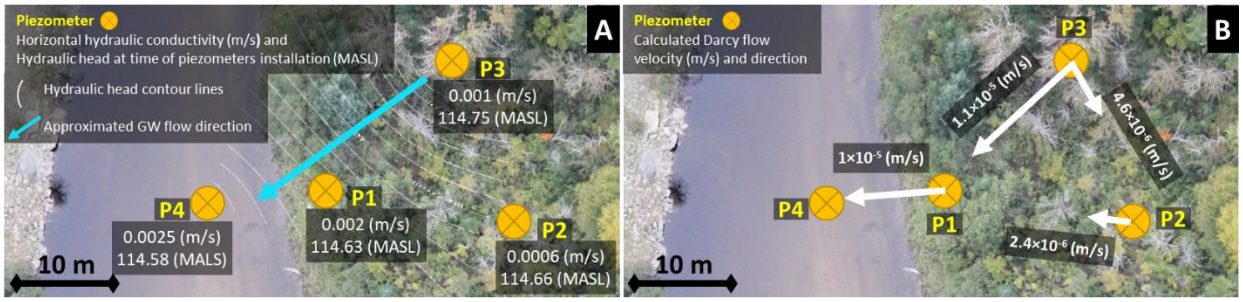

Figure 4.6 **Piezometers' location, calculated hydraulic conductivity from slug tests, measured hydraulic head at the day of installations and hydraulic head contour lines (A) and calculated horizontal Darcy flow velocity vectors between neighboring piezometers (B).**

The time series of GW flow from P1 to P4 was calculated by using the head difference between these two piezometers instead of average yearly values. The piezometer installed in the river (P4) was removed in mid-November because of the risk of losing the instruments was high due to presence of ice sheets in the river in winter and flooding in fall and spring. Thus, the calculation of GW flow time series was from mid-July to mid-November (Figure 4.7).

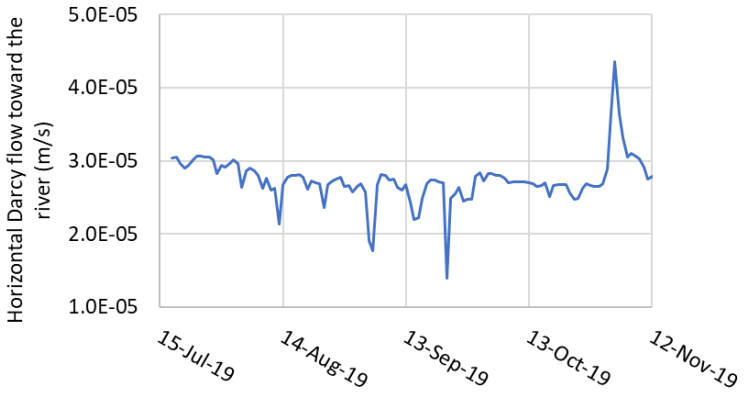

Figure 4.7 Temporal variability of horizontal Darcy flow from piezometers P1 to P4.

4.4.1.2 Vertical flow

Upward vertical flow rate of 5×10^{-5} m/s from the riverbed into the stream was calculated with Darcy equation based on average yearly head difference of two water-level loggers at the same location but different depths, one in the river and one below the riverbed in the piezometer at 80 cm depth (Figure 4.3-A). The vertical hydraulic conductivity of 3.4×10^{-4} m/s for this calculation was measured based on reverse Darcy tests on in situ riverbed column samples (7 cm diameter and 12 cm length). The calculated vertical upward flow to the riverbed is relatively close to the horizontal flow to the river.

The temporal variation of GW-SW interaction upward flux was calculated by using time series of head difference between P4 and R2 (Figure 4.8).

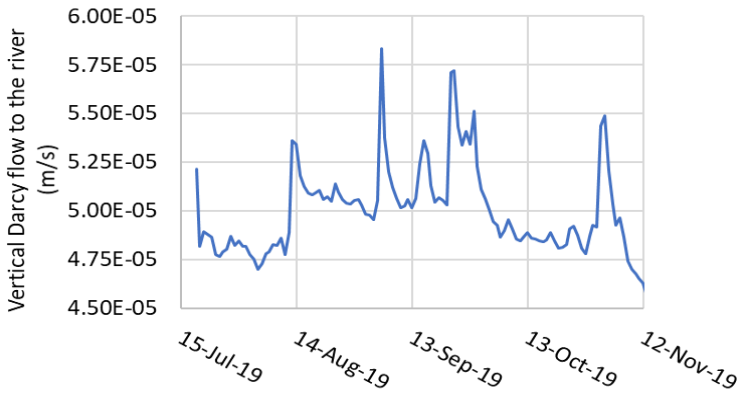

Figure 4.8 **Temporal variability of vertical Darcy flow from the riverbed to the river according to piezometers P4 and R2.**

4.4.2 Active heat tracing

The initial analysis of the two long heat injection tests showed almost similar results. Therefore, analysis of only one long test with duration of 8.5 hours was selected and presented in this paper. In the selected test, out of 35 installed temperature data loggers, only 16 (red dots in Figure 4.3-B) reached a steady temperature after about 2.5 hours with a maximum recorded temperature increase between 1.5 °C to 5 °C (Figure 4.9). Most of these temperature loggers (12) were located close to the riverbank and four (logger numbers 5,13,25, and 32; Figure 4.3-B) were located on the sandbar. Data from other temperature loggers (black dots; Figure 4.3-B) could not be used for further analysis with MILS model since the maximum temperature increase was lower than 1 °C.

Based on MILS analysis of data from reliable temperature sensors (Figure 4.9), the average calculated thermal conductivity, heat capacity and flow rate in coarse sand material of the sandbar were 3.45 W/m K, 3.38 M J/m^3 K, and 4.9×10^{-5} m/s respectively. The results in fine sand material next to the sandbar were 2.33 W/m K, 3.33 M J/m^3 K, and 2.9×10^{-5} m/s for the average calculated thermal conductivity, heat capacity and flow rate correspondingly. The difference in the calculated values of flow rate and thermal conductivity of fine sand zone and coarse sand zone was shown to be significant considering a 95% confidence level (Figure 4.10, *p* values of 0.012 and 0.032). However, the small difference in calculated heat capacity of the two zones was not identified as significant (Figure 4.10-C, p=0.89>0.05). The MAPE of fitted curves to observation data was lower than 3 % for all data sets with MILS model analysis (Table 4.2).

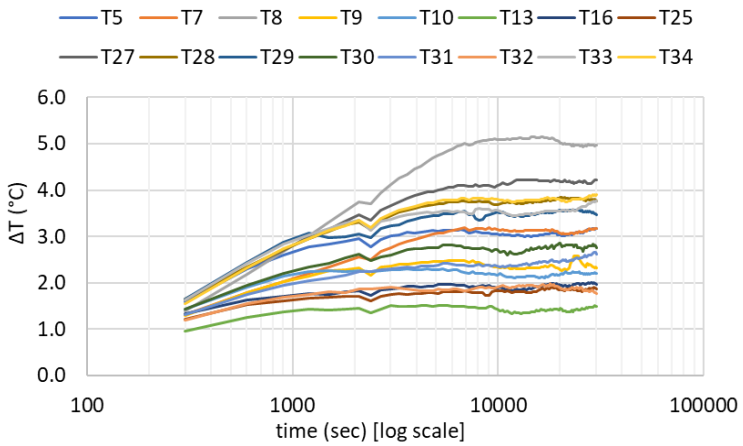

Figure 4.9 **Temperature increase of selected temperature sensors during the heat injection test.**

Note. Numbers after "T" identify the temperature sensor and are the same as what is shown in Figure 4.3.

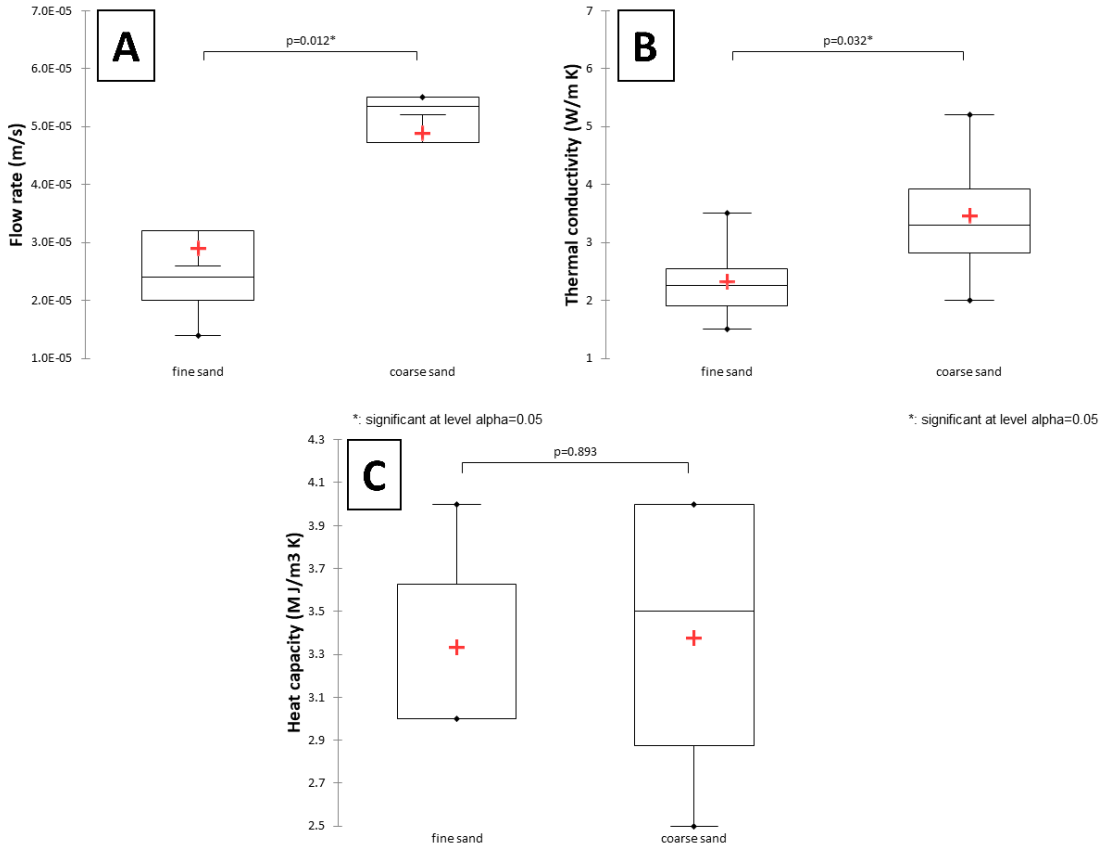

Figure 4.10 **Box plot of T-test on calculated flow rate (A), thermal conductivity (B) and heat capacity (C) in fine and coarse sand materials at the study site using the MILS method and active heat tracing.**

Table 4.2 Calculated flow rate and MAPE of selected temperature sensors.

Sensor	ρc (MJ/m^3 K)	λ (W/m K)	q (m/s)	MAPE	sensor	ρc (MJ/m^3 K)	λ (W/m K)	q (m/s)	MAPE
5*	3	2	3.3×10^{-5}	1.8	27	4	1.7	2.0×10^{-5}	1.6
7	3.5	2.5	2.0×10^{-5}	2.7	28	3	2	1.9×10^{-5}	1
8	3.5	1.5	1.4×10^{-5}	1.9	29	3	2	2.3×10^{-5}	1.5
9	4	2.5	5.0×10^{-5}	2.9	30	3	2.7	2.6×10^{-5}	2
10	4	2.5	5.5×10^{-5}	2.5	31	3	3.2	2.6×10^{-5}	2.7
13*	2.5	5.2	5.5×10^{-5}	2.2	32*	3	3.5	5.0×10^{-5}	2.5
16	4	3.1	5.5×10^{-5}	2.9	33	3	1.9	2.5×10^{-5}	2
25*	4	3.5	5.2×10^{-5}	2.8	34	3	1.9	2.0×10^{-5}	1.1

* Temperature loggers located on the sandbar (coarse sand material).

4.4.3 Underground temperature sensors

The recorded temperature during the cold season (November to April) when the river freezes was 0 °C for the logger installed just below the riverbed while the temperature 40 cm below the riverbed did not go down to 0 °C (Figure 4.11-A). The calculated vertical flow based on the *Vflux* model was more or less constant around 1×10^{-5} m/s during the warm season with few daily maximum values around 2×10^{-5} m/s (Figure 4.11; start and end of the graph), especially when compared to the cold season when the calculated flux had more variation and ten times higher daily maximum values of around 1×10^{-4} m/s (Figure 4.11; middle section of the graph).

4.5 Discussion

Based on calculated average seepage rate from all methods of this study and considering the width and length of the river at this site, the GW discharge at the selected site was about 6×10^{-3} m^3/s. The river flow rate at this site was about 6 m^3/s based on our measurements made with an ADCP device. This means that only 0.1 % of river flow was contributed by GW at the time of experiments. This low contribution of GW to river flow is in accordance with our previous study with radon measurements for identification and quantification of GW-SW interactions (Fakhari et

al., 2023). The low GW contribution to Sainte-Marguerite River can be due to low thickness of the aquifer below the river and presence of rocky river valley walls. Rock outcrops not far from the river on both sides are evidence of such shallow aquifer. The selection of this site was mostly based on ease of access and field measurement feasibility. Although all methods showed to be effective in quantifying this low GW presence in the river, the results could potentially be more significant and better justified if a site with higher GW seepage rate had been initially targeted.

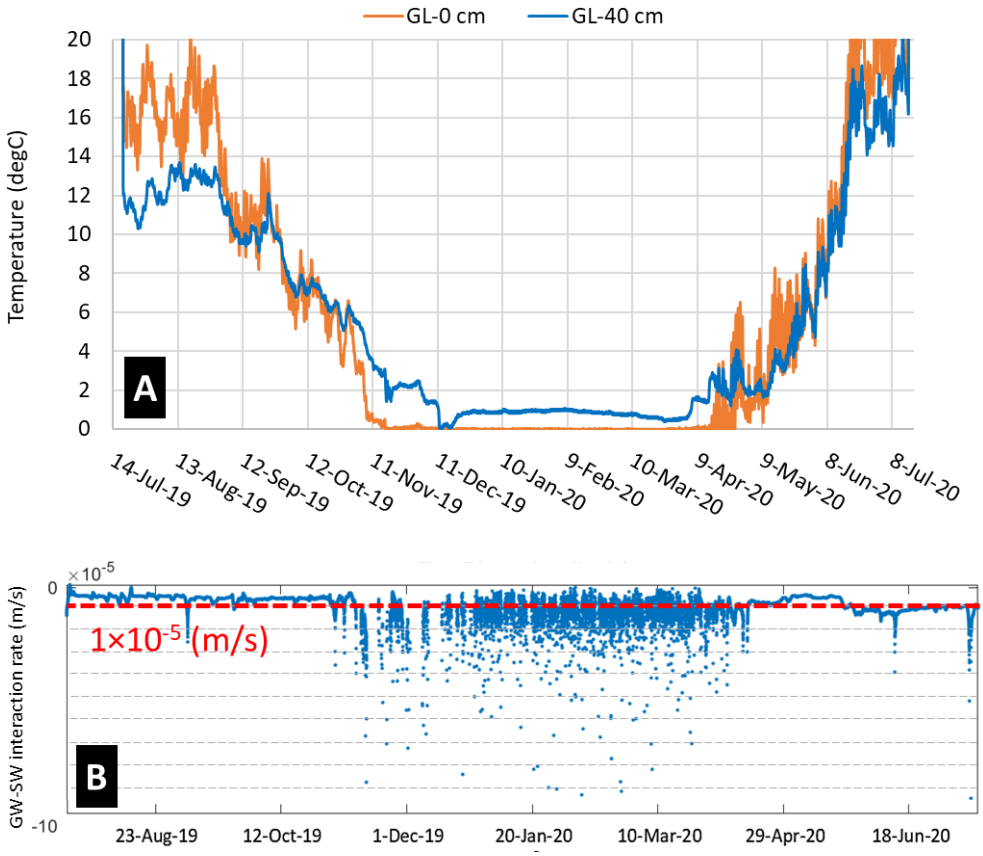

Figure 4.11 **Recorded temperature of the riverbed at two depths (A) and daily GW-SW interaction flux from Vflux (blue dots) and average yearly value (red line) (B) according to underground temperature sensors.**

4.5.1 Seepage meters

The use of several seepage meters at different locations showed spatial variation of GW discharge at the selected study site. The difference in GW discharge at location of the sandbar compared to other areas was significant based on the T-tests.

Based on T-tests, the temporal variation showed change of GW discharge rate which was significant even during short daily time periods. Monitoring river water level during seepage meter

tests made in 2020 showed close dependency of temporal variation in GW-SW interaction rate to the river water level.

Difficulty of application in deep water, leakages from damaged tube and plastic bags, lack of complete seal between inside and outside of the barrel and presence of trapped gas in tubes and bags, which disrupt the natural flow of GW to plastic bags, were possible limitation and source of error in our measurements and through previous studies (e.g., Rosenberry et al., 2008). Small-scale temporal variations (e.g., hourly) could not be evaluated with this method since low GW discharge rate requires seepage meters reading to be done after a minimum of few hours and seepage meters give a representative value of GW flux for the whole duration in between measurements. On the other hand, variation over a long period of time (e.g., monthly) could not be analyzed easily with this method since the measurements are manual and emptying the plastic bags after one or a couple of days (depending on the bag size and GW flow rate) is needed. New type of seepage meter which can automate measurements is possible solution for a longer study (Rosenberry, 2008). However, these new seepage meters are expensive and require complex installations.

4.5.2 Piezometer and water-level loggers

Yearly to sub-hourly variation in GW flow was analyzed by flow network analysis through installed piezometers and water-level loggers, which was an advantage of this method (Rosenberry et al., 2008). However, the calculated horizontal and vertical GW flow has an accuracy of about 1.2×10^{-5} m/s and 1.2×10^{-6} m/s when considering the accuracy of pressure measured with the level loggers, which was 0.005 mH_2O. Thus, variations in calculated GW flow that are smaller than the approximated accuracy should be considered insignificant. The direction of GW flow and its rate magnitude are expected to spatially vary according to heterogeneity in the subsurface (Martinez, 2010). An advantage of this method is the possibility of separating vertical and horizontal flow by having piezometer and level logger at different locations and depths (Rosenberry et al., 2008). A better coverage of GW flow network could be possible with more piezometers, which in our case was difficult and costly due to field logistics. One of the difficulties faced was high river water level and overflow on riverbanks during the wet season. This called for long above ground casing of piezometers to avoid flooding and disconnection to air, which is necessary for loggers that measure water level based on pressure differential between water and air. Another difficulty was to have stable piezometers installed in the river remaining in place at the end of the cold season when high flow and large ice sheets in the river are present.

4.5.3 Active heat tracing

Active heat tracing with combination of a heating cable and temperature sensors showed variation in GW seepage at different locations. The temperature response curve obtained with combination of heating cables and temperature sensors displayed similar pattern to that of Active-DTS made with FO-cable (e.g., Simon et al., 2021b). Thus, the combination of heating cable and temperature sensors can be a cheaper alternative to FO-cable measurements for GW flow assessment at different locations that can help evaluate the heterogeneity of the subsurface (e.g., Giordano et al., 2021) but with a lower resolution. The use of this method in a natural river was new and based on the challenges that were encountered, we recommend some improvement for future use. One issue faced was relatively low temperature increase during the tests compared to actively heated FO-DTS (e.g., Simon et al., 2021a). Temperature measurements in a FO cable are made inside the cable and beside the heating wire where the cable jacket acts as an insulator. Similarly, separated heating and FO cables were used by des Tomb et. al. (2019), with measurements carried out in a borehole with PVC cover acting as an insulator. Temperature measurements with our new method were made outside the heating cable without presence of an insulator, which might be the source of heat loss and low temperature increase. The absence of a steady temperature increase resulting in a constant slope, which is required for estimation of thermal properties with the MILS method (Simon et al., 2021a) was another encountered issue. This low temperature increase was related to high flow over the temperature sensors. This can be explained since the location of most of the inconclusive temperature loggers were in the middle of the river, where higher river flow was expected in coarser riverbed material. The calculated thermal conductivity and heat capacity of fine and coarse sand materials of the riverbed with the MILS method were in the expected range when compared to other studies (e.g., Kodesová et al., 2013; Márquez et al., 2016; Zhirkov et al., 2021; Rakic et al., 2014) and values obtained from lab analysis of soil samples of the studied river reach. However, the calculated heat capacity was sometimes high (4 M J/m^3 K), which is close to the heat capacity of water and suggests very high porosity of coarse sand and gravel material of the sandbar and thus high hyporheic flow conditions. Some temperature sensors may have been partially or completely out of the riverbed and in the water. Therefore, the depth of installed temperature sensors in the riverbed plays an important role, as it has been documented before that a change in cable burial depth of ± 2 cm can result in ± 50 % change in calculated flow rate (Simon et al., 2021b). Additionally, it can be assumed that due to the moving nature of the riverbed, some of the temperature sensors were unburied, which is another reason explaining why some of the recorded temperature did not reach steady state. Therefore, installing the cable deeper and at a constant depth in the riverbed where

flow is expected to be less affected by river flow and where the cable is more stable is our suggestion for future implementation although it can be difficult to achieve in the field.

4.5.4 Passive heat tracing

Monitoring riverbed temperature at different depths was previously used to show the temporal variation of GW seepage rate (Constantz, 2008; Lay et al., 2019; Gordon et al., 2012). This method can be used to record sub-daily to yearly variations. For the selected river of this study, the important variation of flow rate during the cold season when the river surface freeze was an interesting result. Even though the temperature in the river is almost constant and around zero, the change of temperature at the depth of 40 cm below the riverbed is characteristic of the GW flux to the river varying during this period. However, some large variations in calculated flux, for example during January 2020 when temperature of both sensors seems constant, can be considered inaccurate and possibly due to calculations errors. Installation of temperature sensor in deeper layers below the riverbed and use of more accurate sensors with better protection against freezing is suggested in future works for more accurate results. Considering the accuracy of the temperature sensors, which was ± 0.5 °C, the accuracy of flow calculated with this method is approximated to 1×10^{-5} m/s and variations lower than this value should be considered insignificant. Overall, passive heat tracing showed that even with limited shallow GW flow system due to frozen ground and presence of ice and snow on the ground, the deep GW system is still connected to the river and can be a source of water to the river. GW seepage can be an important contributor to the river water temperature due to its higher average and steady temperature during the cold season. Here, only two temperature sensors at one location but two depths were used in the analysis (the data from a third temperature sensor 80 cm below the riverbed was unsalvageable), which showed the temporal variation of shallow upward GW flow. Using more sets of temperature sensors at different locations can help to better evaluate the spatial variation of GW flow. Additionally, deeper temperature sensors could help to better evaluate the deep GW system.

4.5.5 Method comparison

The GW seepage rate measured by passive heat tracing, heat injection, piezometer and water-level loggers are in the same order of magnitude (Table 4.3). However, measured values with seepage meters were the lowest with two orders of magnitude difference compared to other methods. This difference and the low seepage rate obtained with the seepage meters can be

related to riverbed material and their high hydraulic conductivity. The seepage meters can underestimate the GW seepage significantly since bypass flow around the seepage cylinder can occur in highly conductive riverbeds made of sand and gravel according to Rosenberry et. al. (2020). On the other hand, the highest seepage rates were measured with the heat injection method, which had the least depth of investigation. The high measured flux and absence of stability for some temperature sensors suggested the influence of river flow on recorded temperature. Based on the low depth of investigation and the influence of the river flow it can be assumed that this method was measuring the horizontal hyporheic flow within the riverbed rather than the vertical upward GW seepage to the river.

Piezometer with water-level and temperature loggers installed in the riverbed provided a reliable evaluation of GW flow and GW-river interaction rate with information on the direction and amount of flow considering a large depth of investigation. Passive heat tracing seems the more reliable solution for long-term analysis of GW-SW interaction rate since temperature sensors (if installed properly) are stable and easily left in the site over the year. However, the uncertainty of each method should be considered. For instance, passive heat tracing was previously shown to have a higher uncertainty compared to active heat tracing (Simon et al., 2021b).

Ultimately, the choice of the method depends on the specific needs of the project, as well as the availability of equipment and expertise. Nevertheless, the use of different techniques can provide valuable information on GW and SW interaction, but each technique has its advantages and limitations, and a combination of techniques may be necessary to fully understand GW-river interaction. For example, the two best suited methods regarding quantifying and analyzing temporal variations of the GW-SW interaction rate in this study (piezometers and water-level loggers and passive heat tracing) have the least spatial coverage of the studied river reach (Figure 4.3) and were most difficult to implement at large-scale. The seepage meter and heat injection methods allowed to cover large areas and better assessed spatial variations, while lacking a complete temporal variation coverage. In an ideal situation where all mentioned equipment and methods in this study are applicable, we suggest using seepage meters and active heat tracing methods to firstly estimate the spatial variability and secondly estimate the variations through time with piezometers and temperature sensors in specific areas.

Table 4.3 Summary of measured GW seepage with different methods.

Method	Depth of investigation (cm)	Measured GW seepage rate (m/s)	
		Fine sand	Coarse sand
Seepage meter	20	1.3×10^{-7}	2.4×10^{-7}
Piezometers and water-level loggers	80	-	5.0×10^{-5}
Heat injection	5	2.9×10^{-5}	4.9×10^{-5}
Passive heat tracing	40	1.0×10^{-5}	-

4.6 Conclusions

All methods used in this study allowed to emphasis spatial and temporal variation in GW-SW interaction rate at the river reach scale. The statistical T-tests indicated that variable flow rates measured in different sediment materials were meaningful and subsurface heterogeneities played a significant role in GW-SW exchange. GW-SW interaction was proven to be temporally variable in small- and large-time scales and even during cold season with limited GW flow in the studied river. All methods used in this study were shown to be applicable for characterization of fish habitats in riverine systems for a better protection plans. Additionally, these studies can be implemented for better understanding spawning areas with regard to riverbed materials, GW seepage rate and water temperature, which are important selection factors for spawners. The new approach involving buried temperature sensors attached to a heating cable can be an advantageous method for fish habitat studies since it can provide information regarding the heterogeneity and characteristics of riverbed materials and GW seepage rate over a decent coverage area. This method recorded similar temperature response curves to active heat tracing with FO-DTS and, if applied properly, could allow to evaluate the spatial variation of seepage rate. Heterogeneities of the riverbed materials were also evidenced by using the MILS equation to analyze the recorded temperature responses. Although it was the first time used in a natural river and our equipment would require improvements, results demonstrate that the heating cable method can be a promising alternative to FO-DTS. Depending on the achievable heat injection rate, there are lower and higher limits for measuring flow or thermal conductivity. If the flow is very low, it requires a high heat injection rate and a long test to be able to reach steady state and calculate the flow rate. For instance, Giordano et al. (2021) preformed some tests with the same

equipment used in this study and that took more than four days to reach stability and be able to measure low GW flow between two boreholes. On the other hand, if the flow is too high the temperature increase is low, and the linear temperature increase due to conductive heat transfer is not visible. Thus, the accuracy of sensors used for temperature measurements and the measurement pace is important to accurately evaluate the thermal conductivity. Sandbox experiments made in the laboratory are a suggestion for future work to evaluate the limits of the heating cable method that could ultimately allow optimizing equipment with respect to heat injection rate and duration.

4.7 References

Anderson M.P. (2005) « Heat as a ground water tracer. » Ground Water 43 (6): 951-968. doi:10.1111/j.1745-6584.2005.00052.x.

Angermann L., Krause S. & Lewandowski J. (2012) « Application of heat pulse injections for investigating shallow hyporheic flow in a lowland river. » Water Resources Research 48 (10): 1-16. doi:10.1029/2012WR012564.

Banks E.W., Simmons C.T., Love A.J. & Shand P. (2011) « Assessing spatial and temporal connectivity between surface water and groundwater in a regional catchment: Implications for regional scale water quantity and quality. » Journal of Hydrology 404 (1-2): 30-49. doi:10.1016/j.jhydrol.2011.04.017.

BAPE (1993) « Sainte-Marguerite-3 Hydroelectric Development Project. » enquiry and public hearing report, bureau d'audiences publiques sur l'environnement (BAPE) quebec, quebec, canada.

Baxter C.V. & Hauer F.R. (2000) « Geomorphology, hyporheic exchange, and selection of spawning habitat by bull trout (Salvelinus confluentus). » Canadian Journal of Fisheries and Aquatic Sciences 57 (7): 1470-1481. doi:10.1139/cjfas-57-7-1470.

Briggs M.A., Buckley S.F, Bagtzoglou A.C., Werkema D.D. & Lane J.W. (2016) « Actively heated high-resolution fiber-optic-distributed temperature sensing to quantify streambed flow dynamics in zones of strong groundwater upwelling. » Water Resources Research 52: 5179-5194. doi:10.1002/2015WR018219.

Briggs M.A., Lautz L.K. & Mckenzie J.M. (2012) « A comparison of fibre-optic distributed temperature sensing to traditional methods of evaluating groundwater inflow to streams. » Hydrological Processes 26: 1277-1290. doi:10.1002/hyp.8200.

Cardenas B.M. (2008) « The effect of river bend morphology on flow and timescales of surface water-groundwater exchange across pointbars. » Journal of Hydrology 362 (1-2): 134-141. doi:10.1016/j.jhydrol.2008.08.018.

CERM (2015) « Coupes stratigraphique. » Online Geological Map dataset, Équipe de géomatique du Université du Québec à Chicoutimi. http://paces.uqac.ca/stratigraphie_chcn.html.

ClimateData.ca (2021) « Data Source: Environment and Climate Change Canada and (ClimateData.ca) See: https://eccc-msc.github.io/open-data/licence/readme_en/. » Page Web, consulté le 1er septembre 2021 à l'adresse https://climatedata.ca/explore/location/?loc=EJLMJ&location-select-temperature=tx_mean&location-select-precipitation=rx1day&location-select-other=frost_days.

Constantz J. (2008) « Heat as a tracer to determine streambed water exchanges. » Water Resources Research 46 (4). doi:10.1029/2008WR006996.

Decagon Devices Inc. (2016) « KD2 Pro Thermal Properties Analyzer. » Device Manual. Decagon Devices, Inc WA, United States https://library.metergroup.com/Manuals/13351_KD2%20Pro_Web.pdf.

Fakhari M., Raymond J., Martel R., Drolet J.-P., Dugdale S.J. & Bergeron N.E. (2023) « Analysis of Large-Scale Groundwater-Driven Cooling Zones in Rivers Using Thermal Infrared Imagery and Radon Measurements. » Water 15 (5). doi:10.3390/w15050873.

Fraser N.H.C., Metcalfe N.B. & Thorpe H.E. (1993) « Temperature-dependent switch between diurnal and nocturnal foraging in salmon. » Proceedings of the Royal Society B: Biological Sciences 252: 135-139.

Fritz B.G., Mackley R.D. & Arntzen E.V. (2016) « Conducting Slug Tests in Mini-Piezometers. » Groundwater 54 (2): 291-295. doi:10.1111/gwat.12335.

Giordano N., Lamarche L. & Raymond J. (2021) « Evaluation of subsurface heat capacity through oscillatory thermal response tests†. » Energies 14 (18). doi:10.3390/en14185791.

Gleeson T. & Paszkowski D. (2014) « Perceptions de l'échelleen hydrologie: Qu'entend-on paréchelle régionale? » Hydrological Sciences Journal 59 (1). Taylor & Francis: 99-107. doi:10.1080/02626667.2013.797581. http://dx.doi.org/10.1080/02626667.2013.797581.

Gordon R.P., Lautz L.K., Briggs M.A. & McKenzie J.M. (2012) « Automated calculation of vertical pore-water flux from field temperature time series using the VFLUX method and computer program. » Journal of Hydrology 420-421. Elsevier B.V.: 142-158. doi:10.1016/j.jhydrol.2011.11.053. http://dx.doi.org/10.1016/j.jhydrol.2011.11.053.

Hatch C.E., Fisher A.T., Revenaugh J.S., Constantz J & Ruehl C. (2006) « Quantifying surface water-groundwater interactions using time series analysis of streambed thermal records: Method development. » Water Resources Research 42 (10): 1-14. doi:10.1029/2005WR004787.

Hayashi M. & Rosenberry D.O. (2002) « Effects of ground water exchange on the hydrology and ecology of surface water. » Ground Water 40 (3): 309-316. doi:10.1111/j.1745-6584.2002.tb02659.x.

Helsel D.R., Hirsch R.M., Ryberg K.R., Archfield S.A. & Gilroy E.J. (2020) « Statistical Methods in Water Resources. » In Hydrologic Analysis and Interpretation (Supersedes USGS Techniques of Water-Resources Investigations, book 4), 1re éd., 458. Reston, Virginia: U.S. Geological Survey. doi:https://doi.org/10.3133/tm4a3. https://pubs.er.usgs.gov/publication/tm4A3.

Jensen A.J., Johnsen B.O. & Saksgard L. (1989) « Temperature requirements in Atlantic salmon (Salmo salar), brown trout (Salmon trutta), and Arctic char (Salvelinus alpinus) from hatching to initial feeding compared with geographic distribution. » Canadian Journal of Fisheries and Aquatic Sciences 46 (5): 786-789. doi:10.1139/f89-097.

Kodesová R., Vlasáková M., Fér M., Teplá D., Jakšík O., Neuberger P. & Adamovsky R. (2013) « Thermal properties of representative soils of the Czech Republic. » Soil and Water Research 8 (4): 141-150. doi:10.17221/33/2013-swr.

Lay H.L., Thomas Z., Rouault F., Pichelin P. & Moatar F. (2019) « Characterization of diffuse groundwater inflows into streamwater (part II: Quantifying groundwater inflows by coupling FO-DTS and vertical flow velocities). » Water (Switzerland) 11 (12): 1-22. doi:10.3390/W11122430.

Magliozzi C., Grabowski R., Packman A. & Krause S. (2017) « Scaling down hyporheic exchange flows: from catchments to reaches. » Hydrology and Earth System Sciences Discussions (January): 1-53. doi:10.5194/hess-2016-683.

Malcolm I.A., Soulsby C., Youngson A.F. & Petry J. (2003) « Heterogeneity in ground water-surface water interactions in the hyporheic zone of a salmonid spawning stream. » Hydrological Processes 17 (3): 601-617. doi:10.1002/hyp.1156.

Márquez Andújar J.M, Martínez Bohórquez M.A. & Melgar S.G. (2016) « Ground thermal diffusivity calculation by direct soil temperature measurement. application to very low enthalpy geothermal energy systems. » Sensors (Switzerland) 16 (3). doi:10.3390/s16030306.

Martinez C.J. (2010) « Mini-piezometers for Measuring Groundwater to Surface Water Exchange. » Report by IFAS Extension Service, University of Florida, FL. USA. doi:10.32473/edis-ae454-2009.

Miller R.B., Heeren D.M., Fox G.A., Halihan T. & Storm D.E. (2016) « Heterogeneity influences on stream water–groundwater interactions in a gravel-dominated floodplain. » Hydrological Sciences Journal 61 (4). Taylor & Francis: 741-750. doi:10.1080/02626667.2014.992790. http://dx.doi.org/10.1080/02626667.2014.992790.

Munz M., Oswald S.E. & Schmidt C. (2016) « Analysis of riverbed temperatures to determine the geometry of subsurface water flow around in-stream geomorphological structures. » Journal of Hydrology 539. Elsevier B.V.: 74-87. doi:10.1016/j.jhydrol.2016.05.012. http://dx.doi.org/10.1016/j.jhydrol.2016.05.012.

Munz M. & Schmidt C. (2017) « Estimation of vertical water fluxes from temperature time series by the inverse numerical computer program FLUX-BOT. » Hydrological Processes 31 (15): 2713-2724. doi:10.1002/hyp.11198.

Pouladi B., Linde N., Longuevergne L. & Bour O. (2021) « Individual and joint inversion of head and flux data by geostatistical hydraulic tomography. » Advances in Water Resources 154 (February). Elsevier Ltd: 103960. doi:10.1016/j.advwatres.2021.103960. https://doi.org/10.1016/j.advwatres.2021.103960.

Power G., Brown R.S. & Imhof J.G. (1999) « Groundwater and fish - Insights from northern North America. » Hydrological Processes 13 (3): 401-422. doi:10.1002/(SICI)1099-1085(19990228)13:3<401::AID-HYP746>3.0.CO;2-A.

Rakic D. & Basaric I. (2014) « Geotechnical Aspects of the Use of Geothermal Energy. » Conference Paper In 7th International Scientific Conference Science and Higher Education in Function of Sustainable Development. Uzice, Serbia.

Ren J., Cheng J., Yang J. & Zhou Y. (2018) « A review on using heat as a tool for studying groundwater–surface water interactions. » Environmental Earth Sciences 77 (22). Springer Berlin Heidelberg: 0. doi:10.1007/s12665-018-7959-4. http://dx.doi.org/10.1007/s12665-018-7959-4.

Rosenberry D.O. (2008) « A seepage meter designed for use in flowing water. » Journal of Hydrology 359 (1-2): 118-130. doi:10.1016/j.jhydrol.2008.06.029.

Rosenberry D.O., Klos P.Z. & Neal A. (2012) « In situ quantification of spatial and temporal variability of hyporheic exchange in static and mobile gravel-bed rivers. » Hydrological Processes 26 (4): 604-612. doi:10.1002/hyp.8154.

Rosenberry D.O. & LaBaugh J.W. (2008) « Field Techniques for Estimating Water Fluxes Between Surface Water and Ground Water Techniques and Methods 4 – D2. » Technical Publication Report by U.S. Geological Survey, Reston, Virginia.

Rosenberry D.O., Manuel J. López N., Webb R.M.T. & Müller S. (2020) « Variable seepage meter efficiency in high-permeability settings. » Water (Switzerland) 12 (11). doi:10.3390/w12113267.

Saltveit S.J. & Brabrand A. (2013) « Incubation, hatching and survival of eggs of Atlantic salmon (Salmo salar) in spawning redds influenced by groundwater. » Limnologica 43 (5). Elsevier GmbH.: 325-331. doi:10.1016/j.limno.2013.05.009. http://dx.doi.org/10.1016/j.limno.2013.05.009.

SIGÉOM (2022) « Surface deposits map. » système d'information géominière du Québec. Page Web, consulté le 1er juin 2020 à l'adresse https://sigeom.mines.gouv.qc.ca/signet/classes/I1108_afchCarteIntr.

Simon N., Bour O., Lavenant N., Porel G., Nauleau B., Pouladi B., Longuevergne L. & Crave A. (2021a) « Numerical and Experimental Validation of the Applicability of Active-DTS Experiments to Estimate Thermal Conductivity and Groundwater Flux in Porous Media. » Water Resources Research 57 (1): 1-27. doi:10.1029/2020WR028078.

Simon N., Bour O., Faucheux M., Lavenant N., Lay H.L., Fovet O., Thomas Z. & Longuevergne L. (2021b) « Combining passive- and active-DTS measurements to locate and quantify groundwater discharge into streams. » Hydrology and Earth System Sciences Discussions (June): 1-36. doi:10.5194/hess-2021-293.

Sophocleous M. (2002) « Interactions between groundwater and surface water: The state of the science. » Hydrogeology Journal 10 (1): 52-67. doi:10.1007/s10040-001-0170-8.

Stonestrom D.A. & Constantz J. (2003) « Heat as a tracer of water movement near streams. » Report chapter, In Heat as a Tool for Studying the Movement of Ground Water Near Streams - USGS Circular 1260, Circular 1, 1-6. Reston, Virginia: U.S. Geological Survey. http://pubs.water.usgs.gov/circ1260/.

Surfleet C. & Louen J. (2018) « The influence of hyporheic exchange on water temperatures in a headwater stream. » Water (Switzerland) 10 (11). doi:10.3390/w10111615.

Swanson T.E. & Cardenas B.M. (2011) « Ex-Stream: A MATLAB program for calculating fluid flux through sediment-water interfaces based on steady and transient temperature profiles. » Computers and Geosciences 37 (10). Elsevier: 1664-1669. doi:10.1016/j.cageo.2010.12.001. http://dx.doi.org/10.1016/j.cageo.2010.12.001.

des Tombe B.F., Bakker M., Smits F., Schaars F. & van der Made K.J. (2019) « Estimation of the Variation in Specific Discharge Over Large Depth Using Distributed Temperature Sensing (DTS) Measurements of the Heat Pulse Response. » Water Resources Research 55 (1): 811-826. doi:10.1029/2018WR024171.

Tonina D., de Barros F.P.J., Marzadri A. & Bellin A. (2016) « Does streambed heterogeneity matter for hyporheic residence time distribution in sand-bedded streams? » Advances in Water Resources 96. Elsevier Ltd: 120-126. doi:10.1016/j.advwatres.2016.07.009. http://dx.doi.org/10.1016/j.advwatres.2016.07.009.

Trimble Navigation Limited (2009) « Trimble R8 GNSS, R6 and R4 GPS Receivers User Guide. » Device manual, Trimble, Navigation Limited Inc. CA, USA. https://www.orient-mediterranee.com/IMG/pdf/R8-R6-R4-5800M3_UserGuide.pdf.

Winter T.C. (1995) « Recent advances in understanding the interaction of groundwater and surface water. » Reviews of Geophysics 33 (2 S): 985-994. doi:10.1029/95RG00115.

Winter T.C., Harvey J.W., Franke O.L. & Alley W.M. (1999) « Ground Water and Surface Water A Single Resource. » Report, U.S. Geological Survey circular : 1139. Denver, Colorado. doi:10.1088/1751-8113/44/8/085201. https://pubs.er.usgs.gov/publication/cir1139.

Zhirkov A., Permyakov P., Wen Z. & Kirillin A. (2021) « Influence of rainfall changes on the temperature regime of permafrost in central yakutia. » Land 10 (11). doi:10.3390/land10111230.

Zimmermann, A.E. & Lapointe M. (2005) « Intergranular flow velocity through salmonid redds: Sensitivity to fines infiltration from low intensity sediment transport events. » River Research and Applications 21 (8): 865-881. doi:10.1002/rra.856.

5 HYDROTHERMAL MODELING OF GROUNDWATER AND RIVER INTERACTIONS UNDER SHORT-TERM EXTREME ATMOSPHERIC EVENTS AND LONG-TERM CLIMATE CHANGE SCENARIOS

Modélisation hydrothermale des interactions entre les eaux souterraines et les rivières dans le cadre d'évènements atmosphériques extrêmes à court terme et de scénarios de changement climatique à long terme

Milad Fakhari [1,*], Jasmin Raymond [1], Richard Martel [1]

1 Institute national de la recherche scientifique, Centre Eau Terre Environnement,

Quebec City, QC G1K 9A9, Canada

* Correspondance: milad.fakhari@inrs.ca

Soumis au ***Journal of Hydrology***

Soumis le 13 novembre 2023

Numéro du manuscrit: HYDROL56220

Contribution des auteurs :

Conceptualisation, Milad Fakhari, Jasmin Raymond et Richard Martel; méthodologie, Milad Fakhari, Jasmin Raymond, Richard Martel; analyse formelle, Milad Fakhari; conservation des données, Milad Fakhari; rédaction - préparation de la version originale, Milad Fakhari; rédaction - révision et édition, Milad Fakhari, Jasmin Raymond, Richard Martel; visualisation, Milad Fakhari.

Lien entre l'article ou les articles précédents et le suivant :

Dans cet article, deux sites d'étude, un sur la rivière Sainte-Marguerite et un sur la rivière Bérard, ont été sélectionnés sur la base de l'analyse TAI effectuée dans les chapitres deux et trois. Les modèles de ces deux sites ont été construits et calibrés sur la base des données collectées et de l'analyse présentée dans l'article trois.

Abstract: Groundwater interaction with surface water in rivers can affect water quantity (availability) and temperature, consequently impacting aquatic life. Simulating flow and heat transfer with coupled aquifer-river models can help predict river water temperature during short- and long-term atmospheric events to anticipate the effect of heat waves and climate warming. The objective of this study was to quantify the role of groundwater on northern river water temperature during a heat wave and evaluating changes in groundwater flow and its interaction to rivers due to climate change. Groundwater and river temperature was monitored for the two study sites known for fishing in Quebec, Canada; the Sainte-Marguerite River found in a continental humid climate and the Berard River found in a subarctic climate. A 3D hydrothermal model at each selected study sites showed that groundwater can affect river thermal budget by more than 30% during heat waves of low-flow seasons. Additionally, 2D hydrothermal models showed that, due to predicted climate change scenarios, groundwater seepage to rivers increased for both case studies. However, this change of ground to surface water interaction rate is more significant in permafrost regions. Simulations showed that completely frozen ground near Berard River is expected to vanish by 2040 in high emission scenario and around 2070 in low emission scenario, potentially leading to an increase in groundwater flow by more than three orders of magnitude.

Résumé : L'interaction entre les eaux souterraines et les eaux de surface dans les rivières peut affecter la quantité (disponibilité) et la température de l'eau, ce qui a un impact sur la vie aquatique. La simulation de l'écoulement et du transfert de chaleur à l'aide de modèles couplés aquifère-rivière peut aider à prévoir la température de l'eau des rivières lors d'évènements atmosphériques à court et à long terme afin d'anticiper l'effet des vagues de chaleur et du réchauffement climatique. L'objectif de cette étude était de quantifier le rôle des eaux souterraines sur la température de l'eau des rivières du Nord pendant une vague de chaleur et d'évaluer les changements dans l'écoulement des eaux souterraines et leur interaction avec les rivières en

raison du changement climatique. La température des eaux souterraines et des rivières ont été enregistrées sur deux sites d'étude connus pour la pêche au Québec (Canada) : la rivière Sainte-Marguerite, située dans un climat continental humide, et la rivière Bérard, située dans un climat subarctique. Un modèle hydrothermal 3D sur chacun des sites d'étude sélectionnés a montré que les eaux souterraines peuvent affecter le bilan thermique des rivières de plus de 30 % pendant les vagues de chaleur des saisons à faible débit. En outre, les modèles hydrothermaux 2D ont montré que, en raison des scénarios de changement climatique prévus, l'infiltration des eaux souterraines dans les rivières a augmenté pour les deux études de cas. Toutefois, cette modification du taux d'interaction entre les eaux souterraines et les eaux de surface est plus importante dans les régions de pergélisol. Les simulations ont montré que le sol complètement gelé près de la rivière Berard devrait disparaitre d'ici 2040 dans un scénario à fortes émissions et aux alentours de 2070 dans un scénario à faibles émissions, ce qui pourrait entrainer une augmentation du flux des eaux souterraines de plus de trois ordres de grandeur.

5.1 Introduction

Groundwater (GW) and surface water (SW) are connected and the extent of the interconnection between GW and SW bodies depends on the climate and the geological setting (Brunke et al., 1997; Hayashi et al., 2002; Spanoudaki et al., 2009). Changes in GW quantity or quality due to climate change (i.e., changes in precipitation and recharge patterns) or human activity (GW extraction or contamination) can have a direct influence on the water quantity, quality and temperature of GW-dependent wetlands, lakes or rivers (Hancock, 2002; Saha et al., 2017; Havril et al., 2018).

In arid or semi-arid regions, GW exchange with SW is more important in terms of water quantity and river flow rates, especially in low-flow seasons (Lamontagne et al., 2005; Hassan et al., 2014; Tian et al., 2015). In other climate conditions where precipitation is higher, the effect of GW-SW interaction is noticeable on SW quality and temperature.

GW can play a role for contaminant or heat transport to SW. The GW flow velocity is slow (between 0.15 m/d to 15 m/d in sand or gravel aquifers) compared to SW velocity. Thus, contamination like heavy metals, fertilizers or pesticides from areas with mining or agricultural activities can appear in the rivers after several years, by means of GW flow even if the source of contamination has been previously removed (Goel, 2006).

The thermal regime of rivers also plays an important role in the health of aquatic ecosystems. Rivers in northern Quebec are known for the abundance of *Salmonidae* (brook/lake and sea trout, Arctic char and Atlantic salmon). Fishing is important for local communities and for revenues from sport fishing (Poesch et al., 2016). The optimal temperature range for *Salmonidae* growth varies according to species but is generally between 7 °C and 17 °C while the lethal temperature range is 25-27 °C (Jensen et al., 1989; Finstad et al., 2012; Nyanti et al., 2018). In summer, salmonids experience thermal stress in rivers as a result of higher average water temperature. This affects their growth and even threatens their survival.

Specific zones in the rivers constitute thermal refuges allowing fish to be more comfortable to grow and to survive in some extreme cases (Lorenz et al., 1989; Geist et al., 1998). One of the main sources of thermal refuges is the contribution of GW to rivers by upwelling or lateral seepage (Power et al., 1999; Saltveit et al., 2013; Fakhari et al., 2022; Fakhari et al., 2023). GW has less daily and seasonal variations compared to SW. Therefore, GW can be considered as a source of cold or warm water during summer and winter, respectively (Caissie, 2006).

The spatiotemporal variation of GW-SW interaction can significantly affect river ecosystems (Hynes, 1983; Zhang et al., 2004; Tang et al., 2015). For instance, population and distribution of fish habitats in rivers and lakes can be affected by GW exchange to rivers. GW can influence fish distribution, reproductive success, biomass and productivity, fish behavior and movements in rivers during extreme temperature conditions in warm seasons, or where rivers are affected by ice as well as in low-flow rivers (Power et al., 1999; Saltveit et al., 2013; Willms et al., 2016).

Based on recorded long-term data, the maximum daily air temperature and amplitude of heat waves are increasing. In addition, the warm days (maximum air temperature > 30 °C) and the heat waves are likely to occur more frequently in Quebec due to climate change (Khaliq et al., 2005; Fortin et al., 2017; Finstad et al., 2012). These days can be considered as an example of extreme atmospheric events that can trigger high increase in river water temperature when life of fish in the rivers can be potentially threatened. During these extreme conditions, which are more common during low-flow season (Khaliq et al., 2005), the impact of GW on river thermal budget can be noteworthy. The exposure of fish to high water temperature even for short periods can significantly reduce their productivity, and threaten their survivability (Gismervik et al., 2019).

GW-SW interaction is a complex process which depends on several controlling parameters and it plays an important role in catchment hydrology (Brunke et al., 1997; Spanoudaki et al. 2009; Evans et al., 2017). The presence of permafrost can make the process of GW-SW interaction more complex (Walvoord et al., 2012). Due to the presence of permafrost, the movement of contaminants through GW to SW can be limited. However, by the thawing of permafrost and increase in GW flow (Walvoord et al., 2007), some SW bodies that are not affected by pollution from mining or any other type of activities, can be exposed to risks in the future. Moreover, thawing of permafrost will cause release of carbon and nutrients, which can also affect the health of aquatic systems (Walvoord et al., 2007; Neilson et al., 2018). The effect of climate change and thawing permafrost on the future of river water quality and temperature is important and unclear (Neilson et al., 2018). Having a multidimensional fully coupled hydrothermal model is helpful to better understand water flow and heat transfer. In addition, it can be used to predict the temperature evolution of aquatic ecosystems considering different climate change scenarios (Cho et al., 2010; Tian et al., 2012; Havril et al., 2018; Hunt et al., 2016).

The objective of this study is to better understand the impact of GW seepage into northern rivers in two different climatic contexts with and without permafrost and facing an evolving climate. Increasing precipitation and temperature due to climate change can augment GW fluxes to river systems in Quebec but how this can affect the river water temperature was unclear and needed

more work. Thus, we used a fully couple flow and heat transfer model to quantify the role of GW on neutralizing river water temperature increase caused by atmospheric phenomena such as heat waves. We additionally evaluate the future of GW systems considering climate change scenarios and its effects on river water temperature.

5.2 Study site

The two rivers selected for this study are the Sainte-Marguerite River located about 12 km from the Sacre-Coeur municipality in the Côte-Nord region of the Quebec Province, and the Berard River that discharges into the Ungava Bay in the northern village of Tasiujaq in Nunavik, northern Quebec. The Sainte-Marguerite River is located in the south of Quebec, has no surrounding permafrost and is in a continental cold and humid climate. The Berard River is located in the north of the province, in a zone at the boundary of continuous and discontinuous permafrost (Allard et al., 2020) and in a continental subpolar climate. The depth of the active layer (mean annual temperature below 0 °C) near Berard River varies between 2 m and 10 m from the ground surface (Smith et al., 2002; Lévesque et al., 1990; Allard et al., 2020). The depth of the permafrost base (mean annual ground temperature above 0 °C) is expected to be around 200 m or 280 m from the surface according to the extrapolation of recorded ground temperature profiles (Gray et al., 1979).

On each river, a study site was selected for instrumentation and further analysis, where higher GW seepage was expected due to topography or geology. The study site on the Sainte-Marguerite River is located on the main branch, 36 km upstream from the river mouth. The study site on the Berard River is located 5.5 km upstream from the river mouth. Based on 1971-2000 climate data for Sacré-Coeur, the annual average temperature and the total annual precipitation were 2.6 °C and 1002 mm, while the annual average temperature was -5.9 °C and the average annual precipitation was 484 mm for Tasiujaq (ClimateData.ca, 2021).

In the studied rivers, salmonids such as arctic char, brook and sea trout, and Atlantic salmon have been identified (Mookerji et al., 2004; Mainguy et al., 2019). These fish species are temperature dependent, and fishing is popular in these rivers such that studies regarding water temperature is imperative.

Geology near the study site consists of bedrock outcropping on both sides of the valley that is partly filled with quaternary deposits in the central depression. At Sainte-Marguerite River site, the bedrock is made of Mesoproterozoic igneous rocks of the Grenville Province, overlaid by quaternary sediments consisting of glacial till with a maximum thickness of 30 m and alluvial sand,

sandy silt and gravel with 1-30 m thickness (SIGÉOM, 2022). At Berard River site, the bedrock is made of Paleoproterozoic sedimentary rocks of the Churchill Province, overlaid by quaternary sediments consisting of glacial till with thickness of 1-40 m and alluvial sand, sandy silt and gravel with 15 m maximum thickness (SIGÉOM, 2022; Allard et al., 2020).

The topographic elevation difference between the riverbed and top of close-by hills is about 200 m for Sainte-Marguerite River cross-section and about 30 m for Berard River cross-section. Both rivers have almost symmetric cross-section at the selected site, therefore half of cross-sections was used for modeling and visualization of geological units in Figure 5.1.

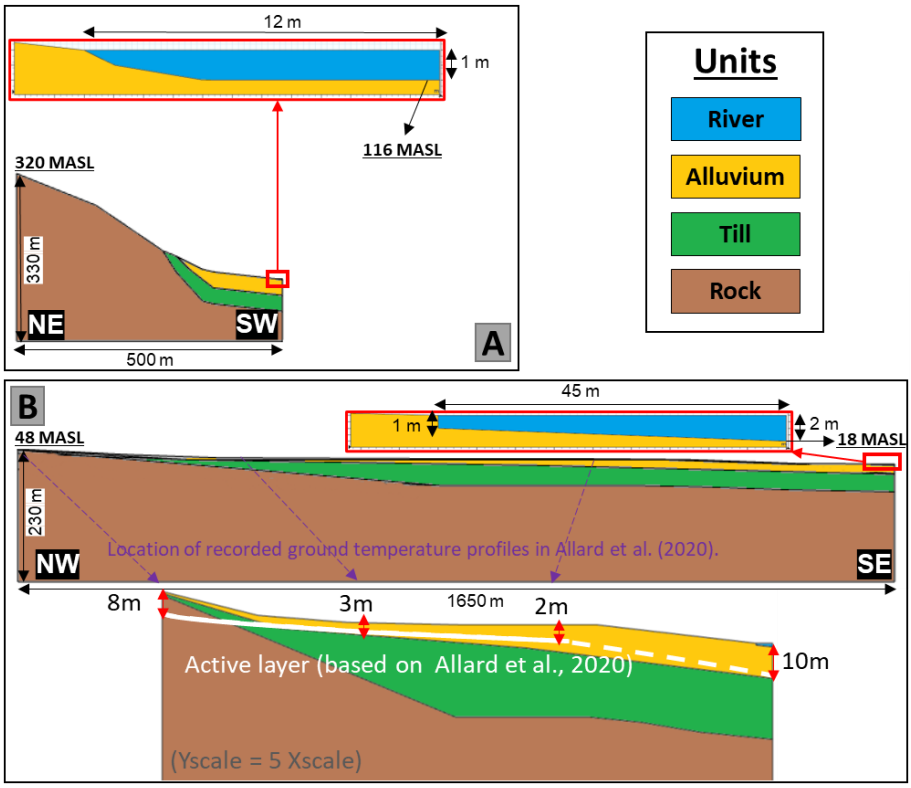

Figure 5.1 **Simplified cross-section of study sites showing geological units of Sainte-Marguerite River (A) and Berard River (B).**

5.3 Methodology

Simulating variation of water temperature in rivers affected by GW seepage requires a combined GW-SW simulation of flow and heat transfer. Combined GW and heat transfer models are well established and have been extensively applied to hydrogeological (Ingebritsen et al., 1998) and geothermal (Raymond et al., 2014) studies and recently for the simulation of permafrost evolution (Kurylyk et al., 2016). Combined GW-SW models have been used for assessing the quantity of

available water resources (Rathfelder, 2016), water quality (Wayland et al., 2002), and climate change effects on the future of water resources (Havril et al., 2018).

In a combined flow and heat transfer model, water and energy balance equations of the system is solved. Complex coupling of all equations in the system was carried out using the COMSOL Multiphysics Software, a finite element model suitable for varieties of engineering fields (COMSOL, 2023).

Measurement of riverbed seepage rate, river discharge, water level and temperature provide important data to monitor and measure GW-SW interaction and to calibrate and validate models. Shallow piezometers (maximum depth of 3.7 m from the ground surface) have been installed on the riverbank and below the riverbed to monitor GW level and temperature at each site. River water level and temperature have also been monitored at the same period. Temperature sensors have been installed in the ground at different depths from zero to two meters below the surface to have detailed temperature profiles. All loggers have collected data with 15-minute intervals. Water-level sensors in piezometers recorded data for a period of one year and temperature sensors recorded data for two years starting in July 2019 (Figure 5.2). Moreover, seepage meters have been installed on the riverbed at different locations to measure GW seepage rate to the river at the selected reach. The river flow rate was also measured with an acoustic doppler current profiling (ADCP) device at selected cross-sections of the river.

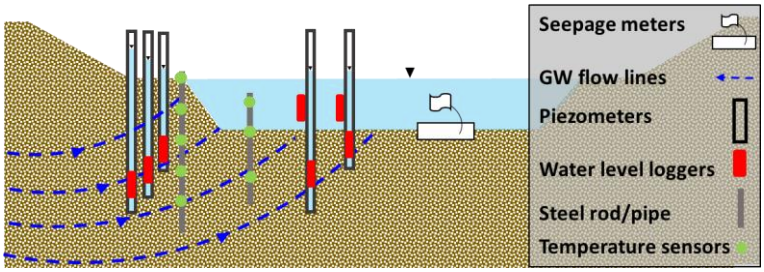

Figure 5.2 **Schematic cross-section view of the river showing location of installed instruments.**

5.3.1 3D heat wave simulations

Studying heat transfer in a fully combined GW-SW flow system with realistic simulations of river flow is complex. In a coupled GW-SW model of a river, simulating free SW flow requires 3D simulations. 3D models were used to reproduce extreme short-term atmospheric event (heat wave), based on recorded data of the study sites. The discharge at upstream and downstream cross-sections is a key parameter for such 3D simulations. Selected rivers of this study are not gauged. River flow measurements were carried out only in warm season (in July for Sainte-

Marguerite River and in August for Berard River) when the water level was low and the rivers were accessible. Rainfall runoff and historical river flow of the selected rivers were not available. The river flow during short-term simulation was consequently considered constant.

The system was divided in two main zones of porous media flow and free flow (Figure 5.3).

In the free flow domain (river), a low Reynolds number (Re ≤ 2300) was assumed and the Stokes equation for a single-phase flow was chosen as governing equation. As a second simplification, the porous media zone (aquifer) was considered fully saturated, and Darcy's law was used in this zone. In this hydrothermal model, riverbed is an internal model boundary and the exchanges of water (seepage or infiltration) and heat due to convection and conduction is simulated by the model. Latent heat and phase change are not considered in short-term simulations, since river ice formation and ice break flow are not expected to occur during simulated heat wave (i.e., warm season) and permafrost condition was presumed unchanged during short simulation periods.

Porous media zones can be divided into subdomain based on the three present geological units (Figure 5.1). The Sainte-Marguerite River model has a total thickness of around 300 m on the left side reaching the river valley top and a thickness of 100 m on the right side below the river center line. Berard River has a thickness of 250 m on the highlands and 220 m thickness below the river center line. The permafrost is present for the Berard River case study. Drawing from prior research conducted near Tasiujaq (e.g., Smith et al., 2002; Lévesque et al., 1990; Allard et al., 2020; Gray et al., 1979), we anticipate a ground temperature profile resembling the depiction provided in Figure 5.4. Based on this expected ground temperature profile, the average yearly temperature is below 0 °C between around 10 m to 230 m of depth, which corresponds to the depth of permafrost. Nevertheless, owing to the influence of groundwater salinity in the vicinity of Tasiujaq, the freezing point of the gathered soil samples was determined to be -2 °C (Allard et al., 2020). Therefore, based on expected ground temperature profile (Figure 5.4), the frozen porous media (where temperature is below -2 °C) is located between 15 m and 40 m depth. Thus, this layer was considered as frozen in this study. Based on GPR measurements near Tasiujaq, an ice-rich layer is present everywhere in the region even in the areas close to the bay (Allard et al., 2020). The presence of an ice-rich layer at a depth around 15 m and the location of Tasiujaq at the boundary of continuous and discontinuous permafrost zones are arguments to consider a continuous permafrost layer of about 25 m thickness for modeling of Berard River case study.

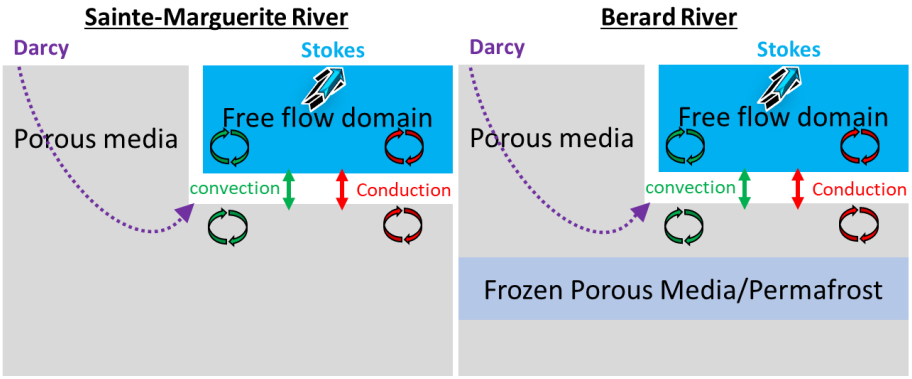

Figure 5.3 **Schematization of flow and heat transfer system for short-term simulations of 3D models.**

Two 3D models for each study site were developed to evaluate the effect of GW inflow to the river. The first model was a free flow model only (M:R), simulating the river flow and water temperature changes caused by air temperature increase during the heat wave. The second model was a combination of both free flow in the river and GW flow in porous media (M:R+GW), simulating the same event. The difference between the two models was used to quantify the effects of GW on river water temperature mitigation.

3D models simulate an actual heat wave recorded at both study sites. The details of the simulated events, which include important model inputs over the simulation period, like ambient (air) temperature, river flow, GW and river water temperature are explained in the next section.

3D models were built by laterally extending one cross-section over a distance and making a 3D geometry with the Extrude function in COMSOL geometry (Figure 5.5). A 200 m river reach was modeled for both rivers of this study. The topography of the river valley does not change significantly over the selected 200 m reach. Thus, extending the cross-sections shown in Figure 5.1 to make 3D models was an acceptable simplification.

Hydraulic and thermal properties of materials (Table 5.1 and Table 5.2) were initially set based on available literatures (Freeze et al., 1979; Chesnaux, et al., 2011a; Chesnaux et al., 2011b; Comeau et al., 2017; Allard et al., 2020) and then further refined during calibration of models to observed temperatures and riverbed seepage rates from field instrumentation (Fakhari et al., 2023; Fakhari et al., 2024). Parameters of water were assigned to the model free flow domain. Parameters of the porous media domain were based on frozen (subscripts f) and unfrozen (subscript uf) conditions. Only unfrozen conditions (k_{uf}, λ_{uf}, c_{uf}) were considered for geological units of Sainte-Marguerite River since permafrost is not present. Frozen conditions (k_f, λ_f, c_f) were assigned to permafrost domain and unfrozen conditions (k_{uf}, λ_{uf}, c_{uf}) were chosen for the rest of porous media domain in Berard River models.

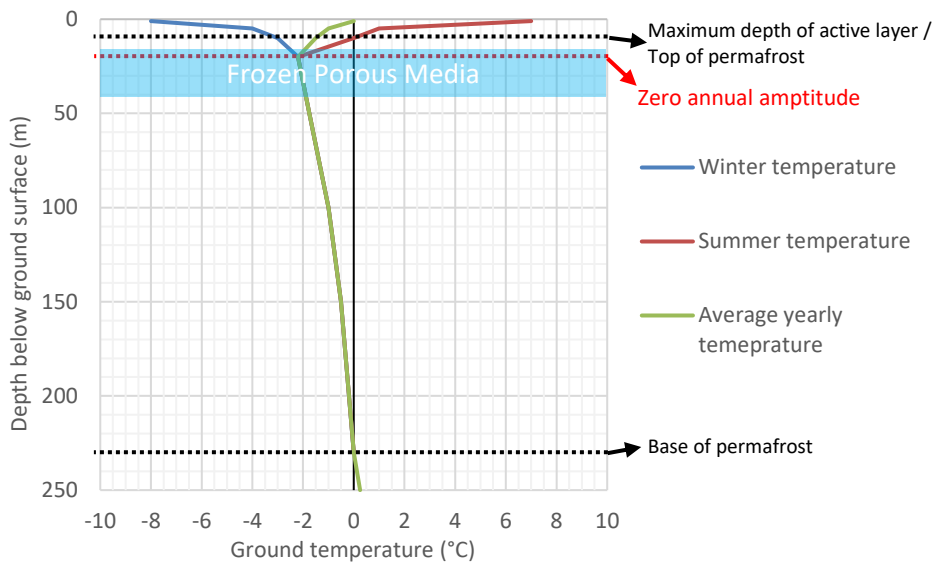

Figure 5.4 **Expected ground temperature profile of Berard River (based on Smith et al., 2002; Lévesque et al., 1990; Allard et al., 2020; Gray et al., 1979).**

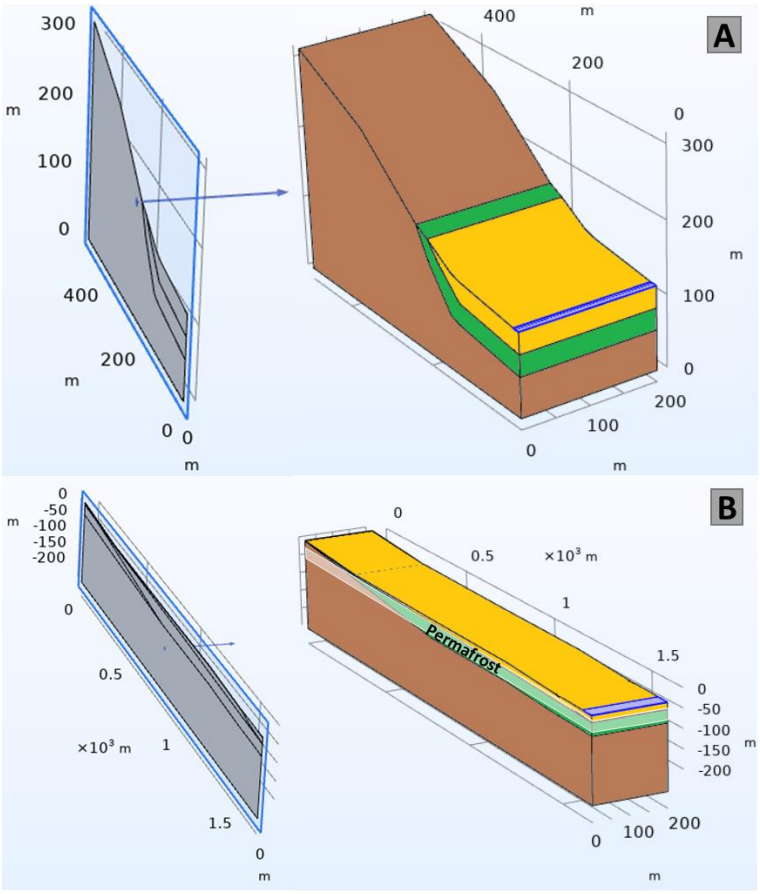

Figure 5.5 **3D model geometry of Sainte-Marguerite River (A) and Berard River (B) study site.**

Note. Color codes for geological units the same as Figure 5.1.

Table 5.1 Hydraulic properties of geological units.

Geological unit	k_{uf} (m^2)*	k_f (m^2)*	Porosity (-)
Alluvial	1×10^{-11}	1×10^{-14}	0.25
Till	1×10^{-14}	1×10^{-17}	0.35
Bedrock	1×10^{-17}	1×10^{-20}	0.05

*An anisotropy factor of 0.1 for vertical hydraulic conductivity/ permeability has been considered (k_v=0.1k_h).

In the frozen condition, permeability should be set to an arbitrary small minimum value (Hu et al., 2018). However, since the model convergence was difficult if permeability of two adjacent cells were more than three orders of magnitude different, the arbitrary small minimum permeability value for each unit in frozen condition was considered 1000 times lower than in the unfrozen condition.

Table 5.2 Thermal properties of geological units' solids.

Geological unit	Thermal conductivity (W m^{-1} K^{-1})	Heat capacity (J kg^{-1} K^{-1})	Density (kg m^{-3})
Alluvial	0.5	300	1500
Till	1	500	1300
Bedrock	2	1000	2500
Water	0.6	4200	1000
Ice	2.14	2100	920

Thermal properties of solids for the three porous media units in Table 5.2 was defined according to laboratory measurements made in dry condition. The solid particles properties were combined in the model to water properties in unfrozen condition or ice in frozen condition (based on Dagher et al., 2014), using volumetrically weighted arithmetical mean method (Eq. 5.1-5.4).

$$\lambda_{\mathrm{uf}} = \varepsilon(\lambda_{\mathrm{w}}) + (1-\varepsilon)\lambda_{\mathrm{s}} \quad (5.1)$$

$$c_{\mathrm{uf}} = \varepsilon(\rho_{\mathrm{w}} c_{\mathrm{w}}) + (1-\varepsilon)\rho_{\mathrm{s}} c_{\mathrm{s}} \quad (5.2)$$

$$\lambda_{\mathrm{f}} = \varepsilon(\lambda_{\mathrm{i}}) + (1-\varepsilon)\lambda_{\mathrm{s}} \quad (5.3)$$

$$c_{\mathrm{f}} = \varepsilon(\rho_{\mathrm{i}} c_{\mathrm{i}}) + (1-\varepsilon)\rho_{\mathrm{s}} c_{\mathrm{s}} \quad (5.4)$$

where, c is the specific heat capacity ($L^2\ t^{-2}\ T^{-1}$); λ is the thermal conductivity ($M\ L\ t^{-3}\ T^{-1}$); ε is the porosity (-); ρ is density ($M\ L^{-3}$). The subscripts i, w, and s denote ice, water, and solid particles, respectively.

The models were made for half of the river cross-section and a symmetry boundary was considered as the right boundary of the model (on the center line of the river). This also helped with calculation time of the models. The hills on the left side of the rivers were considered as the left boundary of the models and has a no flow boundary. The rock unit below the sedimentary deposits and extending to the hills on the left side of the model was to reach no flow boundaries. It would have been difficult to set closer boundaries due to the lack of field information such as measured hydraulic head that would allow to set boundaries based on equipotential lines. A top inflow boundary condition simulates recharge from rainfall. The bottom face was considered a no flow boundary (Figure 5.6, left). The front (upstream) and back (downstream) boundaries were set as no flow in porous media domain. Inflow and outflow were applied to the front (upstream) and back (downstream) boundaries for the free flow domain respectively, simulating the river discharge. The top boundary condition of the free flow domain was set to atmospheric pressure.

The boundary conditions for the heat transfer simulation assume heat insulation for all model boundaries except the top and bottom for both domains (Figure 5.6, right). The temperature dependent heat flux boundary condition was applied at the top for the heat transfer simulations. Inward heat flux is calculated by setting the ambient (air) temperature, the albedo of the material and the initial temperature of the surface. 0.1 and 0.15 were considered as water and soil albedo factor respectively in this study (based on Ponce et al., 1997). The bottom face of the model was set to inward heat flux based on the geothermal heat flux at the study area. The Sainte-Marguerite River is located in Grenville Province of the Canadian Shield with a heat flux of 0.033 W m^{-2} and the Berard River is located at Churchill Province with 0.034 W m^{-2} heat flux (Comeau et al., 2017).

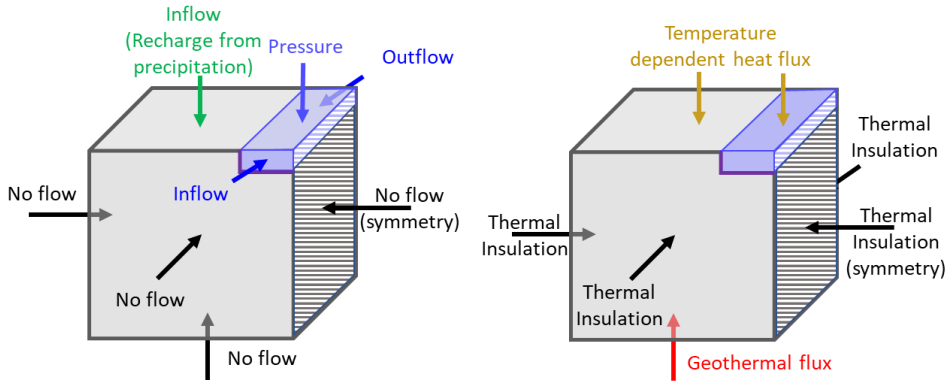

Figure 5.6 Boundary conditions of the flow (left) and heat transfer (right) models.

Steady state flow simulations with velocity and pressure of zero as starting values were made to determine initial flow condition of time-dependent models. The GW flow to the river in steady state model was simulated by applying an average yearly precipitation as a top model boundary. However, for time-dependent models, no precipitation was applied to the model, therefore the GW flow to the river was almost constant and equal to initial condition.

Recorded river and GW temperature with installed temperature sensors were used to define initial heat transfer conditions at the start of simulations (Figure 5.9 and Figure 5.10) for both free flow and porous media domains (Figure 5.7).

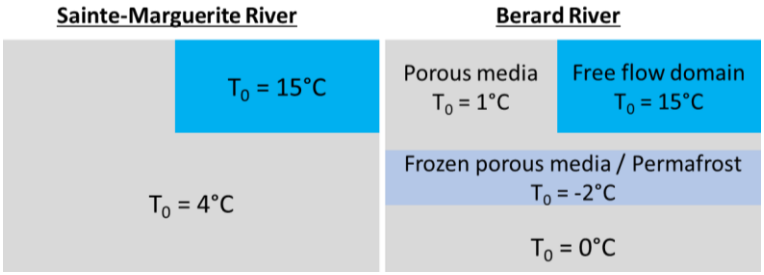

Figure 5.7 Initial condition for heat transfer simulation.

The mesh used in 3D models is made of tetrahedral elements with variable dimensions between 2.5 cm (mostly where two geological units meet) and 25 m. Based on the size of the studied river reach, the Sainte-Marguerite River models has 81,322 elements and the Berard River models has 852,808 elements (Figure 5.8). Maximum element size of 100 m, 75 m, 50 m, 25 m and 10 m were tested in the model for mesh generation. The model converged with all considered cell sizes. Calculated average Darcy flow and temperature in the entire model domains and at the riverbed with all considered cell sizes had less than 1 % difference which shows mesh independency of the models. However, cells larger than 25 m did not show smooth results indicating large

difference between two adjacent cells. Since unsmooth simulated ground temperature does not show evolution of permafrost well, maximum cell size of 25 m was selected.

The models of heat waves simulate 10 days of river water temperature. A daily time step was used since the maximum daily temperature is the main parameter of interest. Application of tested sub-daily time steps such as 12 hours and six hours did not affect the results.

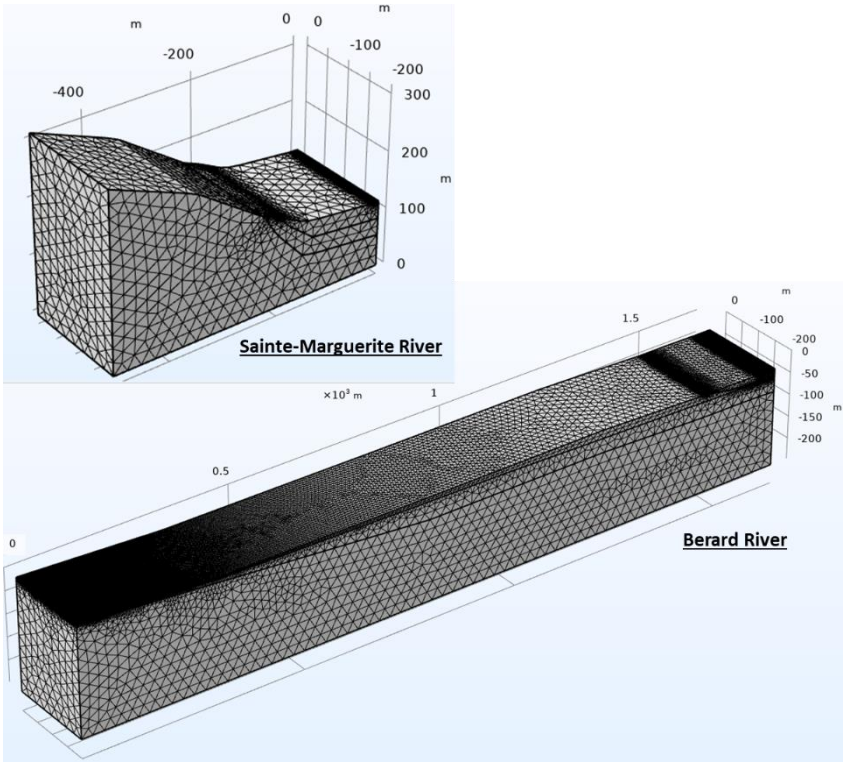

Figure 5.8 Mesh of 3D models.

5.3.1.1 Simulated heat waves with 3D models

According to Sainte-Marguerite River temperature monitoring accomplished during July 2019 to July 2020, the average daily air temperature increase at the study site (difference between maximum and minimum hourly values in one day) was 11.7 °C while the average daily river water temperature increase was 1.5 °C. During the monitored period at this study site, 13 days with air temperature exceeding 30 °C were recorded. During these 13 days, both the daily air and river water temperature increases were higher than calculated average daily temperature increase values based on our one-year data set. Thus, these days can be considered as extreme atmospheric events. The extreme atmospheric event with the longest duration and the highest magnitude was recorded between 17th and 20th of June 2020 (Figure 5.9). Average daily air

temperature increase was 23.3 °C and river water temperature increase was 5.6 °C during this event. This event has been selected for simulation with the numerical models of Sainte-Marguerite River study site. However, to better visualizing the process of temperature increase and decrease before and after the event, three days before and three days after this four-day event were also simulated.

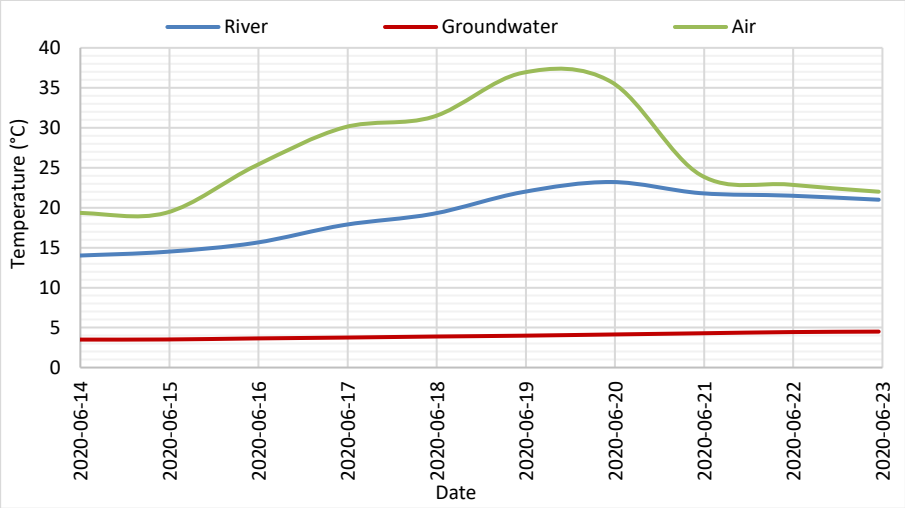

Figure 5.9 **Daily maximum temperature recorded during the selected extreme atmospheric event in Sainte-Marguerite River.**

Based on the temperature monitoring during August 2019 to October 2020 of Berard River study area, the average daily air temperature increase during this period at Berard River study site was 7.6 °C while the average daily river water temperature increase was 1.1 °C. During the monitoring period, only one day with maximum hourly temperature above 30 °C was recorded on the 16th of August 2020. Between 13th and 18th of August 2020, the daily air and river water temperature increases were above the average values. Therefore, 13th to 18th of August 2020 was considered as an extreme atmospheric event (Figure 5.10). Two days before and after this event was simulated for better visualization of this case.

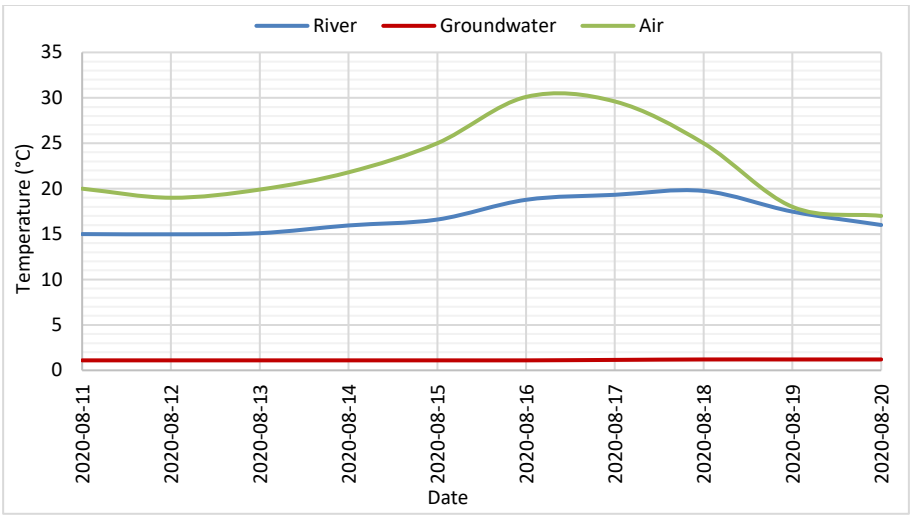

Figure 5.10 **Daily maximum temperature recorded during the selected extreme atmospheric event in Berard River.**

5.3.2 2D climate change simulations

Considering the same assumption of constant river flow for long-term simulations did not seem appropriate since river flow can change with seasons and evolve due to climate change. Additionally, complex simulation of river ice formation and ice break flow was beyond the scope of this study. Moreover, running 3D models for long-term simulations is time consuming. Thus, instead of the 3D models, 2D models were used to simulate GW discharge into rivers under long-term climate change scenarios.

Only a porous media domain was considered in the 2D models, and riverbed temperature and seepage rate were the main output of our model instead of average river temperature. Thermal equilibrium is considered in heat transfer simulations. Thus, riverbed temperature was considered equal to river water temperature at its deepest. Effects of GW on river water temperature regarding fish habitat was of interest. During extreme events, fish is more likely to shelter in zones affected by GW seepage which is close to the riverbed. Moreover, long-term simulations consider average yearly values as input and river temperature at its deepest part (i.e., riverbed) is more stable during the year. Therefore, considering one porous media domain for models and focusing on riverbed temperature instead of average river water temperature can be justified.

Long-term simulations with 2D models evaluate changes in GW system and resulting riverbed GW seepage rate and temperature based on climate change scenarios. Flow in porous media is solved by Darcy's Law. Heat transfer in the Sainte-Marguerite system considers convection and conduction while latent heat and phase change is not considered since permafrost is not present

and average yearly temperature of the area is always above 0 °C according to historical weather data (ClimateData.ca, 2021). However, permafrost is present around the Berard River due to recorded historical sub-zero atmospheric temperature (ClimateData.ca, 2021) and its thaw due to climate change is of interest. Thus, latent heat and phase change were considered in the simulations of the Berard River case study (Figure 5.11).

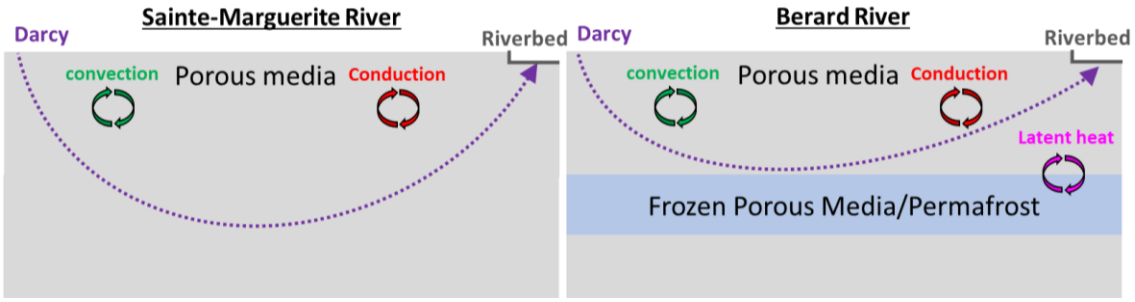

Figure 5.11 Schematization of flow and heat transfer system for long-term simulations with 2D models.

Assigned properties are similar to 3D models for unfrozen condition (k_{uf}, λ_{uf}, c_{uf}) for Sainte-Marguerite River models. However, the hydraulic and thermal properties were introduced as variable temperature dependent values for the Berard River case. -2 °C was set as the phase change temperature and the limit where parameters will change between respective frozen/ice (T < -4 °C) to unfrozen/water (T > 0 °C) condition, since the permafrost in Tasiujaq thaws at -2 °C due to its salinity (Allard et al., 2020). The parameter ω was introduced to show the ratio of unfrozen/water to frozen/ice phases. During the phase change (-4 °C ≤ T ≤ 0 °C), ω varies between zero and one depending on temperature (Eq. 5.5 and Figure 5.12).

$$\omega = \begin{cases} 1 & \text{for} \quad T > 0 \\ 0.25 \times T + 1 & \text{for} \quad -4 \leq T \leq 0 \\ 0 & \text{for} \quad T < -4 \end{cases} \tag{5.5}$$

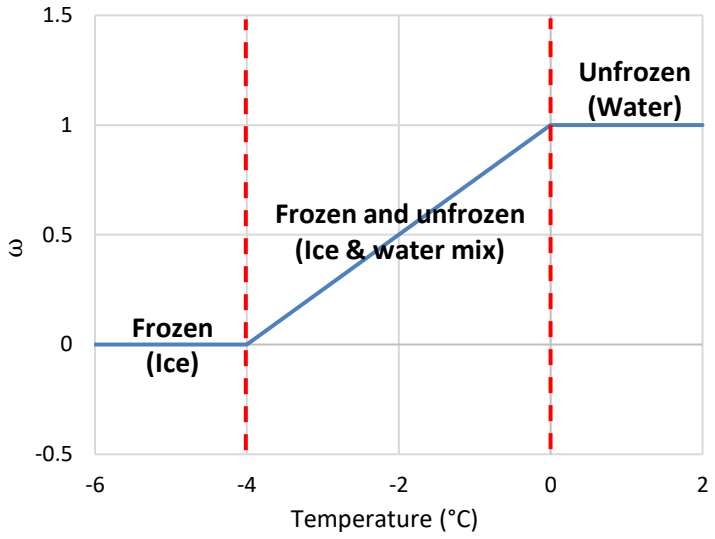

Figure 5.12 Introduced ω factor describing phase change.

During the phase change, hydraulic conductivity of units was calculated with a weighted average (based on Dagher et al., 2014) considering the ω factor (Eq. 5.6).

$$k_{\mathrm{eq}} = \omega k_{\mathrm{uf}} + (1-\omega)k_{\mathrm{f}} \tag{5.6}$$

Thermal conductivity and heat capacity in the model were calculated with a volumetrically weighted arithmetical mean of the parameters (based on Dagher et al., 2014) for solids, water, and ice depending on the ω factor (Eq. 5.7 & 5.8).

$$c_{\mathrm{eq}} = \varepsilon(\omega\rho_{\mathrm{w}}c_{\mathrm{w}} + (1-\omega)\rho_{\mathrm{i}}c_{\mathrm{i}}) + (1-\varepsilon)\rho_{\mathrm{s}}c_{\mathrm{s}} \tag{5.7}$$

$$\lambda_{\mathrm{eq}} = \varepsilon(\omega\lambda_{\mathrm{w}} + (1-\omega)\lambda_{\mathrm{i}}) + (1-\varepsilon)\lambda_{\mathrm{s}} \tag{5.8}$$

The subscript eq denotes that the physical variables are calculated by using the volumetrically weighted arithmetical mean method considering the temperature dependent ω factor.

2D models simulate increase in average yearly air temperature and total yearly precipitation based on two modeled climate change scenarios of the study sites. Details of these scenarios are presented in the following section.

The 2D models' geometry are the same as the study sites topography and stratigraphy shown in Figure 5.1.

Sides and bottom faces of the flow model are no flow boundary conditions. At the top face, an infiltration rate was assigned on the ground surface and the riverbed was set to the pervious layer boundary condition, which describes a flux through a layer connected to an external fluid source at different pressures (Figure 5.13, left).

Sides and bottom faces of the heat transfer model are thermal isolation boundary conditions. At the top face, temperature-dependent heat flux was assigned to the ground surface. The riverbed was set to an outflow boundary condition, which states that the only heat transfer occurring across the boundary is by convection. This boundary condition ensures no direct effect of air temperature on the riverbed and constant GW seepage at its calculated temperature determined by the physical processes simulated in the model (Figure 5.13, right).

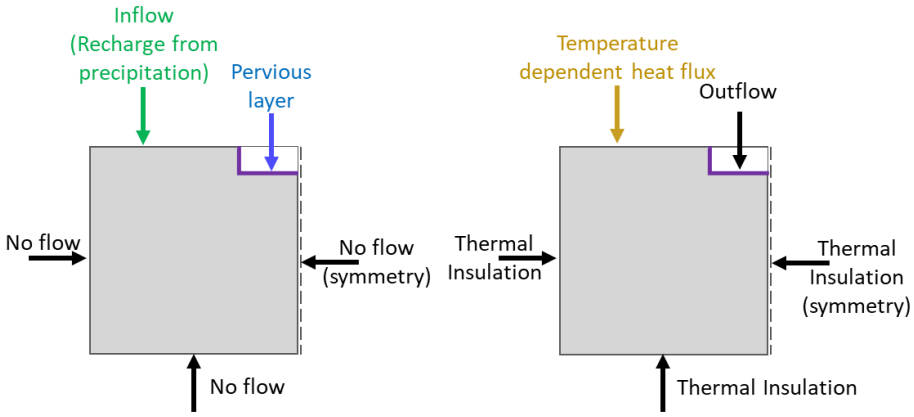

Figure 5.13 Boundary conditions of the flow (left) and heat transfer (right) models.

Initial condition for flow was zero pressure and velocity. Initial temperature for heat transfer simulations was set to 2 °C for the entire domain of Sainte-Marguerite model. A ground temperature profile (Figure 5.4) representative of average yearly temperature based on available sources (Smith et al., 2002; Lévesque et al., 1990; Allard et al., 2020) was applied to the model of the Berard River and this temperature profile defined the initial location of frozen ground and permafrost in the system.

Mesh for 2D models is made of triangular elements minimum and maximum dimensions of 2.5 cm and 25 m respectively. This resulted in 585 elements for Sainte-Marguerite River and 5,745 elements for Berard River (Figure 5.14). Similar to 3D models, other mesh sizes were tested, and models were shown to be mesh independent.

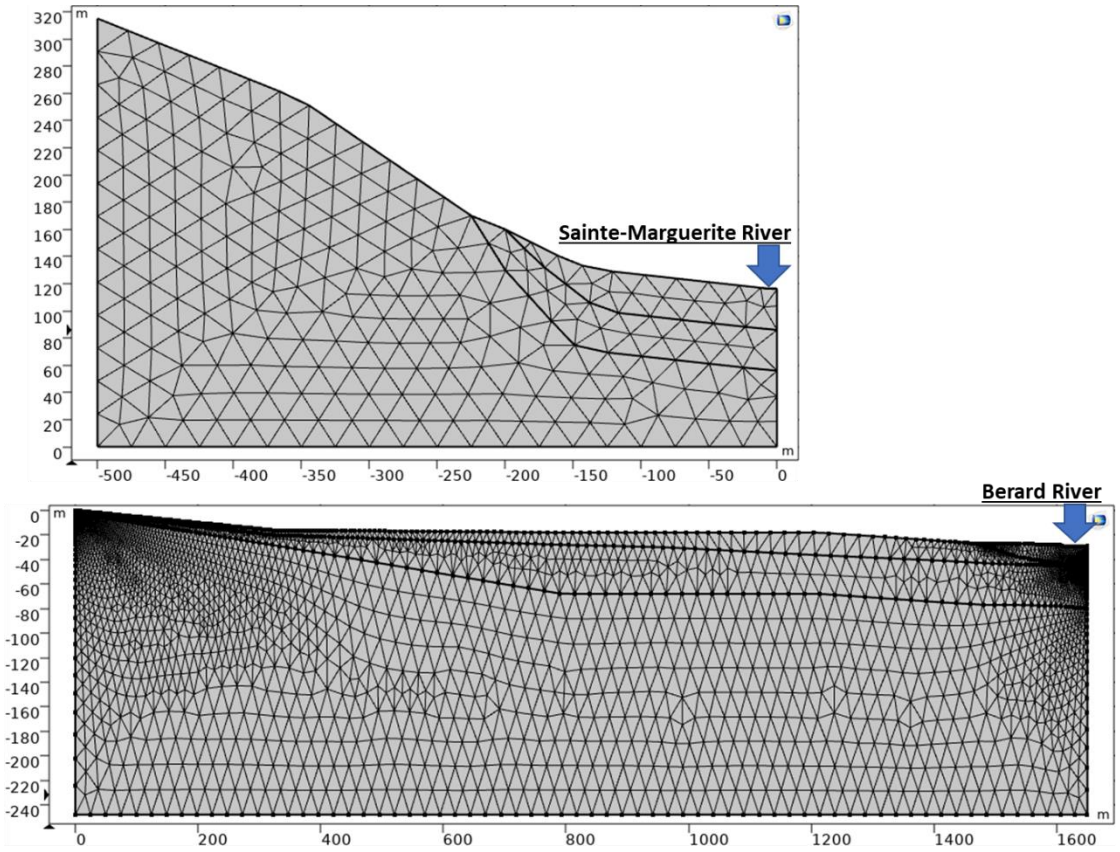

Figure 5.14 Mesh of 2D models.

A yearly time step has been considered since yearly temperature increase and precipitation from climate models were used as input data for climate change simulations. Five- and ten-years time steps were also tested and showed similar results with slightly better calculation time. The yearly changes were of interest and using larger time steps than one year and recording the outputs on yearly basis leads to interpolated results as model output. Therefore, the time step in climate change simulations were set to one year.

5.3.2.1 Simulated climate change scenarios with 2D models

The long-term climate scenarios in this study were selected based on anticipated increased mean annual air temperature and precipitation from Canada's Coupled Model Intercomparison Project Phase 6 (CMIP6) climate models from *Climatedata.ca* (ClimateData.ca, 2021). Climate models, in this source, consider three different Representative Concentration Pathways (RCPs) to provide plausible future scenarios of human emissions patterns. The scenarios are: RCP8.5 or high global emission scenario representative or situation with no measures to limit (mitigate) climate change,

RCP4.5 or medium global emission scenario that includes some mitigation actions, and RCP2.6 or low emission global scenario which requires strong mitigation actions.

Based on these scenarios increase in mean annual air temperature and total yearly precipitation for the two selected study rivers are presented in Figure 5.15 and Figure 5.16.

The average annual temperature and total annual precipitation is almost constant from 1950 to 1990 (almost horizontal linear fitted trend line), while from 1990 onward, a positive increase in annual mean temperature and total precipitation can be identified for both study sites. Climate change scenarios RCP8.5 and RCP 2.5 have been selected for comparison. However, to simplify model inputs, instead of simulated air temperature and precipitation from climate models (Figure 5.15 and Figure 5.16), an extracted linear increase of temperature and precipitation was used as input in the models. The linear increase rate of air temperature and precipitation for Sainte-Marguerite and Berard Rivers based on the two selected climate scenarios are shown in Table 5.3. These estimated trends were used in the 2D models to simulate changes in GW flow to the river and its temperature for the period of 2020 to 2100.

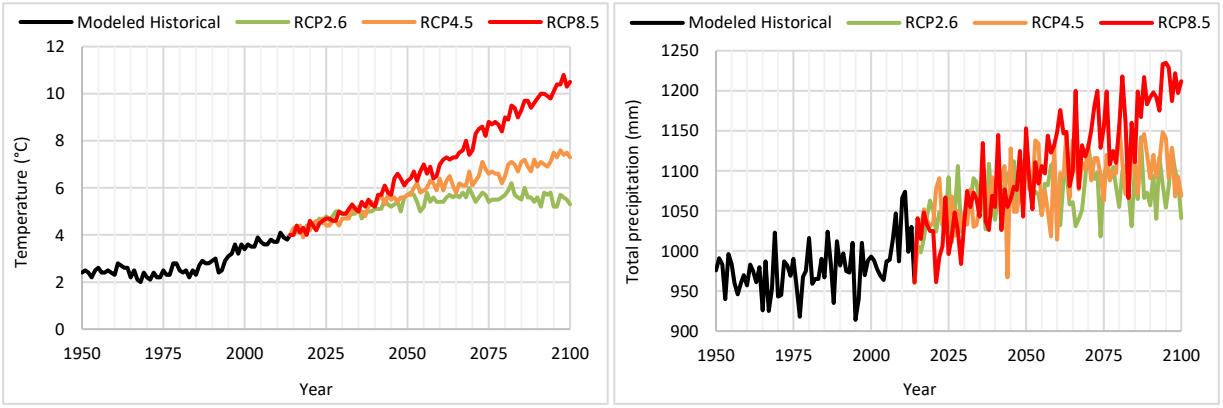

Figure 5.15 **Predicted Sainte-Marguerite River (Sacre-Coeur) mean annual temperature (left) and total precipitation (right) based on low, medium, and high carbon emission scenarios (from ClimateData.ca, 2021).**

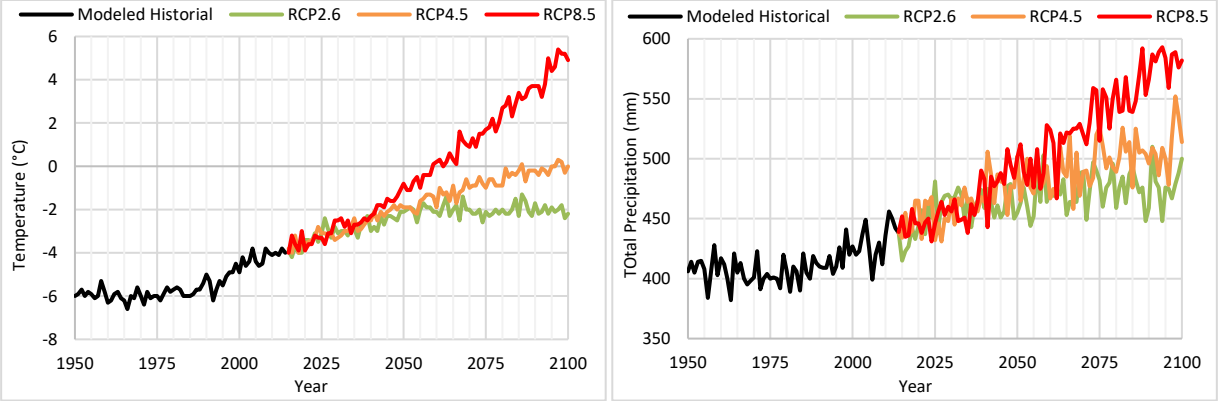

Figure 5.16 **Predicted Berard River (Tasiujaq) mean annual temperature (left) and total precipitation (right) based on low, medium, and high carbon emission scenarios (from ClimateData.ca, 2021).**

Table 5.3 **Annual air temperature and total precipitation increase rate based on low and high carbon emission climate scenarios for the selected rivers.**

	RCP2.6		**RCP8.5**	
River	**Air temperature increase (°C/yr)**	**Total precipitation increase (mm/yr)**	**Air temperature increase (°C/yr)**	**Total precipitation increase (mm/yr)**
Sainte-Marguerite	0.02	1.00	0.07	2.20
Berard	0.03	0.60	0.09	1.60

5.4 Results

5.4.1 Sensitivity analysis and calibration

Sensitivity analysis on input parameters was carried out on 3D and 2D models of both study sites. Here sensitivity analysis with ± 25 % change in parameters is reported as an example of more detailed sensitivity analysis carried out through the work. For example, at the early stages of the work different values for thickness of geological units and hydraulic conductivity from different sources was used with the models and those values were changed by more than one or two orders of magnitude to help select the values and construct the models properly. At each step of sensitivity analysis, only one parameter was changed at a time by either -25 % or +25 % and the

percentage of change in simulated riverbed temperature and seepage rate was assessed. Results revealed that models are most sensitive to hydraulic properties of alluvium unit. Simulated riverbed seepage rate was most sensitive to permeability values, specifically the permeability of alluvium unit since it has the highest permeability and controls the GW and river interaction. Riverbed seepage rate in models with permafrost unit was also sensitive to heat capacity of unit containing the frozen ground. Heat capacity showed to be the controlling factor in timing of permafrost thaw and increase of GW flow due to change of permeability value from frozen condition to unfrozen condition. Simulated riverbed temperature was sensitive to changes in permeability, heat capacity and thermal conductivity of units in this order. While permeability and thermal conductivity had direct correlation to simulated riverbed temperature, heat capacity showed reverse effect. Figure 5.17 shows the results of sensitivity analysis on 2D model of Berard River which showed the highest response to change of model inputs.

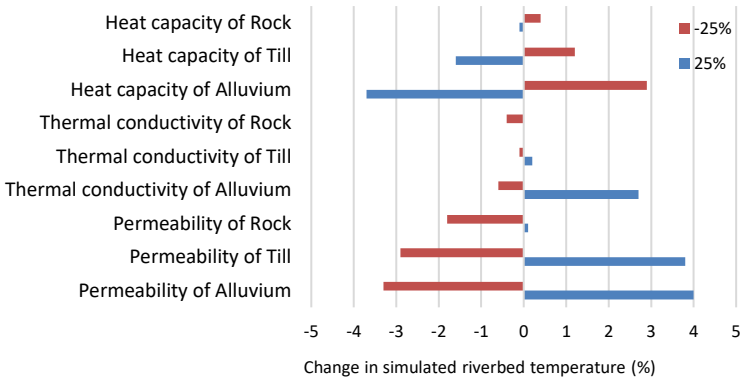

Figure 5.17 **Example of sensitivity analysis results showing effect of parameters on simulated riverbed temperature of Berard River 2D model.**

Calibration of hydraulic and thermal properties was carried out by comparing simulated values to the recorded pressure and temperature of the river and GW adjacent to the river with installed level loggers and measured riverbed GW seepage rate with seepage meters (Fakhari et al., 2024). During the 3D short-term simulations, the GW flow system was considered constant and average GW head from loggers was compared to the simulated head at the same depth in the model. Similarly, for 2D long-term simulations, recorded average yearly GW head close to the river was compared to simulated head by the model at the early time of simulations in 2020. After calibration, comparison between observed and simulated GW pressure head showed less than 10 % for both studied cases for 2D and 3D models. The seepage rate of the riverbed was measured during the warm season and the average measured seepage rate was used for calibration of 3D short-term simulations only. The difference in simulated seepage rate of riverbed

with average measured values by seepage meters was about 15 % after calibrations. Another calibration factor was comparison of GW and river temperature to the recorded data. The simulated river temperature by 3D models, including the GW flow (M:R+GW), had less than 5 % difference to recorded values (Figure 5.18). Simulated ground temperature close to the river at the early simulation time (year 2020) by 2D models showed less than 5 % difference to recorded average yearly ground temperature at the study sites by installed shallow temperature sensors.

5.4.2 Short-term heat wave of 2020

The maximum simulated river water temperature with the model considering the GW inflow to the river (M:R+GW) was 12 °C and 10 °C less than the simulated temperature considering only river flow (M:R) for Sainte-Marguerite River and Berard River respectively (Figure 5.18). Simulated river water temperature for Sainte-Marguerite River and Berard River with M:R model was on average 45 % and 36 % higher than with the M:R+GW model. This can be translated to an influence of 45 % and 36 % on river thermal budget by GW inflow during the simulation period. The GW reduced the maximum river water temperature by 52 % for Sainte-Marguerite River and 47 % for Berard River when considering difference of simulated river water temperature by the two modeling approaches.

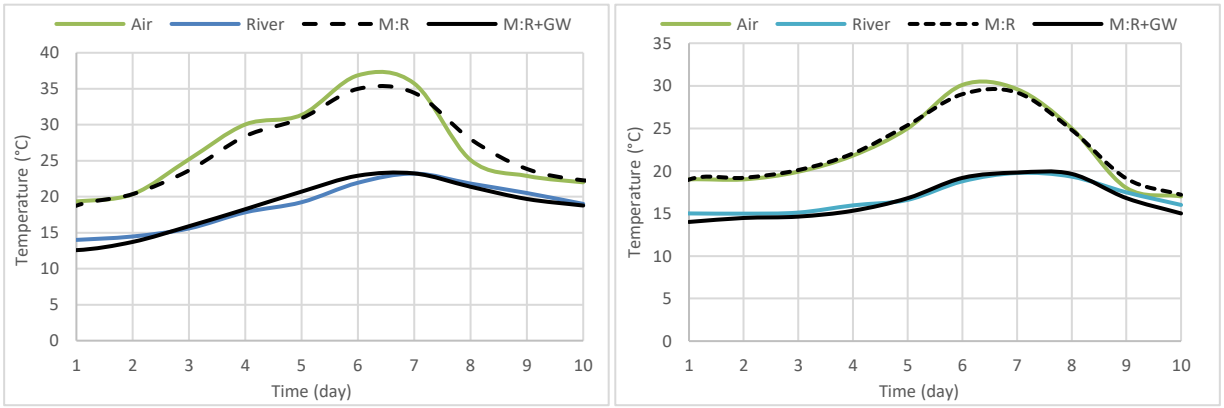

Figure 5.18 **Observed air (green) and river water (blue) temperature compared with simulated river water temperature with the M:R (black dashed line) and M:R+GW (solid black line) modeling approaches for Sainte-Marguerite River (left) and Berard River (right).**

5.4.3 Long-term climate change scenarios

Based on the applied climate scenarios, the GW flowlines do not change significantly over time for the Sainte-Marguerite River case (Figure 5.19). However, the riverbed GW seepage rate (GW.S.R.) increased by 5 % and simulated riverbed temperature (R.B.T.) increased by 40 % over

the period of 2020 to 2100 based on scenario RCP2.6. Likewise, the riverbed GW seepage rate was 40 % and riverbed temperature was 106 % higher based on the scenario RCP8.5 in 2100 compared to 2020 (Figure 5.20).

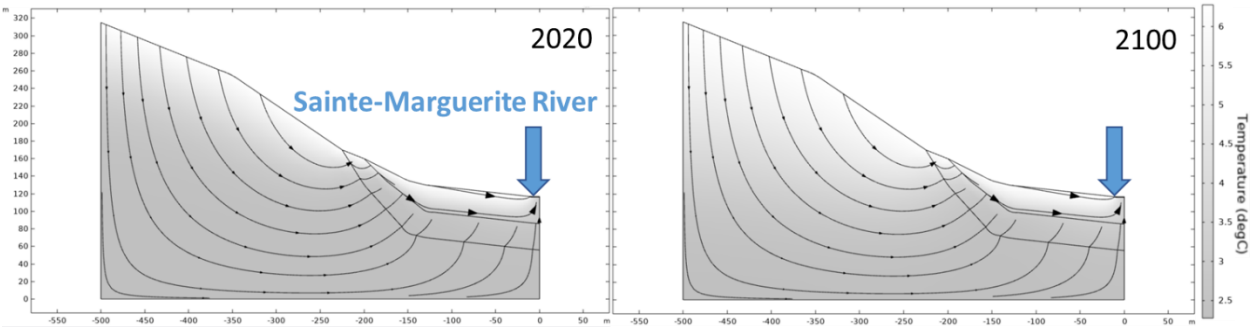

Figure 5.19 Simulated GW flow system of Sainte-Marguerite study site.

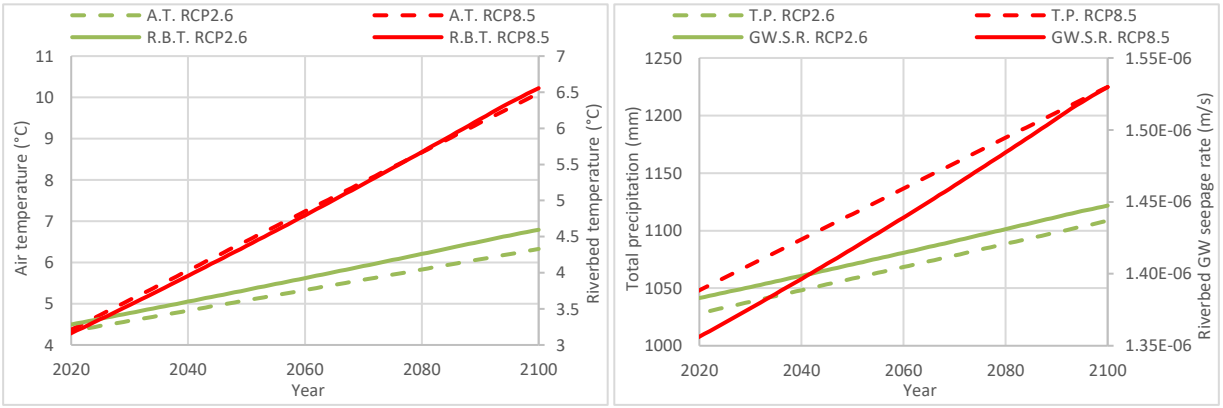

Figure 5.20 Riverbed temperature and GW seepage rate of Sainte-Marguerite River study site based on RCP2.6 and RCP8.5 climate scenarios.

Models of Berard River study site showed significant changes in simulated GW flow system over time based on applied climate change scenarios (Figure 5.21). Simplified climate change models of Berard River suggested linear growth of average annual air temperature and total precipitation from 2020 to 2100 by 68 % and 11 %, respectively, based on RCP2.6 while according to RCP8.5 the linear increases were 218 % and 29 %, respectively. However, according to the 2D models of Berard River site the increase in riverbed temperature and GW seepage rate did not follow a linear increase pattern. From 2020 to 2100, the riverbed temperature and GW seepage rate growth were 33 % and 3749 % based on RCP2.6 scenario and 147 % and 3784 % according to RCP8.5 (Figure 5.22). The simulated GW.S.R in 2100 for scenario RCP8.5 and RCP2.6 were almost similar. However, the sudden non-linear increase (jump in the graph) for scenario RCP8.5 was around 2040 and around 2070 for the scenario RCP2.6.

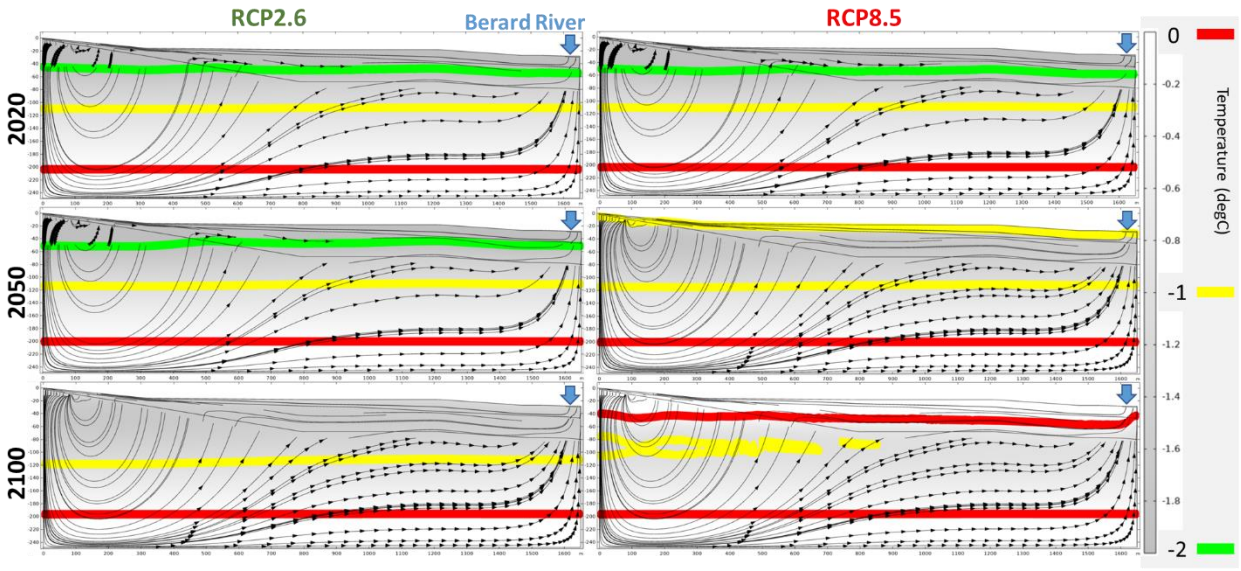

Figure 5.21 **Cross-section view of Berard River study site showing GW flow lines (black lines) and ground calculated temperature.**

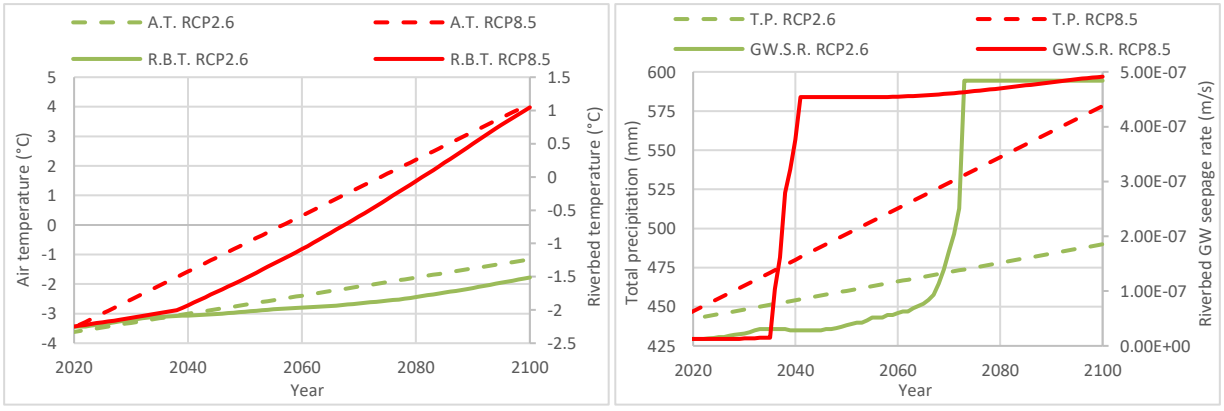

Figure 5.22 **Riverbed temperature and GW seepage rate of Berard River study site based on RCP2.6 and RCP8.5 climate scenarios.**

5.5 Discussion

5.5.1 Assumptions and limitations

Application of temperature dependent heat flux based on air temperature as top boundary condition of models showed good correlation in short-term studies with actual ground measurements at different depths in ground and river. During short-term simulation ground surface condition is constant and in both simulated heat waves there was no precipitation. Therefore, there was no change in emissivity index of surface materials. However, considering same boundary condition for long-term simulations can be a possible source of error. The

emissivity index of ground surface in both studied rivers is different in the cold than in warm season because of presence of snow on the ground (Perreault et al., 2021). Additionally, rivers in the studied region are completely or partially frozen due to cold air temperature, which changes emissivity of the river surface.

Daily time step with maximum daily temperature has been selected as input for the surface of the model in short-term simulation to reproduce the maximum river water temperature of the day, which was the parameter of interest. Smaller time steps such as hourly was not used in this study since this would have required detailed model inputs that were not available such as radiation index and cloud coverage to achieve accurate simulations of hourly river water temperature.

Average annual temperature has been used as model input with considered yearly increase based on climate change scenarios for long-term simulations, since the interest was to anticipate changes over years or decades. However, it is best to use maximum and minimum yearly air temperature from climate scenario with a half-year time step in the models due to warm and cold season differences. This is even more significant in the case of the Berard River study due to presence of permafrost and yearly freeze and thaw cycles in the model top layer which is the most permeable with highest GW flow.

5.5.2 Impacts of heat waves and climate change

The occurrence time of high air temperatures for Sainte-Marguerite River was in low flow season of June and July. This is in accordance with previous studies on heat waves in the region (Khaliq et al., 2005). The highest temperature occurred in August for the Berard River, which is also during the low flow season (Allard et al., 2020).

Based on recorded river and air temperature data of the two selected rivers of this study, it was shown that near or above 30 °C air temperature could trigger near or above 20 °C river water temperature, which is close to the comfort zone limits of most temperature dependent fish. Therefore, 30 °C air temperature can be an effective threshold of extreme atmospheric events during summer for identification of possible life-threatening or uncomfortable condition for fish in the rivers regardless of river morphology and climate.

Comparing models including GW to SW-only showed importance of GW consideration in river thermal budget in short-term simulations of heat waves for the two study sites.

The long-term climate change scenarios in the case of Sainte-Marguerite River resulted in an increase of the riverbed temperature and GW seepage rate following a linear growth pattern

similar to the mean annual air temperature and total precipitation increase. However, the increases in riverbed temperature and GW seepage rate from 2020 to 2100 did not have a linear growth for the Berard River. We think this non-linear and large increase is related to thaw of permafrost. The time when the jump in riverbed seepage rate graph (Figure 5.22-right) or change in the slope of riverbed temperature graph (Figure 5.22-left) occurs corresponds to the disappearance of the frozen ground (soil with temperature below -2 °C). In Figure 5.21, arrow heads on calculated GW flow lines show a specific travel time of several years. Dense arrows mean that the GW flow is small, which always occur at the base of the model where the bedrock unit is located. However, arrows are present on the top of the model in unconsolidated deposits in 2020, which is the starting point of the simulations, and in 2050 for RCP2.6 scenario. Presence of arrows in top units of models coincides with presence of -2 °C contour line (green line in Figure 5.21), meaning the low flow in unconsolidated deposits is due to frozen ground. Based on high emission (RCP8.5) climate scenario, the degradation of permafrost starts in 2033 and after 2041 there is no frozen ground. Based on the low emission climate scenario (RCP2.6), the degradation of permafrost starts around 2064 and by 2074 the ground temperature is above -2 °C everywhere which indicates the absence of the frozen layer.

The simulated rate of permafrost thaw is in accordance with global models and complete disappearance of ice reach and frozen ground by 2100 has been predicted for other regions in the world (Guo et al., 2016; Anisimov et al., 2006; Adiya et al., 2021; Koven et al., 2013). Results indicating the timing of permafrost thaw obtained for the Berard River models in this study are similar to those of Allard et al. (Allard et al., 2020), in which seasonal variation of permafrost due to climate change scenarios is simulated using 1D conceptual heat exchange and energy balance models of ground containing permafrost. However, the GW flow and convective heat transfer was not considered in the work of Allard et al. (Allard et al., 2020). The riverbed GW seepage for our high emission scenario (RCP8.5) before this sudden increase is almost constant (from 2020 to 2035). After 2026 when the jump in the GW seepage rate can be observed (Figure 5.22), the increase in riverbed GW seepage rate is higher and more noticeable. The riverbed GW seepage rate seems constant in the case of the low emission scenario (RCP2.6) although an increase in seepage rate can be seen before the jump in the GW seepage rate. The simulated -1 °C contour line moved about 6 m down toward the base of the model and 0 °C contour line moved 6 m up toward the surface from 2020 to 2050 for both RCP2.6 and RCP8.5 scenarios (Figure 5.21). The thermal state in between these two contour lines can be considered as an indicator of permafrost where partially frozen ground and ice patches can be present in the soil. Simulated changes indicate that thaw of permafrost is both from the top and the base. The simulated thaw rate from

the top and the base of around 7 cm/yr is in accordance with similar studies in the Nunavik region of Quebec Province (Buteau et al., 2004). Our work shows that the thaw of permafrost is expected in the next century around Berard River, which can increase GW flow toward the river. This can result in higher river flow during low precipitation season due to increase in base flow by connection of deeper GW flow pathways to the river in absence of permafrost (Frampton et al., 2011). This increase in GW flow rate may have an impact on riverbed morphology and affect fish habitats and spawning sites within the river. Location of known thermal refuges in the river can be changed and their numbers may increase by anticipated augmented GW seepage. Higher GW seepage with lower temperature compared to river water temperature can change the vertical temperature profile of the river and a higher temperature gradient over depth is possible. The average river water temperature can increase due to increased air temperature which can suggest unsuitable environment for temperature dependent fish of the studied river. However, use of thermal refuges and cooling zones produced by GW seepage during extreme events has been documented before (e.g., Power et al., 1999; Frechette et al., 2018). Higher number of thermal refuges and temperature gradient can be beneficial for survival of the fish during extreme atmospheric events and zones with GW seepage may become the only places where fish can survive in the future. Higher GW flow can be important regarding future activities such as mining in which GW flow can transport contaminants. Under thawing of permafrost and increase in GW flow (Walvoord et al., 2007), some SW bodies that are not affected by pollution from mining or any other type of activities, can be exposed to risks in the future.

5.6 Conclusions

Numerical modeling of northern rivers studied in this research showed that river water temperature is not only related to atmospheric conditions like air temperature but also GW temperature and inflow can have significant effect on river thermal budget (over 30 %). GW temperature has lower temporal and spatial variation in a catchment compared to river water temperature. Along the river, the effect of GW on river water temperature can be variable according to the subsurface materials and the river valley slope. Therefore, numerical models simulating combined GW and SW flow with heat transfer can give reliable results when it comes to simulating river temperature specially in terms of short- and long-term extreme atmospheric events. Observed changes regarding climate change were significantly higher in the zone with permafrost compared to the southern part of Quebec in the zones without permafrost. Hydrothermal models showed that considering heat tracing alongside with GW flow simulations is important in permafrost regions and thaw of permafrost can result in more than three orders of

magnitude higher GW flow (over 3700%). Our conclusions (i.e., increase in GW temperature and seepage) can be extended to rivers in similar geological and climatic environments to anticipate effects of climate change on river and GW interaction. However, for more accurate results regarding a specific river or an area of interest, it is best to perform similar studies to anticipate future of water resources and fish habitats regarding climate change effects on GW systems and GW-SW interactions. Having a 3D combined GW and SW model of a river can give us insights for potential places where thermal refuges and cooling zones in the rivers are present and predict how their location and extent can be changed in the future according to climate warming. GW has a significant role in river thermal budget and its role may become even more significant with predicted GW seepage increase in the future .GW is likely to become a main controlling factor for fish survival and life cycle in the rivers. Therefore, GW-related studies such as identification of GW-driven thermal refuges and cooling zones in the river and their use by fish and related predictions by hydrothermal models can be insightful for wildlife boards to implement management plans.

5.7 References

Adiya S. & Erdenebat E. (2021) « 21st century permafrost distribution under the scenario of RCP2.6 and RCP8.5 in Mongolia. » Proceedings of the Mongolian Academy of Sciences 61 (04): 9-14. doi:10.5564/pmas.v61i04.1927.

Allard M., Chiasson A., St-amour A.B., Aubé-michaud S., Mathon-dufour V., L Hérault E., Bilodeau S. & Deslauriers C. (2020) « Caractérisation géotechnique et cartographie améliorée du pergélisol dans les communautés nordiques du Nunavik : Tasiujaq. » Rapport préparé pour Ministère des Affaires municipales et de l'Habitation, gouvernement du Québec Québec, Centre d'études nordiques, Université Laval, Québec, Québec, Canada.

Anisimov O. & Reneva S. (2006) « Permafrost and changing climate: The Russian perspective. » Ambio: A Journal of the Human Environment 35 (4): 169-175. doi:10.1579/0044-7447(2006)35[169:PACCTR]2.0.CO;2.

Brunke M. & Gonser T. (1997) « The ecological significance of exchange processes between rivers and groundwater. » Freshwater Biology 37 (1): 1-33. doi:10.1046/j.1365-2427.1997.00143.x.

Buteau S., Fortier R., Delisle G. & Allard M. (2004) « Numerical simulation of the impacts of climate warming on a permafrost mound. » Permafrost and Periglacial Processes 15 (1): 41-57. doi:10.1002/ppp.474.

Caissie D. (2006) « The thermal regime of rivers: A review. » Freshwater Biology 51 (8): 1389-1406. doi:10.1111/j.1365-2427.2006.01597.x.

Chesnaux R., Baudement C. & Hay M. (2011) « Assessing and comparing the hydraulic properties of granular aquifers on three different scales. » Conference Paper In Proceedings of Geohydro, Quebec, Quebec, Canada.

Chesnaux R., Lambert M., Walter J., Fillastre U., Hay M., Rouleau A., Daigneault R., Moisan A. & Germaneau D. (2011) « Building a geodatabase for mapping hydrogeological features and 3D modeling of groundwater systems: Application to the Saguenay-Lac-St.-Jean region, Canada. » Computers and Geosciences 37 (11): 1870-1882. doi:10.1016/j.cageo.2011.04.013.

Cho J., Mostaghimi S. & Kang M.S. (2010) « Development and application of a modeling approach for surface water and groundwater interaction. » Agricultural Water Management 97 (1): 123-130. doi:10.1016/j.agwat.2009.08.018.

ClimateData.ca (2021) « Data Source: Environment and Climate Change Canada and (ClimateData.ca) See: https://eccc-msc.github.io/open-data/licence/readme_en/. » Page Web, consulté le 1er septembre 2021 à l'adresse https://climatedata.ca/explore/location/?loc=EJLMJ&location-select-temperature=tx_mean&location-select-precipitation=rx1day&location-select-other=frost_days.

Comeau F.-A., Raymond J., Malo M., Dezayes C. & Carreau M. (2017) « Geothermal potential of Northern Québec: A regional assessment. » Transactions - Geothermal Resources Council 41: 1076-1094.

COMSOL (2023) « COMSOL Multiphysics® Simulation Software. » Software Manual, COMSOL, Inc., MA, USA. https://www.comsol.com/comsol-multiphysics.

Dagher E.E., Su G., and Nguyen T.S. (2014) « Verification of the Numerical Simulation of Permafrost Using COMSOL Multiphysics® Software. » Conference Article, Proceedings of the 2014 COMSOL Conference in Boston.

Evans S.G. & Ge S. (2017) « Contrasting hydrogeologic responses to warming in permafrost and seasonally frozen ground hillslopes. » Geophysical Research Letters 44 (4): 1803-1813. doi:10.1002/2016GL072009.

Fakhari M., Raymond J., Martel R., Dugdale S.J. & Bergeron N.E. (2022) « Identification of Thermal Refuges and Water Temperature Patterns in Salmonid-Bearing Subarctic Rivers of Northern Quebec. » Geographies 2 (3): 528-548. doi:10.3390/geographies2030032.

Fakhari M., Raymond J., Martel R., Drolet J.-P., Dugdale S.J. & Bergeron N.E. (2023) « Analysis of Large-Scale Groundwater-Driven Cooling Zones in Rivers Using Thermal Infrared Imagery and Radon Measurements. » Water 15 (5). doi:10.3390/w15050873.

Fakhari M., Raymond J., Martel R., Klepikova M. & Bour O. (2024) « On the Complementariness of Multiple In-Situ Techniques for Spatiotemporal Assessment of Groundwater-Surface Water Exchanges. » Unpublished article.

Finstad A.G. & Jonsson B. (2012) « Effect of incubation temperature on growth performance in Atlantic salmon. » Marine Ecology Progress Series 454 (1): 75-82. doi:10.3354/meps09643.

Fortin G., Acquaotta F. & Fratianni S. (2017) « The evolution of temperature extremes in the Gaspé Peninsula, Quebec, Canada (1974–2013). » Theoretical and Applied Climatology 130 (1-2). Theoretical and Applied Climatology: 163-172. doi:10.1007/s00704-016-1859-x.

Frampton A., Painter S., Lyon S.W. & Destouni G. (2011) « Non-isothermal, three-phase simulations of near-surface flows in a model permafrost system under seasonal variability and climate change. » Journal of Hydrology 403 (3-4). Elsevier B.V.: 352-359. doi:10.1016/j.jhydrol.2011.04.010. http://dx.doi.org/10.1016/j.jhydrol.2011.04.010.

Frechette D.M., Dugdale S.J., Dodson J.J. & Bergeron N.E. (2018) « Understanding summertime thermal refuge use by adult Atlantic salmon using remote sensing, river temperature monitoring, and acoustic telemetry1. » Canadian Journal of Fisheries and Aquatic Sciences 75 (11): 1999-2010. doi:10.1139/cjfas-2017-0422.

Freeze A. & Cherry J. (1979) « Groundwater. » New Jersey: Prentice-Hall Inc, New Jersey, U.S.

Geist D.R. & Dauble D.D. (1998) « Redd site selection and spawning habitat use by fall chinook salmon: The importance of geomorphic features in large rivers. » Environmental Management 22 (5): 655-669. doi:10.1007/s002679900137.

Gismervik K., Gåsnes S.K., Gu J., Stien L.H., Madaro A. & Nilsson J. (2019) « Thermal injuries in Atlantic salmon in a pilot laboratory trial. » Veterinary and Animal Science 8 (September). Elsevier: 100081. doi:10.1016/j.vas.2019.100081. https://doi.org/10.1016/j.vas.2019.100081.

Goel P.K. (2006) « Water Pollution: Causes, Effects and Control. » New Age International. New Delhi, India.

https://books.google.ca/books?id=4R9CYYoiFCcC&dq=groundwater+and+river+polutipon+caused+by+agricultural+activities&lr=&source=gbs_navlinks_s.

Gray J.T., Pilon J.A. & Poitevin J. (1979) « Le pergélisol et la couche active dans la toundra forestière au sud de la baie aux Feuilles, Nouveau-Québec. » Geographie Physique et Quaternaire 33 (3-4): 253-264. doi:10.7202/1000362ar.

Guo D. & Wang H. (2016) « CMIP5 permafrost degradation projection: A comparison among different regions. » Journal of Geophysical Research: Atmospheres 121: 4449-4517. doi:10.1002/2015JD024108.

Hancock P.J. (2002) « Human impacts on the stream-groundwater exchange zone. » Environmental Management 29 (6): 763-781. doi:10.1007/s00267-001-0064-5.

Hassan S.M.T., Lubczynski M.W., Niswonger R.G. & Su Z. (2014) « Surface-groundwater interactions in hard rocks in Sardon Catchment of western Spain: An integrated modeling approach. » Journal of Hydrology 517. Elsevier B.V.: 390-410. doi:10.1016/j.jhydrol.2014.05.026. http://dx.doi.org/10.1016/j.jhydrol.2014.05.026.

Havril T., Toth A., Molson J.W., Galsa A. & Madl-Szonyi J. (2018) « Impacts of predicted climate change on groundwater flow systems: Can wetlands disappear due to recharge reduction? » Journal of Hydrology 563: 1169-1180. doi:10.1016/j.jhydrol.2017.09.020.

Hayashi M. & Rosenberry D.O. (2002) « Effects of ground water exchange on the hydrology and ecology of surface water. » Ground Water 40 (3): 309-316. doi:10.1111/j.1745-6584.2002.tb02659.x.

Hu R., Liu Q. & Xing Y. (2018) « Case study of heat transfer during artificial ground freezing with groundwater flow. » Water (Switzerland) 10 (10). doi:10.3390/w10101322.

Hunt R.J., Westenbroek S.M., Walker J.F., Selbig W.R., Regan R.S., Leaf A.T. & Saad D.A. (2016) « Simulation of climate change effects on streamflow, groundwater, and stream temperature using GSFLOW and SNTEMP in the Black Earth Creek Watershed, Wisconsin. » Scientific Investigations Report 2016–5091. Reston, Virginia. doi:10.3133/sir20165091. http://pubs.er.usgs.gov/publication/sir20165091.

Hynes H.B.N. (1983) « Groundwater and stream ecology. » Hydrobiologia 100 (1): 93-99. doi:10.1007/BF00027424.

Ingebritsen S.E., Sanford W.E. & Neuzil C.E. (1998) « Groundwater in geologic processes. » Second Edition. Cambridge University Press, Cambridge, U. K. doi:10.1111/j.1468-8123.2009.00253.x.

Jensen A.J., Johnsen B.O. & Saksgard L. (1989) « Temperature requirements in Atlantic salmon (Salmo salar), brown trout (Salmon trutta), and Arctic char (Salvelinus alpinus) from hatching to initial feeding compared with geographic distribution. » Canadian Journal of Fisheries and Aquatic Sciences 46 (5): 786-789. doi:10.1139/f89-097.

Khaliq M.N., St-Hilaire A., Ouarda T.B.M.J. & Bobée B. (2005) « Frequency analysis and temporal pattern of occurrences of southern Quebec heatwaves. » International Journal of Climatology 25 (4): 485-504. doi:10.1002/joc.1141.

Koven C.D., Riley W.J. & Stern A. (2013) « Analysis of permafrost thermal dynamics and response to climate change in the CMIP5 earth system models. » Journal of Climate 26 (6): 1877-1900. doi:10.1175/JCLI-D-12-00228.1.

Kurylyk B.L., Hayashi M., Quinton W.L., McKenzie J.M. & Voss C.I. (2016) « Influence of vertical and lateral heat transfer on permafrost thaw, peatland landscape transition, and groundwater flow. » Water Resources Research 52: 1-20. doi:10.1002/2015WR018057.

Lamontagne S., Leaney F.W. & Herczeg A.L. (2005) « Groundwater-surface water interactions in a large semi-arid floodplain: Implications for salinity management. » Hydrological Processes 19 (16): 3063-3080. doi:10.1002/hyp.5832.

Lévesque R., Allard M., Seguin M.K. & Pilon J.-A. (1990) « Données préliminaires sur la régime thermique du pergélisol dans quelques localités du Nunavik, Québec. » Permafrost-Canada, Proceedings of the Fifth Canadian Permafrost Conference, Nordicana no 54: 207-213. http://pubs.aina.ucalgary.ca/cpc/CPC5-207.pdf.

Lorenz J.M. & Filer J.H. (1989) « Spawning Habitat and Redd Characteristics of Sockeye Salmon in the Glacial Taku River, British Columbia and Alaska. » Transactions of the American Fisheries Society 118 (5): 495-502. doi:10.1577/1548-8659(1989)118<0495:sharco>2.3.co;2. http://citeseerx.ist.psu.edu/viewdoc/download?doi=10.1.1.586.132&rep=rep1&type=pdf.

Mainguy J. & Beaupré L. (2019) « Établissement d'un état de référence pour la population d'omble chevalier de la rivière Bérard à Tasiujaq. » Report by ministère des Forêts, de la Faune et des Parcs, Direction de l'expertise sur la faune aquatique et Direction de la gestion de la faune du Nord-du-Québec, 29 p.

Mookerji N., Weng Z. & Mazumder A. (2004) « Food partitioning between coexisting Atlantic salmon and brook trout in the Sainte-Marguerite River ecosystem, Quebec. » Journal of Fish Biology 64 (3): 680-694. doi:10.1111/j.1095-8649.2004.00333.x.

Neilson B.T., Cardenas B.M., O'Connor M.T., Rasmussen M.T., King T.V. & Kling G.W. (2018) « Groundwater Flow and Exchange Across the Land Surface Explain Carbon Export Patterns in Continuous Permafrost Watersheds. » Geophysical Research Letters 45 (15): 7596-7605. doi:10.1029/2018GL078140.

Nyanti L., Soo C.L., Ahmad-Tarmizi N.N., Abu-Rashid N.N.K., Ling T.Y., Sim S.F., Grinang J., Ganyai T. & Lee K.S.P. (2018) « Effects of water temperature, dissolved oxygen and total suspended solids on juvenile barbonymus schwanenfeldii (Bleeker, 1854) and Oreochromis Niloticus (Linnaeus, 1758). » AACL Bioflux 11 (2): 394-406.

Perreault J., Fortier R. & Molson J.W. (2021) « Numerical Modelling of Permafrost Dynamics under Climate Change and Evolving Ground Surface Conditions: Application to an Instrumented Permafrost Mound at Umiujaq, Nunavik (Québec), Canada. » Ecoscience 28 (3-4). Taylor & Francis: 377-397. doi:10.1080/11956860.2021.1949819. https://doi.org/10.1080/11956860.2021.1949819.

Poesch M.S., Chavarie L., Chu C., Pandit S.N. & Tonn W. (2016) « Climate Change Impacts on Freshwater Fishes: A Canadian Perspective. » Fisheries 41 (7): 385-391. doi:10.1080/03632415.2016.1180285. http://dx.doi.org/10.1080/03632415.2016.1180285.

Ponce V.M., Lohani A.K. & Huston P.T. (1997) « Surface Albedo And Water Resources: Hydroclimatological Impact of Human Activities. » Journal of Hydrologic Engineering 2 (4): 197. https://www.jstor.org/stable/1740662?seq=1#metadata_info_tab_contents.

Power G., Brown R.S. & Imhof J.G. (1999) « Groundwater and fish - Insights from northern North America. » Hydrological Processes 13 (3): 401-422. doi:10.1002/(SICI)1099-1085(19990228)13:3<401::AID-HYP746>3.0.CO;2-A.

Rathfelder K. (2016) « Modelling Tools for Estimating Effects of Groundwater Pumping on Surface Waters. » Technical Report, Ministry of Environment, Water Science Series WSS2016-09, BC, Canada.

Raymond J. & Therrien R. (2014) « Optimizing the design of a geothermal district heating and cooling system located at a flooded mine in Canada. » Hydrogeology Journal 22 (1): 217-231. doi:10.1007/s10040-013-1063-3.

Saha G.C., Li J., Thring R.W., Hirshfield F. & Paul S.S. (2017) « Temporal dynamics of groundwater-surface water interaction under the effects of climate change: A case study in the Kiskatinaw River Watershed, Canada. » Journal of Hydrology 551. Elsevier B.V.: 440-452. doi:10.1016/j.jhydrol.2017.06.008. http://dx.doi.org/10.1016/j.jhydrol.2017.06.008.

Saltveit S.J. & Brabrand A. (2013) « Incubation, hatching and survival of eggs of Atlantic salmon (Salmo salar) in spawning redds influenced by groundwater. » Limnologica 43 (5). Elsevier GmbH.: 325-331. doi:10.1016/j.limno.2013.05.009. http://dx.doi.org/10.1016/j.limno.2013.05.009.

SIGÉOM. 2022. « Surface deposits map. » système d'information géominière du Québec. Page Web, consulté le 1er juin 2020 à l'adresse https://sigeom.mines.gouv.qc.ca/signet/classes/I1108_afchCarteIntr.

Smith S.L. & Burgess M.M. (2002) « A digital database of permafrost thickness in Canada. » Report (open file 4173), Geological Survey of Canada. Ottawa, ON, Canada.

Spanoudaki K., Stamou A.I. & Nanou-Giannarou A. (2009) « Development and verification of a 3-D integrated surface water-groundwater model. » Journal of Hydrology 375 (3-4). Elsevier B.V.: 410-427. doi:10.1016/j.jhydrol.2009.06.041. http://dx.doi.org/10.1016/j.jhydrol.2009.06.041.

Tang Q., Kurtz W., Brunner P., Vereecken H. & Hendricks Franssen H.J. (2015) « Characterisation of river-aquifer exchange fluxes: The role of spatial patterns of riverbed hydraulic conductivities. » Journal of Hydrology 531. Elsevier B.V.: 111-123. doi:10.1016/j.jhydrol.2015.08.019. http://dx.doi.org/10.1016/j.jhydrol.2015.08.019.

Tian W., Li X., Cheng G.D., Wang X.S. & Hu B.X. (2012) « Coupling a groundwater model with a land surface model to improve water and energy cycle simulation. » Hydrology and Earth System Sciences 16 (12): 4707-4723. doi:10.5194/hess-16-4707-2012.

Tian Y., Zheng Y., Wu B., Wu X., Liu J. & Zheng C. (2015) « Modeling surface water-groundwater interaction in arid and semi-arid regions with intensive agriculture. » Environmental Modelling and Software 63. Elsevier Ltd: 170-184. doi:10.1016/j.envsoft.2014.10.011. http://dx.doi.org/10.1016/j.envsoft.2014.10.011.

Walvoord M.A. & Striegl R.G. (2007) « Increased groundwater to stream discharge from permafrost thawing in the Yukon River basin: Potential impacts on lateral export of carbon and nitrogen. » Geophysical Research Letters 34 (12). doi:10.1029/2007GL030216.

Walvoord M.A., Voss C.I. & Wellman T.P. (2012) « Influence of permafrost distribution on groundwater flow in the context of climate-driven permafrost thaw: Example from Yukon Flats Basin, Alaska, United States. » Water Resources Research 48 (7): 1-17. doi:10.1029/2011WR011595.

Wayland K.G., Hyndman D.W., Boutt D., Pijanowski B.C. & Long D.T. (2002) « Modelling the impact of historical land uses on surface-water quality using groundwater flow and solute-transport models. » Lakes and Reservoirs: Research and Management 7 (3): 189-199. doi:10.1046/j.1440-1770.2002.00187.x.

Willms T. & Whitworth G. (2016) « Mapping of critical summer thermal refuge habitats for Chinook salmon, Coho salmon, steelhead and bull trout in the Nicola River Watershed - 2016. » Report of Habitat Stewardship Program for Species at Risk. Vol. 3. Fraser Basin Council: Kamloops, BC, Canada.

Zhang Y.K. & Schilling K. (2004) « Temporal scaling of hydraulic head and river base flow and its implication for groundwater recharge. » Water Resources Research 40 (3): 1-9. doi:10.1029/2003WR002094.

6 DISCUSSION GÉNÉRALE

Les résultats des simulations du changement climatique qui ont révélé l'importance de GW dans l'avenir des rivières constituent le point fort de cette étude. Bien que des études similaires aient déjà été réalisées dans le nord du Québec et dans d'autres régions nordiques du monde (Allard et al., 2020; Guo et al., 2016; Anisimov et al., 2006; Adiya et al., 2021; Koven et al., 2013), l'utilisation de modèles hydrothermaux pour expliquer le processus complexe de la fonte du pergélisol et ses effets potentiels sur les rivières n'a jamais été présentée de cette manière, à la connaissance de l'auteur. Même si toutes les méthodes utilisées dans cette étude n'étaient pas nouvelles, l'utilisation d'une approche multitechnique nous a permis de rassembler les données nécessaires à la construction et à la calibration des modèles sur la base de mesures effectuées sur le terrain et en laboratoire. La combinaison de ces différents types de mesures acquises en laboratoire (données dans les annexes I à V) utilisés dans une étude sur des rivières naturelles situées dans des régions relativement éloignées n’est pas commune au sein de la littérature scientifique (Kalbus et al., 2006; Rosenberry et LaBaugh, 2008; Coluccio et Morgan, 2019). Cela peut être considéré comme un autre aspect important de cette étude. L'approche utilisée dans cette étude peut servir d’exemple pour de futures études dans des zones où l'accès et les données sont limités. Par ailleurs, les travaux ont démontré qu’il est possible d’identifier les zones à fort potentiel d'interaction GW-SW avec une évaluation réalisée à grande échelle telles que l’analyse de TAI et les mesures du radon. Les zones à fort potentiel peuvent ensuite être visées pour des mesures plus détaillées à petite échelle telles que le traçage thermique actif et passif, l'installation des infiltromètres, des piézomètres et d'enregistreurs de niveau d’eau, ainsi que des mesures géophysiques. Ces mesures nous permettent de collecter les données nécessaires à la construction de modèles de prévision des systèmes fluviaux et d’interaction GW-SW.

6.1 Limitations

Les rivières étudiées étaient des rivières naturelles relativement grandes (largeur > 20 m) avec peu d'études de base, ce qui a amené certaines limites. La méthodologie générale de l'étude commence par des analyses à grande échelle telle que les mesures du TAI et du Radon pour l'identification des zones avec un potentiel d'interaction GW-SW plus élevé et, à l'étape suivante, la sélection de ces sites pour une analyse et une instrumentation plus approfondie. Le TAI de la rivière Sainte-Marguerite et de la rivière Bérard a été pris et utilisé pour sélectionner les sites à instrumenter. Cependant, l'accessibilité des sites a été priorisée puisque certains des refuges

identifiés étaient difficiles d’accès ou se prêtaient mal à la mise en place d'instruments en raison d'un débit élevé, de la grande profondeur de l'eau ou de la présence de berges escarpées ou rocheuses.

En outre, l'instrumentation a été concentrée sur la partie centrale du tronçon de rivière sélectionné couvrant seulement quelques centaines de mètres carrés, en raison du nombre limité de piézomètres et d'enregistreurs de niveau d’eau. Cette configuration ne pose pas de problème pour l’application des modèles 2D à partir d'une section transversale de rivière. Toutefois, le nombre limité de données rend difficile et moins fiable la modélisation 3D de ces secteurs.

De plus, en raison de l'éloignement des sites d'étude et de l'indisponibilité des équipements de forage pour ces conditions de terrain, l'installation manuelle des piézomètres a été limitée à moins de 3 m de profondeur. Le manque de mesures de pression et de température de GW en profondeur a été un facteur limitant dans l'étalonnage des modèles, ce qui est responsable d'une faible exactitude du modèle dans les couches profondes.

L’effet du substrat rocheux sur la concentration en radon de GW n’a pas été pris en compte étant donné l'absence d’échantillons de GW profonds.

La géologie des sections modélisées était basée sur les cartes disponibles qui indiquent une épaisseur approximative des unités sans aucun forage disponible à proximité des rivières. L'épaisseur des alluvions joue aussi un rôle important dans les résultats du modèle et peut introduire des incertitudes.

La profondeur et l'épaisseur du pergélisol jouent également un rôle important dans les modèles de la rivière Bérard et la modification de ces paramètres peut donner lieu à différentes prévisions selon les scénarios de changements climatiques considérés.

Des méthodes géophysiques telles que GPR et ERT ont été utilisées sur les sites d'étude pour une meilleure caractérisation de la stratigraphie. Cependant, en raison de la présence de cailloux/blocs rocheux enfouis et d'une couverture végétale épaisse comprenant des racines denses à proximité des rives, ces relevés n'ont pas été concluants de sorte que l'épaisseur de l'aquifère, son hétérogénéité et la présence/profondeur du pergélisol n’ont pu être définies.

Un autre facteur limitant était la disponibilité des données en fonction du temps. La simulation 3D nécessite des mesures de débits en amont et en aval. Les rivières étudiées n’étant pas jaugées, il n’existe pas de séries chronologiques de débit et de niveau d'eau. Par conséquent, pour les simulations à court terme des vagues de chaleur, le débit de la rivière a été considéré comme constant pendant la période de simulation. La prise en compte d'un débit constant limite

l'utilisation de modèles 3D pour les simulations à long terme lorsque des changements dans le débit des rivières et la profondeur de l'eau sont attendus en raison de changements dans le taux de précipitations. Par conséquent, nous avons été contraints de recourir exclusivement à des modèles 2D de milieux poreux (sans zone d'écoulement libre) pour simuler des scénarios de changement climatique. Dans ces simulations, les changements de taux d'infiltration et de température du lit de la rivière ont été signalés au lieu des fluctuations anticipées de la température de l'eau de la rivière. Cela limite l'utilisation des résultats de la modélisation lors de l'évaluation directe de l'impact du changement climatique sur l'avenir des écosystèmes fluviaux en relation avec les habitats du poisson.

6.2 Recommandations

En général, nous suggérons davantage de collectes de données sur le terrain pour aider à surmonter les limites rencontrées au cours de cette étude.

Disposer de puits d'observation profonds pour surveiller la pression et la température de GW pourrait aider à une meilleure calibration des modèles. Les informations sur les couches profondes aident à mieux délimiter le modèle et à poser les conditions limites. Par exemple, si le pergélisol est présent, le modèle devrait être suffisamment profond pour couvrir toute son épaisseur et être capable de simuler la connexion entre l'aquifère sous le pergélisol et la rivière lors du dégel. D'un autre côté, si le pergélisol n'est pas présent et que la perméabilité de l'aquifère rocheux est faible et que sa connexion avec la rivière est limitée, les modèles peuvent se concentrer sur des unités d'alluvions peu profondes. En plus d'une plus grande profondeur d'investigation, des points d'observation plus uniformément répartis dans la zone de modélisation permettent de mieux calibrer les modèles et d'obtenir des résultats fiables. Le fait de placer les points d'observation plus régulièrement le long de la rivière permettrait de mieux présenter le système dans les modèles 3D. De plus, il serait important d'avoir des points d'observation plus éloignés des rivières pour mieux calibrer les modèles 3D et 2D et pour ajuster les conditions limites.

Il serait important de mesurer le débit de la rivière à deux ou plusieurs sections transversales pour obtenir une modélisation fiable de l'écoulement libre. Plusieurs mesures du débit de la rivière à différents moments aident à établir une corrélation entre le débit de la rivière et la profondeur de l'eau qui peut être appliquée dans les modèles. Aussi, pour une meilleure simulation de l'écoulement libre avec un niveau d'eau variable, l'utilisation d'un maillage mobile dans le domaine de l'écoulement libre serait nécessaire pour une simulation précise du débit de la rivière et du

niveau d'eau. La construction de modèles pluie-ruissèlement de la zone d'étude pourrait aider à estimer le débit de la rivière en fonction des précipitations. Ceci permettrait d'utiliser des modèles 3D pour les prévisions futures du débit sur la base d'un taux de précipitations appliqué à partir d'un scénario climatique souhaité.

Le fait de disposer d'un modèle à mailles mobiles et à débit variable permettrait en outre d'utiliser des pas de temps plus petits pour les simulations à court et à long terme. Un pas de temps d'une demi-journée ou d'une heure pour la simulation d'une vague de chaleur à court terme permet de voir les effets de la baisse de température pendant la nuit. Des pas de temps plus petits de simuler la neige à la surface du sol ou la couverture de glace sur la surface gelée de la rivière et de considérer leur effet sur l'isolation du sol ou de l'eau du froid et l'atténuation du transfert de chaleur dans le système.

6.3 Conclusions

Malgré les limites rencontrées, la combinaison de mesures multitechniques sur le terrain a permis d'identifier et de quantifier la contribution de GW au système fluvial étudiés. Grâce à des méthodes à grande échelle, plusieurs kilomètres de rivière ont été étudiés et des zones présentant un potentiel d'infiltration de GW plus élevé ont été identifiées. Les refuges thermiques contrôlés par le GW se sont révélés être les plus courants et la principale source des zones de refroidissement dans la rivière s'est avérée être les infiltrations de GW, sur la base d'une analyse à grande échelle avec le TAI et les mesures de radon. L'analyse de TAI et les mesures de radon ont déjà été utilisées pour la détection de GW dans les rivières (par exemple, Malard et al., 1999; Dugdale et al., 2019). Cependant, la combinaison de ces deux méthodes dans cette étude a permis de sélectionner plus précisément les points d'échantillonnage pour le radon et de limiter le nombre d'échantillons nécessaires pour étudier une grande longueur de rivière et vérifier la présence de GW lorsque l'analyse de TAI seul n'était pas adéquate.

Au sein de ces zones identifiées, des mesures plus détaillées à petite échelle ont permis de cartographier la variation spatiotemporelle du taux d'infiltration dans le lit de la rivière pour un tronçon de rivière de plusieurs dizaines de mètres de longueur. La variation spatiale de l'infiltration de GW a été illustrée par l'installation des infiltromètres à différents endroits et l'utilisation d'un traçage thermique actif. Le traçage thermique actif au moyen d'un câble FO chauffé enterré dans le lit d'une rivière a déjà été utilisé pour étudier l'interaction entre le GW et les rivières, ainsi que les hétérogénéités du lit de la rivière (par exemple, Simon et al., 2021; Briggs et al., 2016). Cependant, l'utilisation de câbles chauffés et de capteurs de température comme alternative aux

câbles FO chauffés dans le lit de la rivière était également nouvelle et, à la connaissance des auteurs, n'avait jamais été réalisée auparavant. Cette méthode a donné des résultats similaires à ceux de la méthode FO-DTS active et a été utile pour suivre les variations spatiales des infiltrations de GW. Des hétérogénéités à l'échelle du tronçon fluvial, telles que la présence d'un banc de sable et une différence dans les matériaux du lit de la rivière, se sont avérées avoir un impact sur le taux d'infiltration du GW.

Les modèles hydrothermaux de ces zones sélectionnées avec un fort potentiel d'interaction GW-SW ont permis de simuler et de prédire l'avenir du système sur la base des scénarios de changement climatique anticipés. Les modèles ont révélé un effet important (supérieur à 30 %) de l'infiltration de GW sur le bilan thermique de la rivière et sur l'atténuation de la température pendant les évènements extrêmes. Selon les scénarios de changement climatique appliqués, avec une augmentation prévue du taux de précipitations annuelles totales et de la température moyenne annuelle de l'air, une augmentation du taux d'infiltration de GW et de la température est attendue. L'augmentation de l'infiltration de GW et de la température du lit de la rivière Sainte-Marguerite suivrait une croissance linéaire influencée par l'augmentation de la température de l'air et des précipitations selon les scénarios de changement climatique. Cependant, l'augmentation simulée de l'infiltration de GW et de la température se sont avérées beaucoup plus élevées pour la rivière Bérard par rapport à la rivière Sainte-Marguerite. L'augmentation simulée de l'infiltration de GW pour la rivière Bérard ne suit pas une croissance linéaire. Une augmentation soudaine est plutôt attendue et dépendra du moment du dégel du pergélisol selon les scénarios climatiques anticipés.

Une température de l'air supérieure à 30 °C a entrainé une température de l'eau de plus de 20 °C dans les deux rivières étudiées, ce qui est proche de la température critique pour la croissance et la survie des poissons (Gunn et al., 2010). Les zones sans infiltration de GW dans les rivières pourraient devenir impropres à la vie aquatique, en raison de l'augmentation prévue de la température de l'air et de la fréquence accrue des évènements extrêmes de chaleur intense (Colombo et al., 1999; Fortin et al., 2017). Toutefois, l'augmentation prévue des infiltrations de GW peut entrainer une augmentation du nombre de zones de refroidissement et de refuges thermiques dans les cours d'eau. Cela peut éventuellement affecter la localisation des poissons dans les rivières étudiées, puisque ceux-ci utilisent les refuges thermiques dans des conditions extrêmes et cherchent refuge dans des zones d'infiltration de GW fraiche pour survivre (Dugdale et al., 2016; Berman et al., 1991; Frechette et al., 2018). Par conséquent, les zones avec une infiltration de GW plus élevée dans les rivières pourraient devenir les principaux endroits où les

poissons se retrouvent dans les rivières (Kaandorp et al., 2019). Cela nécessite davantage d'études dont les effets de GW sur les rivières pour une meilleure compréhension de l'avenir des poissons et de la pêche, ce qui est important pour les communautés et les gestionnaires de la faune.

6.4 Références

Adiya S. & Erdenebat E. (2021) « 21st century permafrost distribution under the scenario of RCP2.6 and RCP8.5 in Mongolia. » Proceedings of the Mongolian Academy of Sciences 61 (04): 9-14. doi:10.5564/pmas.v61i04.1927.

Allard M., Chiasson A., St-amour A.B., Aubé-michaud S., Mathon-dufour V., L Hérault E., Bilodeau S. & Deslauriers C. (2020) « Caractérisation géotechnique et cartographie améliorée du pergélisol dans les communautés nordiques du Nunavik : Tasiujaq. » Rapport préparé pour Ministère des Affaires municipales et de l'Habitation, gouvernement du Québec Québec, Centre d'études nordiques, Université Laval, Québec, Québec, Canada.

Anisimov O. & Reneva S. (2006) « Permafrost and changing climate: The Russian perspective. » Ambio: A Journal of the Human Environment 35 (4): 169-175. doi:10.1579/0044-7447(2006)35[169:PACCTR]2.0.CO;2.

Berman C.H. et Quinn T.P. (1991) « Behavioural thermoregulation and homing by spring chinook salmon, Oncorhynchus tshawytscha (Walbaum), in the Yakima River. » Journal of Fish Biology 39 (3): 301-312. doi:10.1111/j.1095-8649.1991.tb04364.x.

Briggs M.A., Buckley S.F., Bagtzoglou A.C., Werkema D.D. et Lane J.W. (2016) « Actively heated high-resolution fiber-optic-distributed temperature sensing to quantify streambed flow dynamics in zones of strong groundwater upwelling. » Water Resources Research 52: 5179-5194. doi:10.1002/2015WR018219.

Colombo A.F., Etkin D. et Karney B.W. (1999) « Climate variability and the frequency of extreme temperature events for nine sites across Canada: Implications for power usage. » Journal of Climate 12 (8 PART 2): 2490-2502. doi:10.1175/1520-0442(1999)012<2490:cvatfo>2.0.co;2.

Coluccio K. et Morgan L.K. (2019) « A review of methods for measuring groundwater-surface water exchange in braided rivers. » Hydrology and Earth System Sciences 23 (10): 4397-4417. doi:10.5194/hess-23-4397-2019.

Dugdale S.J., Franssen J., Corey E., Bergeron N.E., Lapointe M. et Cunjak R.A. (2016) « Main stem movement of Atlantic salmon parr in response to high river temperature. » Ecology of Freshwater Fish 25 (3): 429-445. doi:10.1111/eff.12224.

Dugdale S.J., Kelleher C.A., Malcolm L.A., Caldwell S. et Hannah D.M. (2019) « Assessing the potential of drone-based thermal infrared imagery for quantifying river temperature heterogeneity. » Hydrological Processes 33 (7): 1152-1163. doi:10.1002/hyp.13395.

Fortin G., Acquaotta F. et Fratianni S. (2017) « The evolution of temperature extremes in the Gaspé Peninsula, Quebec, Canada (1974–2013). » Theoretical and Applied Climatology 130 (1-2). Theoretical and Applied Climatology: 163-172. doi:10.1007/s00704-016-1859-x.

Frechette D.M., Dugdale S.J., Dodson J.J. et Bergeron N.E. (2018) « Understanding summertime thermal refuge use by adult Atlantic salmon using remote sensing, river temperature monitoring, and acoustic telemetry1. » Canadian Journal of Fisheries and Aquatic Sciences 75 (11): 1999-2010. doi:10.1139/cjfas-2017-0422.

Gunn J. et Snucins E. (2010) « Brook charr mortalities during extreme temperature events in Sutton River, Hudson Bay Lowlands, Canada. » Hydrobiologia 650 (1): 79-84. doi:10.1007/s10750-010-0201-3.

Guo D. & Wang H. (2016) « CMIP5 permafrost degradation projection: A comparison among different regions. » Journal of Geophysical Research: Atmospheres 121: 4449-4517. doi:10.1002/2015JD024108.

Kaandorp V.P., Doornenbal P.J., Kooi H., Broers H.P., et de Louw P.G.B. (2019) « Temperature buffering by groundwater in ecologically valuable lowland streams under current and future climate conditions. » Journal of Hydrology X 3. The Authors: 100031. doi:10.1016/j.hydroa.2019.100031. https://doi.org/10.1016/j.hydroa.2019.100031.

Kalbus E., Reinstorf F. et Schirmer M. (2006) « Measuring methods for groundwater - Surface water interactions: A review. » Hydrology and Earth System Sciences 10 (6): 873-887. doi:10.5194/hess-10-873-2006.

Koven C.D., Riley W.J. & Stern A. (2013) « Analysis of permafrost thermal dynamics and response to climate change in the CMIP5 earth system models. » Journal of Climate 26 (6): 1877-1900. doi:10.1175/JCLI-D-12-00228.1.

Malard F., Tockner K. et Ward J.V. (1999) « Shifting dominance of subcatchment water sources and flow paths in a glacial floodplain, Val Roseg, Switzerland. » Arctic, Antarctic, and Alpine Research 31 (2): 135-150. doi:10.2307/1552602.

Rosenberry D.O. et LaBaugh J.W. (2008) « Field Techniques for Estimating Water Fluxes Between Surface Water and Ground Water » Techniques and Methods 4 – D2 rapport. U.S. Geological Survey. s.l.: s.n.

Simon N., Bour O., Lavenant N., Porel G., Nauleau B., Pouladi B., Longuevergne L. et Crave A. 2021. « Numerical and Experimental Validation of the Applicability of Active-DTS Experiments to Estimate Thermal Conductivity and Groundwater Flux in Porous Media. » Water Resources Research 57 (1): 1-27. doi:10.1029/2020WR028078.

7 ANNEXE I : DONNÉES GÉOCHIMIQUES

De nombreuses mesures sur le terrain ont été collectées au cours de cette étude et plusieurs échantillons de sol et d'eau ont été prélevés sur les sites d'étude des rivières Sainte-Marguerite et Bérard pour des analyses plus approfondies en laboratoire. Dans ce chapitre, vous trouverez les résultats d'analyses de laboratoire qui sont mentionnés mais non présentés dans les chapitres précédents et aussi certaines mesures sur le terrain qui sont mentionnées dans les chapitres précédents mais qui n'ont pas été présentées en détail.

Des échantillons de GW provenant de cinq piézomètres installés sur chaque site d'étude et de deux échantillons en plus des rivières ont été collectés. Les échantillons d'eau ont été analysés pour les métaux (Al, As, Ba, Be, Ca, Cd, Co, Cr, Cu, Fe, K, Mg, Mn, Mo, Na, Ni, P, Pb, S, Sb, Se, Si). , Sc, Sn, Sr, Ti, U, V, Zn, Sb, Be, Ag, Tl), les anions (Cl^-, NO_3, NO_2, Br^-, PO_4, SO_4, F), l'alcalinité ($CaCO_3$), le pH, la conductivité électrique, le carbone organique dissout (COD) et le carbone inorganique dissout (CID).

En se basant sur les résultats de l'analyse chimique, la concentration de tous les paramètres se situait dans la fourchette des rivières naturelles et aucune contamination n'a été détectée dans les rivières. Par conséquent, le transport des contaminants, qui constituait une étape possible de cette étude, n'a pas été effectué.

Tableau 7.1 Concentration d'anions, l'alcalinité, le pH, la conductivité électrique, le carbone organique et inorganique détectés dans les échantillons d'eau de la rivière Sainte-Marguerite.

	Br	Cl	F	NO2	NO3	SO4	PO4	Alcalinité	pH	Conductivité	COD	CID
	(mg/L)	(mg/L)	(mg/L)	(mg/L)	(mg/L)	(mg/L)	(mg/L)	(mg/L CaCO3)	-	(µS/cm)	(mg C/L)	(mg C/L)
Limite détection	0.002	0.005	0.004	0.002	0.003	0.005	0.005	1	-	-	0.05	0.05
Limite incluant dilution A	-	-	-	-	-	-	-	-	-	-	0.5	-
StMR-P1	< 0.002	0.547	0.050	< 0.002	0.458	4.691	< 0.005	25	6.33	68.4	2.3	6.23
StMR-P2	< 0.002	0.551	0.043	< 0.002	0.009	2.993	< 0.005	58	6.24	129.4	2	13.4
StMR-P3	< 0.002	0.587	0.068	< 0.002	0.548	3.846	< 0.005	13	5.91	42.3	2.7	3.2
StMR-P4	0.009	1.374	0.274	< 0.002	0.068	9.181	< 0.005	49	7.68	128.2	1.81	12.5
StMR-P5	0.022	1.981	0.339	< 0.002	0.018	9.515	< 0.005	63	8.31	162.8	0.91	15.9
StMR-SW-C	< 0.002	1.152	0.031	< 0.002	0.155	1.631	< 0.005	8	6.6	29.1	4.5	2.2
StMR-SW-S	< 0.002	1.095	0.034	< 0.002	0.183	1.596	< 0.005	8	6.67	29.2	4.7	2.2
StMR-SW-C (unfiltered)	-	-	-	-	-	-	-	-	-	-	-	-
StMR-SW-S (unfiltered)	-	-	-	-	-	-	-	-	-	-	-	-
StMR-P2-Z (duplicate)	< 0.002	0.591	0.051	< 0.002	0.408	4.701	< 0.005	25	6.26	71.3	2.3	7.04

Tableau 7.2 Concentration d'anions, l'alcalinité, le pH, la conductivité électrique, le carbone organique et inorganique détectés dans les échantillons d'eau de la rivière Bérard.

	Br	Cl	F	NO2	NO3	SO4	PO4	Alcalinité	pH	Conductivité	COD	CID
	(mg/L)	(mg/L)	(mg/L)	(mg/L)	(mg/L)	(mg/L)	(mg/L)	(mg/L CaCO3)	-	(µS/cm)	(mg C/L)	(mg C/L)
Limite détection	0.002	0.005	0.004	0.002	0.003	0.005	0.007	1	-	-	0.05	0.05
Limite incluant dilution A	-	-	-	-	-	-	-	-	-	-	0.5	-
BR-P1	< 0.002	6.056	0.041	interf	2.284	9.087	< 0.007	-	-	-	-	-
BR-P2	< 0.002	1.587	0.029	interf	0.608	4.399	< 0.007	35	7.14	86.5	1.12	9.51
BR-P3	< 0.002	0.764	0.026	interf	0.458	0.918	< 0.007	39	7.46	87.8	0.56	9.27
BR-P4	< 0.002	1.493	0.033	interf	3.351	4.478	< 0.007	43	7.16	110.2	0.82	12.05
BR-P5	< 0.002	1.483	0.032	interf	0.549	4.243	0.017	73	7.66	164.9	0.70	18.25
BR-SW1	< 0.002	1.671	0.032	interf	0.490	4.573	< 0.007	45	7.16	115.1	0.80	12.37
BR-SW2	< 0.002	1.495	0.026	interf	0.737	4.186	< 0.007	31	7.14	77.2	2.20	7.98
BR-SW1-UF (unfiltered)	-	-	-	-	-	-	-	-	-	-	-	-
BR-SW2-UF (unfiltered)	-	-	-	-	-	-	-	-	-	-	-	-
BR-P2-Z (duplicate)	< 0.002	1.321	0.029	interf	0.460	4.302	< 0.007	35	6.91	84.1	1.16	9.46

Tableau 7.4 Concentration des métaux détectés dans les échantillons d'eau de la rivière Sainte-Marguerite.

	Al	75As	Ba	9Be	Ca	111Cd	59Co	Cr	52Cr	Cu	63Cu	65Cu	Fe	K	Mg	Mn	95Mo	98Mo	Na	Ni	60Ni	P	208Pb	S	121Sb	82Se	Si	118Sn	Sr	49Ti	205Tl	51V	Zn	66Zn	107Ag	109Ag	238U
	(mg/L)	(µg/L)	(mg/L)	(µg/L)	(mg/L)	(µg/L)	(µg/L)	(mg/L)	(µg/L)	(mg/L)	(µg/L)	(µg/L)	(mg/L)	(mg/L)	(mg/L)	(mg/L)	(µg/L)	(µg/L)	(mg/L)	(mg/L)	(µg/L)	(mg/L)	(µg/L)	(mg/L)	(µg/L)	(µg/L)	(mg/L)	(µg/L)	(mg/L)	(µg/L)	(µg/L)	(µg/L)	(mg/L)	(µg/L)	(µg/L)	(µg/L)	(µg/L)
Limite détection	0.0005	0.008	0.00004	0.003	0.007	0.004	0.005	0.0003	0.02	0.0005	0.007	0.008	0.0003	0.03	0.002	0.00003	0.008	0.008	0.02	0.0005	0.009	0.009	0.003	0.02	0.008	0.04	0.01	0.009	0.0003	0.02	0.003	0.003	0.0003	0.05	0.002	0.002	0.004
Limite incluant dilution A	-	0.024	-	0.009	-	0.012	0.015	-	0.06	-	0.021	0.024	-	-	-	-	0.024	0.024	-	-	0.027	-	0.009	-	0.024	0.12	-	0.027	-	0.06	0.009	0.009	-	0.15	0.006	0.006	0.012
StMR-P1	0.041	0.040	0.012	0.004	10.200	0.013	0.167	< 0.0003	0.290	0.001	0.540	0.560	0.039	0.380	0.982	0.001	0.180	0.180	1.280	0.003	2.820	< 0.009	0.067	1.600	0.011	< 0.04	5.270	< 0.009	0.043	0.370	0.004	0.615	0.001	1.040	< 0.002	< 0.002	0.143
StMR-P2	0.024	0.103	0.026	0.005	22.900	< 0.004	0.512	< 0.0003	0.360	< 0.0005	0.300	0.340	0.739	0.480	0.926	0.021	0.176	0.180	1.300	0.005	4.640	< 0.009	0.392	0.970	0.018	< 0.04	6.280	< 0.009	0.074	0.420	< 0.003	1.440	0.004	3.770	< 0.002	< 0.002	0.065
StMR-P3	0.081	0.043	0.019	0.012	5.350	0.028	0.755	0.001	1.430	0.001	0.580	0.580	0.100	0.250	0.769	0.005	0.320	0.320	1.070	0.007	7.070	0.019	0.038	1.260	0.015	0.050	4.990	< 0.009	0.026	0.320	0.006	0.373	0.005	3.720	< 0.002	< 0.002	0.142
StMR-P4	0.035	0.103	0.009	< 0.003	18.300	0.029	0.070	< 0.0003	0.480	< 0.0005	0.200	0.230	0.046	1.440	2.790	0.008	3.330	3.330	2.520	0.001	1.100	0.050	0.079	3.430	0.009	0.060	5.650	< 0.009	0.091	0.270	< 0.003	0.910	0.006	3.370	< 0.002	< 0.002	0.067
StMR-P5	0.016	0.030	0.014	< 0.003	23.200	0.014	0.043	< 0.0003	0.500	< 0.0005	1.430	1.450	0.034	1.500	3.530	0.017	3.690	3.690	2.850	< 0.0005	0.450	0.038	0.142	4.060	0.008	0.090	5.860	0.162	0.102	0.440	< 0.003	0.783	0.010	10.800	< 0.002	< 0.002	0.044
StMR-SW-C	0.146	0.089	0.008	0.009	3.520	0.017	0.053	< 0.0003	0.155	< 0.0005	0.290	0.290	0.109	0.155	0.401	0.005	0.108	0.109	1.210	< 0.0005	0.250	0.016	0.109	0.590	0.020	0.040	2.610	< 0.009	0.019	0.700	0.005	0.230	0.006	6.110	< 0.002	< 0.002	0.048
StMR-SW-S	0.147	0.090	0.007	0.008	3.550	0.015	0.057	< 0.0003	0.320	0.001	0.350	0.360	0.112	0.090	0.402	0.006	0.099	0.101	1.210	< 0.0005	0.270	0.012	0.121	0.560	0.022	0.040	2.630	< 0.009	0.019	0.740	0.004	0.243	0.004	3.490	< 0.002	< 0.002	0.050
StMR-SW-C (unfiltered)	0.131	0.087	0.008	0.007	4.290	0.032	0.084	0.009	7.870	0.001	0.510	0.510	0.162	0.230	0.456	0.009	0.865	0.873	1.400	0.002	2.570	0.010	0.128	0.620	0.019	< 0.04	2.700	< 0.009	0.021	0.820	0.004	0.297	0.024	23.500	< 0.002	< 0.002	0.055
StMR-SW-S (unfiltered)	0.132	0.084	0.008	0.007	4.060	0.012	0.069	< 0.0003	0.330	< 0.0005	0.260	0.270	0.140	0.130	0.450	0.008	0.119	0.115	1.380	< 0.0005	0.250	< 0.009	0.314	0.600	0.018	0.040	2.690	< 0.009	0.021	0.780	0.003	0.261	0.003	2.400	< 0.002	< 0.002	0.054
StMR-P2-Z (duplicate)	0.044	0.040	0.012	0.004	10.200	0.011	0.177	< 0.0003	0.290	0.001	0.520	0.540	0.040	0.360	0.980	0.001	0.180	0.174	1.280	0.003	2.850	< 0.009	0.180	1.580	0.013	< 0.04	5.280	< 0.009	0.043	0.340	0.003	0.613	0.002	1.520	< 0.002	< 0.002	0.142

Tableau 7.3 Concentration des métaux détectés dans les échantillons d'eau de la rivière Bérard.

	Al	75As	Ba	9Be	Ca	111Cd	59Co	Cr	52Cr	Cu	63Cu	65Cu	Fe	K	Mg	Mn	95Mo	98Mo	Na	Ni	60Ni	P	208Pb	S	121Sb	82Se	Si	118Sn	Sr	49Ti	205Tl	51V	Zn	66Zn	107Ag	109Ag	238U
	(mg/L)	(µg/L)	(mg/L)	(µg/L)	(mg/L)	(µg/L)	(µg/L)	(mg/L)	(µg/L)	(mg/L)	(µg/L)	(µg/L)	(mg/L)	(mg/L)	(mg/L)	(mg/L)	(µg/L)	(µg/L)	(mg/L)	(mg/L)	(µg/L)	(mg/L)	(µg/L)	(mg/L)	(µg/L)	(µg/L)	(mg/L)	(µg/L)	(mg/L)	(µg/L)	(µg/L)	(µg/L)	(mg/L)	(µg/L)	(µg/L)	(µg/L)	(µg/L)
Limite détection	0.001	0.02	0.00006	0.005	0.006	0.003	0.006	0.0003	0.02	0.0009	0.009	0.009	0.001	0.0007	0.002	0.00005	0.02	0.009	0.0006	0.0006	0.02	0.003	0.004	0.02	0.007	0.04	0.002	0.02	0.0002	0.008	0.005	0.002	0.0003	0.02	0.002	0.004	0.006
Limite incluant dilution A	-	0.08	-	0.02	-	0.012	0.024	-	0.08	-	0.036	0.036	-	-	-	-	0.08	0.036	-	-	0.08	-	0.016	-	0.028	0.16	-	0.08	-	0.032	0.02	0.008	-	0.08	0.008	0.016	0.024
BR-P1	0.016	-	0.025	-	39.500	-	-	< 0.0003	-	0.001	-	-	0.009	2.690	14.200	0.001	-	-	5.680	0.002	-	0.010	-	3.390	-	-	1.770	-	0.136	-	-	-	0.001	-	-	-	-
BR-P2	0.007	0.091	0.008	< 0.005	9.900	< 0.003	0.036	< 0.0003	0.200	< 0.0009	0.550	0.560	0.006	0.778	3.280	0.000	0.180	0.173	1.400	< 0.0006	0.540	< 0.003	0.045	1.380	0.030	0.060	0.881	< 0.02	0.026	0.200	< 0.005	0.086	0.001	4.000	< 0.002	< 0.004	0.062
BR-P3	0.015	0.086	0.004	< 0.005	9.170	< 0.003	0.060	< 0.0003	0.290	< 0.0009	0.390	0.390	0.011	0.597	3.530	0.001	0.220	0.220	0.746	0.001	0.660	0.008	0.029	0.300	0.039	< 0.04	0.928	< 0.016	0.017	0.510	< 0.005	0.095	0.002	3.460	< 0.002	< 0.004	0.052
BR-P4	0.007	0.060	0.008	< 0.005	11.900	< 0.003	0.021	< 0.0003	0.151	< 0.0009	0.500	0.500	0.005	0.782	4.190	0.000	0.290	0.300	1.910	0.001	0.350	< 0.003	0.008	1.420	0.023	0.080	0.879	< 0.02	0.031	0.132	< 0.005	0.065	0.002	1.360	< 0.002	< 0.004	0.130
BR-P5	0.014	0.120	0.007	< 0.005	18.100	< 0.003	0.062	0.001	1.070	< 0.0009	0.310	0.330	0.010	1.050	7.030	0.001	0.330	0.340	1.600	< 0.0006	0.650	0.004	0.006	1.340	0.030	0.080	0.971	< 0.02	0.044	0.169	< 0.005	0.150	0.000	0.410	< 0.002	< 0.004	0.330
BR-SW1	0.005	0.076	0.008	< 0.005	12.700	< 0.003	0.017	< 0.0003	0.050	< 0.0009	0.420	0.420	< 0.001	0.791	4.400	0.000	0.200	0.210	1.700	< 0.0006	0.210	0.009	0.016	1.440	0.030	0.070	0.862	< 0.02	0.032	0.116	< 0.005	0.065	0.001	1.530	< 0.002	< 0.004	0.143
BR-SW2	0.005	0.117	0.007	< 0.005	9.040	< 0.003	0.030	< 0.0003	0.420	< 0.0009	0.490	0.500	0.013	0.543	3.100	0.001	0.270	0.270	1.420	< 0.0006	0.270	0.006	0.097	1.360	0.030	0.050	0.608	< 0.02	0.024	0.200	< 0.005	0.078	0.001	1.460	< 0.002	< 0.004	0.108
BR-SW1-UF (unfiltered)	0.007	0.076	0.008	< 0.005	12.600	< 0.003	0.016	< 0.0003	0.060	< 0.0009	0.500	0.520	0.002	0.794	4.380	0.000	0.176	0.180	1.700	< 0.0006	0.210	0.004	0.021	1.430	0.024	0.070	0.859	< 0.02	0.032	0.168	< 0.005	0.068	0.001	0.740	< 0.002	< 0.004	0.190
BR-SW2-UF (unfiltered)	0.013	0.110	0.007	< 0.005	9.200	< 0.003	0.038	< 0.0003	0.240	0.001	0.500	0.500	0.033	0.543	3.120	0.002	0.220	0.230	1.420	< 0.0006	0.270	0.004	0.124	1.330	0.020	0.070	0.616	< 0.02	0.024	0.670	< 0.005	0.084	0.001	1.130	< 0.002	< 0.004	0.130
BR-P2-Z (duplicate)	0.008	0.100	0.009	< 0.005	9.820	0.004	0.116	< 0.0003	0.410	< 0.0009	0.740	0.760	0.012	0.791	3.270	0.001	0.210	0.210	1.420	0.001	1.390	< 0.003	0.047	1.380	0.030	0.060	0.889	< 0.02	0.027	0.142	< 0.005	0.086	0.008	8.750	< 0.002	< 0.004	0.062

8 ANNEXE II : PROPRIETES THERMIQUES

Des échantillons de sol en conditions réelles provenant du lit de la rivière et des berges de la rivière ont été prélevés dans des cylindres de cuivre de 7 cm de diamètre et de 15 cm de hauteur pour chaque zone d'étude. Les échantillons ont été collectés à partir de trous percés à la main à l'aide d'une tarière manuelle allant de 10 à 2,5 m de profondeur.

La conductivité thermique et la capacité thermique des échantillons ont été mesurées à l'aide d'une sonde à double aiguille d'un appareil KD2 Pro (Decagon Devices Inc., 2016). Les échantillons ont été initialement testés dans des conditions in situ tel que récoltés sur le terrain.

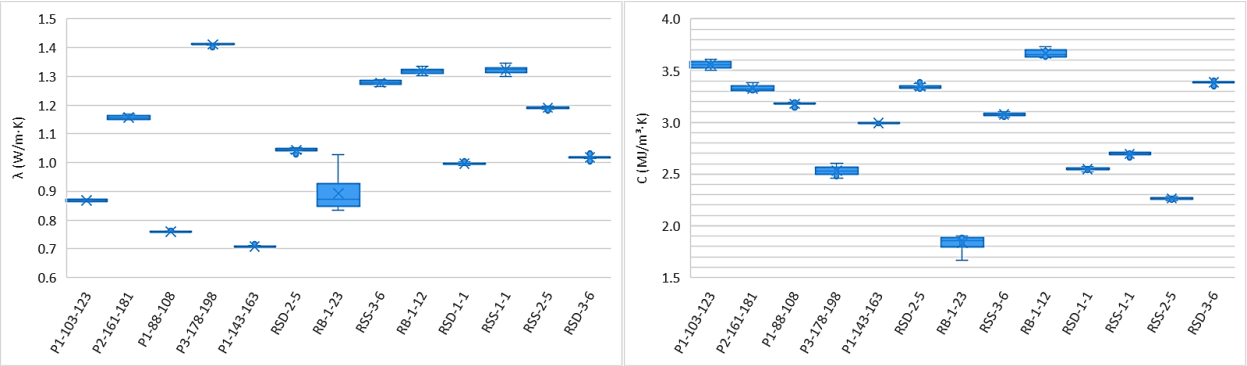

Figure 8.1 **Conductivité thermique (à gauche) et capacité thermique (à droite) des échantillons de sol de la rivière Sainte-Marguerite en condition in situ tel que récoltés sur le terrain.**

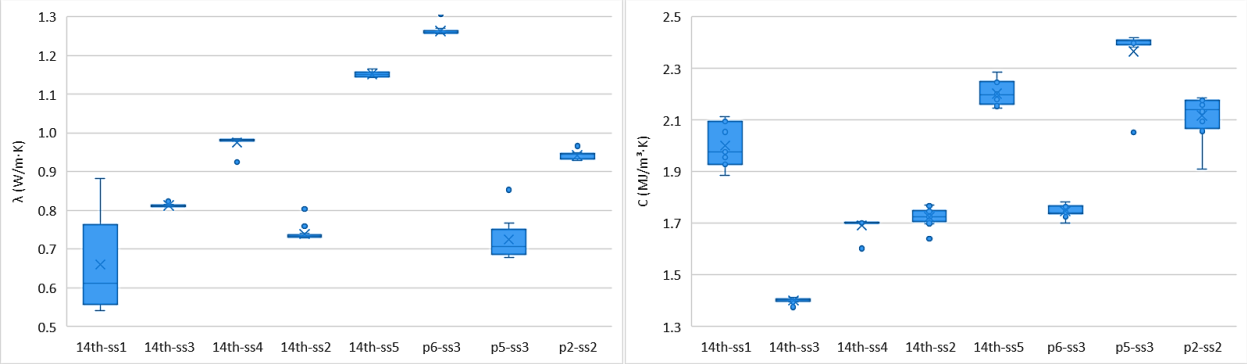

Figure 8.2 **Conductivité thermique (à gauche) et capacité thermique (à droite) des échantillons de sol de la rivière Bérard en conditions in situ tel que récoltés sur le terrain.**

Ultérieurement, quatre échantillons sélectionnés de chaque site ont été choisis pour une analyse en conditions sèches et complètement saturées. L'effet de la saturation en eau s'est avéré significatif. Ces analyses étaient importantes, car dans les modèles développés, les propriétés thermiques des solides composant le sol et l'eau ont été définies comme intrants.

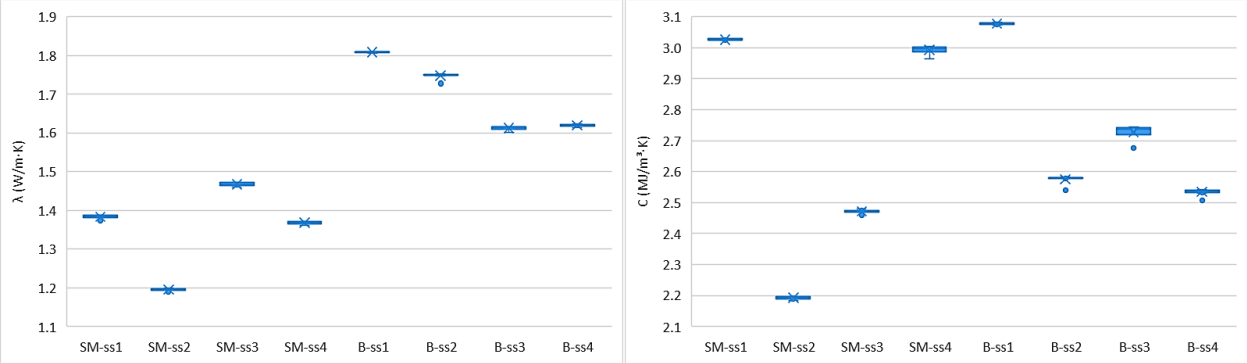

Figure 8.3 **Conductivité thermique (à gauche) et capacité thermique (à droite) d'échantillons de sol des rivières Sainte-Marguerite (SM-ss#) et Bérard (B-ss#) en condition complètement saturée.**

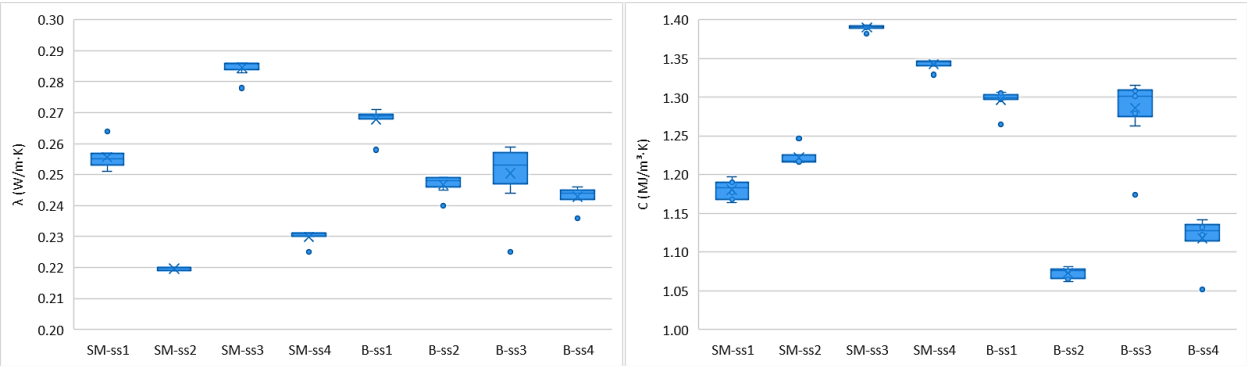

Figure 8.4 **Conductivité thermique (à gauche) et capacité thermique (à droite) d'échantillons de sol des rivières Sainte-Marguerite (SM-ss#) et Bérard (B-ss#) en condition complètement sèche.**

9 ANNEXE III : PROPRIETES HYDRAULIQUES

La conductivité hydraulique des échantillons de sol collectés a été quantifiée par des tests de perméabilité à charge constante et à charge tombante ou tests Darcy inversés (Head, 1982).

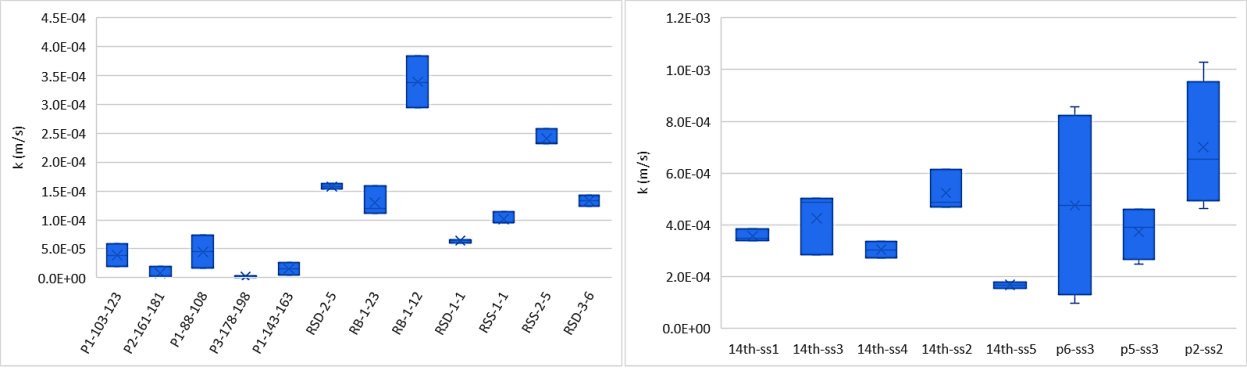

Figure 9.1 **Conductivité hydraulique des échantillons de déversements collectés dans la rivière Sainte-Marguerite (à gauche) et de la rivière Bérard (à droite) basée sur des essais de perméabilité.**

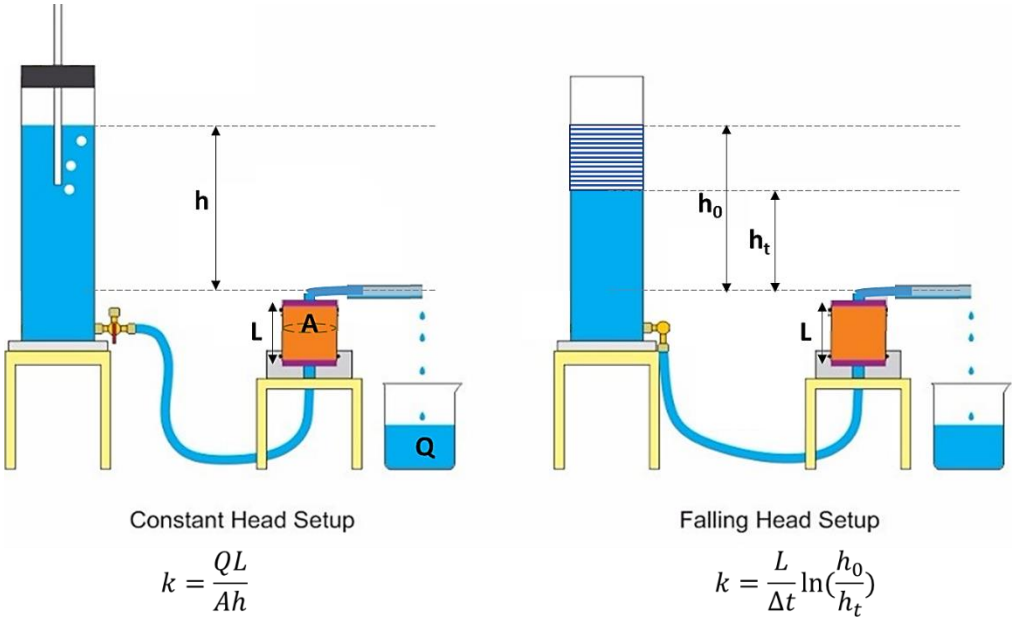

Figure 9.2 **Configuration pour les essais de perméabilité à charge constante et descendante.**

Des essais à choc hydraulique ont également été effectués dans les piézomètres installés pour quantifier la conductivité hydraulique. Ces essais in situ ont été réalisés en laissant tomber une tige en PVC dans les piézomètres et en surveillant la remontée des niveaux d'eau dans les piézomètres à l'aide d'enregistreurs de pression acquérant des données toutes les demi-secondes. Les données ont été analysées selon la méthode de Bouwer et al. (1976) pour les

aquifères non confinés. L'analyse des essais à choc hydraulique offrent un aperçu de la conductivité hydraulique horizontale tandis que les essais en colonne suivant la loi de Darcy ont permis d'évaluer la conductivité hydraulique verticale.

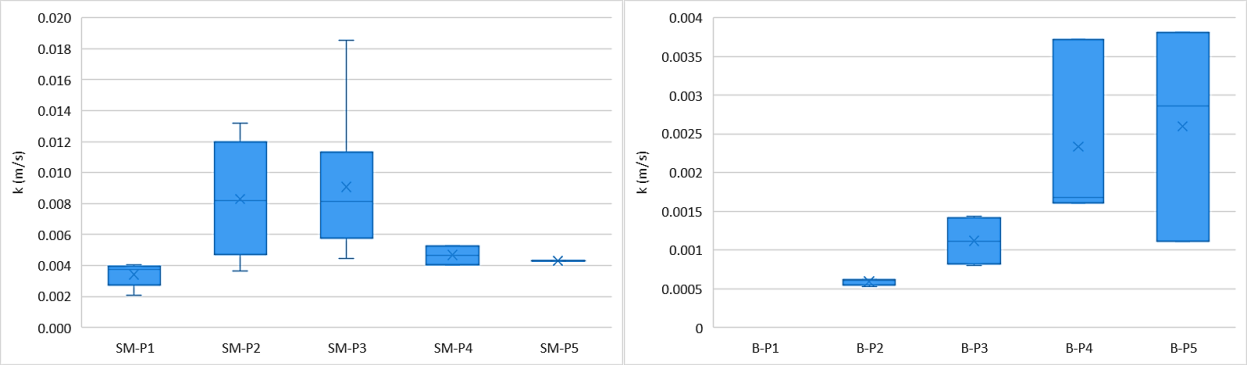

Figure 9.3 **Conductivité hydraulique calculée avec les essais lugeons dans les piézomètres de la rivière Sainte-Marguerite (à gauche) et de la rivière Bérard (à droite).**

La conductivité hydraulique verticale calculée était dix fois plus petite que la conductivité hydraulique horizontale. Par conséquent, ce facteur a été appliqué dans les modèles en tant que facteur d'anisotropie.

10 ANNEXE IV : DÉBIT DE LA RIVIÈRE

Le débit de la rivière a été mesuré avec un appareil Acoustic Doppler Current Profiler ou ADCP (Teledyne RD Instruments, 2008) et les données acquises ont été interprétées avec le logiciel WinRiver II (Teledyne RD Instruments, 2007). Le débit de la rivière a été mesuré sur différentes sections transversales des rivières étudiées avec au moins 2 passages sur chaque section transversale. Un exemple d'une des données interprétées de la meilleure mesure pour les rivières Sainte-Marguerite et Bérard est présenté ci-dessous.

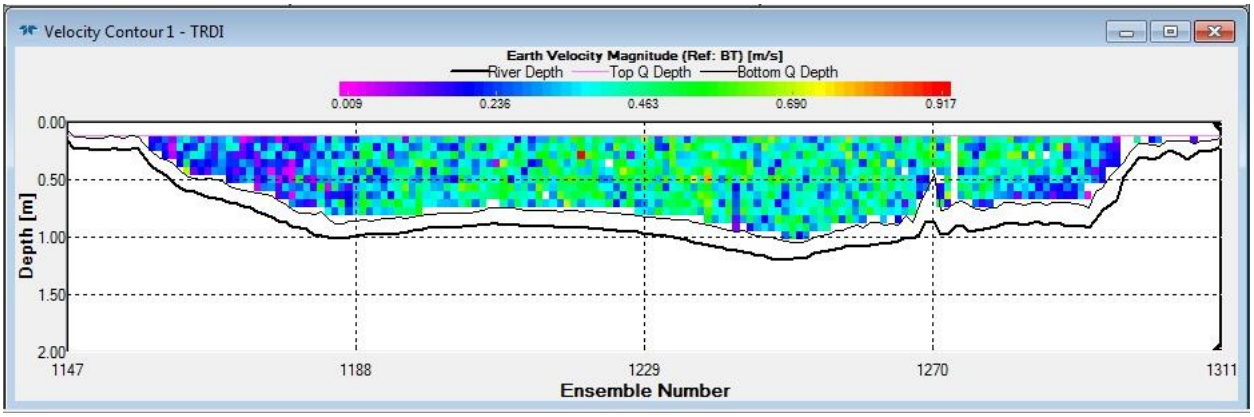

Figure 10.1 Exemple de débit de la rivière Sainte-Marguerite de 6,5 m^3/s mesuré avec appareil ADCP.

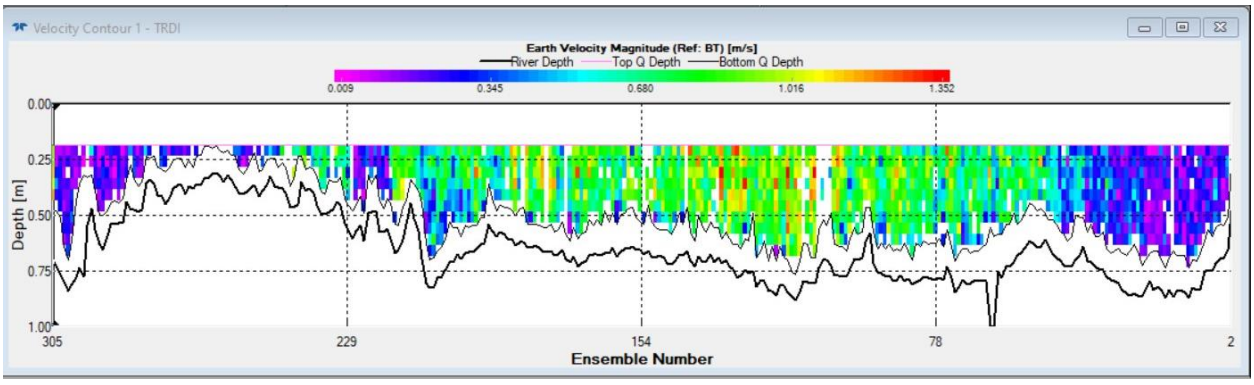

Figure 10.2 Exemple de débit de la rivière Berard de 18,5 m^3/s mesuré avec appareil ADCP.

Le nombre de cellules défectueuses sans données pour la rivière Bérard était plus élevé, car le dispositif ADCP utilisé était petit et n'était pas conçu pour les grandes rivières à fort débit telles que la rivière Bérard. L'utilisation d'un appareil ADCP plus grand avec un bateau flottant plus stable pour les mesures du débit de la rivière Bérard est suggérée pour les travaux futurs.

11 ANNEXE V : DONNÉES GÉOPHYSIQUE

La tomographie de résistivité électrique ou ERT (Loke, 2004) a été utilisée près de la rivière Sainte-Marguerite pour l'approximation de la profondeur de l'aquifère et l'interprétation géologique. Les investigations ont été planifiées en utilisant le logiciel Electre Pro (IRIS INSTRUMENTS, 2023a). Le sondage le plus long avec un nombre maximum d'électrodes de 96 pourrait potentiellement atteindre une profondeur d'investigation d'environ 145 m. Les données acquises ont ensuite été analysées dans le logiciel Prosys II (IRIS INSTRUMENTS, 2023b). Les principaux résultats du levé le plus long n'ont pas montré la profondeur du substrat rocheux qui devait être d'environ 50 à 60 m sur la base des coupes géologiques disponibles dans les parties en aval de la rivière Sainte-Marguerite, près de Sacré-Cœur (CERM, 2015).

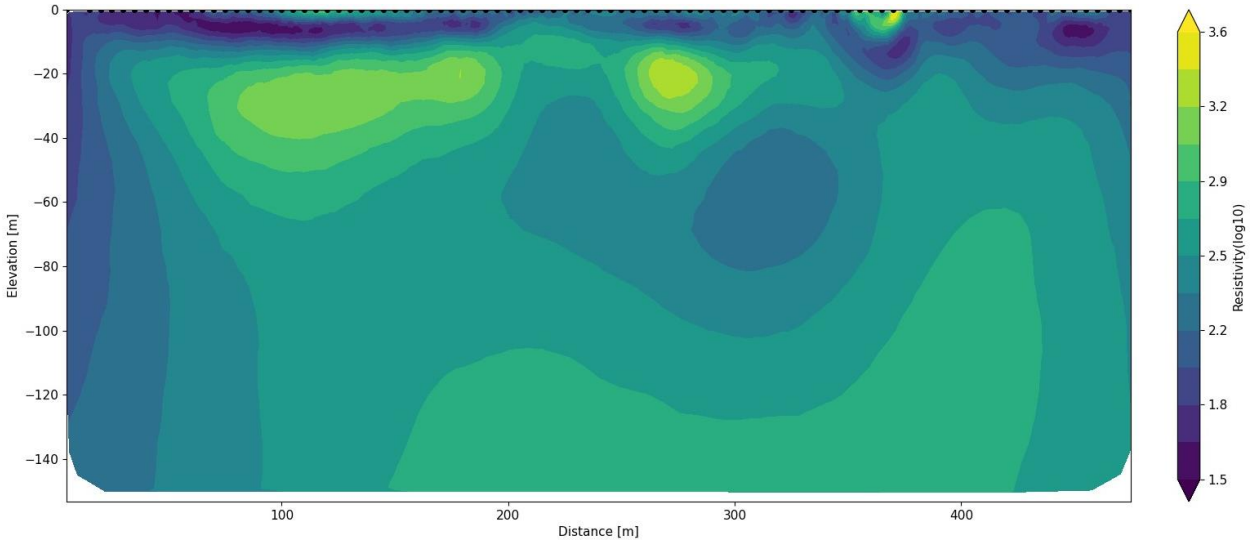

Figure 11.1 Exemple d'analyse ERT le long de la rivière Sainte-Marguerite.

La profondeur d'investigation de 145 m a été obtenue en supposant que toutes les électrodes étaient placées sur une ligne droite. Si des facteurs de correction sont appliqués dans l'analyse, la profondeur d'investigation sera moindre. En outre, le type de fonction de réseau appliquée joue un rôle dans la profondeur maximale d'investigation. En raison des difficultés d'application des mesures ERT près de la rivière (absence d'une ligne droite claire, présence de racines d'arbres et de rochers dans le sol, etc.) et des résultats primaires insatisfaisants, l'analyse des mesures ERT n'a pas été poursuivie.

Le radar à pénétration de sol (GPR) avec l'utilisation de l'unité de contrôle MALA Professional Explorer et MALA XV Monitor (MALA Geoscience, 2023) a été appliqué près de la rivière Bérard

au lieu de l'ERT en raison de la difficulté d'expédier le lourd équipement ERT au nord du Québec et de la possibilité de comparer les mesures GPR aux mesures précédentes effectuées à Tasiujaq par Allard et al. 2020. Contrairement aux mesures GPR précédentes qui ont été effectuées sur les routes, nous avons effectué les levés GPR le long de la rivière, puisque la géologie et la profondeur des sédiments près de la rivière nous intéressaient. Les données acquises ont ensuite été analysées dans le logiciel Reflexw (Sandmeier, 2023). En raison de la présence d'une végétation dense, de gros rochers et d'un sol plat près de la rivière, les données collectées n'ont pas montré clairement les couches de sédiments souterrains et les données n'étaient pas d'une qualité suffisante pour permettre une étude détaillée de la profondeur de la couche active sans l'application de méthodes et de facteurs de correction.

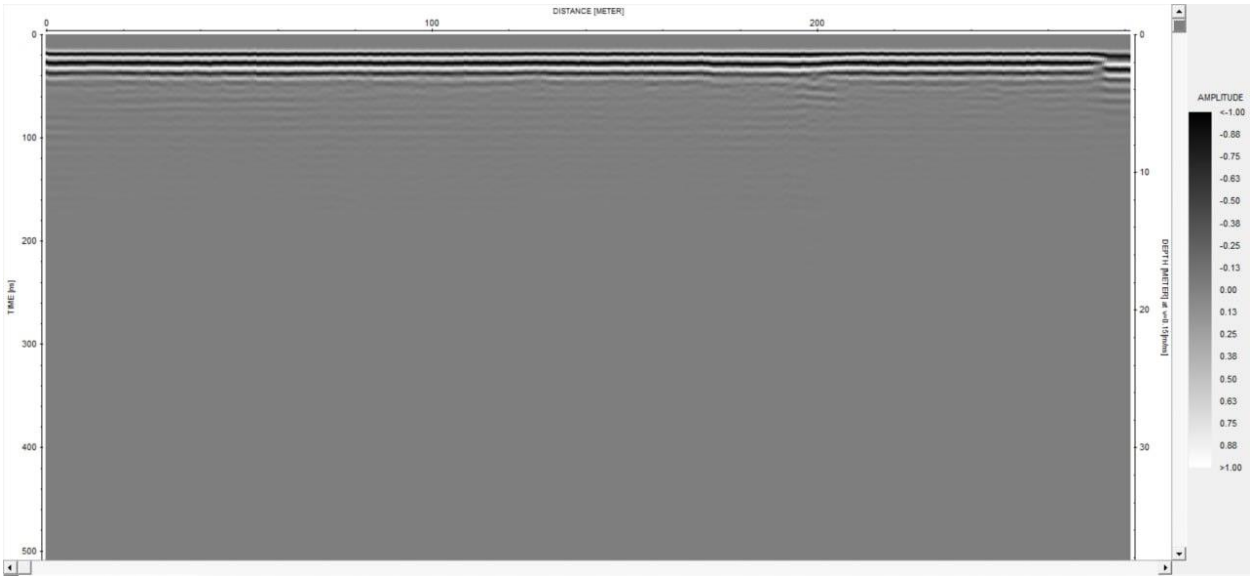

Figure 11.2 Exemple d'analyse GPR près de la rivière Berard.

12 RÉFÉRENCES EN ANNEXES

CERM. 2015. « Coupes stratigraphique. » Online Geological Map dataset, Équipe de géomatique du Université du Québec à Chicoutimi. http://paces.uqac.ca/stratigraphie_chcn.html.

Decagon Devices, Inc., 2016. « KD2 Pro Thermal Properties Analyzer. » Manuel de l'appareil. Decagon Devices, Inc., WA, United States https://library.metergroup.com/Manuals/13351_KD2%20Pro_Web.pdf.

Head, K.H., 1982, « Manual of soil laboratory testing. », Vol 2, Pentech Press, ISBN 0-7273-1305-3.

IRIS INSTRUMENTS, 2023a. « Electre Pro Software » Manuel de logiciel. IRIS INSTRUMENTS, France. https://www.iris-instruments.com/Pdf_file/ElectrePro_Gb.pdf.

IRIS INSTRUMENTS, 2023b. « Prosys II Software » Manuel du logiciel. IRIS INSTRUMENTS, France. https://www.iris-instruments.com/Pdf_file/Prosys_Gb.pdf.

Loke, M.H., 2004. « Tutorial: 2-D and 3-D electrical imaging surveys ». Notes techniques, basées sur Loke, M.H., thèse de doctorat 1994, Université de Birmingham. https://sites.ualberta.ca/~unsworth/UA-classes/223/loke_course_notes.pdf.

MALA Geoscience, 2023. « ProEx - Professional Explorer Control Unit Operating Manual v. 2.0. » Manuel de l'appareil. MALÅ Geoscience USA, Inc., SC, United States. P/N 19-001030.

Sandmeier, K.J., 2023. « REFLEXW Version 6.0 Windows™ 9x/NT/2000/XP/7-programfor the processing ofseismic, acoustic or electromagneticreflection, refraction and transmission data » Manuel du logiciel. Sandmeier geophysical research, Germany. https://www.sandmeier-geo.de/reflexw.html.

Teledyne RD Instruments, 2007. « WinRiver II Quick Start Guide. » Manuel du logiciel. Teledyne RD Instruments, CA, United States. P/N 957-6230-00.

Teledyne RD Instruments, 2008. « StreamPro ADCP Operation Manual. » Manuel de l'appareil. Teledyne RD Instruments, CA, United States. P/N 95B-6003-00.

13 DISPONIBILITÉ DES DONNÉES

Les données brutes de différentes mesures telles que les températures enregistrées du sol et de l'eau, les séries chronologiques des niveaux d'eau, ERT, GPR et les emplacements GPS sont disponibles pour une utilisation future avec le lien suivant. Dans l'ensemble de données accessible à l'aide du lien fourni, vous pouvez également trouver les modèles COMSOL complets expliqués au chapitre 5.

https://doi.org/10.5683/SP3/S1LDNF

Ensemble de données également accessible en suivant :

Borealis>Institut national de la recherche scientifique (INRS)>Dataverse de Jasmin Raymon>ÉVALUATION DE LA CONTRIBUTION DES EAUX SOUTERRAINES À LA TEMPÉRATURE DES EAUX DE SURFACE DANS DES RIVIÈRES DU QUÉBEC NORDIQUE>